

**EXPERIMENTAL INVESTIGATION OF SOLID
FLOW PATTERN IN GAS-SOLID CIRCULATING
FLUIDIZED BED RISER**

A thesis

submitted in partial fulfillment of the requirements

for the degree of

DOCTOR OF PHILOSOPHY

By

TRILOKPATI TRIBEDI

(Roll no:166107008)



**DEPARTMENT OF CHEMICAL ENGINEERING
INDIAN INSTITUTE OF TECHNOLOGY GUWAHATI
GUWAHATI-781039**

April, 2024



CERTIFICATE

It is certified that the work contained in the thesis entitled “*Experimental Investigation of Solid Flow Pattern in Gas-Solid Circulating Fluidized Bed Riser*” by Trilokpati Tribedi, a student in the Department of Chemical Engineering, Indian Institute of Technology Guwahati, Guwahati, India, for the award of the degree of Doctor of Philosophy has been carried out under my supervision and this work has not been submitted elsewhere for the degree.



Dr. Pankaj Tiwari

Professor

Department Of Chemical Engineering,
Indian Institute of Technology Guwahati



Dr. Rajesh Kumar Upadhyay

Professor

Department of Chemical Engineering and
Technology
Indian Institute of Technology (BHU)
Varanasi

09-04-2024



Acknowledgments

Without the sincere believers in my potential and capabilities who provided opportunities, offered timely assistance, and unwaveringly supported me, submitting my thesis and obtaining this degree successfully would have remained out of reach and a distant dream . My heartfelt appreciation extends to the supervisors, teachers, family members, and friends who have helped me to turn this into reality and collectively paved the way for me to attain this level of accomplishment.

I am profoundly grateful and deeply indebted to my supervisor, Prof. Rajesh Kumar Upadhyay, from the Department of Chemical Engineering and Technology at IIT-BHU. His constant support and encouragement have been instrumental in guiding me throughout this challenging journey. His belief and trust instilled in me pushed me forward to confront and overcome all challenges at every juncture, both in my professional and personal spheres, nurturing my growth and development. I would also like to thank my supervisor, Prof. Pankaj Tiwari, for his excellent, persistent guidance, helpful suggestions, time-to-time advice, and the kind support offered throughout this project. His timely assistance was truly appreciated and marked a significant difference in my journey.

I extend my heartfelt gratitude to the esteemed members of my doctoral committee: Prof. Anugrah Singh, Prof. Raghvendra Gupta, and Prof. Pankaj Kalita, whose valuable comments and suggestions have been a constant source of guidance and encouragement throughout my research journey. The support and insights they provided have significantly enhanced the quality of my work. I am truly grateful to Dr. H. J. Pant from the Isotope and Radiation Applications Division BRAC Mumbai, for guiding and motivating me during

my research journey. His assistance in providing the exact measurements of radioactive particle tracers, vital for my research, is quite invaluable.

I would also like to acknowledge the current and former heads of the Department of Chemical Engineering, namely Prof. Kaustubha Mohanty, Prof. Anugrah Singh and Prof. Bishnupada Mandal, for their generous provision of access to the department's state-of-the-art facilities, which have been instrumental in the successful execution of my research endeavors. Also, I want to express my gratitude to Prof. V. L. Yadav, the Head of the Department of Chemical Engineering and Technology at IIT-BHU, for granting me permission to work there and also to Mr. R.C. Sachiv, Senior Technical Superintendent, IIT-BHU for providing immense assistance & help for facilitating the laboratory set-up for executing my research works successfully at IIT-BHU.

Moreover, I wish to express my sincere appreciation to the entire faculty of the Chemical Engineering Department, with a special mention to Dr. Prakash Kotecha and Prof. Subrata Kumar Majumdar.

Their engaging conversations, deep expertise, exceptional skills, and invaluable guidance, along with their timely assistance, have greatly enriched my understanding of the subject. This has propelled my research in significant directions and significantly improved the quality of my research and thesis projects.

I extend my heartfelt appreciation to Dr. Richa Sharma, Dr. Lipika Kala, and Dr. Jitendra Rawat for their invaluable guidance and support offered. I would also like to express my gratitude to my research group colleagues: Prem Sagar, Roushni Kumari, Keshav Kumar, Punampriya Borgohain, Sachin Viswakarma, Avishak Anand, and Anjali Boudh. I wish to genuinely thank Prem Sagar, Rukshar Parveen, Sakshi Garg, and Roushni Kumari for

assisting me with the experimental works at all stages. Their extended support and cooperation have enabled me to carry out and complete all the experiments in a large setup.

I draw immense strength from the unwavering support of my parents. Their constant shower of love, guidance, and encouragement acts as a driving force, pushing me to embrace every opportunity for growth and development and to strive for loftier goals. In the absence of their unshakable and firm belief in my potential and capabilities and the motivation they have instilled in me, I would not find myself composing this thesis. In addition to these, I would like to dedicate my heartfelt appreciation to my wife, Sanghamitra, for her consistent support throughout this tough phase of life. Her presence and inspiring words have been a pillar of strength, continuously propelling me forward on this academic journey and beyond.

Moreover, I would like to thank MHRD (Ministry of Human Resources and Development) for providing the assistantship during the period of my Ph.D.

At the end, I would like to express my gratitude to all of those who have helped me during the research works and stood beside me to guide and support me unconditionally.

Trilokpati Tribedi

Trilokpati Tribedi

IIT Guwahati

Abstract

Circulating fluidized bed (CFB) technology finds extensive applications across various industries, including petrochemical, chemical, fine chemical, metallurgical, and power generation. Its widespread use can be attributed to its exceptional heat and mass transfer capabilities, higher throughput rates, and operational versatility. CFBs are employed in various applications, each tailored to handle different levels of solid fluxes. Low-solid-flux CFBs are instrumental in processes such as drying, alumina calcination, and iron ore reduction. On the other hand, high-solid-flux CFBs are mostly used for fluid catalytic cracking (FCC), making maleic anhydride, burning gasifying coal and biomass, and chemical looping combustion, among other things. Although CFB has been in use for many decades, there is still a lack of fundamental knowledge. CFB is still designed empirically and scaled up based on experience rather than science. The complexity of gas-particle, particle-particle, and particle-wall interactions is primarily to blame for this. Geometry and scale have an impact on these interactions. There is a scarcity of detailed velocity flow field data especially in the case of Geldart Group B particles.

In the current work, radioactive particle tracking techniques and single particle residence time distribution are used to investigate the solid phase velocity field and solid mixing. Experiments are conducted at the bottom and middle sections of the risers, as well as at the laboratory and pilot-scale CFB setups. Lagrangian and Eulerian velocity flow field data are presented at the bottom and middle sections of the riser. Mean velocity, root mean square (RMS) velocities, granular temperature, stress and turbulence intensity are estimated for all conditions at both the bottom and the middle sections of the riser. It is found that solid motion is predominantly in the axial direction and mean radial motion is negligible. Though mean axial velocity is higher at the center irrespective of the operating conditions, mean velocity profiles are comparatively flat in the case of laboratory scale w.r.t. pilot scale riser.

Instantaneous velocity PDF plot shows that solid back mixing decreases with increasing gas velocity. However, in pilot scale riser, solid back mixing is comparatively higher under similar operating conditions. At the pilot scale riser, significant amount of particle downward motion is observed at a gas velocity of 7.6 m/s. However, in the case of the laboratory scale riser, solids' downward motion is not visible even at a gas velocity of 7 m/s; at below 7 m/s, the downward motion of solids is visible even though the mean motion is always in the upward direction.

Solid mixing is analyzed using residence time distribution study at different heights. It is observed that the solid mixing at the bottom section dominates the overall solid mixing. Increasing the solid flux at a constant gas velocity results in greater solid mixing, while decreasing the gas velocity at a constant solid flux also enhances mixing. However, solid flux has a lesser impact on solid mixing compared to gas velocity. A simplified scaling correlation is developed based on operating conditions to predict the solid phase mean velocity for Geldart Group B particles.

Table of Contents

	Page No
Abstract	iv
Table of Contents	v
List of Figures	viii
List of Tables	xv
CHAPTER 1: Introduction	1
Scope	1
1.1 Introduction to Fluidization	1
1.1.1 Regimes of Fluidization	2
1.1.2 Classification of Particles	5
1.2 Circulating Fluidized Bed	8
1.2.1 Applications of Circulating Fluidized Bed	9
1.3 Hydrodynamics of Circulating Fluidized Bed	10
1.3.1 Solids' Velocity	13
1.3.2 Solid Mixing	22
1.4 Scale Up of Circulating Fluidizing Bed	31
1.5 Motivation	32
1.6 Objectives	35
1.7 Structure of the Thesis	36
Notations	37
References	37
CHAPTER 2: Measurement Techniques in Fluidized Bed and Application of Radiotracer	47
Scope	47
2.1 Introduction	47
2.2 Invasive Techniques	48
2.2.1 Pressure	48
2.2.2 Capacitance probe	50
2.2.3 Optical fiber probe	50
2.3 Non-intrusive Techniques	51
2.3.1 X-ray or γ -ray Tomography	51
2.3.2 Electrical Capacitance Tomography	53
2.3.3 Laser Doppler Velocimetry (LDV)	54
2.3.4 Particle Image Velocimetry (PIV)	55
2.3.5 Positron Emission Particle Tracking (PEPT)	57
2.3.6 Radioactive Particle Tracking (RPT)	58
2.3.7 Selection of experimental technique in CFB	60
2.4 Radioactive Particle Tracking Technique and Velocity Measurements	61
2.4.1 RPT Setup Components	62
2.4.2 Methodology and Implementation of RPT	67
2.4.2.1 Arrangement of Detectors	67
2.4.2.2 Calibration	68
2.4.2.3 Monte Carlo method (Beam et al., 1978; Upadhyay, 2010)	69
2.4.2.4 Reconstruction Algorithm	73
2.4.2.5 Post Processing and Velocity Calculations	74

Notations	78
References	80
CHAPTER 3: Experimental Investigation on a Laboratory- Scale CFB Riser: Solid-phase Flow Fields and Mixing Characteristics	89
Scope	89
3.1 Introduction	89
3.2 Experimental Setup	93
3.3 Solid Flux Measurement	96
3.4 Radioactive Particle Tracking (RPT) Measurements	99
3.5 RPT Results and Discussion	104
3.5.1 Lagrangian Track of Particle Position	106
3.5.2 PDF of Instantaneous Velocity	114
3.5.3 Velocity Vector Plots	121
3.5.4 Ensemble Averaged Velocity	123
3.5.5 Solid Velocity Fluctuations	130
3.5.6 Granular Temperature	137
3.5.7 Solid Stress	143
3.5.8 Turbulence Intensity	149
3.6 Solids Mixing in Laboratory Scale Setup	152
3.6.1 Residence Time Distribution	156
3.6.2 Trajectory Length Distribution (TLD)	162
3.7 Summary	166
Notations	167
References	168
CHAPTER 4: Experimental Investigation on a Pilot-Scale CFB Riser: Solid-phase Flow Fields and Mixing Characteristics	175
Scope	175
4.1 Introduction	175
4.2 Experimental Setup	176
4.3 Solid Flux Measurement	179
4.4 Radioactive Particle Tracking (RPT) Measurements	183
4.5 RPT Results and Discussion	188
4.5.1 Lagrangian Track of Particle Position	189
4.5.2 PDF of Instantaneous Velocity	197
4.5.3 Velocity Vector Plots	204
4.5.4 Ensemble Averaged Velocity	205
4.5.5 Solid velocity fluctuations	212
4.5.6 Granular Temperature	218
4.5.7 Solid Stress	221
4.5.8 Turbulence Intensity	224
4.6 Solids Mixing in Laboratory Scale Setup	227
4.6.1 Residence time distribution	229
4.6.2 Trajectory Length Distribution (TLD)	233
4.7 Scale Up	236
4.8 Summary	240
Notations	243
References	244
CHAPTER 5: Conclusions and Recommendations	249
5.1 Conclusions	249
5.2 Recommendations and Future Directions	252

References	254
Appendix A: Axial Dispersion Model	255
Appendix B: Reproducibility and stationarity	258
BIO-DATA	261



List of Figures

Figure No.	Figure Title	Page No
Figure 1.1	Flow patterns in gas solids fluidized beds (adapted from Grace (1997))	5
Figure 1.2	Geldart classification of particles for air at ambient conditions (Geldart (1973))	6
Figure 1.3	Schematic diagram of a typical Circulating Fluidized Bed (CFB) setup	9
Figure 2.1	Schematic of the five-fiber optical probe (Zhu et al. 2001).	51
Figure 2.2	Schematic of the γ -ray Tomography	52
Figure 2.3	Schematic of Electrical capacitance tomography	53
Figure 2.4	Schematic of LDA technique	55
Figure 2.5	Schematic of PIV measurement technique	56
Figure 2.6	Schematic diagram of PEPT for a single particle (Parker and Fan 2008)	57
Figure 2.7	Typical configuration of the detectors around the fluidized bed for RPT	59
Figure 2.8	Schematic diagram of NaI(Tl) scintillation detector	65
Figure 2.9	Schematic diagram of data acquisition system	66
Figure 2.10	Schematic diagram for relative positioning of source and detector (a) when the source is outside detector flat face, and (b) within the detector flat face (Beam et al., 1778)	70
Figure 2.11	The four possible cases of travel of photons through the detector. (Beam et al., 1778)	72
Figure 2.12	Flow chart of RPT data acquisition and processing	75
Figure 3.1	Schematic diagram of laboratory-scale cold flow CFB setup	94
Figure 3.2	Photograph of laboratory-scale (a) overall CFB setup, (b) detector assembly at the middle section and (c) detector assembly at the bottom section	95
Figure 3.3	Schematic diagram of detectors and pressure probe assembly for solid flux measurement.	98
Figure 3.4	Contours of resolution and sensitivity for RPT experiments	100
Figure 3.5	Lagrangian track of tracer in a different plane	101
Figure 3.6	Azimuthally averaged (a) mean axial velocity, (b) mean radial velocity, (c) axial RMS velocity and (d) radial RMS velocity profiles with different grid sizes for operating condition of $G_s = 100 \text{ kg/m}^2\text{s}$ and $U_g = 8 \text{ m/s}$	102
Figure 3.7	Azimuthally averaged (a) mean axial velocity, (b) mean radial velocity, (c) axial RMS velocity and (d) radial RMS velocity profiles at different heights for operating condition of $G_s = 100 \text{ kg/m}^2\text{s}$ and $U_g = 8 \text{ m/s}$	103
Figure 3.8	Flow regime diagram (Bi and Grace, 1995) with operating conditions	105
Figure 3.9	Tracer particle motion for a track (a) without back mixing, (b) with back mixing and (c) internal recirculation.	106
Figure 3.10	Particle position after 50 and 100 milliseconds when the tracer enters the scan zone from the center	108

Figure 3.11	Particle position after 50 and 100 milliseconds when the tracer enters the scan zone from the wall region (solid inlet side)	109
Figure 3.12	Particle position after 50 and 100 milliseconds when the tracer enters the scan zone from the wall region (Opposite of solid inlet side)	110
Figure 3.13	Normalized number of occurrence contour plots at different heights and operating conditions at the bottom section	112
Figure 3.14	Normalized number of occurrence contour plots at different operating conditions at the middle section	113
Figure 3.15	Normalized histogram diagram of instantaneous velocity at three radial locations for the bottom section ($h = 0.2$ m) of the riser for lower gas velocities.	116
Figure 3.16	Normalized histogram diagram of instantaneous velocity at three radial locations for bottom section ($h = 0.2$ m) of the riser for higher gas velocities.	117
Figure 3.17	Normalized histogram diagram of instantaneous velocity at three radial locations for the bottom section ($h = 0.4$ m) of the riser for lower gas velocities.	118
Figure 3.18	Normalized histogram diagram of instantaneous velocity at three radial locations for the bottom section ($h = 0.4$ m) of the riser for higher gas velocities.	119
Figure 3.19	Normalized histogram diagram of instantaneous velocity at three radial locations for the middle section ($h = 1.6$ m) of the riser for lower gas velocities.	120
Figure 3.20	Normalized histogram diagram of instantaneous velocity at three radial locations for the middle section ($h = 1.6$ m) of the riser for higher gas velocities.	121
Figure 3.21	Velocity vector plot at the bottom section for different operating conditions	122
Figure 3.22	Velocity vector plot for the middle section for different operating conditions	123
Figure 3.23	Radial variation of azimuthally averaged mean axial velocity profile at the bottom section ($h = 0.2$ m) (a) effect of solid flux and (b) effect of inlet gas velocity	124
Figure 3.24	Radial variation of azimuthally averaged mean axial velocity profile at the bottom section ($h = 0.4$ m) (a) effect of solid flux and (b) effect of inlet gas velocity	126
Figure 3.25	Radial variation of azimuthally averaged mean axial velocity profile at the middle section ($h = 1.6$ m) (a) effect of solid flux and (b) effect of inlet gas velocity	127
Figure 3.26	Radial variation of azimuthally averaged mean radial velocity profile at the bottom section ($h = 0.2$ m) (a) effect of solid flux and (b) effect of inlet gas velocity	128
Figure 3.27	Radial variation of azimuthally averaged mean radial velocity profile at the bottom section ($h = 0.4$ m) (a) effect of solid flux and (b) effect of inlet gas velocity	129
Figure 3.28	Radial variation of azimuthally averaged mean radial velocity profile at the bottom section ($h = 1.6$ m) (a) effect of solid flux and (b) effect of inlet gas velocity	130

Figure 3.29	Radial variation of azimuthally averaged axial RMS velocity profile at the bottom section ($h = 0.2$ m) (a) effect of solid flux and (b) effect of inlet gas velocity	132
Figure 3.30	Radial variation of azimuthally averaged axial RMS velocity profile at the bottom section ($h = 0.4$ m) (a) effect of solid flux and (b) effect of inlet gas velocity	133
Figure 3.31	Radial variation of azimuthally averaged axial RMS velocity profile at the middle section ($h = 1.6$ m) (a) effect of solid flux and (b) effect of inlet gas velocity	134
Figure 3.32	Radial variation of azimuthally averaged radial RMS velocity profile at the bottom section ($h = 0.2$ m) (a) effect of solid flux and (b) effect of inlet gas velocity	135
Figure 3.33	Radial variation of azimuthally averaged radial RMS velocity profile at the bottom section ($h = 0.4$ m) (a) effect of solid flux and (b) effect of inlet gas velocity	136
Figure 3.34	Radial variation of azimuthally averaged radial RMS velocity profile at the middle section ($h = 1.6$ m) (a) effect of solid flux and (b) effect of inlet gas velocity	137
Figure 3.35	Radial variation of azimuthally averaged granular temperature profile at the bottom section ($h = 0.2$ m) (a) effect of solid flux and (b) effect of inlet gas velocity	139
Figure 3.36	Radial variation of azimuthally averaged granular temperature profile at the bottom section ($h = 0.4$ m) (a) effect of solid flux and (b) effect of inlet gas velocity	140
Figure 3.37	Radial variation of azimuthally averaged granular temperature profile at the middle section ($h = 1.6$ m) (a) effect of solid flux and (b) effect of inlet gas velocity	142
Figure 3.38	Radial variation of azimuthally averaged normal stress profile at the bottom section ($h = 0.2$ m) (a) effect of solid flux and (b) effect of inlet gas velocity	143
Figure 3.39	Radial variation of azimuthally averaged normal stress profile at the bottom section ($h = 0.4$ m) (a) effect of solid flux and (b) effect of inlet gas velocity	145
Figure 3.40	Radial variation of azimuthally averaged normal stress profile at the middle section ($h = 1.6$ m) (a) effect of solid flux and (b) effect of inlet gas velocity	146
Figure 3.41	Radial variation of azimuthally averaged shear stress at the bottom section ($h = 0.2$ m) (a) effect of solid flux and (b) effect of inlet gas velocity	147
Figure 3.42	Radial variation of azimuthally averaged shear stress at the bottom section ($h = 0.4$ m) (a) effect of solid flux and (b) effect of inlet gas velocity	148
Figure 3.43	Radial variation of azimuthally averaged shear stress at the middle section ($h = 1.6$ m) (a) effect of solid flux and (b) effect of inlet gas velocity	149
Figure 3.44	Radial variation of azimuthally averaged turbulence intensity at the bottom section ($h = 0.2$ m) (a) effect of solid flux and (b) effect of inlet gas velocity	150

Figure 3.45	Radial variation of azimuthally averaged turbulence intensity at the bottom section ($h = 0.4$ m) (a) effect of solid flux and (b) effect of inlet gas velocity	151
Figure 3.46	Radial variation of azimuthally averaged turbulence intensity at the middle section ($h = 1.6$ m) (a) effect of solid flux and (b) effect of inlet gas velocity	152
Figure 3.47	Detector arrangement for RTD experiment for laboratory scale riser	154
Figure 3.48	Count vs time data obtained at different detectors to find residence time of the particle in a particular zone	155
Figure 3.49	Flowchart to obtain the RTD curve from single particle tracking data: (a) histogram of time of flight, (b) normalized histogram and (c) E curve and Axial dispersion model fitting.	156
Figure 3.50	RTD for inlet section (D1-D2), inlet to start of the middle section (D1-D3), inlet to end of the middle section (D1-D3) and overall section of the riser (D1-D5)	159
Figure 3.51	RTD for inlet section (D1-D2), inlet to start of the middle section (D1-D3), inlet to end of the middle section (D1-D3) and overall section of the riser (D1-D5)	160
Figure 3.52	RTD for inlet section (D1-D2), inlet to start of the middle section (D1-D3), inlet to end of the middle section (D1-D3) and overall section of the riser (D1-D5)	161
Figure 3.53	Tracer trajectory for a single pass in the scan zone	163
Figure 3.54	Trajectory length distribution at (a) bottom section and (b) middle section	164
Figure 4.1	Schematic diagram of the experimental setup with detector assembly	178
Figure 4.2:	Photograph of (a) pilot scale circulating fluidized bed, (b) bottom section with detector assembly and (c) middle section with detector assembly	179
Figure 4.3:	Detector assembly at the dipleg to measure the solid flux	181
Figure 4.4:	Contours of resolution and sensitivity for RPT experiments	185
Figure 4.5:	Lagrangian track of tracer in a different plane	185
Figure 4.6:	Azimuthally averaged (a) mean axial velocity, (b) mean radial velocity, (c) axial RMS velocity and (d) radial RMS velocity profiles with different grid sizes for operating condition of $G_s = 150$ kg/m ² s and $U_g = 7.6$ m/s	187
Figure 4.7:	Azimuthally averaged (a) mean axial velocity, (b) mean radial velocity, (c) axial RMS velocity and (d) radial RMS velocity profiles at different heights for operating condition of $G_s = 150$ kg/m ² s and $U_g = 7.6$ m/s	188
Figure 4.8:	Flow regime diagram (Bi and Grace, 1995) with operating conditions	189
Figure 4.9:	Typical tracer particle tracks (a) without back mixing and (b) with back mixing for gas inlet velocity of 7.6 m/s and solid flux of 150 kg/m ² s	190
Figure 4.10:	Particle position after 50 and 100 milliseconds when the tracer enters the scan zone from the center	192
Figure 4.11:	Particle position after 50 and 100 milliseconds when the tracer enters the scan zone from the wall region (solid inlet side)	193

Figure 4.12:	Particle position after 50 and 100 milliseconds when the tracer enters the scan zone from the wall region (opposite of solid inlet side)	194
Figure 4.13:	Normalized number of occurrence contour plots at different heights and operating conditions at the bottom section	196
Figure 4.14:	Normalized number of occurrence contour plots for (a) different solid flux at a gas velocity of 8.2 m/s and (b) different gas velocities at a solid flux of 150 kg/m ² s at the middle section of riser	197
Figure 4.15:	Normalized histogram diagram of instantaneous velocity near the wall (solid inlet side) at the center and near the wall (opposite side of the solid inlet) at the height of 25 cm from the primary air inlet	199
Figure 4.16:	Normalized histogram diagram of instantaneous velocity near the wall (solid inlet side) at the center and near the wall (opposite side of the solid inlet) at the height of 45 cm from the primary air inlet	200
Figure 4.17:	Normalized histogram diagram of instantaneous velocity near the wall (solid inlet side) at the center and near the wall (opposite side of the solid inlet) at the height of 65 cm from the primary air inlet	201
Figure 4.18:	Normalized histogram diagram of instantaneous velocity at three radial locations (column center, core-annular zone, and adjacent to the wall) for middle section of the riser	203
Figure 4.19:	Velocity vector plot for the bottom section for different operating condition	204
Figure 4.20:	Velocity vector plot for the middle section for different operating conditions	205
Figure 4.21:	Radial variation of azimuthally averaged mean axial velocity with height at the bottom section for (a) different solid flux at a gas velocity of 8.2 m/s and (b) different gas velocities at a solid flux of 150 kg/m ² s	206
Figure 4.22:	Radial variation of azimuthally averaged mean axial velocities at the middle section for (a) different solid flux at a gas velocity of 8.2 m/s and (b) different gas velocities at a solid flux of 150 kg/m ² s	207
Figure 4.23:	Radial variation of azimuthally averaged mean radial velocity with height at the bottom section for (a) different solid flux at a gas velocity of 8.2 m/s and (b) different gas velocities at a solid flux of 150 kg/m ² s	210
Figure 4.24:	Radial variation of azimuthally averaged mean radial velocities at the middle section for (a) different solid flux at a gas velocity of 8.2 m/s and (b) different gas velocities at a solid flux of 150 kg/m ² s	211
Figure 4.25:	Radial variation of azimuthally averaged axial RMS velocity with height at the bottom section for (a) different solid flux at a gas velocity of 8.2 m/s and (b) different gas velocities at a solid flux of 150 kg/m ² s	212
Figure 4.26:	Radial variation of azimuthally averaged axial RMS velocities at the middle section for (a) different solid flux at a gas velocity of	215

	8.2 m/s and (b) different gas velocities at a solid flux of 150 kg/m ² s	
Figure 4.27:	Radial variation of azimuthally averaged radial RMS velocity with height at the bottom section for (a) different solid flux at a gas velocity of 8.2 m/s and (b) different gas velocities at a solid flux of 150 kg/m ² s	216
Figure 4.28:	Radial variation of azimuthally averaged axial RMS velocities at the middle section for (a) different solid flux at a gas velocity of 8.2 m/s and (b) different gas velocities at a solid flux of 150 kg/m ² s	217
Figure 4.29:	Radial variation of azimuthally averaged granular temperature with height at the bottom section for (a) different solid flux at a gas velocity of 8.2 m/s and (b) different gas velocities at a solid flux of 150 kg/m ² s	219
Figure 4.30:	Radial variation of azimuthally averaged granular temperature at the middle section for (a) different solid flux at a gas velocity of 8.2 m/s and (b) different gas velocities at a solid flux of 150 kg/m ² s	220
Figure 4.31:	Radial variation of azimuthally averaged normal stress with height at the bottom section for (a) different solid flux at a gas velocity of 8.2 m/s and (b) different gas velocities at a solid flux of 150 kg/m ² s	222
Figure 4.32:	Radial variation of azimuthally averaged shear stress with height at the bottom section for (a) different solid flux at a gas velocity of 8.2 m/s and (b) different gas velocities at a solid flux of 150 kg/m ² s	223
Figure 4.33:	Radial variation of azimuthally averaged normal stress at the middle section for (a) different solid flux at a gas velocity of 8.2 m/s and (b) different gas velocities at a solid flux of 150 kg/m ² s	224
Figure 4.34:	Radial variation of azimuthally averaged shear stress at the middle section for (a) different solid flux at a gas velocity of 8.2 m/s and (b) different gas velocities at a solid flux of 150 kg/m ² s	224
Figure 4.35:	Radial variation of azimuthally averaged turbulence intensity with height at the bottom section for (a) different solid flux at a gas velocity of 8.2 m/s and (b) different gas velocities at a solid flux of 150 kg/m ² s	226
Figure 4.36:	Radial variation of azimuthally averaged turbulence intensity at the middle section for (a) different solid flux at a gas velocity of 8.2 m/s and (b) different gas velocities at a solid flux of 150 kg/m ² s	227
Figure 4.37:	Detector arrangement for RTD experiment for pilot scale riser	229
Figure 4.38:	RTD for (a,b) inlet section, (c,d) inlet to start of the middle section, (e,f) inlet to end of the middle section and (g,h) overall riser at inlet gas velocities $U_g = 9.2$ m/s and $U_g = 7.6$ m/s	231
Figure 4.39:	Trajectory length distribution for solid flux of 150 kg/m ² s and different gas inlet velocities of (a) 7.6 m/s and (b) 9.2 m/s	234
Figure 4.40:	Comparison of the mean velocity predicted from the empirical correlation and the actual mean velocity	239

List of Tables

Table No.	Title	Page No
Table 1.1	Applications of CFB	10
Table 1.2	Literature review of experimental work on solid velocities in CFB	15
Table 1.3	Literature review of experimental work on solid residence time distribution (RTD) in CFB	24
Table 2.1	Look up table showing calibration data	72
Table 2.2	Quantities calculated from RPT experimental data (Roy et al., 2005; Upadhyay, 2010)	77
Table 3.1	Operating condition with time solid flux measurement	98
Table 3.2	Residence time distribution and Peclet number	162
Table 4.1	Operating condition with time solid flux measurement	183
Table 4.2	Residence time distribution and Peclet number	233
Table 4.3	Trajectory length distribution of the bottom and middle section of the riser	236
Table 4.4	Experimental and solid particles used for empirical correlation	238



CHAPTER 1:

Introduction

Scope

This chapter presents the introduction of gas-solid fluidization and the concept of circulating fluidized bed. The evaluation, application, advantages and disadvantages of circulating fluidized bed is explained. Moreover, the hydrodynamics of circulating fluidized bed and the literature review is briefed. The motivation for carrying out the present work and the objectives of the study are also presented in this chapter. The structure of the complete thesis is mentioned in this chapter's last section.

1.1 Introduction to Fluidization

Fluidization is the operation by which solid particles are transformed into a fluid-like state through suspension in upward flowing fluid. The fluid may be a liquid or gas but is most commonly a gas. Fluidization hit the industrial scenario in a massive way in the year 1942 with catalytic cracking and has since revolved around several other areas. At present times, gas-solid fluidized beds are widely used in various industries like pharmaceuticals, petroleum refineries, power plants, mineral processing, and metallurgical industries. It is also for drying and coating of particles. The increase in the usage of fluidized bed reactors in today's industrial world is mainly due to the inherent advantages of this technology.

Some of them are as follows:

- Uniform particle mixing: Due to the intrinsic fluid-like behavior of the solid material, fluidized beds do not experience poor mixing as in packed beds. This complete mixing allows for the generation of a uniform product that can often be difficult to achieve in other reactor designs. The elimination of radial and axial

concentration gradients also enables better fluid-solid contact, which is essential for reaction efficiency and quality.

- Uniform temperature gradients: Many chemical reactions require the addition or removal of heat. Local hot or cold spots generated within the reaction bed, which is often a problem in the case of packed beds, are avoided in a fluidized situation. In other reactor types, these local temperature differences, especially hotspots, can result in product degradation. Thus, Fluidized Bed Reactors (FBR) are well-suited for exothermic reactions. Bed-to-surface heat transfer coefficients for FBRs are high.
- Ability to operate reactor in continuous state: The fluidized bed nature of these reactors allows for the ability to continuously withdraw of product and introduce new reactants into the reaction vessel. Operating at a continuous process state allows manufacturers to generate their various products more efficiently due to the removal of start-up conditions in batch processes.

1.1.1 Regimes of Fluidization

The efficiency of fluidized bed reactors largely depends on the gas-solids contacting pattern, and gas-solids contacting, in turn, depends on the gas flow rate and particle size/type. Different patterns of contact are classified into various regimes, as shown in Figure 1.1. At low flow rates, when gas passes through the bed void spaces without disturbing the solids, the drag force exerted on solids is very low compared to the force due to gravity. This is known as a *fixed bed*. As the gas flow rate increases, particles start to vibrate, but the movement is restricted. It is known as an *expanded bed*. With a further increase in gas velocity, at a certain point, the drag force is balanced by the weight of the particles, and all the particles are just suspended by the upward flow of gas. This gas velocity achieved is called *minimum fluidization velocity*, and this bed is called an *incipient*

fluidized bed or bed at minimum fluidized condition. The performance of a minimum fluidized bed mainly depends on factors such as particle shape, size, density, and fluid property. At a fluid velocity higher than the minimum fluidization velocity, different fluidization behaviors can be observed. In the case of a liquid-solids system, when the column is operated beyond the minimum fluidization velocity, a smooth and homogeneous fluidization is observed and the bed expands uniformly, known as *smooth, homogeneous or particulate fluidization*. In the case of a gas-solid system with fine particles (Geldart Group A), homogeneous or smooth fluidization can be observed. On the other hand, in the case of gas-solid systems with relatively bigger particles beyond the minimum fluidization velocity, a huge degree of instability with the bubbling and channeling of gas can be observed. Such a bed is called a *heterogeneous fluidized bed*, or a *bubbling fluidized bed*. For fine particles, a bubbling fluidized bed can be observed with an increase in gas velocity. At this stage, bubbles are relatively small in size. As the velocity increases further, bubbles grow larger and, at a point of time, they encompass the whole cross-section of the bed. This is called a *slugging fluidized bed*. In the case of fine particles, they flow smoothly down the wall around the rising bubble. This process is called slugging with an axial slug. In the case of coarse particles, the portion of the bed above the bubble is pushed upward. After a certain height, the slug above the bubble finally disintegrates and particles rain down from the slug. This is called flat slug. These slugging phenomena become more severe in long and narrow fluidized beds. As the gas velocity increases and the terminal velocity of the solids is exceeded, the upper surface of the bed disappears and the particles are carried out of the bed. This is known as a *turbulent fluidized bed*. The transition to the turbulent fluidization phase is characterized by the breakdown of bubbles or slugs due to rapid coalescence and splitting beyond a certain point (Bi et al. 1995). This transition can occur quite sharply for fine particles. But the transition from bubbling to turbulent phase happens more gradually

with coarse particles, where slugging occurs initially. The transition involves intermittent periods of slug-like and turbulent character. To maintain steady state operation in these contacting modes, entrained particles have to be collected and returned to the beds. To capture the solids, internal or external cyclones are used, and the captured solids are again recycled at the bottom of the bed. This kind of arrangement of the bed with recirculation of solids is termed a "*circulating fluidized bed*." With a further increase in gas velocity, the entrainment rate increases and bigger cyclones are required to capture the solids. This is called a *fast fluidized bed*. This regime is characterized by a particle rich, dense bottom section and a particle lean, dilute top section. Bi et al. (1995) showed that the transition from turbulent to fast fluidization corresponds to a critical superficial velocity U_{se} , which corresponds to the onset of significant entrainment of particles from the riser. $U_{se} > U_t$ (terminal velocity) for Geldart Group A and B particles but U_{se} is almost equal to U_t for group B particles. If gas velocity is raised further at fixed solid flux or solids-to-gas loading ratio, one eventually reaches a gas velocity at which there is no accumulation of solids at the bottom. The bed becomes diluted from top to bottom. This regime is called lean phase fluidized bed, pneumatic transport or dilute transport regime of solids. The point where solids accumulation commences on lowering the gas velocity is called Type A (or accumulative) choking (Bi et al. 1993). This superficial gas velocity is denoted by U_{CA} , which can be well predicted by equation 1 Bi & Fan (1991) .

$$U_{CA} = 7.34(g\bar{d}_p)^{0.324} \left(\frac{G_s}{\rho_G}\right)^{0.352} Ar^{0.068} \quad 1.1$$

Apart from accumulative choking, there are two other phenomena causing choking in riser (Bi et al. 1993). Type B (or blower/standpipe induced) choking occurs when the blower has insufficient capacity or the standpipe has an insufficient length to permit the system with the required circulation rate at a given gas velocity. Type C (or classical choking) happens due to severe slugging in the transport line. Bi et al. (1993) suggest approaches to

predict these transitions which occur with decreasing gas velocity at a fixed value of circulation flux.

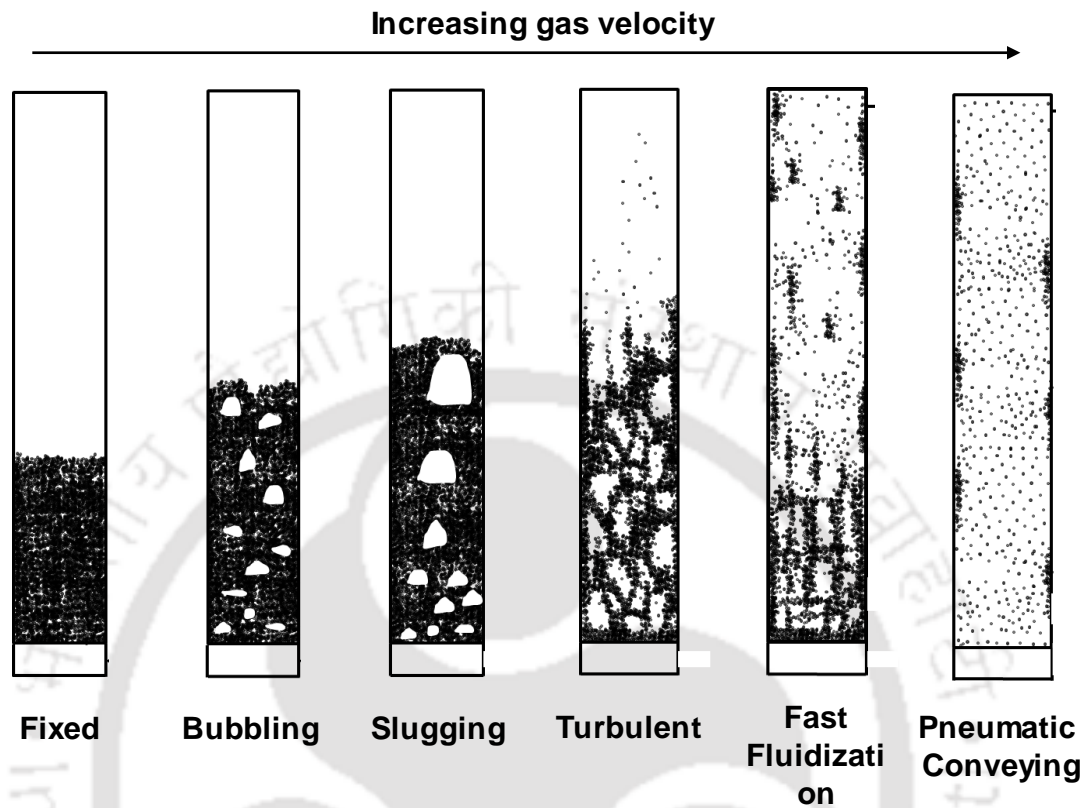


Figure 1.1: Flow patterns in gas solids fluidized beds (adapted from Grace (1997))

1.1.2 Classification of Particles

Numerous attempts have been made to predict the mode of fluidization and the transition from one mode to another. Some used different dimensionless groups like the Reynolds and Froude numbers (Wilhelm and Kwauk, 1948; Romero and Johanson, 1962) and some researchers made efforts to present an empirical plot of bed voidage versus ρ_p/ρ_g with different particle sizes as a parameter (Zenz et al., 1957). Geldart approached this problem based on the characteristics of particles. Geldart (1973) has classified solids into four groups: A, B, C and D based on their size and relative fluid-solids density, which is shown in Figure 1.2.

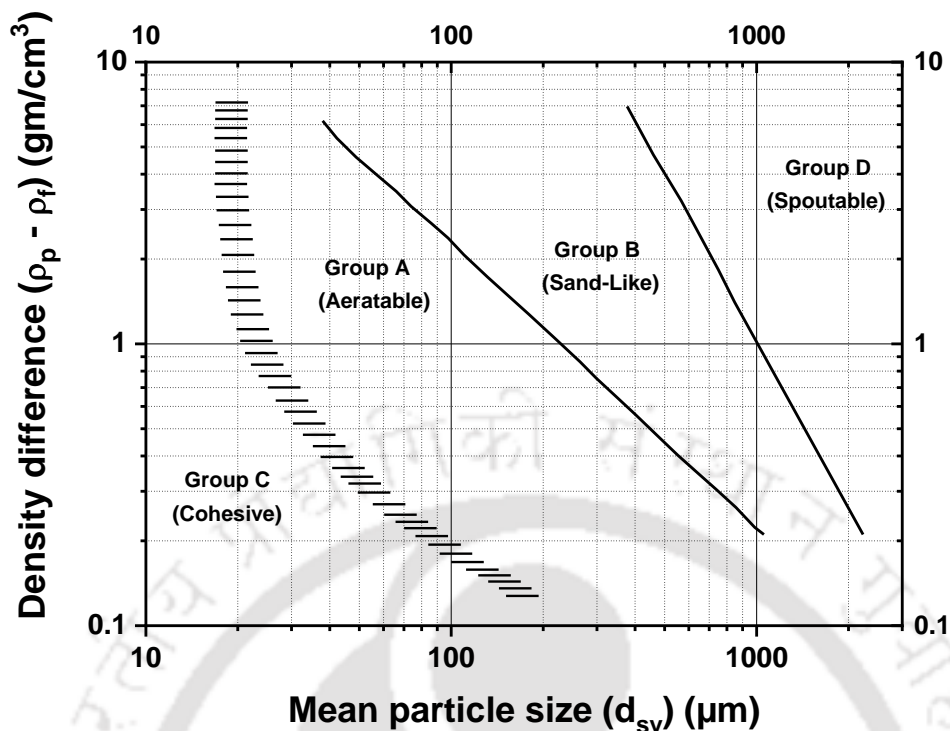


Figure 1.2: Geldart classification of particles for air at ambient conditions (Geldart, 1973)

Group-A: The particles which belong to this category usually possess a small diameter range, i.e. from 30 to 100 μm and a low particle density ($< \sim 1.4 \text{ g/cm}^3$). These particles are also termed as aeratable particles. While fluidizing at minimum fluidization velocity, these particles fluidize easily and smoothly without forming bubbles. But when the velocity is increased to its minimum bubbling velocity, bubbles start forming with the expansion of the bed. These particles provide controlled bubbling with small bubbles and bubbles coalesce and split as they progress towards the top. The bubble size is always less than 10 cm. Only axial slug formation occurs in these types of particles. The cloud to bubble volume ratio is negligible in this case. The rise velocity of a bubble is greater than the interstitial gas velocity. For these particles, the minimum bubbling velocity is always greater than minimum fluidization velocity. Particles like fluid catalytic cracking (FCC) catalyst, milk powder etc. come under this category.

Group-B: These particles' size range is from 100 to 1000 μm and their density ranges from 1.4 to 4 g/cm^3 . While fluidizing these particles at minimum fluidization velocity, bubbles start forming, which grow larger in size with increasing velocity. The cloud to bubble volume ratio is not

negligible in this case. Examples of group B particles are glass beads and sand. For these particles, the minimum bubbling velocity and the minimum fluidization velocity are the same. The majority of gas-solid reactions, metallurgical and others, run in this regime because the mean size and size distribution of feed particles are usually determined by the upstream processing of the raw materials.

Group-C: These particles' sizes are less than 30 μm . For particles with a size less than 60 μm , relative density is less than 500 kg/m^3 and for particle size less than 20 μm , relative density is greater than 1000 kg/m^3 . The particles of this group are cohesive and very fine. These particles do not fluidize easily as the inter particle force is larger than the force exerted by the gas. Channelling occurs in small diameter beds. They rise as plugs of solids when fluidized, and they even need external forces like mechanical agitation to fluidize. Particle mixing and heat transfer are poorer as compared to other particles. Examples of these particles are flour, cement, face powder, fly ash and starch.

Group-D: These particles are also termed spoutable particles. They are very large and dense. Their particle size is greater than 1000 μm . Large particle beds are usually undesirable for physical or chemical operations. However, in some industries, for instance, in the processing of agricultural products, in chemical agglomeration, and in the reaction of composite pellets, one cannot avoid this. They need high fluid flow rates, and fluidizing them leads to abrasion. They exhibit spouting behaviour and channeling. They form a flat slug. Solid mixing in this case is relatively poor and no back mixing in dense regions can take place due to high gas velocity. An enormous amount of gas is needed to fluidize these solids, often far more than that required for the physical or chemical operations. The rise velocity of the bubble is less than interstitial gas velocity; hence, gas enters at the bottom of the bubble and comes out at the top. Examples of these particles are coffee beans, peas, and dried grains.

1.2 Circulating Fluidized Bed

Any vessel in which solids are transported upwards by gas and then recycled back to the system can be termed as *circulating fluidized bed* (CFB). Circulating fluidized bed reactors are a type of gas-solid contactor that has been applied in many different processes due to its intrinsic properties such as efficiency, operational flexibility and overall profitability. For example, they are extensively utilized in the petroleum, energy, and metallurgical industries. A CFB consists of a riser where gas-solids are transported upwards. Then the gas-solids mixture is separated at the top of the riser and the solids are recycled to the bottom of the riser via a standpipe and other equipment such as strippers, regenerators, etc. Commercial application of CFB can be traced back to the 1940s when the fluid cracking process first developed (Grace, 1990). The term “*circulating fluidized bed*” was first applied to alumina calciners (Reh, 1971). Though many other synonyms have been used to describe this system: fast fluidized bed, riser reactor, entrained bed, transport bed, pneumatic transport reactor, recirculating solids riser, highly expanded fluid bed, dilute phase transported bed, transport line reactor and suspended catalyst bed in co-current gas flow. However, due to low catalyst reactivity and other technical difficulties, it was not until the 1970s when high velocity fluidized bed or CFB technology was “re-invented” (Yerushalmi et al., 1976). CFB riser reactors provide many advantages over conventional bed reactors such as higher gas-solids contacting efficiency, high heat and mass transfer rate, high gas and solid throughput, reduced axial gas and solids’ back mixing, almost isothermal condition throughout the reactor and reduced tendency for particles to agglomerate (Grace, 1990; Berruti et al., 1995). Another advantage of CFB over bubbling and turbulent bed is that catalyst can be regenerated continuously during recirculation which is very essential for the continuous operation of plant.

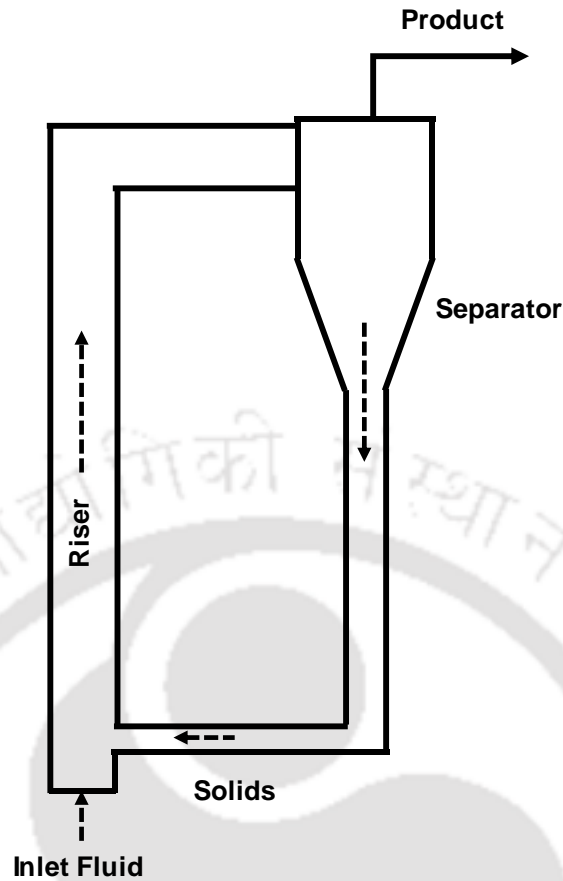


Figure 1.3: Schematic diagram of a typical Circulating Fluidized Bed (CFB) setup

1.2.1 Applications of Circulating Fluidized Bed

The first documented commercial application of CFB is a fluid catalytic cracking (FCC) unit at the Baton Rouge refinery in 1942. A group of companies lead by the engineers of the Standard Oil Development Company (now ExxonMobil) created the first instance of gas-solid contacting in a CFB. Since that time, other industrial applications are developed like Fischer-Tropsch synthesis (1950's), solids processing, including alumina calcination (1970's), high-temperature operation which comprises combustion (1980s) and partial oxidation for the production of chemicals (1990's). The main reason for the popularity of CFBs over the conventional fluidized bed is its operating flexibility. Fluid catalytic cracking (FCC) and circulating fluidized bed combustion (CFBC) are the two most important technologies using CFB technology. A handful of the applications are

shown in Table 1.1. Berruti et al. (1995) and Grace and Bi (1997) provide more information on the application of CFB technology. There are two type of CFB: One solid-catalyst system where solids act as a catalyst (eg. FCC) and a solid-reactant system where solids itself take part in reactions (e.g CFBC).

Table 1.1 Applications of CFB

I. Gas-solids reactions	II. Solid-catalyzed gas-phase reactions
Combustion of coal, woods (Reh, 1995)	Fluid catalytic cracking (FCC) (Squires, 1986)
Gasification of coal, biomass.(Reh, 1995)	Fischer-Tropsch Synthesis (Chanchlani, 1994)
Desulphurization of flue gas (Salazar et al., 1995)	Paraffin Oxidation (Pugsley et al., 1992)
Chemical Looping Combustion (Lyngfelt, (2020))	Acrylonitrile from propylene (Hu et al., 2007)
Calcination of Al(OH) ₃ , to alumina (Al ₂ O ₃) (Reh, 1995)	Allylic Oxidation (Patience and Mills, 1994)
Metallurgical and inorganic chemical industries (Reh, 1995)	Ethylene oxide from ethylene (Park and Gau, 1986)
Reduction of iron ore, lateritic nickel ore. (Reh, 1995)	Dehydrogenation (Vrieland and Murchison, 1993)
Roasting of sulphidic ores (ZnS, Cu ₂ S, gold ores) (Reh, 1995)	Simultaneous NO and SO ₂ removal from off-gases (Reh, 1995)
Cement production (Reh, 1986)	

1.3 Hydrodynamics of Circulating Fluidized Bed

There are two aspects to the hydrodynamics of circulating fluidized beds. One is with the dynamics of gas-solid suspensions over a specific solid concentration range; the other is with the hydrodynamic characteristics of particular types of gas-solid contacting devices. From a scientific perspective, the primary focus of interest should be the clustering behavior of diluted suspensions, which was initially noted from the significant gas-solid slip velocity. From engineering-wise, the main hydrodynamic concerns relate to how

operating conditions and design elements like column diameter, wall shape, gas distributor design, exit structure, solid separation and recycling devices, and operating conditions affect circulating system performance. However, both engineering and scientific aspects are closely interrelated. In examining the evolution of fluidization technologies, a clear pattern emerges revealing progressive advancements in understanding with each passing decade. The study, which was launched by the creation of the first fluid catalytic cracking (FCC) process in the late 1930s, looked fruitlessly for the reasons for the disappointingly low process conversions. Following Toomey and Johnstone's (1952) two-phase concept, systematic structural study was made feasible since, without such a flow allocation, even the determination of the gas exchange coefficient from experimental conversion was not feasible. Davidson (1961) developed a thorough theory from a pure hydrodynamic perspective to quantitatively describe gas bypassing and gas interchange. The majority of hydrodynamic phenomena were systematically examined in the 1960s using the principle of bubble hydrodynamics. This three-step paradigm came in circulating fluidized bed research, shifting focus from chaotic to structural and then to essential. Though Despite initial hurdles encountered in the developmental phase, FCC units ultimately emerged as technological marvels. Understanding was only limited in the initial times. It took several decades, before the circulating fluidized bed was acknowledged as distinct from the bubbling fluidized bed and pneumatic conveying. Before 1960s Some efforts have been made to revive the up-flow concept, with forts concentrated on the bubbling bed. One of such is a circulating fluidized bed roaster, which leads the way in the development of circulating fluidized bed combustor. The need to investigate the suspension properties in circulating fluidized beds arose in the early 1970s. Yerushalmi et al. (1976) formally introduced the term "fast fluidized bed" first time in 1975 at the International Fluidization Conference. This marks the start of a systematic and comprehensive investigation and

evaluation of the circulating fluidized bed. From the beginning there was a fundamental misunderstanding of the concept concerning the reactor, which differ very much between combustors and catalytic reactors. The CFB combustors evaluation and success boost the CFB research. One hand in the case of CFBC pressure drop limits the height of the lower dense region. Other hand in catalytic system extended dense region with constant voidage is favorable. Internal solids circulation in the upper, diluted region of CFB combustors is advantageous for heat transfer to membrane walls and for returning the heat produced by the combustion of volatiles and char to the dense region. However, internal solid circulation due to down flow is not desirable in the case of solids catalytic CFB system as it increases the back mixing which decreases the yields. In the case of a solids catalytic CFB system, internal solid circulation caused by down flow is undesirable because it increases back mixing, which lowers yields. In contrast to a CFB reactant system, external circulation is significantly higher in a CFB catalyst system because most CFB catalysts offer quick reactions. However, the CFB catalyst system needs to regenerate the catalyst.

Early experiments were typically conducted in tall columns with a large length to diameter ratio, or L/D , and a smooth recycle of solids into the risers. This had the tendency to draw attention to the characteristics of the long, dense region that forms in a vessel with a large L/D ratio, which may not have been apparent to those developing combustor designs. The differences between catalytic reactors and boilers are not only in riser design but also in riser exit and downer configurations. In rapid catalytic reactions with regeneration, catalyst regeneration is done in catalyst inventory slowly. It required a large inventory storage and regenerator in the case of catalytic CFB. In a combustor, the down-comer is much smaller in volume compared to the riser.

1.3.1 Solids' Velocity

In CFBs, the motion of solids is significant, and local solid velocity might reveal critical information about riser behavior. Table 1.2 contains a collection of previously published experimental research on solid velocity in gas-solid risers. Experimental methods can be either invasive or non-invasive. Examples of intrusive procedures include pitot tubes, optical fiber probes, extraction probes, and iso-kinetic probes. Two advantages of using such probes are the ease of experimental measurement and usage in high flux conditions, both of which are crucial to the industry. However, disadvantages of intrusive methods as follows:

- i. Complex calibration process.
- ii. Manual placement of the probe,
- iii. Fouling effects due to the ports on the walls,
- iv. One can only acquire a mean radial profile of axial velocity from point observations.

The majority of non-invasive approaches use optical technologies like PIV, LDV, and high-speed cameras, while some rely on radioisotopes. Stellema (1998) used Positron Emission Particle Tracking (PEPT) and Godfroy et al. (1997) Bhusarapu (2005) used gamma ray emitting Radioactive Particle Tracking (RPT) techniques to track and analyses solid motion in circulating fluidized bed riser. Prior to that RPT technique applied in fluidized bed by Kondukov et al. (1964), Lin et al. (1985) and Moslemian (1987). Godfroy et al. (1999) worked at lower solids flux up to $75 \text{ kg/m}^2\text{s}$ where Bhusarapu (2005) worked upto solid flux of $144 \text{ kg/m}^2\text{s}$. However, both of them worked with glass beads of $150 \mu\text{m}$. Bhusarapu (2005) reported both core annular flow regime and dilute transport regime. It is known that a core-annular type radial solids flow with a dense particle layer in the wall region and a diluted core region exists in the riser. The core annular flow pattern is defined

as a low density, high velocity gas-solids core region surrounded by a high solids concentration, slower or even downward-flowing annular region (Bai et al.1995). According to Grace et al. (1997), particle exchanges between the dense wall and the dense core regions happen as a result of temporal and spatial accumulations of particles in the wall region that result in transient dense particle layers or streamers. Particle clusters frequently lead to non-uniform particle distributions or the presence of localized dense zones, which have a significant impact on the system's hydrodynamic properties.



Reference	Measurement Technique	Riser Dia (cm) x Height (m)	Bed material, Geldart Group	U_g (m/s); G_s (kg/m²s)	Measurement region (m)	Measured solids velocity	Remarks
Bader et al. (1988)	Pitot tube	30.5 x 12.2	FCC, 76 μ m, Group A	3.7; 98	H = 4, 9.1	Mean radial profile	Core annulus flow structure with a parabolic profile
Horio et al. (1988)	Optical fiber probe	5 x 2.79	FCC, 60 μ m Group A	1.17, 1.29; 11.7, 11.25	H = 0.36, 1.06, 1.63	Mean radial profile	Annular flow with clusters
Ishii et al. (1989)	Optical fiber probe	5 x 2.79 Smooth exit	FCC, 60 μ m, Group A	1.29; 10.7	H = 0.36, 1.06, 1.63	Mean radial profile (clusters)	Cluster velocity profiles
Miller and Gidaspow (1992)	Extraction probe	7.5 x 6.58 Smooth exit	FCC, 75 μ m, Group A	2.61–3.84; 12 – 32.8	H = 1.86 – 5.52 m	Mean radial profile	Core-annulus flow structure
Harris et al. (1994)	Pitot tube / isokinetic probe	14 x 5.1 Abrupt exit	FCC, 60 μ m, Group A	2.6, 3; 26 - 52	H = 4.4 m Mean radial	H = 4.4 m Mean radial	H = 4.4 m Mean radial
Qian and Li (1994)	Optical fiber probe /	7.5 x 10 -	FCC, 54 μ m, Group A	2.5; 62	H = 6.5 m	Instantaneous and mean radial profile	Radial profiles

Reference	Measurement Technique	Riser Dia (cm) x Height (m)	Bed material, Geldart Group	U_g (m/s); G_s (kg/m²s)	Measurement region (m)	Measured solids velocity	Remarks
Zhou et al. (1995)	Optical fiber probe	14.6 x 14.6 x 914 cm ³	Sand, 213 μ m, Group B	5.5, 7; 20, 40	H = 5.13, 6.2, 8.98	Vertical and lateral profiles of particle velocities	Core annulus flow structure. Thickness of the annulus layer increases with the height
Wang et al. (1998)	LDV	14 x 10.4	FCC, 36 μ m, Group A	3.49 – 4.78; 2.6 – 78.3	H = 4 - 6	Mean Radial profile	Radial profiles obeys 1/7 power law of turbulent flow
Godfroy et al. (1999)	Radioactive particle tracking	8.2 x 7	Sand, 150 μ m, Group B	4; 23 – 75	H = 4 - 5 (above distributor)	3 D Eulerian and Lagrangian velocity field (of a large particle)	Clusters formation; dispersion coefficient variation
Herbert et al. (1999)	Optical fiber probe	41 x 8.5	FCC, Glass beads; 42 - 300 μ m, Group A, Group B	≤ 13 ; ≤ 250	H = 4, 4.2	Mean radial profile	Core annulus with the influence of particle diameter

Reference	Measurement Technique	Riser Dia (cm) x Height (m)	Bed material, Geldart Group	U_g (m/s); G_s (kg/m²s)	Measurement region (m)	Measured solids velocity	Remarks
Parssinen and Zhu (2001)	Five fiber optical probe	7.6 x 10	FCC, 67 μ m, Group A	5.5, 8, 10; 100, 300, 400, 550	H = 1.53 – 9.42	Mean radial and averaged axial profiles	Dense, intermediate dense, dilute, exit section can be distinguished. Upward velocity near the wall in bottom dense region.
Zhang et al. (2003)	LDV	41.8 x 18	FCC, 77 μ m, Group A	2.7 – 3.7; 29.7 – 44	H = 6, 14	Instantaneous and time-averaged radial profile,	Dispersed particle phase and dense cluster phase exists.
Yan et al. (2003)	Five fiber optical probe	7.6 x 10	FCC, 67 μ m, Group A	5.5, 8; 20, 100, 200, 300, 400, 550	H = 0.98 – 9.42	Mean radial profiles	Exit and entrance effects are more pronounced in high solid flux
Tartan and Gidaspow (2004)	PIV	7.62 x 6.99	Glass beads, 530 μ m Group B	4.9, 5.1, 5.6, 6.0; 14.2, 14.9, 21.4, 28.7, 43.9	H = 4.2 - 5	Mean velocity and granular temperature	Reynolds stresses increases with solid flux and also high near the wall

Reference	Measurement Technique	Riser Dia (cm) x Height (m)	Bed material, Geldart Group	U_g (m/s); G_s (kg/m²s)	Measurement region (m)	Measured solids velocity	Remarks
Bhusarapu et al. (2005)	RPT	15.2 x 7.93 14 x 5.77	Glass, 150 μ m Group B	3.2 – 4.5; 26.6 – 36.8; 5.49 – 7.71; 102 - 119	H = 5 to 5.7 H = 2.08 to 2.79	Instantaneous, ensemble averaged velocity, turbulent kinetic energy, Reynolds stress	Dilute and core annular flow profiles are different.
Yan and zhu (2005)	Five fiber optical probe	7.6 x 10 20.3 x 10	FCC, 67 μ m Group A	3.5, 5.5, 8; 50, 75, 100, 200	H = 1.47 - 8.79 H = 1.53 – 9.42	Mean radial profile	Solid velocity is similar at the center of two risers. Particle velocity is higher in the smaller column. Flow development becomes faster with increasing U_g and slower with increasing G_s .
Wilde et al. (2005)	LDA	10 x 8.765	77 μ m Group A	3 – 12 , 2 – 400	H = 1.64 , 1 m	Mean velocity profile	Radial mixing is poor but best in the inlet zone of the riser

Reference	Measurement Technique	Riser Dia (cm) x Height (m)	Bed material, Geldart Group	U_g (m/s); G_s (kg/m²s)	Measurement region (m)	Measured solids velocity	Remarks
Van engelandt et al. (2007)	LDA	10 X 8.765m	FCC 77 μ m, silica 260 μ m Group B	0.5–4.5 , 5.3–7.4 m/s.	H = 0.05, 0.5	Mean velocity profile	Larger particles extend the length of the acceleration zone
Yan et al. (2008)	Optical fiber probe	7.6 x 10 10 x 10	FCC 67 μ m Group A	3.5 – 8; 50 – 200	H = 1.53 – 9.42 H = 0.95 – 14.08	Mean radial profile	Multi-tube distributor gives more uniform profiles than the orifice distributor
Chan et al. (2010)	PEPT	4.6, 9, 16 x 6.5	Sand 120 μ m Group B	1 – 10; 5 – 622	Whole column	Instantaneous and average velocity.	Residence time distribution and solid mixing are reported. Velocity distribution is also reported.
Kashyap et al. (2011)	PIV	3.048 x 15.78	Polypropylene 750 μ m Group B	7.6; 39.31, 19.50	H = 6.98	Granular temperature, Reynolds stress	Solid dispersion coefficient is higher in the radial direction than axial direction

Reference	Measurement Technique	Riser Dia (cm) x Height (m)	Bed material, Geldart Group	U_g (m/s); G_s (kg/m²s)	Measurement region (m)	Measured solids velocity	Remarks
Pantzali et al. (2013)	LDA	10 x 8.7	FCC, 77 μ m Group B	3.5 and 5.3; 1	H = 0.9 - 5.5	Mean and rms velocities, and turbulence quantities	Operated at very low flux. RMS profile is contrary to the mean velocity profile.
Gopalan and Shaffer (2013)	HSPIV	30.5 x 15.5 0.203 x 22	HDPE, 802 FCC, 81 Group B, A	5.71, 7.58; 76, 96, 195 18.3, 9.15; 49, 390	H = 9.75 H = 20	Mean axial velocities, RMS velocities and Granular temperature	Flat RMS profiles are reported for HDPE. In case of FCC, peaking at the wall is reported. Granular temperature decreases towards the wall.
Wang et al. (2014)	Optical fiber probe	7.6 x 10	FCC 76 μ m Group A	5, 7, 9; 100 - 1000.	H = 0.59 - 10	Mean axial and radial profile	With increases in solid flux, axial distribution of particle velocity is more uniform, radial distribution becomes steeper and flow development becomes slower.

Reference	Measurement Technique	Riser Dia (cm) x Height (m)	Bed material, Geldart Group	U_g (m/s); G_s (kg/m²s)	Measurement region (m)	Measured solids velocity	Remarks
Chang et al. (2016)	Optical fiber probe	6 x 5.6	149 μ m Group B	5,7,8; 200-1000	H = 1.1 , 1.9, 3.3, 5.0	Radial and axial solid holdup and mean velocity	Transition mass flux defines fluidization shift from dense suspension upflow to high-density CFB
Zhang et al. (2018)	2 D Euler Euler Simulation EMMS Drag Model	8 x 18	89 . 154 μ m Group B	8.6, 8, 4; 200, 580, 900	H = 2, 6	Axial solid velocity and solid holdup profiles	Effect of temperature and pressure solid phase hydrodynamics
Su et al. (2019)	Optical fiber probe	8 x 18	FCC 85 μ m Group A	5, 9; 100-600, 200 - 600	H = 120.06 m	Mean axial and radial profile	Parabolic velocity profile at high G_s condition and core-annular flow structure at a lower G_s .

1.3.2 Solid Mixing

The exchange of solids between heterogeneous flow structures in CFB risers causes internal recirculation of solids. Because of this, the residence time of any particle in the riser can range from a few seconds to over an hour. In CFB reactor, different solids RTD curves are feasible for different applications to achieve better efficiency. For gas-solid catalytic reactions, which are in general very fast in reaction kinetics, where particles act as both heat transfer media and catalysts, a short contact is desirable. Then solids RTD configuration towards the plug flow is promoted. In the case of a gas-solid reaction system (e.g. coal combustion), where the solid phase directly takes part in the reaction, longer contact time between the solid and gas phase is favorable. A typical solid residence time in FCC and CFBC can be respectively 2-4 s and 20-40 s (Zhu and Bi, 1995). The two primary applications of CFB technology, catalytic gas-phase and gas-solids reactions, reactors, differ significantly in many ways to meet this need, including operating condition, particle property, reactor geometry, feeding control device and riser exit structure. Tracer techniques are used for RTD studies. For the determination of solid RTDs, a variety of tracer injection-detection techniques were used, which are listed in Table 1.3. For particle RTD or mixing investigation purposes, a wide range of tracer techniques have been employed, including radioactive tracers, salt tracers, thermal tracers, ferromagnetic tracers, phosphor tracers, and tracers for various sized particles. All solid RTD measurement techniques have flaws and limitations in their use that make them difficult to use. These limitations are: choice of tracer particle, method of tracer injection, experimental boundary conditions, and invasiveness of the technique. Ambler et al. (1990), Lin et al. (1999), Milne and Berruti, (1990), Patience et al. (1991) Viitanen, (1993) introduced small number of radioactive particle for RTD studies. Where Bhusarapu et al. (2004), and Mahmoudi et al. (2011) used single radioactive particle for solid phase RTD experimental studies. A sodium

chloride tracer was used to study RTD in CFB riser by Bader et al. (1988), Rhodes et al. (1991), Zheng et al. (1992), Smolders and Baeyens (2000), and Andreux et al. (2008). Wei et al. (1995,1996,1998), Ran et al. (2001), Harris et al. (2003), and Yan et al. (2009) developed a phosphor tracer technique to measure lateral and axial solids dispersion and solids mixing in a variety of CFB units. The method made use of a tracer particle made of phosphorescent material, usually alumina powder coated with a phosphorescing substance. When excited by a powerful light source, the phosphorescent material can emit light right away and continue to emit light with a waning intensity for few minutes.

Measurement of the RTD over the entire riser is the general goal of experimental studies of residence time distributions in circulating fluidized beds. To counter this, some authors have attempted to inject and sample a tracer at various axial locations that correspond to the various postulated mixing zones within a riser.

Table 1.3 Literature review of experimental work on solid residence time distribution (RTD) in CFB

Reference	Riser Dia (cm) x Height (m)	Bed material	Geldart Group	Tracer	U_g (m/s); G_s (kg/m ² s)	RTD Model
Zoonen (1962)	5 x 10	FCC, $\rho_p = /$, $d_p = 20-150 \mu\text{m}$	Group A	FCC particles tagged with ammonium chloride, ρ_t and d_t same as bed material	1.5–12; 40–1000 2.5–12; 100–700	Dispersion model
Bader et al. (1988)	30.5 x 12.2	FCC, $\rho_p = 1714 \text{ kg/m}^3$, $d_p = 76 \mu\text{m}$	Group A	Sodium chloride, $\rho_t = /$ and $d_t = /$, Terminal velocity of tracer is the same as that of bed material	4.57; 147	/
Kojima et al. (1989)	5 x 3.6	FCC, $\rho_p = 1000 \text{ kg/m}^3$, $d_p = 60 \mu\text{m}$	Group A	Fluorescent dye, ρ_t and d_t same as bed material	$U_g = 1.5$ and 2.0 m/s , $G_s = /$, Total loading is $15.4-44.6 \text{ g/cm}^2$	Dispersion model
Ambler et al. (1990)	5 x 3	Sand, $\rho_p = 2470 \text{ kg/m}^3$, $d_p = 106 \mu\text{m}$	Group B	Radioactive sand, $\rho_t = /$ and $d_t = /$	$4.5-7.1 \times 124-305$	Core-annulus flow model
Chesonis et al. (1990a)	10 x 6.4	Alumina, $\rho_p = 3460 \text{ kg/m}^3$, $d_p = 120 \mu\text{m}$	Group B	Alumina impregnated with CaCl_2 , $\rho_t = 3460 \text{ kg/m}^3$, $d_t = 127 \mu\text{m}$	$3.5-4.5$; $7-11$	Core-annulus flow model

Table 1.3 Literature review of experimental work on solid residence time distribution (RTD) in CFB

Reference	Riser Dia (cm) x Height (m)	Bed material	Geldart Group	Tracer	U_g (m/s); G_s (kg/m ² s)	RTD Model
Chesonis et al. (1990b)	10 x 6.4	Alumina, $\rho_p = 3460 \text{ kg/m}^3$, $d_p = 120 \mu\text{m}$	Group B	Coke, $\rho_t = 2000 \text{ kg/m}^3$, $d_t = 168 \mu\text{m}$	3.5 ; 9	/
Patience et al. (1991)	8.28 x 5	Sand, $\rho_p = /$, $d_p = 277 \mu\text{m}$	Group B	Radioactive sand, $\rho_t = /$, $d_t = 108, 275, \text{ and } 513 \mu\text{m}$ (sieved from bed material)	4.1–6.2 ; 25–166	Dispersion model
Rhodes et al. (1991)	15.2, 30.5 x 6.2, 6.6	FRF5 powder, $\rho_p = 2456 \text{ kg/m}^3$, $d_p = 71 \mu\text{m}$	Group A	Sodium chloride, $\rho_t = 2160 \text{ kg/m}^3$, $d_t = 71 \mu\text{m}$	2.8–5.0; 5.0–80.0	Dispersion model
Bai et al. (1992)	14 x 10	Silica gel, $\rho_p = 710 \text{ kg/m}^3$, $d_p = 99.6 \mu\text{m}$	Group A	Particle soaked with an organic substance, ρ_t and d_t same as bed material	2–10; 10–100	Dispersion model
Zheng et al. (1992)	9 x 10	FCC, $\rho_p = 929.5 \text{ kg/m}^3$, $d_p = 46.7 \mu\text{m}$	Group A	Sodium chloride, ρ_t and d_t same as bed material	1.75 -2.62 ; 18.6- 39.8	Dispersion model
Viitanen (1993)	100-130 x 39	FCC, $\rho_p = 2400 \text{ kg/m}^3$, $d_p = 70 \mu\text{m}$	Group A	Radioactive FCC, $\rho_t = 2400 \text{ kg/m}^3$, $d_t = 70 \mu\text{m}$	$U_g = 7 \text{ m/s}$, Solids mass flow rate = 1380 t/h	Dispersion model

Table 1.3 Literature review of experimental work on solid residence time distribution (RTD) in CFB

Reference	Riser Dia (cm) x Height (m)	Bed material	Geldart Group	Tracer	U_g (m/s); G_s (kg/m ² s)	RTD Model
Koenigsdorff and Werther (1995)	20 x 3.5	Silicon carbide, $\rho_p = 3217 \text{ kg/m}^3$, $d_p = 60 \text{ }\mu\text{m}$	Group A	Electrical thermal conductivity	3 – 4 ; 6.4–30.7	Core-annulus flow model and energy balance equations
Patience and Chaouki (1995)	8.3 x 5	Sand, $\rho_p = /$, $d_p = 277 \text{ }\mu\text{m}$	Group B	Radioactive sand, $\rho_t = /$, $d_t = 108, 275, \text{ and } 513 \text{ }\mu\text{m}$ (sieved from bed material)	8.2 ; 140	Dispersion model
Wei et al. (1995)	Circular, $d = 0.14 \text{ m}$, $h = 12 \text{ m}$	Alumina, $\rho_p = 1710 \text{ kg/m}^3$, $d_p = 54 \text{ }\mu\text{m}$	Group A	Non-disruptive phosphorescent tracer method, ρ_t and d_t same as bed material	2.67–7.84 ; 3–160	Dispersion model
Westphalen and Glicksman (1995)	20 x 7	Quartz sand, $\rho_p = 2350 \text{ kg/m}^3$, $d_p = 180 \text{ }\mu\text{m}$	Group B	Thermal sand, ρ_t and d_t same as bed material	3–5; 0–30	Mass balance equations and energy balance equations
Wang et al. (1996)	Square, $0.2 \times 0.2 \text{ m}^2$, $h = 4 \text{ m}$	$\rho_p = /$, $d_p = 471 \text{ }\mu\text{m}$	Group A	Sieved from bed material, $\rho_t = /$, $d_t = 400–600, 600–800, \text{ and } 800–1000 \text{ mm}$	3.0–4.7; 2.75–10.1	Core-annulus flow model

Table 1.3 Literature review of experimental work on solid residence time distribution (RTD) in CFB

Reference	Riser Dia (cm) x Height (m)	Bed material	Geldart Group	Tracer	U_g (m/s); G_s (kg/m ² s)	RTD Model
Wei et al. (1996)	14 x 12	Alumina, $\rho_p = 1710 \text{ kg/m}^3$, $d_p = 54 \mu\text{m}$	Group A	Non-disruptive phosphorescent tracer method, ρ_t and d_t same as bed material	1.5–9.0; 10–140	Dispersion model
Weinell et al. (1997)	Square, $0.14 \times 0.18 \text{ m}^2$, $h = 3.0 \text{ m}$	Sand, $\rho_p = 2600 \text{ kg/m}^3$, $d_p = 180\text{--}240 \mu\text{m}$	Group B	Non-disruptive a single radioactive particle tracking, $\rho_t = 700\text{--}1700 \text{ kg/m}^3$, $d_t = 400\text{--}15000 \mu\text{m}$	0–3.6; 5–25	/
Wei et al. (1998)	14 x 10.4	Fine particle: $\rho_p = 1710 \text{ kg/m}^3$, $d_p = 54 \mu\text{m}$; Coarse particle: $\rho_p = 1473 \text{ kg/m}^3$, $d_p = 1810 \mu\text{m}$	Group A Group B	Non-disruptive phosphorescent tracer method (phosphor material contained only in fine particles), $\rho_t = 1710 \text{ kg/m}^3$, $d_t = 54 \mu\text{m}$	2.2–7.84; 3–160	Dispersion model
Godfroy et al. (1999)	8.2 x 7	Sand, $\rho_p = 2600 \text{ kg/m}^3$, $d_p = 150 \mu\text{m}$	Group B	Non-disruptive a single radioactive particle tracking, $\rho_t = 2600 \text{ kg/m}^3$, $d_t = 500 \mu\text{m}$	4; 23–75	Autocorrelation of particle velocity fluctuations
Lin et al. (1999)	Square, $4 \times 6.2 \text{ m}^2$, $h = 22.8 \text{ m}$	Straw and coal, $\rho_p = 3000 \text{ kg/m}^3$, $d_p = /$	Group B	Radioactive particles, $\rho_t = 3000 \text{ kg/m}^3$, $d_t = 200 \mu\text{m}$	2.42; 1.86	Tank-in-series model

Table 1.3 Literature review of experimental work on solid residence time distribution (RTD) in CFB

Reference	Riser Dia (cm) x Height (m)	Bed material	Geldart Group	Tracer	U_g (m/s); G_s (kg/m ² s)	RTD Model
Smolders and Baeyens (2000)	10 x 6.5	Sand, $\rho_p = 2600 \text{ kg/m}^3$, $d_p = 90 \mu\text{m}$	Group A	Sodium chloride, $\rho_t = 2200 \text{ kg/m}^3$, $d_t = 150 \mu\text{m}$, Terminal velocity of tracer is the same as that of bed material	2.82–4.92 ; 4.03–34.1	Dispersion model
Ran et al. (2001)	18.6 x 9	FCC, $\rho_p = 1710 \text{ kg/m}^3$, $d_p = 79 \mu\text{m}$	Group A	Non-disruptive phosphorescent tracer method, ρ_t and d_t same as bed material	1.5–5.5; 10–180	Dispersion model
Du and Wei (2002)	14 x 10.4	FCC, $\rho_p = 1545 \text{ kg/m}^3$, $d_p = 74 \mu\text{m}$	Group A	Disruptive phosphorescent tracer method, $\rho_t = 760\text{--}10000 \text{ kg/m}^3$, $d_t = 15\text{--}1600 \mu\text{m}$, sphericity = 0.718–1.0	2.0–8.0; 9.8–39	Dispersion model
Harris et al. (2003)	Square, $0.14 \times 0.14 \text{ m}^2$, $h = 5.8 \text{ m}$	Cu and ZnS composed, $\rho_p = 4060 \text{ kg/m}^3$, $d_p = 25 \mu\text{m}$	Group A	Non-disruptive phosphorescent tracer method, ρ_t and d_t same as bed material	1.3–4.6 ; 1.6–26.9	Dispersion model
Bhusarapu et al. (2004)	15.2 x 7.9	Glass bead, $\rho_p = 2550 \text{ kg/m}^3$, $d_p = 150 \mu\text{m}$	Group B	Non-disruptive a single radioactive particle tracking, ρ_t and d_t same as bed material	3.2, 3.9 - 4.5 m/s; 26.6–36.8	Dispersion model

Table 1.3 Literature review of experimental work on solid residence time distribution (RTD) in CFB

Reference	Riser Dia (cm) x Height (m)	Bed material	Geldart Group	Tracer	U_g (m/s); G_s (kg/m ² s)	RTD Model
Andreux et al. (2008)	Square, 0.11×0.11 m ² , $h = 9$ m	FCC, $\rho_p = 1400$ kg/m ³ , $d_p = 70$ μ m	Group A	Sodium chloride, $\rho_t = /$, $d_t = 55-60$ μ m, Terminal velocity of tracer is the same as that of bed material	7; 46-133	Dispersion model
Breault et al. (2008)	30.5 x 15.3	Cork, $\rho_p = 189$ kg/m ³ , $d_p = 812$ μ m	Group A	Particle velocity measurement by LDV	3.7-5.5 ; 3.5-15.3	Autocorrelation of particle velocity fluctuations
Yan et al. (2009)	18.6 x 10	Sand, $\rho_p = 1225$ kg/m ³ (bulk density), $d_p = 78$ μ m	Group A	Disruptive phosphorescent tracer method, $\rho_t = /$, d_t similar to bed material	3.156-5.989; 40.8-229.4	Dispersion model
Mahmoudi et al. (2011)	$d = 0.09$ m, $h = /$ 9 x	Sand, $\rho_p = 2260$ kg/m ³ , $d_p = 120$ μ m	Group B	Non-disruptive a single radioactive particle tracking, ρ_t and d_t same as bed material	1-9 ; 20-600	/
Guío-Pérez et al. (2014)	$d = 0.054$ m, $h = /$	Bronze, $\rho_p = 8730$ kg/m ³ , $d_p = 64$ μ m	Group B	Non-disruptive ferromagnetic particles, $\rho_t = 7579$ kg/m ³ , $d_t = 72$ μ m.	0.85, 1.21 - 1.82 ; 22.1-92.57	Tank-in-series model

Table 1.3 Literature review of experimental work on solid residence time distribution (RTD) in CFB

Reference	Riser Dia (cm) x Height (m)	Bed material	Geldart Group	Tracer	U_g (m/s); G_s (kg/m ² s)	RTD Model
Lu et al. (2017)		FCC, Glass beads $\rho_p = 1400$, 2550 kg/m^3 , $d_p = 70, 150 \mu\text{m}$	Group A, Group B	CFD-DEM simulation with NaCl crystal	3.9, 4.5; 33.3, 36.8	CFD simulation RTD data is compared with experimental data
Bérard et al. (2021)	$d = 8 \text{ mm}$ $h = 0.36 \text{ m}$	FCC, VPOP, VPPC, VPPE, Sand $\rho_p = 2280 \text{ kg/m}^3$, $d_p = 87 \mu\text{m}$	Group A, Group B	Step injection, Pulse injection non-adsorbing Kr tracer.	10, 30 mm/s	RTD curve with Geldart Group A and Geldart Group B particles are compared.
Yu et al. (2021)	Square 11*11 cm x $h = 8.5 \text{ m}$	$\rho_p = 1400 \text{ kg/m}^3$, $d_p = 58 \mu\text{m}$	Group A	CFD TFM simulation data validated with experimental data	5,7; 76,133	E and F curves are compared with CFD simulation results
Guo et al. (2023)	$d = 5 \text{ cm}$ $h = 3.3 \text{ m}$	$\rho_p = 2550 \text{ kg/m}^3$, $d_p = 537 \mu\text{m}$	Group A	Multiphase particle-in-cell CFD simulation	2—7 ; 10-90	Filtered drag model is used to simulate solid dynamics
Kulah et al., (2024)	$d = 7.6 \text{ cm}$ $h = 6.1 \text{ m}$	FCC, $\rho_p = 1700 \text{ kg/m}^3$, $d_p = 70 \mu\text{m}$	Group A	FCC particle coated with with phosphorescent pigment	4,6,8 ; 250,250,450	Axial dispersion model

1.4 Scale Up of Circulating Fluidizing Bed

Gas-solid circulating fluidized bed scale-up is a very challenging process. Due to expensive commercial interest, data available to the industry is not available in the open domain. There is very limited literature available in the public domain related to CFB scale-up, reflecting a notable gap in scholarly discourse on the subject matter. When scaling up CFB, the behavior of large CFB differs significantly from lab-scale behavior. The main barrier to fluidized bed scale-up is the inherent scale dependence of many vital parameters, including operating conditions and design specifications. If one parameter, such as bed diameter, is changed, the majority of the other parameters, such as gas velocity, won't change at the same time. Due to this discrepancy, the hydrodynamics and transport in the scaled fluidized bed will ultimately differ significantly. In a multiphase flow system, there are always coexisting flow structures with various length scales. At least three scales are involved in circulating fluidized beds: the microscopic issue of the flow field surrounding each particle; the mesoscale issue of clusters and velocity fluctuations; and the macroscopic issue of axial and radial time-average voidage and velocity distributions. A completely similar flow for all different scales is difficult to achieve. The decline in reactor performance is a discouraging issue when scaling-up gas-solid fluidized beds. When scaled up to the commercial level, DuPont's partial oxidation of butane to produce maleic anhydride did not produce the desired results in CFB. Although it was claimed that the performance was better at lab and pilot plant scales (Contractor, 1999). This resulted in the commercial plant being decommissioned (Duduvokic, 2010). Poor solid mixing, undesirable gas flow patterns, or operational physical issues could all be to blame for such

a problem. As a result, achieving hydrodynamic similarity is both a crucial and difficult aspect of any scale-up methodology.

Numerous studies have been conducted in the last few decades on the scaling-up of gas-solid CFB. Fluidized bed scale-up methodology can be categorized into two methods: Scale-Up based on Dimensionless Groups, Scale-Up based on Chaotic Analysis. Anderson and Jackson (1967), Glicksman (1988), Glicksman et al. (1993), and Horio et al. (1986) proposed scaling laws based on different non-dimensional groups. The average bubble diameter, average rise velocity, average bed expansion, and average local bed voidage are some examples of time-averaged quantities that are frequently used in the literature to study fluidized bed hydrodynamics. This approach ignores the time-dependent dynamical behavior, despite the fact that it is widely acknowledged that it is an essential characteristic feature of the fluidized bed and crucial for its performance. Van den Bleek and Schouten (1993) recommended the chaos scale-up methodology, which is based on the idea that in addition to the laws of conservation of mass, energy, and momentum in dimensionless groups, the law of conservation of information should also be taken into consideration when scaling fluidized bed reactors. The fundamental tenet of the chaos scale-up methodology is that, in order to maintain similar hydrodynamic properties between two fluidized beds, the rate of information loss (or degree of disorder) should be maintained when scaling up a fluidized bed from the small to the large scale. Therefore, the rate of information change (or degree of disorder) in both systems should be the same for fluidized beds to scale up properly.

1.5 Motivation

The profitability of any chemical plant is determined by reactor performance. There are basically three factors which influence the reactor performance: feed conditions, reaction

kinetics, and contacting (Levenspiel, 1999). Reaction kinetics is fixed for a particular type of solid reaction or solid catalyst system. In order to achieve the highest product yield per unit volume, gas-solid residence times are carefully chosen to maximize profitability. In CFBC reaction kinetics are relatively slower compared to FCC application. FCC typically has very fast reaction kinetics as it requires a short residence time to achieve maximum product yield. To put it another way, shorter and more uniform solids residence times are desired, so a uniform radial profile of solids velocity and little back mixing in the riser are preferred. Where CFBC requires a relatively higher mean residence time and maximum mixing is preferable for better conversion. In a CFB combustor, internal solid recirculation and lateral mixing ensure the temperature of the riser is consistent. Consequently, lateral and longitudinal mixing is beneficial in a CFB combustor but detrimental in an FCC unit. Therefore, it is crucial to comprehend how operating conditions affect the solid residence time distribution, velocity, holdup, mass flux profile. For some application high gas velocity and low holdup are preferable. For some application lower gas velocity is preferable as it requires to maintain higher solids holdup. To achieve the desired flow structure for a particular application, reactor design, operating conditions, and particle characteristics should be carefully considered. The solid flow field must be understood at the most basic level possible. Accurate complex gas-solid flow dynamics prediction is necessary for CFB modeling, design, and scale-up. Even for the development of empirical correlation, significant and relevant experiment data with similar operating conditions and solid particles are needed as input.

It can be seen from Tables 1.2 and 1.3 that most of the experimental data available for solid velocity measurement in CFB riser are with Geldart Group A particles. There is a scarcity of data for Geldart Group B particles. Godfary et al. (1999) and Busharapu (2005) worked on the Geldart Group B particles, which was too small in size. No velocity data is available

for the larger Geldart Group B particles. One major application of CFB with Group B particle is coal combustions. However, nitrogen enters with the combustion air frequently dilutes carbon dioxide in combustion exhaust, hence, it is challenging to develop technologies for carbon capture. It takes a lot of energy to separate the carbon dioxide from the extra nitrogen for storage. In contrast chemical looping combustion (CLC) technology presents a potential remedy by offering a different approach to fuel combustion that can produce a pure carbon dioxide exhaust and also reduce the energy required for carbon capture and separation from nitrogen. The integrated coal gasification combined cycle is another important application of CFB with Geldart Group B particles. Dual-bed circulating fluidized bed gasifier (DBCFB) and triple-bed combined circulating fluidized bed (TBCFB) gasifier has been developed for coal and biomass gasification (Guan et al., 2010). With growing application of CFB, it is important to understanding the solid flow dynamics inside riser with bigger size Geldart Group B particles.

It is very important to identify a suitable and accurate measurement technique to measure solid flow in a riser. The invasive technique often disrupts the local flow structure, which is very important for understanding the solid flow field from a microscopic point of view. Most of the experimental data available in the literature is based on intrusive techniques. Non-invasive techniques, such as Laser-Doppler Velocimetry (LDV) and Particle Image Velocimetry (PIV) are used by several researchers. Nevertheless, each has its own limitations in applicability, as they cannot be used in opaque systems or high-density systems. Godfary et al. (1999) and Busharapu et al. (2005) used non-invasive RPT technique to map velocity flow fields at the fully developed section of the riser .

1.6 Objectives

The overall objective of the current research work is to understand the solid phase flow field in the gas-solid circulating fluidized bed at two different scales with Geldart Group B particles. The specific objectives are given below.

- Investigation of solid flow field in a laboratory scale gas-solid circulating fluidized bed with Geldart Group B particles.
 - Effect of solid flux
 - Effect of gas velocity
- Investigation of solid flow field in a pilot-scale gas-solid circulating fluidized bed with Geldart Group B particles.
 - Effect of solid flux
 - Effect of gas velocity
- Solid phase RTD analysis at laboratory and pilot scale gas-solid circulating fluidized bed with Geldart Group B particles.

Scale up study

1.7 Structure of the Thesis

This thesis comprises of five chapters. The initial chapter provides an overview of fluidization and conducts an extensive literature review on the hydrodynamics of circulating fluidized beds. The second chapter delves into the fundamental experimental methodologies employed in the examination of fluidized bed reactors. Within this chapter, the RPT measurement technique employed for the investigation of hydrodynamics in the circulating fluidized bed riser is elucidated.

In the third chapter, the utilization of RPT in a laboratory-scale gas-solid circulating fluidized bed is discussed. The first method for measuring solid flux is explained.

Subsequently, RPT data is examined, progressing from Lagrangian motion to the Eulerian velocity flow field. Using RPT data, the effects of gas velocity and solid flux on variables like mean solid velocity, RMS solid velocity, granular temperature, and turbulence intensity are discussed for both the bottom and middle sections of the riser. Furthermore, solid mixing is addressed, with a focus on the analysis of data from residence time distribution.

In the fourth chapter, the utilization of RPT in a pilot-scale gas-solid circulating fluidized bed is discussed. Then solid fraction measurement methodology is explained. The analysis of RPT data then moves from Lagrangian motion to Eulerian velocity flow field. For both the lower and middle portions of the riser, RPT data are used to discuss how gas velocity and solid flux affect various parameters, including mean solid velocity, RMS solid velocity, granular temperature, and turbulence intensity. The analysis of data from the residence time distribution is also discussed, along with solid mixing. Finally, a simplified scale-up methodology is discussed. The overall conclusion and future recommendations are presented in Chapter 6.

Notations

U_{CA}	Choking velocity	[m/s]
d_p	Particle diameter	[m]
G_s	Solid flux	[kg/m ² s]
Ar	Archimedes number	[-]
ρ_p	Particle density	[kg/m ³]
ρ_g	Air density	[kg/m ³]
U_{mf}	Minimum fluidization velocity	[m/s]
U_t	Terminal velocity	[m/s]

References

- Ambler, P.A., Milne, B.J., Berruti, F., Scott, D.S., 1990. Residence time distribution of solids in a circulating fluidized bed: experimental and modeling studies. *Chemical Engg. Sci.*, (45) 8, 2179-2188.
- Anderson, T.B., Jackson, R., 1967. Fluid mechanical description of fluidized beds. Equations of motion. *Ind. Eng. Chem. Fundam.* 6(4), 527–539.
- Andreux, R., Petit, G., Hemati, M., Simonin, O., 2008. Hydrodynamic and solid residence time distribution in a circulating fluidized bed: experimental and 3D computational study. *Chem. Eng. Process.: Process Intensif.* 47, 463–473.
- Bader, R., Findlay, J., Knowlton, T.M., 1988. Gas solids flow patterns in a 30.5cm diameter circulating fluidized bed. In: Basu, P., Large, J.F. (Eds.), *Circulating Fluidized Bed Technology II*. Pergamon Press, pp. 123–137.

- Bai, D., Jin, Y., Yu, Z., 1992. Residence time distributions of gas and solids in a circulating fluidized bed. In: Proceedings of the 7th Engineering Foundation Conference on Fluidization, pp. 195–202.
- Bai, D., Zhu, J.X., Jin, Y., Yu, Z., 1995. Internal recirculation flow structure in vertical upflow gas-solids suspensions Part I. A core-annulus model. Powder Technol. 85, 171–177.
- Bérard, A., Blais, B., Patience, G.S., 2021. Residence time distribution in fluidized beds: diffusion, dispersion, and adsorption. Adv. Powder Technol. 32, 1677–1687.
- Berruti, F., Chaouki, J., Godfroy, L., Pugsley, T.S., Patience, G.S., 1995. Hydrodynamics of Circulating Fluidized Bed Risers : A Review. Can. J. Chem. Eng. 73, 579–602.
- Bhusarapu, S., 2005. Solid Flow Mapping in Gas-Solid Risers (D.Sc. Thesis). Washington University, USA.
- Bhusarapu, S., Al-Dahhan, M., Dudukovic, M.P., 2004. Quantification of solids flow in a gas-solid riser: Single radioactive particle tracking. Chem. Eng. Sci. 59, 5381–5386.
- Bhusarapu, S., Al-Dahhan, M.H., Duduković, M.P., Trujillo, S., O’Hern, T.J., Dudukovic, M.P., Trujillo, S., Hern, T.J.O., 2005. Experimental Study of the Solids Velocity Field in Gas - Solid Risers. Ind. Eng. Chem. Res. 44, 9739–9749.
- Bi, H. T., Fan, L.S., 1991 Regime transitions in gas-solid circulating fluidized beds. Presented at the AIChE Annual Mtg, Los Angeles, CA, paper 101e.
- Bi, H.T., Grace, J.R., Lim, K.S., 1995. Transition from Bubbling to Turbulent Fluidization. Ind. Eng. Chem. Res. 34, 4003–4008.
- Bi, H.T., Grace, J.R., Zhu, J.X., 1993. Types of choking in vertical pneumatic systems. Int. J. Multiph. Flow 19, 1077–1092.
- Breault, R.W., Guenther, C.P., Shadle, L.J., 2008. Velocity fluctuation interpretation in the near wall region of a dense riser. Powder Technol. 182, 137–145.

- Chan, C.W., Brems, A., Mahmoudi, S., Baeyens, J., Seville, J., Parker, D., Leadbeater, T., Gargiuli, J., 2010. PEPT study of particle motion for different riser exit geometries. *Particuology* 8, 623–630.
- Chang, J., Zhang, K., Zhu, W., Yang, Y., 2016. Gas–solid flow in a high-density circulating fluidized bed riser with Geldart group B particles. *Particuology* 29, 103–109.
- Chanchlani, K.G., Hudgins, R.R., Silveston, P.L., 1994. Methanol synthesis under periodic operation: An experimental investigation. *Can. J. Chem. Eng.* 72, 657–671.
- Chesonis, D.C., Klinzing, G.E., Shah, Y.T., Dassori, C.G., 1990a. Hydrodynamics and mixing of solids in a recirculating fluidized bed. *Indust. Eng. Chem. Res.* 29, 1785–1792.
- Chesonis, D.C., Klinzing, G.E., Shah, Y.T., Dassori, C.G., 1990b. Solids mixing in a recirculating fluidized bed. In: Basu, P., Horio, M., Hasatani, M. (Eds.), *Circulating Fluidized Bed Technology III*. Pergamon Press, pp. 587–592.
- Contractor, R.M., 1999. Dupont’s CFB technology for maleic anhydride. *Chem. Eng. Sci.* 54, 5627–5632.
- Davidson, J.F. (1961) Symposium on Fluidization-discussion. *Transactions Institution of Eng. Prog.* 48, 220-226.
- de Salazar, R.O., Ollero, P., Cabanillas, A., Otero-Ruiz, J., Salvador, L., 1995. Flue gas desulfurization in a circulating fluidized bed. *Coal Sci. Technol.* 24, 1843–1846.
- Du, B., Wei, F., 2002. Lateral solids mixing behavior of different particles in a riser with FCC particles as fluidized material. *Chem. Eng. Process.: Process Intensif.* 41, 329–335.
- Dudukovic, M.P., 2010. Reaction engineering: Status and future challenges. *Chem. Eng. Sci.* 65, 3–11.

- Guo, J., Liu, D., Ma, J., Liang, C., Chen, X., 2024. Particle residence time distribution and axial dispersion coefficient in a pressurized circulating fluidized bed by using multiphase particle-in-cell simulation. *Chinese J. Chem. Eng.*
- Geldart, D., 1973. Types of Gas Fluidization. *Powder Technol.* 7, 285–292.
- Glicksman, R. L., 1988. Scaling relationships for fluidized beds. *Chem. Eng. Sci.* 43, 1419–1421.
- Glicksman, L.R., Hyre, M., Woloshun, K., 1993. Simplified scaling relationships for fluidized beds. *Powder Technol.* 77, 177–199.
- Godfroy, L., Patience, G.S., Chaouki, J., 1999. Radial Hydrodynamics in Risers. *Ind. Eng. Chem. Res.* 38, 81–89.
- Gopalan, B., Shaffer, F., 2013. Higher order statistical analysis of Eulerian particle velocity data in CFB risers as measured with high speed particle imaging. *Powder Technol.* 242, 13–26.
- Grace, J.R., 1990. High-velocity fluidized bed reactors. *Chem. Eng. Sci.* 45, 1953–1966.
- Grace, J.R., Bi H.T, 1997. Introduction to circulating fluidized beds, in *Circulating Fluidized Beds* (eds, Grace JR., Avidan AA. & Knowlton TM.), Engineering Foundation, New York, 1-19. Illinois.
- Guan, G., Fushimi, C., Tsutsumi, A., 2010. Prediction of flow behavior of the riser in a novel high solids flux circulating fluidized bed for steam gasification of coal or biomass. *Chem. Eng. J.* 164, 221–229
- Guío-Pérez, D.C., Pröll, T., Hofbauer, H., 2014. Influence of ring-type internals on the solids residence time distribution in the fuel reactor of a dual circulating fluidized bed system for chemical looping combustion. *Chem. Eng. Res. Des.* 92, 1107–1118.
- Harris, A.T., Davidson, J.F., Thorpe, R.B., 2003. Particle residence time distributions in circulating fluidised beds. *Chem. Eng. Sci.* 58, 2181–2202.

- Harris, B.J., Davidson, J.F. and Xue, Y., 1994. Axial and radial variation of flow in circulating fluidized bed risers. *Circulating Fluidized Bed Technology IV*, A.A.Avidan, Ed., American Institute of Chemical Engineers, New York, 103-110.
- Herbert, P., Reh, L., Nicolai, R., 1999. The ETH experience: experimental database and results from past eight years. *AICHE symposium series*, 321 95, 61-66.
- Horio, M., Morishita, K., Tachibana, O. and Murata, M., 1988. Solids distribution and movement in circulating fluidized beds. *Circulating fluidized bed technology II*, Eds. P.Basu and J.F. Large, Pergamon Press, Toronto, 147-154.
- Horio, M., Nonaka, A., Sawa, Y., Muchi, I., 1986. A new similarity rule for fluidized bed scale-up. *AICHE J.* 32, 1466–1482.
- Hu, Y., Zhao, F., Wei, F., Jin, Y., 2007. Ammoxidation of propylene to acrylonitrile in a bench-scale circulating fluidized bed reactor. *Chem. Eng. Process. Process Intensif.* 46, 918–923.
- Ishii, H., Nakajima, T. and Horio, M., 1989. The clustering annular flow model of circulating fluidized beds. *J. Chem. Eng. Japan*, 22, 484-490.
- J.B. Romero and L.N. Johanson, *Chem. Eng. Prog. Symp. Ser.*, 58(38), 28 (1962).
- Kashyap, M., Chalermisinsuwan, B., Gidaspow, D., 2011. Measuring turbulence in a circulating fluidized bed using PIV techniques. *Particuology* 9, 572–588.
- Koenigsdorff, R., Werther, J., 1995. Gas-solids mixing and flow structure modeling of the upper dilute zone of a circulating fluidized bed. *Powder Technol.* 82, 317– 329.
- Kojima, T., Ishihara, K.-i., Guilin, Y., Furusawa, t.I.T., 1989. Measurement of solids behaviour in a fast fluidized bed. *J. Chem. Eng. Japan* 22, 341–346.
- Kondukov, N.B., Kornilaev, A.N., Skachko, I.M., Akhromenkov, A.A. and Kurglov, A.S., 1964, An investigation of the parameters of moving particles in a fluidized bed by a radioisotope method. *Int. Chem. Eng.*, 4, 43-47.

- Kulah, G., Bi, X.T., Lim, C.J., Grace, J.R., 2024. Solids dispersion in high density circulating fluidized beds. *Powder Technol.* 431.
- Levenspiel, O., 1999. *Chemical reaction engineering*. John Wiley & Sons, Third Ed.
- Lin, J.S., Chen, M.M., and Chao, B.T., 1985. A novel radioactive particle tracking facility for measurement of solids motion in gas fluidized beds. *AIChE J.*, 31, 465- 473.
- Lin, W., Weinell, C.E., Hansen, P.F.B., and Dam-Johansen, K., 1999. Hydrodynamics of a commercial scale CFB boiler-study with radioactive tracer particles. *Chem. Eng. Sci.*, 54, 5495-5506.
- Lu, L., Gao, X., Li, T., Benyahia, S., 2017. Numerical Investigation of the Ability of Salt Tracers to Represent the Residence Time Distribution of Fluidized Catalytic Cracking Particles. *Ind. Eng. Chem. Res.* 56, 13642–13653.
- Lyngfelt, A., 2020. *Chemical Looping Combustion: Status and Development Challenges*. *Energy and Fuels* 34, 9077–9093.
- Mahmoudi, S., Baeyens, J., Seville, J., 2011. The solids flow in the CFB-riser quantified by single radioactive particle tracking. *Powder Technol.* 211, 135–143.
- Miller, A. and Gidaspow, D., 1992. Dense, vertical gas-solid flow in a pipe. *AIChE Journal*, 38, 11, 1801-1815.
- Milne, B.J. and Berruti, F., 1990. Modeling the mixing of solids in circulating fluidized beds, in: Basu, P., Horio, M, and Hasatani, M. (Eds.), *Circulating Fluidized Bed Technology III*, Pergamon Press, New York, 235-242.
- Moslemian, D., 1987. Study of solids motion, mixing and heat transfer in gas-fluidized beds. Ph.D Dissertation, University of Illinois at Urbana-Champaign, Urbana, Illinois.
- Pantzali, M.N., Lozano Bayón, N., Heynderickx, G.J., Marin, G.B., 2013. Three-component solids velocity measurements in the middle section of a riser. *Chem. Eng. Sci.* 101, 412–423.

- Park, D., Gau, G., 1986. Simulation of ethylene epoxidation in a multitubular transport reactor. *Chem. Eng. Sci.* 41, 143–150.
- Parssinen, J.H. and Zhu, J.X., 2001b. Particle velocity and flow development in a long and high-flux circulating fluidized bed riser. *Chemical Engineering Science*, 56, 5295-5303.
- Patience, G. S., Chaouki J., and Kennedy, G., 1991. Solids residence time distribution in CFB reactors, *Circulating Fluidized Bed Technology III*, P.Basu, M. Horio and M. Hasatani, Eds., Pergamon Press, New York, 627-632.
- Patience, G.S., Chaouki, J., 1995. Solids hydrodynamics in the fully developed region of CFB risers. In: Large, J.F., Laguerie, C. (Eds.), *Fluidization VIII*. Engineering Foundation, Tours, France, pp. 33–40.
- Patience, G.S., Mills, P.L., 1994. Modelling of propylene oxidation in a circulating fluidized-bed reactor. *Stud. Surf. Sci. Catal.* 82, 1–18.
- Pugsley, T.S., Patience, G.S., Berruti, F., Chaouki, J., 1992. Modeling the Catalytic Oxidation of n-Butane to Maleic Anhydride in a Circulating Fluidized Bed Reactor. *Ind. Eng. Chem. Res.* 31, 2652–2660.
- Qian, C. and Li, J., 1994. Particle velocity measurement in CFB with an integrated probe. *Circulating Fluidized Bed Technology IV*, A.A.Avidan, Ed., American Institute of Chemical Engineers, New York, 274-278.
- Ran, X., Wei, F., Wang, Z., Jin, Y., 2001. Lateral solids dispersion in a high-density riser with swirling air flow. *Powder Technol.* 121, 123–130.
- Reh, L. 1971. Fluidized bed processing. *Chem Engg Prog*, 67, 58–63.
- Reh, L., 1986. The circulating fluid bed reactor - its main features and applications. *Chem. Eng. Process.* 20, 117–127.

- Reh, L., 1995. New and efficient high-temperature processes with circulating fluid bed reactors. *Chem. Eng. Technol.* 18, 75–89.
- Rhodes, M.J., Zhou, S., Hiramata, T., Cheng, H., 1991. Effects of operating conditions on longitudinal solids mixing in a circulating fluidized bed riser. *AIChE J.* 37, 1450–1458.
- Smolders, K., Baeyens, J., 2000. Overall solids movement and solids residence time distribution in a CFB-riser. *Chem. Eng. Sci.* 55, 4101–4116.
- Squires, A.M., 1986. Story of Fluid Catalytic Cracking: the First “Circulating Fluid Bed”., in: *Circulating Fluidized Bed Technology*. Elsevier, pp. 1–19.
- Stellema, C.S., 1998. Radiotracers for gas/solids flows in (Interconnected) fluidized beds. Ph.D Dissertation, Delft University of Technology, Delft, Netherlands.
- Su, X., Wang, C., Pei, H., Li, J., Lan, X., Gao, J., 2019. Experimental Study of Solids Motion in an 18 m Gas-Solids Circulating Fluidized Bed with High Solids Flux. *Ind. Eng. Chem. Res.* 58, 23468–23480.
- Tartan, M., Gidaspow, D., 2004. Measurement of granular temperature and stresses in risers. *AIChE J.* 50, 1760–1775.
- Toomey, R.D. and Johnstone, H.F. 1952 Gaseous fluidization of solid particles. *Chem. Eng. Prog.* 48, 220-226
- Van den Bleek, C.M., Schouten, J.C., 1993. Deterministic chaos: a new tool in fluidized bed design and operation. *Chem. Eng. J. Biochem. Eng. J.* 53, 75–87.
- Van engelandt, G., De Wilde, J., Heynderickx, G.J., Marin, G.B., 2007. Experimental study of inlet phenomena of 35 ° inclined non-aerated and aerated Y-inlets in a dilute cold-flow riser. *Chem. Eng. Sci.* 62, 339–355.
- Viitanen, P.I., 1993. Tracer studies on a riser reactor of a fluidized catalyst cracking plant, *Ind. Eng. Chem. Res.*, 32, 577-583.

- Vrieland, G.E., Murchison, C.B., 1996. Anaerobic oxidation of butane to butadiene over magnesium molybdate catalysts. I. Magnesia supported catalysts. *Appl. Catal. A Gen.* 134, 101–121.
- Wang, C., Zhu, J., Li, C., Barghi, S., 2014. Detailed measurements of particle velocity and solids flux in a high density circulating fluidized bed riser. *Chem. Eng. Sci.* 114, 9–20.
- Wang, Q., Zhou, J., Tu, J., Luo, Z., Li, X., Fang, M., Cheng, L., Ni, M., Cen, K., 1996. Residence time in circulating fluidized bed. *Circulat. Fluidised Bed Technol.*, 128–133.
- Wei, F., Chen, W., Jin, Y., Yu, Z., 1996. Solids residence time distribution in a CFB riser. *J. Chem. Eng. Chinese Universit.* 10, 264–270 (in Chinese).
- Wei, F., Cheng, Y., Jin, Y., Yu, Z., 1998. Axial and lateral dispersion of fine particles in a binary-solid riser. *Canadian J. Chem. Eng.* 76, 19–26.
- Wei, F., Jin, Y., Yu, Z., Chen, W., Mori, S., 1995. Lateral and axial mixing of the dispersed particles in CFB. *J. Chem. Eng. Japan* 28, 506–510.
- Wei, F., Zhu, J.-X., 1996. Effect of flow direction on axial solid dispersion in gas- solids concurrent up flow and down flow systems. *Chem. Eng. J. Biochem. Eng. J.* 64, 345–352.
- Weinell, C.E., Dam-Johansen, K., Johnsson, J.E., 1997. Single-particle behaviour in circulating fluidized beds. *Powder Technol.* 92, 241–252.
- Westphalen, D., Glicksman, L., 1995. Lateral solid mixing measurements in circulating fluidized beds. *Powder Technol.* 82, 153–167.
- Wilhelm, R. H. and Kwauk, M.. 1948, Fluidization of solid particles. *Chem. Engg Prog.* 44, 201-218.
- Yan, A., Pa, J.H., Zhu, J., 2003. Flow properties in the entrance and exit regions of a high-flux circulating fluidized bed riser. *Powder Technol.* 131, 256–263.

- Yan, A., Zhu, J., 2005. Scale-up effect of riser reactors: Particle velocity and flow development. *AIChE J.* 51, 2956–2964.
- Yan, C., Fan, Y., Lu, C., Zhang, Y., Liu, Y., Cao, R., Gao, J., Xu, C., 2009. Solids mixing in a fluidized bed riser. *Powder Technol.* 193, 110–119.
- Yerushalmi, J., Turner, D.H., Squires, A.M., 1976. The Fast Fluidized Bed. *Ind. Eng. Chem. Process Des. Dev.* 15, 47–53.
- Zhang, Y., Lei, F., Xiao, Y., 2018. The influence of pressure and temperature on gas-solid hydrodynamics for Geldart B particles in a high-density CFB riser. *Powder Technol.* 327, 17–28.
- Zhang, M., Qian, Z., Yu, H., Wei, F., 2003. The solid flow structure in a circulating fluidized bed riser / downer of 0.42-m diameter. *Powder Technol.* 129, 46–52.
- Zheng, C., Tung, Y., Li, H., Kwauk, M., 1992. Characteristics of fast fluidized beds with internals. In: *Proceedings of the 7th Engineering Foundation Conference on Fluidisation, Australia: Brisbane*, pp. 275–283
- Zheng, C., Tung, Y., Li, H., Kwauk, M., 1992. Characteristics of fast fluidized beds with internals. In: *Proceedings of the 7th Engineering Foundation Conference on Fluidisation, Australia: Brisbane*, pp. 275–283.
- Zhou, J., Grace, J.R., Lim, C.J. and Brereton, C.M.H., 1995. Particle velocity profiles in a circulating fluidized bed riser of square cross-section. *Chem. Eng. Sci.*, 50-2, 237-244.
- Zoonen, D.V., 1962. Measurements of diffusional phenomena and velocity profiles in a vertical riser. In: *Rottenburg, P.A., Shepherd, N.T. (Eds.), Proceedings on the Symposium on the Interaction Between Fluids and Particles. The Institute of Chemical Engineers, Loudon*, pp. 64–71.

CHAPTER 2

Measurement Techniques in Fluidized Bed and Application of Radiotracer

Scope

This chapter provides an overview of the measurement methods that can be used to measure the hydrodynamic parameters discussed. This chapter gives an outline of the two categories of measuring techniques used in fluidized beds: intrusive and non-intrusive. In-depth explanations are provided for the radioactive particle tracking (RPT) technique and its implementation. This chapter aims to outline the potential of various techniques for the characterization of the hydrodynamic parameters and flow patterns in fluidized beds and to familiarize with the RPT technique, which is used to analyze velocity flow fields in CFB risers.

2.1 Introduction

Very unique flow structures define the gas-solid flow within a fluidized bed. Low-velocity fluidization results in nearly solid-free bubbles that form at the gas distributor and spread out quickly as they move through the bed. In the case of solid-catalyzed reactions, the presence of bubbles causes a bypass of the reaction gas. A separation of the gas-solid flow into a more concentrated dispersed phase of clusters or strands and a continuous lean phase is seen in high-velocity fluidization or in circulating fluidized beds (Werther, 1999). Fluidized beds require measurements of local solid volume concentrations, solid velocities, solid mass flows, as well as vertical and horizontal solid distributions within the system. The industry needs these measurements to track plant performance, improve procedures,

assess plant problems, assess gas-solid contacting, and assess basic flow phenomena in fluidized beds.

Understanding the complex flow structures requires accurate and reliable methods to measure the hydrodynamic properties in fluidized beds. Numerous measurement techniques have been proposed and reviewed by numerous researchers (Grace and Baeyens, 1986; Yates and Simons, 1994; Simons 1995; Chaouki et al., 1997; Louge, 1997; Werther, 1999; Dyakowski and Jaworski 2001; and van Ommen and Mudde, 2008) to address this issue. Measuring techniques in gas-solid fluidized beds can be grouped into intrusive and non-intrusive techniques. The majority of the measurement techniques that are used to characterize fluidized beds in literature are intrusive in nature due to their widespread and commercial viability. However, due to their intrusiveness, which can change the local hydrodynamics of the bed, these techniques are unreliable for understanding the macroscopic analysis.

2.2 Invasive Techniques

2.2.1 Pressure

It is common practice to use pressure to describe the fluid dynamics of gas-solid fluidized beds. A pressure measurement system is reliable and reasonably priced. It consists of a pressure sensor and a pressure tap. The average bed density and bed height are frequently calculated using time-averaged pressure measurements. The use of pressure has the benefit that it is simple to measure even in challenging industrial settings. The upward-flowing gas keeps the solid particles in suspension in the fluidized bed. The weight of the solids less their buoyancy per unit cross-sectional area of the bed is then approximately equal to the pressure drop of the gas.

Time-series pressure signals obtained from fluidized bed recordings can be analyzed using a variety of techniques. These techniques can be broadly divided into three categories: time domain, frequency domain, and state space. The most popular time domain analysis methods include the probability density function of pressure increment, standard deviation of pressure single, cycle time, Hurst analysis, and autoregressive models. Frequency domain method includes power spectrum via non-parametric methods, power spectrum via autoregressive models, transient power spectral density (PSD) and wavelet analysis. State space analysis includes attractor reconstruction, information entropy, correlation dimension, Lyapunov exponent and attractor comparison methods.

Fan et al. (1984) developed a model to describe the correlation between the amplitude of pressure signals and excess gas velocity. Puncochar et al. (1985) suggested that the standard deviation of the pressure fluctuation is related to superficial velocity, which can be used to determine the minimum fluidization velocity. Johnsson et al. (2000), categorize the bubbling beds into single bubbles, multiple bubbles, and exploding bubble regimes based on the shape of the PSD function of the pressure fluctuation signals. Shou and Leu (2005) used the PSDF and wavelet analysis of absolute pressure fluctuations to characterize various flow regimes of sand and fluid catalytic cracking (FCC) catalysts in a CFB. van Ommen and Mudde (2008) reviewed techniques for figuring out the distribution of gas and solids in fluidized beds. van Ommen et al. (2011) reviewed time-series, frequency domain, and state space analysis techniques for time-series analysis of pressure fluctuations in gas-solid fluidized beds for various fluidization regimes. All of these findings suggest that pressure fluctuation measurements can be used to fully characterize fluidized beds, which can be classified into groups for regime transition detection, hydrodynamic structure detection, bubble characteristics detection, cluster detection and fluidized bed monitoring.

2.2.2 Capacitance probe

The capacitance probe measures the local dielectric constant of the gas-solid suspension, which is affected by the local solid fraction. Capacitance probes come in a variety of designs. A capacitance probe with two parallel rectangular plates and a gap between them was used by Geldart and Kelsey (1972) to measure the solid concentration. A needle-shaped capacitance probe was developed by Werther and Molerus (1973). It has a metal enclosure and a centrally protruding needle that act as its two poles. The needle probe has a significant advantage over the plate probe in terms of low hydrodynamic disturbance. Almstedt and Olsson (1982) used cross-correlation to determine the bubble rise velocities in a pilot-scale pressurized bubbling fluidized bed combustor. Almstedt and Zakkay (1990) studied the bubble dynamics in an atmospheric bubbling fluidized bed combustor using a similar probe. Hage and Werthe (1996) measured the local solid concentrations inside the CFB combustor using a water-cooled guarded capacitance probe. Sharma et al. (2000) examined the cluster properties in the fast fluidized bed using a needle-type capacitance probe.

2.2.3 Optical fiber probe

Optical fiber probe is the most commonly used instrument to measure local solid velocity and solid fraction. Ohki and Shirai (1976) developed a small optical fiber probe made-up of three fibers bound together so that the fiber in the center of the bundle provided the illumination that the other two fibers detected. The illuminating and detecting fibers were bent into a horseshoe shape, with a 5 mm gap between them. The illuminating fiber was illuminated with light from a stroboscope with a known flash frequency, and the detected light was sent to the photomultiplier. It is possible to eliminate the background light by utilizing a pulsed light source. Background noise can be effectively reduced with modern light sources like light-emitting diodes (LED).

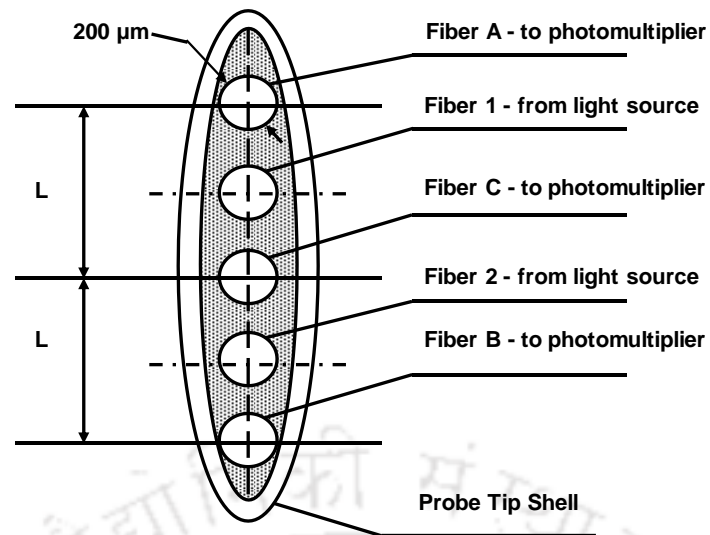


Figure 2.1: Schematic of the five-fiber optical probe (Zhu et al. 2001).

2.3 Non-intrusive Techniques

2.3.1 X-ray or γ -ray Tomography

Tomography is a useful tool to obtain the voidage distribution in a cross-section of the bed. Electric capacitance tomography (ECT) and nuclear (X-ray or γ -ray) tomography are different methods of this technique. The Electric capacitance tomography (ECT) is fast, but it has poor spatial resolution. Nuclear tomography's image reconstruction is much simpler and has a better spectral resolution, but its temporal resolution is limited. X-ray tomography has been used to visualize gas-solid FB since 1990s. The source and detector in this nuclear tomography procedure are placed on the opposite side of the bed. The medium and column absorb a portion of the X-ray or gamma ray that passes through them. The Beer-Lambert law governs the intensity that the detector detects. The detector's intensity varies depending on the medium's attenuation coefficient, solid fraction, and other factors.

$$I = I_0 e^{(-\mu d)} \quad 2.1$$

in which:

I_0 = Initial intensity of the monochromatic beam.

μ = The attenuation coefficient,

d = Distance between source and detector

I = The intensity after passage.

Grassler and Wirth (2000) used X-ray computed imaging to assess the solid concentration in a CFB. X-ray tomography was also used by Franka and Heindel (2009) to calculate the local time-averaged gas hold-up using various solids, superficial gas velocities, and side air injection flow rate. Heindel et al. (2008) provide a description of X-ray tomography procedure they. Escudero and Heindel (2011) used X-ray tomography to investigate how material density and bed height affect fluidized bed hydrodynamics. Wu et al. (2007) used polyethylene particles to characterize the flow behavior of a gas-solid fluidized bed using X-ray tomography. Yates and Simons (1994) reviewed techniques created over the previous 50 years for examining the flow of gases and solids in fluidized suspensions.

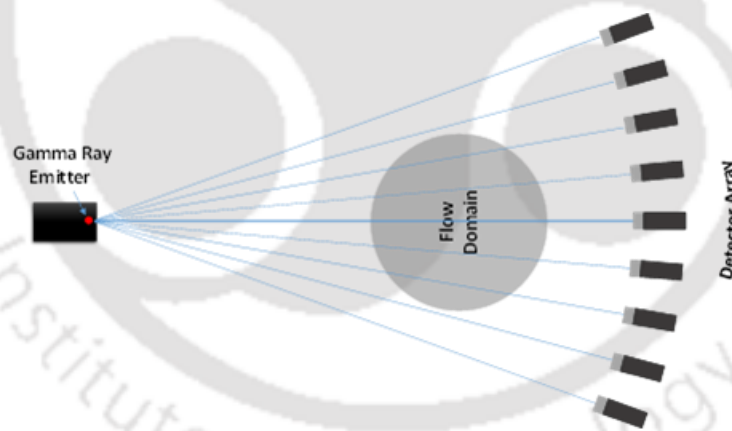


Figure 2.2: Schematic of the γ -ray Tomography

The successful implementation of γ -ray tomography and radioactive particle tracking (RPT) for the characterization of multiphase flow was described by Dudukovic (2002). Bhusarapu et al. (2006) used γ -ray tomography coupled with RPT to identify different regimes of the CFB riser. The schematic diagram of γ -ray tomography is presented in Figure 2.2

2.3.2 Electrical Capacitance Tomography

Electrical capacitance tomography (ECT) technique is widely used to measure the concentration of a two-phase flow inside a vessel. To apply this technique in a fluidized bed the vessel walls are needed to be non-conducting. This method's main goal is to ascertain the mixture's dielectric permittivity distribution through capacitance measurements made between electrode pairs positioned all around the vessel. A schematic of an ECT system equipped with 8 electrodes is shown in Figure 2.3. As part of the experiment, one of the electrodes is used as a source electrode, and the capacitances between it and the other electrodes are then measured. The main objective of ECT is to measure the spatial distribution of the dielectric permittivity from the measured capacitances, which is then converted to the spatial distribution of concentration.

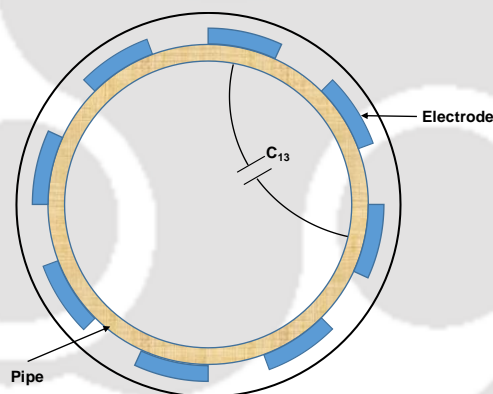


Figure: 2.3: Schematic of Electrical capacitance tomography

McKeen and Pugsley (2002) made suggestions about the potential use of the ECT as a non-intrusive measurement tool that can deliver valuable data on the cross-sectional distribution of solids and gas in addition to the dynamic behavior of the fluidized bed. Pugsley et al. (2003) validated the semi-quantitative nature of ECT images using an optical fiber probe of the voidage profiles inside the riser of a circulating fluidized bed and in a conical bubbling fluidized bed. White (2005) demonstrated how the ECT method can be used to observe the behavior of particles in a bubbling fluidized bed. Du et al. (2004) investigated

whether the ECT method could be used to identify the choking phenomenon in fluidized beds.

2.3.3 Laser Doppler Velocimetry (LDV)

Laser doppler velocimetry (LDV) is a method that enables high temporal resolution velocity measurement at a point in a flow field. It is also known as Laser Doppler Anemometry (LDA). The monochromatic laser beam used by the laser Doppler velocimetry is directed at the target, and the reflected light is then collected. The Doppler effect states that the relative velocity of the targeted object determines how the wavelength of the reflected radiation changes. Thus, by creating an interference fringe pattern, which measures the change in wavelength of the reflected laser light, the velocity of the object can be determined. Schematic diagram of LDA is given in Figure 2.4, a laser beam with a known frequency illuminates the particles. A photo-multiplier tube (PMT), a device that produces a current proportional to absorbed photon energy and then amplifies that current, detects the scattered light. The Doppler shift is the difference in frequency between the incident and scattered light. The local particle velocity can be determined by measuring the Doppler-equivalent frequency of the laser light scattered by the seeded particles in the flow (intensity modulations within the crossed-beam probe volume). This technique cannot be implanted in a high density bed. It is essential to have a transparent wall in the column and a transparent medium.

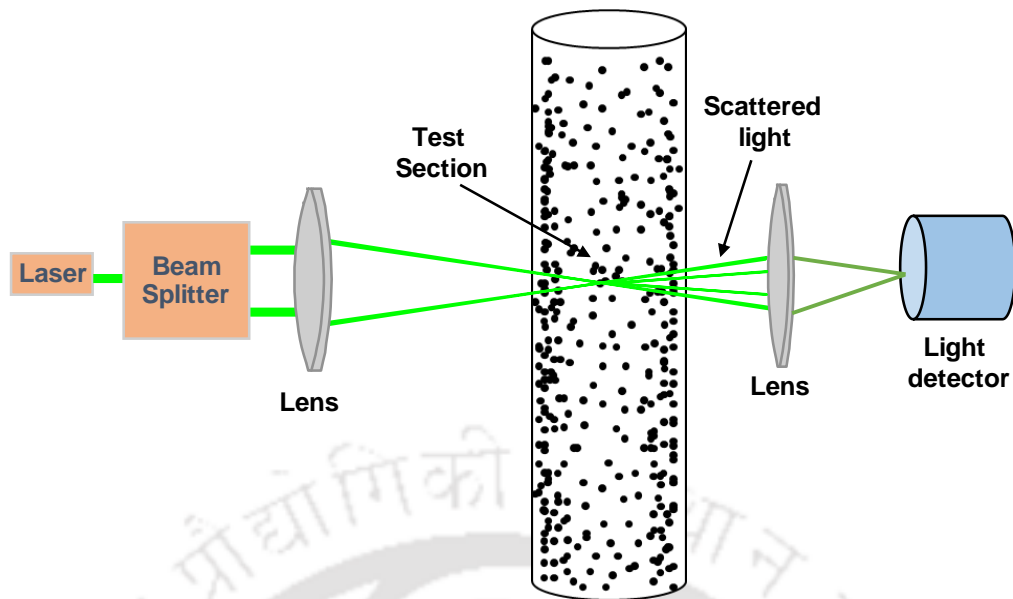


Figure 2.4: Schematic of LDA technique

Mathiesen (2000) used the LDA technique in a riser to measure solid velocity at the fluctuation level. Later, the LDA method was applied by Pantzali et al. (2013) and De Wilde (2005) to measure the solid velocity inside low-density CFB risers. Using this method, they calculated the mean velocity and higher-order momentum of the fluctuating velocity.

2.3.4 Particle Image Velocimetry (PIV)

Particle Image Velocimetry (PIV) is a technique providing instantaneous velocity vector measurements in a cross-section of a flow. It measures field values, which allow for the measurement of all values within a specific area. In PIV, seeded particles are photographed at sufficiently frequent intervals, allowing the movement of the seeded particle to be determined from the subsequent images. A high-power laser, a CCD camera, an optical setup that turns the laser's output light into a light sheet, tracer particles, and the synchronizer make up a typical PIV setup, as shown in Figure 2.5. A high-speed camera synchronized with laser pulse is used to capture the first image quickly enough to be prepared for the second exposure. Two single-exposure images with a time difference of

the order of microseconds are acquired using a CCD camera. To prevent image blurring, laser pulses should be used when analyzing fast flows. They also serve as a photographic flash for the digital camera, stopping any motion. To generate a lot of light energy quickly, a pulsed laser is preferred.

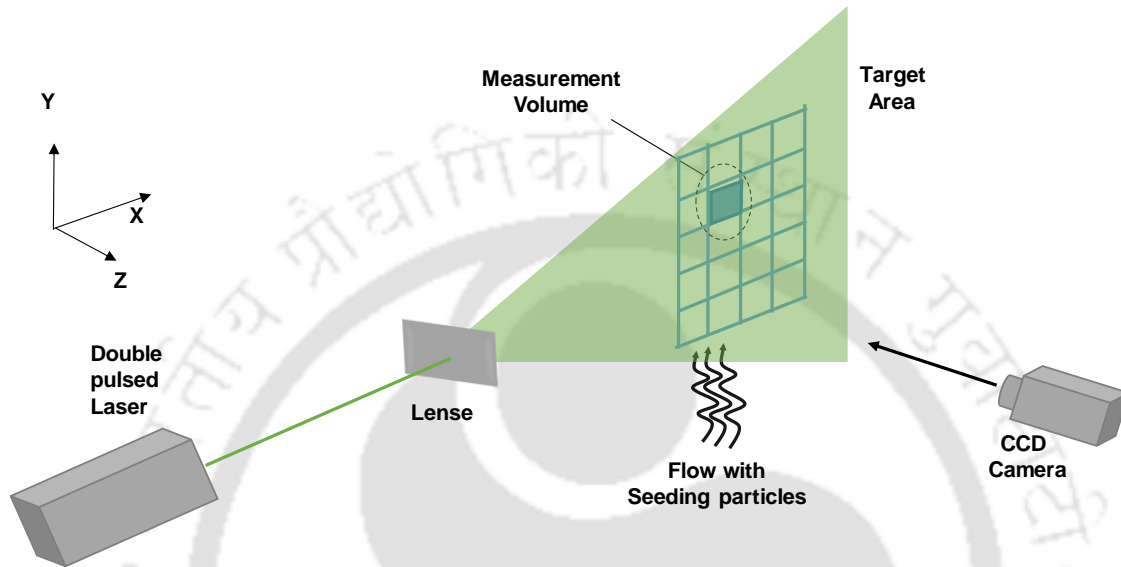


Figure 2.5: Schematic of PIV measurement technique

A 2D planar PIV is the most widely used. However, in recent years, 3D volumetric PIV has also been developed to measure the three velocity components. The inability of PIV to measure in high-volume fraction systems and matching refractive indices at the various interfaces are its two main problems. The resolution of time is also constrained. The temporal resolution constraint has recently been overcome using High-Speed Particle Image Velocimetry (HSPIV). However, it is difficult to take local measurements in the essentially opaque system.

PIV is commonly used to access the CFB flow structure and measure the solid phase velocity at a fluctuation level. The PIV technique was used by Shaffer et al. (2013), Kashyap et al. (2011), Tartan and Gidaspow (2004), and Gopalan and Shaffer (2013) to

measure the solid phase velocity. Shi (2007) and Carlos et al. (2016) used PIV to analyze the formation of solid structures or clusters.

2.3.5 Positron Emission Particle Tracking (PEPT)

Positron Emission Particle Tracking (PEPT) is a method that enables high temporal and spatial resolution imaging of the three-dimensional internal dynamics of opaque systems. The PEPT method is used to track the movement of a single tracer particle attached to a moving rigid body moving in a system of granular or liquid flow.

When a positron and an electron collide, two equally energetic anti-parallel γ rays are created, leading to annihilation. PEPT uses multiple instances of detecting a pair of γ rays from the same annihilation to determine the location of the tracer. Typically, a tracer that is similar to the phase of interest is prepared using ^{18}F , ^{61}Cu , and ^{66}Ga radionuclides. γ -ray cameras that are position sensitive are used. As seen in Figure 2.6, cameras are situated on either side of the column. By using highly penetrating (511 keV) γ -rays, the internal dynamics of even large, dense, optically opaque systems may be analyzed.

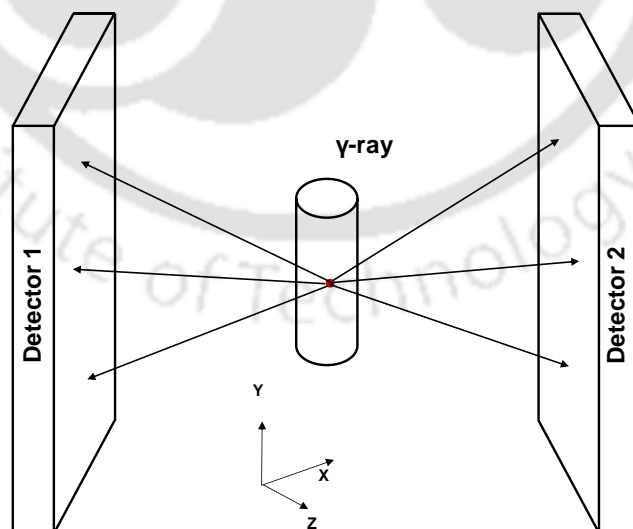


Figure 2.6: Schematic diagram of PEPT for a single particle (Parker and Fan 2008)

The system is introduced to a single tracer particle that emits positrons. The line passing through the tracer is represented by two back-to-back γ -rays that are created when the positron emitted by the tracer annihilates with the electron present in the material surrounding the tracer. Triangulation is used to reconstruct positions along multiple such lines of resolution. Theoretically, a reconstruction can be completed with just two lines. However, in reality, only about 50 are employed. This is due to the possibility that many of the detected events are tainted by Compton scattering and/or that two detected γ rays may not have come from the same annihilation. Prior to using triangulation to determine the position, these corrupted events are removed. The detectors are run simultaneously with a 7 ns resolving time at both ends (Parker et al., 2002). Thus, events recorded within this resolving time can be considered to be of the same annihilation.

Chan et al., (2009,2010) Van de Velden et al., (2007,2008) used PEPT technique to track and analyse solid motion and solid mixing inside CFB riser. Windows-Yule (2022) recently reviewed the advancement of PEPT technique

2.3.6 Radioactive Particle Tracking (RPT)

Like PEPT, radioactive particle tracking (RPT) is also a radiation-based phase tracking technique. It tracks the motion of a tracer particle (high energy γ ray emitter) with the help of scintillation detectors strategically placed around the zone of interest, as shown in Figure 2.7. Tracer particles used in experiments should have hydrodynamic properties similar to the phase of interest whose velocity is to be mapped. The size, shape, and density of the tracer particles used to track solid particles should match those of the solids already present in the system. Tracer particles in a liquid should be neutrally buoyant so that they follow the path of the liquid phase. The primary component of RPT are scintillation detectors, PMT, data acquisition system and a radioactive tracer particle. NaI (TI) is the most

commonly used scintillation detector because of its low cost compared to bismuth germanate (BGO) crystals. However, the scintillation detector with a BGO crystal is much more sensitive and accurate.

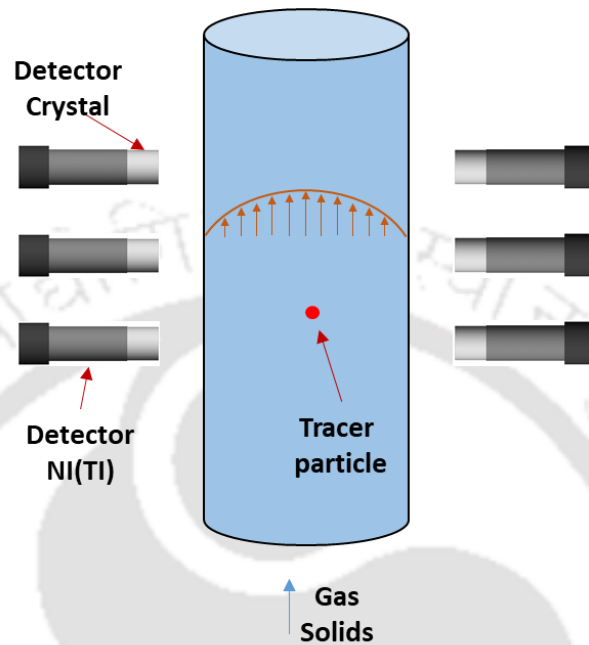


Figure 2.7: Typical configuration of the detectors around the fluidized bed for RPT

Each detector measures and records count data with the help of a data acquisition system the incoming radiation from the tracer particles. The fundamental idea is that the counts (photons) that are recorded change with position. The recorded counts are a unique function of the acquisition time, solid angle, attenuation, and separation between the detector and the tracer particle. Calibration for count data versus position is crucial because the solid angle and attenuation depend on the tracer particle position, detector location, and solid fraction profile in the system. As the solid fraction profile is a function of gas inlet velocity and solid flux, it is vital to perform the calibration in all cases. A tracer is kept at known locations during calibration, and counts recorded on each detector for this known location are recorded. A distance count map is created under in-situ conditions for each detector used in the measurement at each location inside the column of interest. During the actual

experiment, radiotracer is allowed to flow with the solid and radiation detected by each detector is recorded as a count value. Tracer position is reconstructed from the experimental count data of each detector, which is then compared with the count vs position data generated during the calibration process. A Lagrangian position time series of the tracer particle is obtained from time series count data. The instantaneous velocity of the tracer particle is calculated by time-differentiating displacement between two consecutive lagrangian particle positions.

2.3.7 Selection of experimental technique in CFB

Understanding the complex hydrodynamics of a circulating fluidized bed reactor necessitates an understanding of the phenomena occurring in time and length scale. Such techniques need to be of high temporal and spatial resolution. The technique should be flexible enough to implement at different scales of setup and different positions of the riser. An intrusive technique (e.g. optical fiber probe) can disrupt the local hydrodynamics. Tebianian et al. (2015) used Optical fibre probes RPT, PEPT, PIV to investigate local particle velocities in a ‘traveling fluidized bed’ operated under similar operating conditions using FCC particles. Although there were some significant quantitative differences, the profiles predicted by the four experimental techniques showed a fair amount of agreement. The technical limitations of each technique bring on this discrepancy. The reasons include the intrusiveness of optical fiber probes, variations in the physical characteristics of the bulk bed material, sensitivity to particle concentration and angle of travel, inequalities in measurement volumes, and variations in acceptance algorithms of techniques.

The main objectives of the current work are to investigate the flow dynamics in CFB at different scales and develop scale up correlations. Therefore, a technique that is portable, non-invasive, and whose accuracy does not change with scale is needed. Optical-based

techniques have a high temporal resolution like PIV and LDA compared to radiation based techniques. However, this technique cannot be applied to dense flow conditions. The accuracy of this technique differs with the position and scale of the column. Hence, PEPT can be used only for low diameter systems and, hence, not for different diameter systems. RPT is a tested method successfully used in other fluidized bed solid phase hydrodynamics investigations (Kalo et al., 2019a,b, Bhusarapu et al., 2006, Godfroy et al., 1999) and satisfies all the requirements for this one. The methodology, hardware and software for RPT implementation are covered in the following sections.

2.4 Radioactive Particle Tracking Technique and Velocity Measurements

Radioactive particle tracking is first implemented by Kondukov et al. (1964). The 3D trajectory of the tracer was measured using six scintillation detectors fixed in pairs along three mutually perpendicular axes surrounding a gas fluidized bed. Borlai et al. (1967) designed a single detector system to be positioned beneath the distributor in order to track the vertical displacements of the tracer inside a gas fluidized bed. Van Velzen et al. (1974) preferred the option of mounting a single detector above the fountain region of their gas-spouted bed. Masson et al. (1981) described some qualitative characteristics of the recirculation of a large, light radioactive plastic sphere in the majority of a gas-fluidized bed of small, dense glass beads. They used two scintillation detectors that were partially collimated and vertically spaced apart. Bascoul et al. (1993) used a similar detector assembly to analyze the movement of particles in monolayer liquid fluidized beds. In all the above studies, the accuracy and spatial resolution of the measured tracer trajectories were inadequate, making it impossible for them to yield useful quantitative information.

Three-dimensional tracers in gas fluidized beds were first described by Lin et al. (1985). They improved the signal processing algorithm, reducing the impact of intrinsic noise

caused by the quantized nature of γ -emission. The radioactive particle tracking (RPT) method developed by Larachi et al. (1995) was conceptually comparable to that of Lin et al. (1985), but it produced better spatial resolution as a result of the incorporation of a phenomenological model to explain the interactions of the γ -rays with the vessel geometry. Subsequently, Moslemian et al. (1989) pursued the improvement of RPT electronics and circuits, which led to a significant decrease in tracer positioning mistakes. Two more RPT improvements were developed (Devanathan et al., 1990; Moslemian et al., 1992; Yang et al., 1993) to track liquid flow behavior in bubble columns and further quantify solid motions in gas fluidized beds. Chaouki and co-workers (Roy et al., 1994, 1996; Godfroy et al., 1997; Larachi et al., 1995; Cassanello et al., 1995, 1996) studied the solid movement in conical spouted beds, CFB risers, monolayer and binary liquid fluidized beds, and monolayer and binary three-phase fluidized beds. Prof. Roy and co-workers (Upadhyay et al., 2010, 2013, Sharma et al., 2017, Yadav et al., 2020) developed and implemented RPT at a variety of multiphase flow reactors. Using RPT, they studied binary fluidized beds, bubble columns, convective boiling fluids, and two-phase flow in a helical geometry. Upadhyay and co-workers (Jain et al., 2017, Kalo et al., 2019a,b) implemented RPT to study hydrodynamics behavior in liquid-solids and gas-solids systems. Prof. Roy, Prof. Upadhyay and colleagues mostly use Monte-Carlo technique along with Chi square technique for position tracking. However, Yadav et al. (2017) implemented Artificial Neural Network (ANN) for position tracking.

2.4.1 RPT Setup Components

The main components of the RPT setup consisted of detectors, a data acquisition system, and radioactive particles or tracer particles. The brief description of the different components is given below :

Radioactive Tracer Particle:

The radioactive particles used to track the solid phase are selected based on the criteria as given by Roy et al. (2002) and Upadhyay (2010). Tracer isotope should be selected in such a way that it emits high energy γ -rays so that it can easily transmit through the reactor and reactor wall medium and can be detected by the detector. The half-life of the tracer isotope should not be too short. The activity of the tracer will be reduced during the experiment if the half-life is too low, possibly requiring daily calibration. Also, it requires multiple radioactive tracers at regular intervals, which is always challenging because of strict regulations regarding nuclear materials in any country. On the other hand, a long half-life is not desirable for radiation safety reasons. In the RPT technique, Sc-46 is typically used as the tracer particle. With a half-life of 83 days, scandium is suitable for a specific set of experiments in any multiphase flow reactor. It exhibits two photopeaks, which is good enough to penetrate through the metal wall of the experimental setup. The density of scandium is 2990 kg/m^3 , which is closer to the density (2500 kg/m^3) of the solid (glass beads) used in this study.

The method used to prepare the tracer, however, varies across the literature based on different phase and different applications. Like for liquid phase tracking, tracer particles should be neutrally buoyant. Hollow polypropylene or polystyrene balls that have a small amount of ^{46}Sc embedded in them are used to track liquids. The particles are made neutrally buoyant by maintaining some hollow air gap inside the ball (Devanathan, 1991; Degaleesan, 1997; Upadhyay, 2010). For solid phase tracking in a fluidized bed, small amount of Sc-46 powder is doped inside the solid particle and the shape, size, and density is matched. For solid phase tracking, small amounts of Sc-46 powder are doped inside of solid particles, maintaining the size, shape, and density of the particles the same as in the fluidized beds. Moslemian et al. (1989) used tracer particle made up of Sc-46 and matched

their density and diameter closely with the glass beads used in their experiment. Upadhyay (2010) used Sc-46 powder doped in a glass bead and polystyrene as a tracer in order to match the density of the tracer with the glass beads and sago used in the experiment. Lin (1981), Moslemian et al. (1989), Upadhyay (2010), Zaid (2013), Efhaima and Al-Dahhan (2017) and Kalo et al. (2019a,b) tracked solid particles in a gas-solid fluidized bed. Roy et al. (2005), Jain et al. (2014), and Jain et al. (2017) tracked solid particles in the liquid-solid fluidized bed. Sc-46 was doped into a particle that was the same size and density as the solids used in the experiment by Limtrakul et al. (2005), Jain et al. (2014), Jain et al. (2017), and Kalo et al. (2019).

However, the tracer particles used for the RPT experiment in the current study were produced by doping scandium powder into glass beads and radioactively irradiated in a nuclear reactor at BARC Facility, Mumbai (Biswal et al., 2016,2021,2022). Hence, the tracer will be similar to the solids being tracked in size and density. They developed different techniques to prepare Sc-46 tracer dispersed in glass beads for RPT application. Details of preparation techniques and methodology for radioactive tracer particles suitable for RPT experiments can be found in Biswal et al. (2016, 2021, 2022).

Scintillation Detectors:

The scintillation detector measures radiation by detecting the minute light bursts that radiation emits when it interacts with matter. When radiation interacts with scintillating materials, it transfers its energy, which excites the scintillation molecules. During the process of de-excitation, the excited scintillating molecules emit energy (light photons). Scintillations are light flashes that are converted into electrical pulses that, when fed into the right electronics, can distinguish between various radiation types as well as various photon energies emanating from the same radioactive source. Scintillation counters come in a variety of shapes and sizes, but they all have two optically coupled components as part

of their detector systems. A scintillator, which is essentially a solid crystal that emits light pulses when radiation deposits energy in it, makes up the main part of the device. The second element is the photo-multiplier, which turns this light pulse into an electrical current pulse. The photocathode of a photo-multiplier tube, which is physically and hermetically coupled, interacts with these light photons (PMT). The result of this process is a photoelectric voltage with a small corresponding current. A series of dynodes installed inside the PMT amplify the photoelectric voltage generated by the cathode before being finally collected on the anode and producing an electric current. To attract electrons to the following dynode, each succeeding dynode has a higher potential than the one before it. The high voltage supply to the PMT via coaxial wires provides the necessary potential difference.

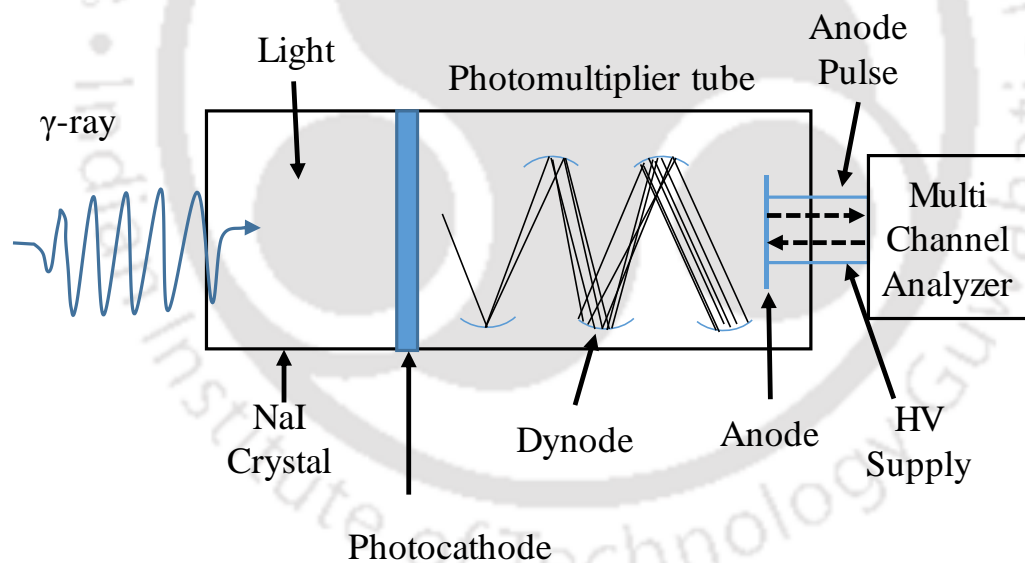


Figure 2.8: Schematic diagram of NaI(Tl) scintillation detector

Photon Detection And Counting:

The pulse processing unit (PPU) processes the signals from the detector. The Multi-input data acquisition system (MIDAS) collects analog signals from each PPU and converts them

into digital signals. The instruments MIDAS and PPU are designed by Electronic Enterprises (I) Pvt. Ltd., for tracer experiments like RPT. It supports communication through the LAN/USB ports. The information acquired during the experiment is transferred to the PC via the USB/LAN cable and stored on the PC. The power supply has been designed to provide sufficient current to all the modules. This power supply gives +5V to +12V outputs. The output of the detector is the input to the amplifier and single-channel analyzer (SCA). The millivolt signal is amplified up to 1000 times by the amplifier. The SCA eliminates noise to remove unwanted pulses. The single channel analyzer selects the useful signals and eliminates the unwanted signals by using a threshold. It removes the data below the LLD (low-level discriminator) threshold and above the ULD (upper-level discriminator) threshold. The schematic diagram of the data acquisition system is given in Figure 2.9.

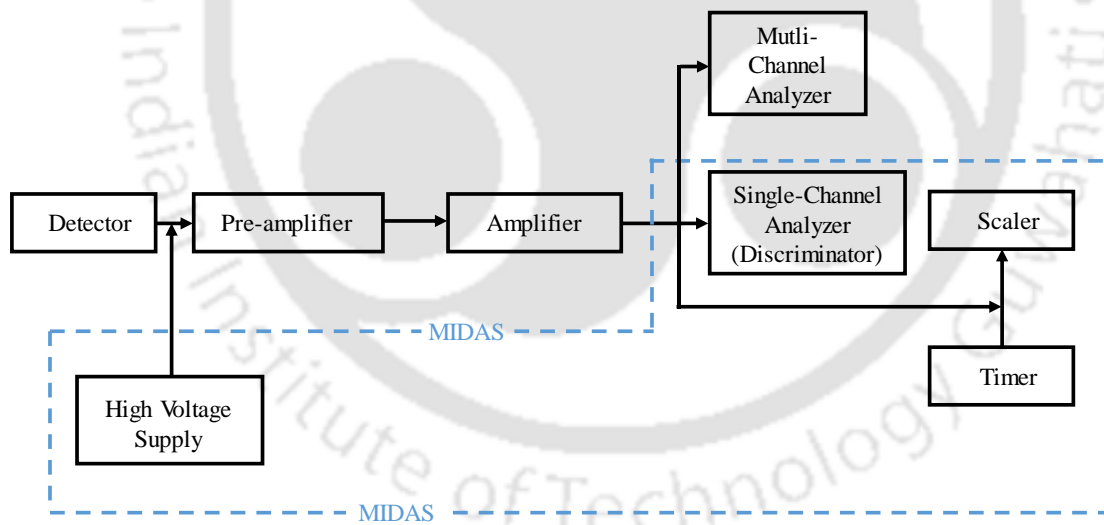


Figure 2.9: Schematic diagram of data acquisition system

The number of photopeak counts recorded in a sampling time is given by Larachi et al. (1994), which is shown in equation 2.2

$$C = \frac{T\nu A\epsilon_{abs}\phi}{(1+\tau\nu A\epsilon_{abs}\phi)} \quad 2.2$$

where,

T = sampling time(s),

ν = number of γ -ray photons emitted per disintegration. A = source strength

ϕ = Photo peak fraction

τ = Detector dead time(s)

2.4.2 Methodology and Implementation of RPT

The application of radioactive isotopes in flow mapping of multiphase flow using RPT technique is based on the emission and detection principle. Basically, RPT setup is made up of a collection of scintillation detectors placed external to the reactor and measures the radiation emitted from inside the reactor. In RPT a high-energy radioactive particle is used to map the motion of solids inside a system of interest. To map the motion of solid phase in a fluidized bed reactor tracer particle should resemble the shape, size, and density of the solids to be followed (Lin et al., 1985). The radioactive particle is free to move around inside the column of particles. Numerous scintillation detectors are placed outside the column to gather information on the radiation the radioactive particle emits. Each detector's intensity is influenced by the tracer particle's distance from the detector, the phases between them, the type of wall being used, and the solid angle that the tracer particle forms on the detector. The position of the particle is established using a calibration procedure following the experiment. The calibration is performed in in-situ to mimic the composition of the phases and materials between the radioactive particles and the detectors.

2.4.2.1 Arrangement of Detectors

In the RPT experiment, the location of the detectors is crucial and needs to be precisely known. Both placing the detector too far from the column and placing it too close to it can result in the detector becoming blinded from recording too many counts, which lowers the

spatial resolution of the detector and solid angle. Therefore, the detector should be positioned in the best possible way. Detector arrangement varies from case to case on the basis of the scan geometry of the zone of interest. If the diameter of the scan zone is large, the multiple detectors are favourable in one plane (four detectors in one plane or more). Roy et al. (2002) worked extensively to optimize the detector arrangement in the RPT experiment in the gas-liquid riser. They suggested that the optimal number of the detector at one plane is three, and the detector should be arranged in such a way that it is symmetrically distributed around the column. They also suggested putting detectors in a staggered manner in an alternative plan where detectors on alternate planes are farthest from each other. In larger diameter columns, the central plane developed poor resolution. This can be minimized by installing more detectors off the central plane. Optimal detector arrangement depends on radiation source activity, the number of detectors available, and the geometry of the zone of interest. However, performing resolution and sensitivity tests before proceeding for calibration and experiment is essential. In the present work, the diameter of the column is small (riser id 5 and 10 cm), which is one and two times the crystal size of the detector. It was observed that two detectors in each plane in a staggered position are good enough based on scan zone and detector availability. Details of the resolution and sensitivity counter are given in the experimental section.

2.4.2.2 Calibration

Calibration is done prior to the experiment, where the tracer particle is placed at various known locations. This step is crucial because the accuracy of the RPT experiment heavily depends on the accuracy of the calibration. During calibration, a tracer particle is positioned inside the target vessel at known locations in an "in-situ" condition with detectors, which are placed around the target column as previously mentioned. And then, the detectors around the column record the intensity of the radiation (counts) this count are stored with correspond

tracer position. The count that each detector records is influenced by the solid angle the tracer particle makes with the detector as well as the distance, phase, and wall material between them. As the distance between the tracer particle and the detector increases, the amount of radiation detected at each detector decreases exponentially. This data is used to plot the calibration curve, which relates the radiation intensity recorded at a detector to the distance between the tracer and the detector. However, this process is practically impossible due to the tedious work involved and the time and effort needed. For photon emission, transmission, and detection, the Monte Carlo code was developed by Larachi et al. (1994). Upadhyay (2010) modified this code to generate the counts recorded on the detector for a known particle location. It required a few points in 'in-situ' calibration to optimize the unknown fitting variables using modified Monte Carlo code (Upadhyay, 2010). The position-count map is generated in the current work using the Monte Carlo program and a small set of calibration data. There are other three-technique to generate this position vs count map all over the coloumn. Weighted Least Square Regression; Cross-Correlation Method; Feed Forward Neural Network

2.4.2.3 Monte Carlo method (Beam et al., 1978; Upadhyay, 2010)

The Monte Carlo program tracks the photon histories as they travel from source to medium to detector for final detection (Larachi et al., 1994; Beam et al., 1978). The estimation of detector efficiencies in photon capture and recording takes into account the effects of both geometry and radiation. There are two ways in which the geometry of the vessel under investigation and its position in relation to the detectors affect the issue. First, in calculating the physical distance between the tracer, which is assumed to be a point source and the center of the crystal. Only a fraction of the photons that the tracer particle emits in the direction of the detectors are intercepted and absorbed by the detector, which primarily depends on the solid angle as the tracer particle emits photons in all directions in three-dimensional space. Even though it can be calculated using three-dimensional co-ordinate

geometry, the process is time-consuming. However, ray tracing is necessary in order to determine the detector efficiency or the likelihood that a photon striking a detector crystal will actually be absorbed. The Monte Carlo method accomplishes both objectives by using random number generation and random path selection algorithms.

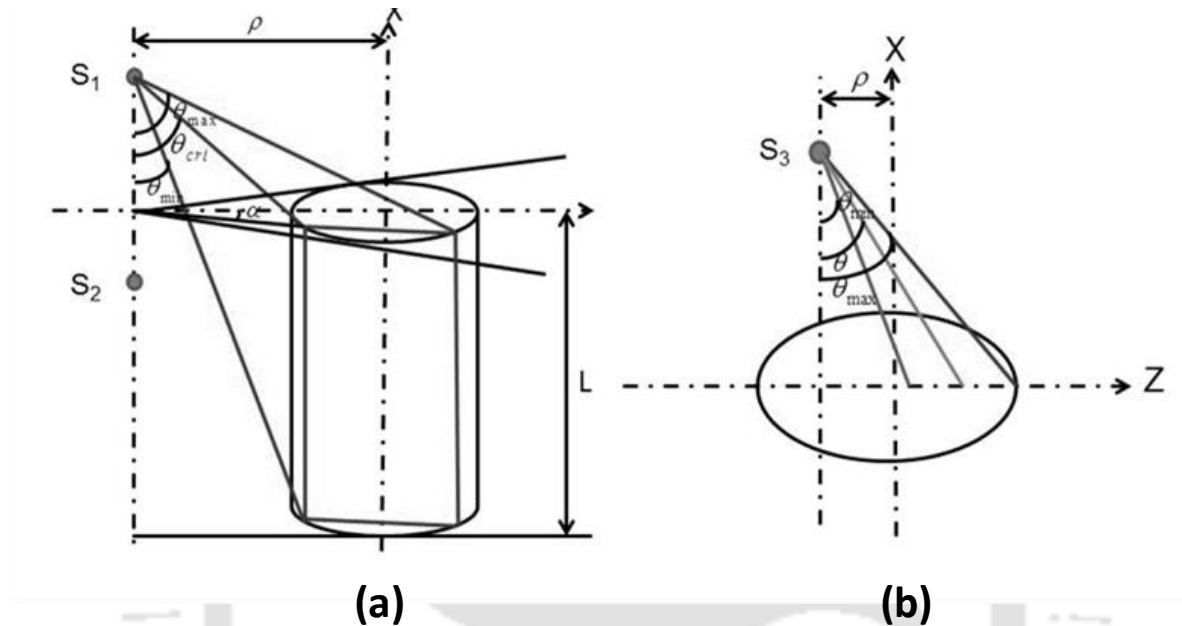


Figure 2.10: Schematic diagram for relative positioning of source and detector (a) when the source is outside detector flat face, and (b) within the detector flat face (Beam et al., 1778)

In equation 2.3, mass attenuation, solid angle subtended by the detector disk and surface on the tracer particle, and penetration depth of photons in the detector are unknowns (Roy (2000)). Geometrical arguments can be used to determine the penetration depth of photons. Since photons are emitted from particles in all directions and each direction has a unique path length, the solid angle function is complicated. It is calculated using the Monte Carlo method to follow a large number of photon histories traveling in various directions. Suitable optimization algorithms evaluate source strength, attenuation, and dead time for each detector using limited experimental values.

$$\epsilon_{abs} = \iint_{\Omega} \frac{(\vec{r} \cdot \vec{n})}{r^3} \exp[-\sum_{j=1}^N \mu_j l_j] (1 - \exp(-\mu_D d)) d\Sigma \quad 2.3$$

where,

\vec{n} is the unit normal vector to the curved surface of the detector.

\vec{r} is the radius vector from source to the detector.

μ_D is the mass attenuation coefficient of the detector crystal material.

d is the penetration depth of photons in the detector crystal.

μ_j is the mass attenuation coefficient of all the material that comes in the path of photons between the source and the detector.

In this equation, there are three unknown mass attenuation coefficients of the detector crystal (μ_D), the penetration depth of photons in the detector crystal (d) and the solid angle subtended the detector surface and tracer (Ω). The solid angle is calculated by tracking the particle histories in all directions through the Monte Carlo method. The solid angle subtended by the detector to the tracer particle is measured based on the possible tracer position with respect to the detector. There can be three possible positions of a tracer particle with respect to the detector position. Figure 2.10 shows the schematic diagram of the source and detector positioning when the source is outside the detector's flat face and within the detector's flat face. If the particle is in position S₁, photon can enter through both the flat and curved surface of the detector. If the particle is in position S₂, the photon can enter only through the curved surface; if it is in position S₃, the photon can enter only through the flat surface. The angular quantities α_{max} , α_{min} , θ_{max} , θ_{min} and θ_{cri} are defined as the boundary of the surface, as shown in the Figure 2.10. Using random generators, different photon histories are produced for each photon defined by α and β and between the angular extrema (Beam et al., 1978).

All directions in the solid angle provided by the combination (α, θ) are not equivalent regardless of how precisely the detector is oriented. Individual directional weights $\zeta(\alpha)$, $\zeta(\theta)$ were calculated by Beam et al. (1978) using geometrical arguments. Consequently, the averaged solid angle value is provided by

$$\tilde{\Omega} = \frac{1}{N} \sum_{j=1}^N \zeta(\alpha_j) \zeta(\theta_j) \quad 2.4$$

where,

N is the total number of photon trajectories tracked.

$\zeta(\cdot)$ is the weighting function in each sampled direction.

The point of entry and exit determines the depth of penetration of the photon within the crystal. The photon can enter and exit the crystal in one of four different ways, including:

- Lateral entrance, bottom exit.
- Lateral entrance, lateral exit.
- Top entrance, bottom exit.
- Top entrance, lateral exit.

Figure 2.11 shows a schematic representation of various possible penetration depths.

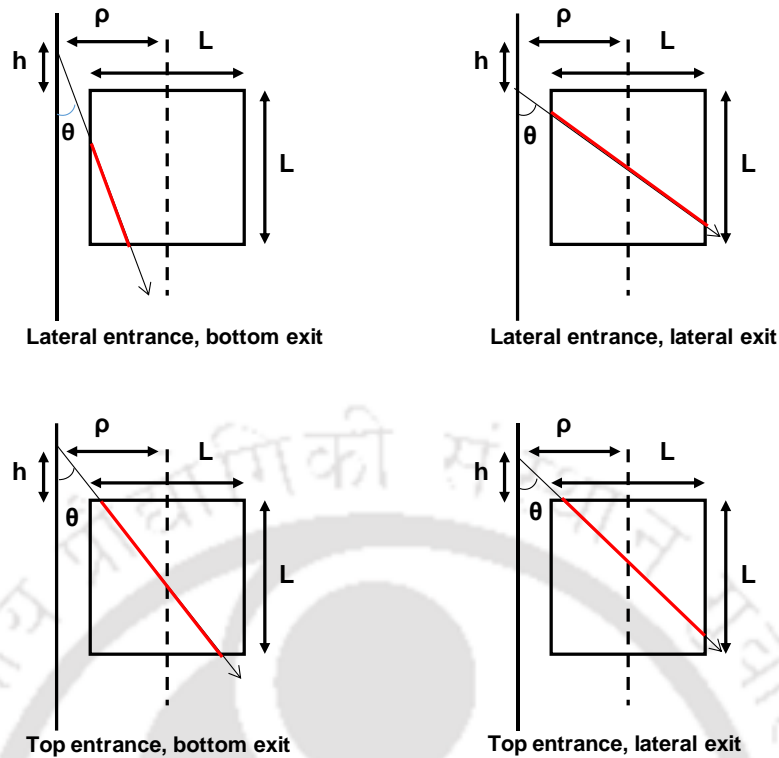


Figure 2.11: The four possible cases of travel of photons through the detector. (Beam et al., 1778)

Angle θ is used to determine the entry point, and geometric reasoning is used to determine the depth of penetration (Figure 2.11). If the depth of penetration exceeds the chord length of the detector, it is not counted. Only photons with a depth of penetration below the detector's length, or photons that the detector crystal will absorb, are counted.

2.4.2.4 Reconstruction Algorithm

In RPT, the tracer allows to flow with solid phase throughout the column. During the travel through the scan zone, tracer emits γ -ray, which is detected and recorded by the detector placed around the zone of interest. There are ways reported in the literature to reconstruct position of tracer particle from this count data. They are,

- Weighted Least Square Regression Method

- Monte Carlo Method
- Feed Forward Neural Network Method
- Cross Correlation Method

The above mentioned methods' advantages and disadvantages are reported by Upadhyay (2010). In the current work, the Monte Carlo method is used for particle position reconstruction, which is explained in the previous section. This is a basic two-stage method. The first stage is preparing a count vs position map or look up table, which is explained briefly in the 'Monte Carlo method' section. After experiments, count data recorded by each detector is compared with the lookup table (Table 2.1) and positions are reconstructed.

Table 2.1 Look up table showing calibration data

r	θ	z	C1	C2	C3	C4	C5	C6	C7	C8
0	0	5	400	385	400	150	125	150	40	30
5	0	5	390	280	380	170	170	190	60	40
5	10	5	250	230	350	210	390	250	75	50

Here r , θ and z are coordinates of tracer particles and C1, C2, C3,..C8 are counted and recorded by the 1st, 2nd, 3rd, 8th detectors. This table gives the position vs count map for all the possible positions in the zone of interest, However, in practice, this count generated by the detector cannot match exactly with the table. So the chi (χ) square test (equation 2.5) is

performed at every node point for which simulated calibration data is recorded in a look-up table to reconstruct the best possible position of the tracer.

$$\chi^2(j) = \sum_{i=1}^{N_D} \frac{(C_i - M_i)^2}{\sigma_j^2} \quad 2.5$$

Where,

C_i is count generated during the experiment.

M_i is count generated in Monte-Carlo method.

2.4.2.5 Post Processing and Velocity Calculations

Instantaneous positions are reconstructed from the experiment data. This instantaneous time-series data is actually the lagrangian track of the tracer. Velocity can be calculated from dividing displacement by the time difference between two consecutive events, which is fundamentally data acquisition time. This instantaneous velocity is then assigned to the corresponding virtual Eulerian grid. RPT is an experiment that is continued until statistically significant data is accumulated for each eulerian grid. Similar to computational fluid dynamics (CFD), the entire column is divided into small cells to obtain the ensemble average velocity. The fluctuation velocity is determined by the difference between the instantaneous and ensemble averaged velocities. In addition to providing instantaneous, mean, or fluctuation velocities, RPT measurement also offers PDFs of instantaneous velocities at all locations. Dispersion coefficient, auto-correlation coefficient, hurst exponent, time of flight, circulation time distribution, and RTD can also be calculated in addition to turbulence parameters (Larachi et al., 1997; Degaleesan, 1997; Godfroy et al., 1999; Roy et al., 2000; Bhusarapu, 2005, Kalo et al., 2019).

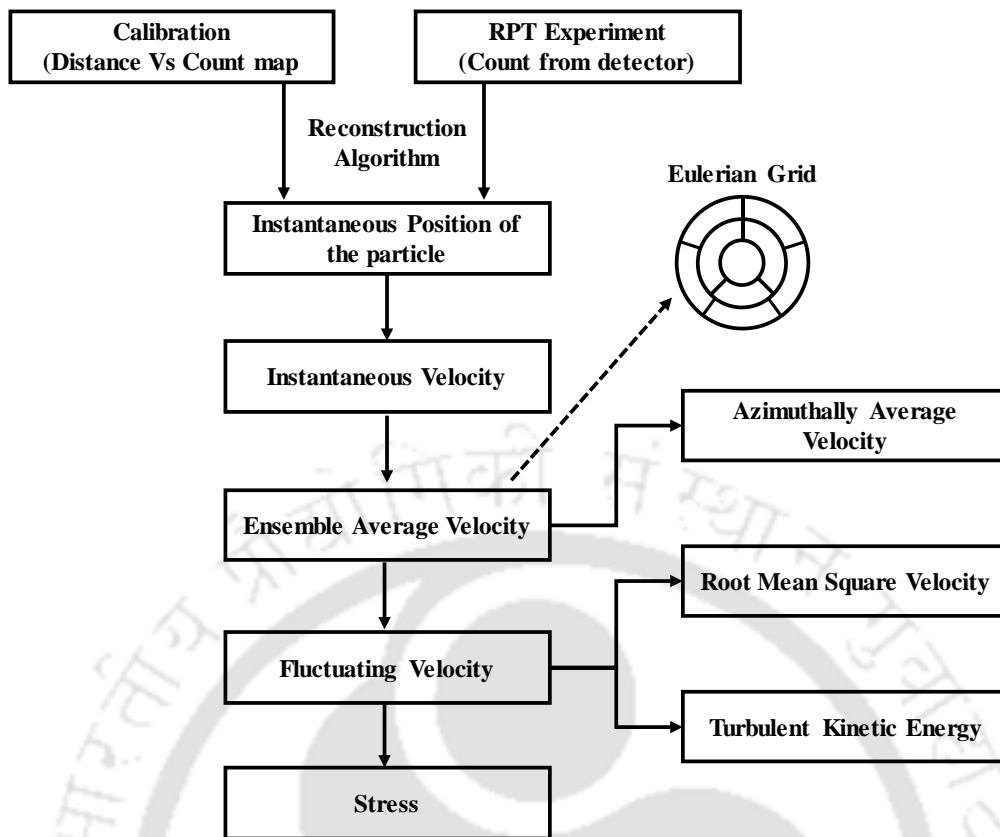


Figure 2.12: Flow chart of RPT data acquisition and processing

Figure 2.12 shows the RPT technique's flowchart. Table 2.2 provides the equations for mean velocity, fluctuating velocity, root mean square (RMS) velocity stress, and granular temperature.

Table 2.2 Quantities calculated from RPT experimental data (Roy et al., 2005; Upadhyay, 2010)

Instantaneous Velocity	$v_r = \frac{2}{\Delta t} [r_2 \cos(\theta_2 - \theta_1) - r_1]$ $v_\theta = \frac{2}{\Delta t} [r_2 \sin \theta_2 - \theta_1]$ $v_z = \frac{\Delta z}{\Delta t}$ <p>where</p> $r = \frac{1}{2} \sqrt{r_1^2 + r_2^2 + 2r_1 r_2 \cos(\theta_1 - \theta_2)}$
Ensemble average velocity at cell (i,j,k)	$\langle v_q(i, j, k) \rangle = \frac{1}{N(i, j, k)} \sum_{n=1}^{N(i, j, k)} v_{q,n}(i, j, k)$ <p>where, q refers the polar coordinates r, θ, z</p>
Fluctuating velocity component	$v_{q(i',j,k)} = v_q(i, j, k) - \langle v_q(i, j, k) \rangle$
Azimuthally average velocity component	$\langle v_q(i, k) \rangle^{az} = \frac{\sum_{j=1}^{Tdim(i)} \langle v_q(i, j, k) \rangle N(i, j, k)}{\sum_{j=1}^{Tdim(i)} N(i, j, k)}$
RMS velocity	$\langle v_q \rangle^{RMS} = \sqrt{\langle v_q^2 \rangle}$
Stress	$\tau_{qs} = \langle v_{q(i,j,k)} v_s(i, j, k) \rangle$
Granular temperature	$\Theta = \frac{1}{3} \sum v_q^2$
Turbulent Intensity	$TI = \frac{\sqrt{\Theta}}{\bar{v}}$

Notations

A	Source strength	[Ci]
C	Photo peak count	[-]
C_i	Counts registered by the i^{th} detector for the tracer particle at j^{th} node	[-]
d	Penetration depth of photons in the detector crystal	[m]
i	Index of radial component	[-]
j	Index of azimuthal component	[-]
k	Index for axial component	[-]
l_j	Length of intervening medium between source and detector	[m]
M_i	Counts measured by the i^{th} detector for unknown particle position	[-]
N	Total number of photon trajectories tracked	[-]
N_D	Number of detector	[-]
$N(i, j, k)$	Number of occurrence in compartment index by (i, j, k)	[-]
q	Index for co-ordinate (r, θ, z direction)	[-]
t	Time of acquisition	[s]
T	Sampling time	[s]
v_r, v_z, v_θ	Velocity in r, θ, z direction respectively	[m/s]
v_q	q^{th} component of instantaneous velocity	[m/s]
v_q'	q^{th} component of fluctuating velocity	[m/s]
$\langle v_q \rangle$	q^{th} component of ensemble average velocity	[m/s]
$\langle v_q \rangle^{az}$	q^{th} component of azimuthal average velocity	[m/s]
$\langle v_q \rangle^{RMS}$	q^{th} component of RMS velocity	[m/s]
$\langle v \rangle$	Mean velocity calculated through RPT experiments	[m/s]

z	Axial level in the column	[m]
Greek letters		
α	angle formed by line connecting tracer particle and detector center, and the x-axis	[radian]
(α, β, γ)	The direction cosines of the point (x, y, z)	[-]
ε_{abs}	Absolute efficiency of detector	[-]
ϕ	Photo peak fraction	[-]
μ	Medium attenuation coefficient	[m ⁻¹]
μ_j	Mass attenuation coefficient of all the materials that comes in the path of photons between the source and the detector	[m ⁻¹]
μ_D	Mass attenuation coefficient of the detector crystal material	[m ⁻¹]
ν	Number of gamma ray photons emitted per disintegration	[-]
Ω	Solid angle	[steradian]
ρ_p	Particle density	[kg/m ³]
τ_{qs}	Reynolds stress	[kg/m.s ²]
τ	Detector dead time	[s]
θ	Angle in osculating plane formed by source and detector curved surface	[radian]
$\zeta(\cdot)$	Weighting function in each sampled direction	[-]

Subscript

cri	Critical
max	Maximum
min	Minimum
r, θ, z	Cylindrical co-ordinate
x, y, z	Cartesian co-ordinate

References

- Almstedt, A.E., Olsson, E., 1982. Measurements of bubble behavior in a pressurized fluidized bed burning coal, using capacitance probes, Proc. 7th Int. Conf. Fluidized Bed Combustion, Philadelphia, PA, pp. 89–98.
- Almstedt, A.E., Zakkay, V., 1990. An investigation of fluidized bed scaling-capacitance probe measurements in a pressurized fluidized bed combustor and a cold model, Chem. Eng. Sci. 45 1071–1078.
- Bascoul, A., Couderc, J. P., Delmas, H. 1993. Solids Motion in Liquid- Solid Fluidization (Mouvement des particules solides en fluidisation liquide-solide). Chem. Eng. J. 51, 135.
- Beam, G.B., Wielopolski, L., Gardner, R.P., Verghese, K., 1978. Monte Carlo calculation of efficiencies of right-circular cylindrical NaI detectors for arbitrarily located point sources. Nucl. Instruments and Methods 154, 501–508.
- Bhusarapu, S., 2005. Solids Flow Mapping in Gas-Solid Risers, D.Sc. Thesis.
- Bhusarapu, S., Al-Dahhan, M.H., Duduković, M.P., 2006. Solids flow mapping in a gas-solid riser: Mean holdup and velocity fields. Powder Technol. 163, 98–123.
- Biswal J, Goswami S, Upadhyay RK, Pant HJ. 2021. Methods of preparation of microparticles for radioactive particle tracking experiments. Appl Radiat Isot. Feb;168:109380.
- Biswal, J., Jagat, H., Kumar, V., Joseph, A., 2022. Preparation and characterization of cobalt-60 glass microspheres for radioactive particle tracking applications. Appl. Radiat. Isot. 185, 110249.
- Biswal, J., Joseph, A., Shah, J.G., Pant, H.J., Dash, A., 2016. Preparation of ⁴⁶Sc glass microspheres by combined melt-quenching and microwave methods for applications in radioactive particle tracking experiments. J. Radioanal. Nucl. Chem. 308, 335–340.
- Borlai, O., Hodany, L., Blicke, T. 1967. Investigation into the mixing in fluidized beds. Proceedings of the International Symposium on Fluidization; Drinkenburg, A. A. H., Ed.; The Netherlands University Press: Amsterdam, The Netherlands, p 433.
- Carlos Varas, A.E., Peters, E.A.J.F., Kuipers, J.A.M., 2016. CFD-DEM simulations and experimental validation of clustering phenomena and riser hydrodynamics. Chem. Eng. Sci. Van de Velden, M., Baeyens, J., Seville, J.P.K., Fan, X., 2008. The solids flow in the riser of a Circulating Fluidised Bed (CFB) viewed by Positron Emission Particle Tracking (PEPT). Powder Technol. 183, 290–296.

- Cassanello, M., Larachi, F., Guy, C., Chaouki, J. 1996. Solids mixing in gas-liquid-solid fluidized beds: Experiments and modeling. *Chem. Eng. Sci.* 51, 1011.
- Cassanello, M., Larachi, F., Marie, M.-N., Guy, C., Chaouki, J. 1995. Experimental characterization of the solid phase chaotic dynamics in three-phase fluidization. *Ind. Eng. Chem. Res.* 34, 2971.
- Chan, C.W., Seville, J., Yang, Z., Baeyens, J., 2009. Particle motion in the CFB riser with special emphasis on PEPT-imaging of the bottom section. *Powder Technol.* 196, 318–325.
- Chan, C.W., Seville, J.P.K., Parker, D.J., Baeyens, J., 2010. Particle velocities and their residence time distribution in the riser of a CFB. *Powder Technol.* 203, 187–197.
- Chaouki, J., Larachi, F., and Dudukovic, M. P. 1997. Noninvasive tomographic and velocimetric monitoring of multiphase flows. *Ind. Eng. Chem. Res.* 36 (11):4476–4503.
- De Wilde, J., Van Engelandt, G., Heynderickx, G.J., Marin, G.B., 2005. Gas-solids mixing in the inlet zone of a dilute circulating fluidized bed. *Powder Technol.* 151, 96–116.
- Degaleesan, S., “Turbulence and Liquid Mixing in Bubble Columns”. D.Sc. Thesis, Washington University, USA, (1997).
- Devanathan, N., 1991. Investigation of Liquid Hydrodynamics in Bubble Columns via Computer Automated Radioactive Particle Tracking (CARPT) (D.Sc. Thesis). Washington University in St. Louis, USA.
- Devanathan, N., Moslemian, D., Dudukovic, M. P. 1990. Flow mapping in bubble columns using CARPT. *Chem. Eng. Sci.* 45, 2285.
- Du, B., Warsito, W. , and Fan, L. S. 2004. ECT studies of the choking phenomenon in a gas-solid circulating fluidized bed. *AIChE J.* 50 (7):1386-1406.
- Dudukovic, M. P. 2002. Opaque multiphase flows: experiments and modeling. *Exp. Therm. Fluid Sci.* 26 (6):747-761.
- Dyakowski, T., and Jaworski, A. J. 2001. Application of non-invasive techniques for imaging fluidized beds—A review. In *Handbook of conveying and handling of particulate solids* (volume 10 of *Handbook of powder technology*), ed. A. Levy and H. Kalman, 807-823. Amsterdam: Elsevier.
- Efhaima, A., Al-Dahhan, M.H., 2017. Assessment of scale-up dimensionless groups methodology of gas-solid fluidized beds using advanced non-invasive measurement techniques (CT and RPT). *Can. J. Chem. Eng.* 95, 656–669.

- Escudero, D., and Heindel, T. J. 2011. Bed height and material density effects on fluidized bed hydrodynamics. *Chem. Eng. Sci.* 66 (16):3648-3655.
- Fan, L.T., Hiraoka, S., and Shin, S. H. 1984. Analysis of pressure fluctuations in a gas-solid fluidized bed. *AIChE J.* 30 (2):346-349.
- Franka, N. P., and Heindel, T. J. 2009. Local time-averaged gas holdup in a fluidized bed with side air injection using X-ray computed tomography. *Powder Technol.* 193 (1):69-78.
- Geldart, D., and Kelsey, J. R. 1972. The use of capacitance probes in gas fluidised beds. *Powder Technol.* 6 (1):45-50.
- Godfroy, L., Larachi, F., Chaouki, J., 1999. Position and velocity of a large particle in a gas/solid riser using the radioactive particle tracking technique. *Can. J. Chem. Eng.* 77, 253–261.
- Godfroy, L., Larachi, F., Kennedy, G., Grandjean, B. P. A., Chaouki, J. 1997. On-line flow visualization in multiphase reactors using neural networks. *Appl. Radiat. Isot.* 48, 225.
- Gopalan, B., Shaffer, F., 2013. Higher order statistical analysis of Eulerian particle velocity data in CFB risers as measured with high speed particle imaging. *Powder Technol.* 242, 13–26.
- Kashyap, M., Chalermssinsuwan, B., Gidaspo, D., 2011. Measuring turbulence in a circulating fluidized bed using PIV techniques. *Particuology* 9, 572–588.
- Grace, J. R., and Baeyens, J. 1986. Instrumentation and experimental techniques. In *GasFluidization Technology*, ed. D. Geldart, 415-462. Chichester: Wiley.
- Grassler, T., and Wirth, K. E. 2000. X-ray computer tomography--potential and limitation for the measurement of local solids distribution in circulating fluidized beds. *Chem. Eng. J.* 77 (1- 2):65-72.
- Hage, B., Werther, J., Narukawa, K., Mori, S., 1996 Capacitance probe measurement technique for local particle volume concentration in circulating fluidized bed combustors, *J. Chem. Eng. Jpn.* 29.594–602.
- Heindel, T. J., Gray, J. N., and Jensen, T. C. 2008. An X-ray system for visualizing fluid flows. *Flow Meas. Instrum.* 19 (2):67-78.
- Jain, S., Saraswat, P., Jain, V., Pant, H.J., Upadhyay, R.K., 2014. Investigation of liquid-solids fluidized bed of different particle size through radioactive particle tracking techniques. *J. Radioanal. Nucl. Chem.* 302, 1309–1313.

- Jain, V., Kalo, L., Kumar, D., Pant, H.J., Upadhyay, R.K., 2017. Experimental and numerical investigation of liquid–solid binary fluidized beds: Radioactive particle tracking technique and dense discrete phase model simulations. *Particuology*.
- Johnsson, F., Zijerveld, R. C., Schouten, J. C., van den Bleek, C. M., and Leckner, B. 2000. Characterization of fluidization regimes by time-series analysis of pressure fluctuations. *Int. J. Multiphase Flow* 26 (4): 663-715.
- Kalo, L., Kamalanathan, P., Pant, H.J., Cassanello, M.C., Upadhyay, R.K., 2019a. Mixing and regime transition analysis of liquid-solid conical fluidized bed through RPT technique. *Chem. Eng. Sci.* 207, 702–712.
- Kalo, L., Pant, H.J., Cassanello, M.C., Upadhyay, R.K., 2019b. Time series analysis of a binary gas-solid conical fluidized bed using radioactive particle tracking (RPT) technique data. *Chem. Eng. J.* 377, 119807.
- Kondukov, N. B., Kornilaev, A. N., Skachko, I. M., Akhromenkov, A. A., Kruglov, A. S., 1964 An investigation of the parameters of moving particles in a fluidized bed by a radioisotopic method. *Int. Chem. Eng.* 4, 43.
- Larachi, F., Chaouki, J., Kennedy G., and Dudukovic, M.P., 1997, Radioactive Particle tracking in Multiphase Reactors: Principles and Applications. in *Non-Invasive Monitoring of Multiphase Flows*, eds., Chaouki, J., Larachi, F., and Dudukovic, M. P., 335- 406.
- Larachi, F., Chaouki, J., Kennedy, G., 1995. 3-D Mapping of Solids Flow Fields in Multiphase Reactors with RPT 41, 439–443.
- Larachi, F., Kennedy, G., Chaouki, J. 1994. A γ -ray detection system for 3-D particle tracking in multiphase reactors. *Nucl. Instrum. Methods.* A338, 568.
- Limtrakul, S., Chen, J., Ramachandran, P.A., Dudukovic, M.P., 2005. Solids motion and holdup profiles in liquid fluidized beds. *Chem. Eng. Sci.* 60, 1889–1900.
- Lin, J. S., Chen, M. M., Chao, B. T. 1985. A novel radioactive particle tracking facility for measurement of solids motion in gas fluidized beds. *AIChE J.* 31, 465.
- Lin, J., 1981. Particle-Tracking Studies for Solids Motion in a Gas Fluidized Bed. Ph.D. thesis, University of Illinois, Urbana, Illinois.
- Louge, M. 1997. Experimental techniques. In *Circulating fluidized beds*, ed. J. Grace, A. Avidanand T. Knowlton, 312-368. London: Chapman and Hall
- Masson, H., Dang Tran, K., Rios, G. 1981 Circulation of a large isolated sphere in a gas-solid fluidized bed. *Int. Chem. Eng. Symp. Ser.* 65, S2/K/1-13,

- Mathiesen, V., Solberg, T., Hjertager, B.H., 2000. An experimental and computational study of multiphase flow behavior in a circulating fluidized bed. *Int. J. Multiph. Flow* 26, 387–419.
- McKeen, T. R., and Pugsley, T. S. 2002. The influence of permittivity models on phantom images obtained from electrical capacitance tomography. *Meas. Sci. Technol.* 13 (12):1822-1830.
- Moslemian, D., Devanathan, N., Dudukovic', M. P. 1992. Radioactive particle tracking for investigation of phase recirculation and turbulence in multiphase systems. *Rev. Sci. Instrum.* 63, 4361.
- Moslemian, D.; Chen, M. M.; Chao, B. T. 1989. Experimental and numerical investigations of solids mixing in a gas-solid fluidized bed. *Part. Sci. Technol.* 7:4, 335-355.
- Ohki, K., and Shirai, T. 1976. Particle velocity in fluidized bed. In *Fluidization technology*, ed. D. Kearns, 95-110. Washington: Hemisphere Pub. Corp.
- Pantzali, M.N., Lozano Bayón, N., Heynderickx, G.J., Marin, G.B., 2013. Three-component solids velocity measurements in the middle section of a riser. *Chem. Eng. Sci.* 101, 412–423.
- Parker, D.J., Fan, X., 2008. Positron emission particle tracking-Application and labelling techniques. *Particuology* 6, 16–23.
- Parker, D.J., Forster, R.N., Fowles, P., Takhar, P.S., 2002. Positron emission particle tracking using the new Birmingham positron camera. *Nucl. Instrum. Meth. A* 477, 540–545.
- Pugsley, T., Tanfara, H., Malcus, S., Cui, H., Chaouki, J., Winters, C., 2003. Verification of fluidized bed electrical capacitance tomography measurements with a fibre optic probe. *Chem. Eng. Sci.* 58, 3923–3934.
- Punčochář, M., Drahoš, J., Čermák, J., and Selucký, K. 1985. Evaluation of minimum fluidizing velocity in gas fluidized bed from pressure fluctuations. *Chem. Eng. Commun.* 35 (1-6):81-87.
- Roy, D., Larachi, F., Legros, R., Chaouki, J. 1994. A study of solid behavior in spouted beds using 3-D particle tracking. *Can. J. Chem. Eng.* 72, 945
- Roy, D., Larachi, F., Legros, R., Chaouki, J. 1994. A study of solid behavior in spouted beds using 3-D particle tracking. *Can. J. Chem. Eng.* 72, 945.
- Roy, D., Larachi, F., Legros, R., Chaouki, J. 1996. Experimental and theoretical investigations on the solids mixing in gas spouted beds. 5th World Conference on Chemical Engineering San Diego, CA, July 14-18, Paper 96e.

- Roy, S., 2000. Quantification of Two-Phase Flow in Liquid-Solid Risers. Ph.D. thesis, Washington University, USA.
- Roy, S., Larachi, F., Al-dahhan, M.H., Dudukovi, M.P., 2002. Optimal design of radioactive particle tracking experiments for flow mapping in opaque multiphase reactors. *Appl. Radiat. Isot.* 56, 485–503.
- Shaffer, F., Gopalan, B., Breault, R.W., Cocco, R., Karri, S.B.R., Hays, R., Knowlton, T., 2013. High speed imaging of particle flow fields in CFB risers. *Powder Technol.* 242, 86–99.
- Sharma, A. K., Tuzla, K., Matsen, J., and Chen, J. C. 2000. Parametric effects of particle size and gas velocity on cluster characteristics in fast fluidized beds. *Powder Technol.* 111 (1-2):114-122.
- Sharma, L., Nigam, K.D.P., Roy, S., 2017. Investigation of two-phase (oil-water) flow in coiled geometries using “Radioactive Particle Tracking-Time of Flight (RPT-TOF)” and “Radioactive Particle Tracking-Volume Fraction (RPT-VOF)” measurements. *Chem. Eng. Sci.* 170, 422–436.
- Shi, Hx. 2007. Experimental Research of Flow Structure in a Gas-Solid Circulating Fluidized Bed Riser by PIV. *J Hydrodyn* 19, 712–719 (2007).
- Shou, M. C., and Leu, L. P. 2005. Energy of power spectral density function and wavelet analysis of absolute pressure fluctuation measurements in fluidized beds. *Chem. Eng. Res. Des.* 83 (5):478-491.
- Simons, S. J. R. 1995. Imaging techniques for fluidized bed systems: a review. *Chem. Eng. J.* 56(3):83-93.
- Ssi, H. xian, 2007. Experimental Research of Flow Structure in A Gas-Solid Circulating Fluidized Bed Riser by PIV. *J. Hydrodyn.* 19, 712–719.
- Tartan, M., Gidaspow, D., 2004. Measurement of granular temperature and stresses in risers. *AIChE J.* 50, 1760–1775.
- Tebianian, S., Dubrawski, K., Ellis, N., Cocco, R.A., Hays, R., Reddy Karri, S.B., Leadbeater, T.W., Parker, D.J., Chaouki, J., Jafari, R., Garcia-Trinanes, P., Seville, J.P.K., Grace, J.R., 2015. Investigation of particle velocity in FCC gas-fluidized beds based on different measurement techniques. *Chem. Eng. Sci.* 127, 310–322.
- Tribedi, T., Pillajetti, P., Kumari, R., Pant, H.J., Tiwari, P., Upadhyay, R.K., 2022. Measurements of Solid Velocity in a Pilot-Scale Geldart’s Group B Circulating Fluidized Bed Using a Radioactive Particle Tracking Technique. *Ind. Eng. Chem. Res.* 61, 9110–9121.

- Upadhyay, R. K., 2010. Investigation of multiphase reactors using radioactive particle tracking (Ph.D. thesis). IIT Delhi, India.
- Upadhyay, R.K., Pant, H.J., Roy, S., 2013. Liquid flow patterns in rectangular air-water bubble column investigated with Radioactive Particle Tracking. *Chem. Eng. Sci.* 96, 152–164.
- Upadhyay, R.K., Roy, S., 2010. Investigation of hydrodynamics of binary fluidized beds via radioactive particle tracking and dual-source densitometry. *Can. J. Chem. Eng.* 88, 601–610.
- Van de Velden, M., Baeyens, J., Seville, J.P.K., Fan, X., 2008. The solids flow in the riser of a Circulating Fluidised Bed (CFB) viewed by Positron Emission Particle Tracking (PEPT). *Powder Technol.* 183, 290–296.
- Van de Velden, M., Baeyens, J., Smolders, K., 2007. Solids mixing in the riser of a circulating fluidized bed. *Chem. Eng. Sci.* 62, 2139–2153.
- van Ommen, J. R., Sasic, S., Van der Schaaf, J., Gheorghiu, S., Johnsson, F., and Coppens, M.O. 2011. Time-series analysis of pressure fluctuations in gas-solid fluidized beds-a review. *Int. J. Multiphase Flow* 37 (5):403-428.
- van Ommen, J.R., and Mudde, R. F. 2008. Measuring the Gas-Solids Distribution in Fluidized Beds - A Review. *Int. J. Chem. React. Eng.* 6(1):R3.
- van Velzen, D., Flamm, H. J., Langenkamp, H., Casile, A. 1974. Motion of solids in spouted beds. *Can. J. Chem. Eng.* 1974, 52, 156.
- Volpicelli, G.; Massimila, L.; Zenz, F. A. Non-homogeneities in solid-liquid fluidization. *Chem. Eng. Prog. Symp. Ser.* 62, 42.
- Werther, J., 1999. Measurement techniques in fluidized beds. *Powder Technol.* 102, 15–36.
- Werther, J., Molerus, O., 1973. The local structure of gas fluidized beds: I. A statistically based measuring system, *Int. J. Multiphase Flow* I, 103–122.
- Windows-Yule, C.R.K., Herald, M.T., Nicușan, A.L., Wiggins, C.S., Prax, G., Manger, S., Odo, A.E., Leadbeater, T., Pellico, J., De Rosales, R.T.M., Renaud, A., Govender, I., Carasik, L.B., Ruggles, A.E., Kokalova-Wheldon, T., Seville, J.P.K., Parker, D.J., 2022. Recent advances in positron emission particle tracking: A comparative review. *Reports Prog. Phys.* 85.
- Wu, B., Yu, G., Bellehumeur, C., and Kantzas, A. 2007. Dynamic flow behavior measurements in gas-solid fluidized beds using different non-intrusive techniques and polyethylene powder. *Flow Meas. Instrum.* 18 (5-6):197-203.

- Yadav, A., Pant, H.J., Roy, S., 2020. Velocity measurements in convective boiling flow using radioactive particle tracking technique. *AIChE J.* 66, 1–11.
- Yadav, A., Ramteke, M., Pant, H.J., Roy, S., 2017. Monte Carlo Real Coded Genetic Algorithm (MC-RGA) for Radioactive Particle Tracking (RPT) experimentation. *AIChE J.* 63 (7), 2850-2863, 2017.
- Yang, Y. B., Devanathan, N., Dudukovic, M. P. 1993. Liquid backmixing in bubble columns via computer automated particle tracking (CARPT). *Chem. Eng. Sci.* 47, 2859,
- Yates, J. G., and Simons, S. J. R. 1994. Experimental methods in fluidization research. *Int. J. Multiphase Flow* 20:297-330.
- Zaid, F.M., 2013. Gas-solid fluidized bed reactors: scale-up, flow regimes identification and hydrodynamics. Ph.D. thesis, Missouri University of Science and Technology, USA.
- Zhu, J., Li, G., Qin, S., Li, F., Zhang, H., Yang, Y., 2001. Direct measurements of particle velocities in gas – solids suspension flow using a novel five-fiber optical probe. *Powder Technol.* 115, 184–192.



CHAPTER 3

Experimental Investigation on a Laboratory- Scale CFB Riser: Solid-phase Flow Fields and Mixing Characteristics

Scope

This chapter discusses the solid phase velocity flow field, such as mean and RMS velocity, granular temperature and solid stress at the bottom and middle sections of the laboratory-scale CFB riser. Section-wise solid phase residence time distribution investigations are presented, and solid mixing behavior is discussed. Operating conditions are selected in such a way to analyze the effect of inlet gas velocity and solid flux on solid dynamics inside the riser.

3.1 Introduction

Circulating fluidized beds (CFBs) possess a wide range of applications in industries (e.g. fluidized catalytic cracking calcinator, coal combustor, etc) due to their excellent gas solids contacting and higher heat and mass transfer coefficient (Berruti et al., 1995). There exist immense advantages of CFBs such as high efficiency, flexibility in catalyst or heat-carrier regeneration, feed control, etc (Berruti et al., 1995; Manyele et al., 2002). CFBs, on the other hand, have extremely non-uniform spatial and temporal flow structures. Spatial flow inhomogeneities result from solid retention and radial gradients of gas velocities, while axial flow variation arises from the gradual development of the flow (e.g. inlet/entrance zone, acceleration zone/ fully developed middle section, and top dilute zone). Despite the fact that CFB was used for the first time in a fluid catalytic cracker in 1942, the hydrodynamics study of CFB was largely chaotic until Yerushalmi et al. (1976) raised the

requirement for a systematic study of an up-flow fluidized bed with the name of "circulating fluidized bed." This is considered as a paradigm shift in CFB research (Chew et al., 2022). However, the success attained with the CFB combustor (CFBC) has been the primary driving force to achieve new heights in the field of CFB research.

Several researchers have intensively worked on the CFB risers to understand the complex solid flow dynamics in the last half of the century. The highly complicated nature of the interaction between gas-solids, solids-solids, and solids-wall results in complex flow dynamics. Despite extensive studies being carried out, the complicated hydrodynamics of CFB risers are still not fully understood and are difficult to predict, posing a significant constraint in design and scale-up. In addition to this, the lack of relevant and reliable experimental data (especially in the case of Geldart Group B particles) limits the development and refinement of theoretical models and empirical equations that enables a more accurate simulation of solid flow dynamics in the riser (Bhusarapu et al., 2006; Godfroy et al., 1999). In order to fully comprehend and quantify solids flow inside risers, the solids flow field inside the riser need to be adequately mapped.

Most of the experimental results reported in the literature utilize invasive techniques that disturb the local flow structures. The commonly used non-intrusive techniques such as LDV or PIV cannot be employed since the system is opaque, especially at high solid flux conditions. In this case, non-invasive methods such PEPT and RPT are the only viable approaches for precisely quantifying the solid flow field in the riser.

Stellema (1988) used the PEPT technique to track solid flow in gas-solid risers and reported three-dimensional Eulerian flow fields. Godfroy et al. (1999) and Bhusarapu et al. (2005) used the RPT technique to depict particle trajectories in a CFB riser in an entire 3-D domain and measured particle velocities at both mean and fluctuating levels at a fully-developed section of the riser. Godfroy et al. (1999) observed that when solid flux increases, the axial

solid velocity and dispersion coefficient decreases, which they attributed to the occurrence of clusters. Bhusarapu et al. (2006) reported velocity flow field in the fast fluidized bed and dilute transport regime. They reported occasional downflow of particles in the core region in fast fluidization regime unlike in dilute transport regime. They quantified and analyzed the core-annular flow regime with the help of particle counter plot. Zhou et al. (1995) reported velocity core-annular flow pattern of solid phase velocity with the help of an optical fiber probe. The local time average ascending particle velocity was lower near the wall and gradually increased towards the axis of the column. The magnitude of the descending particle velocity increased with the solid circulation rate but remained nearly unaffected by an increase in gas velocity. Anantharaman et al. (2017) analyzed the effect of particle size and particle density on the formation of a core-annular flow pattern with Geldart Group B particles. They observed that particle diameter has a significant influence in determining the upflow or downflow of solids near the wall. Rhodes et al. (1992) described particle downward motion as "swarms of particles" near the wall. They reported a continuous bulk downflow of solids at a farther distance from the wall, immediately at the back of the falling swarms of particles in close proximity to the wall, at higher solid fluxes. Wilhelm and Kwauk, (1948) were the first to identify the occurrence of this type of heterogeneous particle swarming or clustering which impacts the velocity profile and fluctuating velocity. Chew et al. (2012) reported a reverse core annular flow structure near the outlet section of the riser with Geldart Group B particles. However, it is essential to note that clustering phenomena are not as dominant for Geldart Group B particles as that for Geldart Group A particles.

In CFB research, most of the experimental data presented the velocity flow fields, specially the radial profile for a fully developed section of the riser. There are limited research articles (Arastoopour, 2001; Chan et al., 2009; Cheng et al., 1998; Pantzali et al., 2015)

available in the open domain about the velocity profile at the bottom section of the riser and the effect of the inlet configuration. As slip velocity is maximum at the bottom section, gas-solid goes through a rapid momentum exchange phase. Inlet configuration and design are one of the main influential factors that directly influence the length of the acceleration zone or a developing section. Further, both the reactant (gas phase) and catalyst (solids) are fresh and hence, the rate of reaction is also very high and hence mass transfer becomes critical. Cheng et al. (1998) divided inlet configurations into mild restriction and strong restriction based on their global and local effects on the riser's flow structure. Van engelandt et al. (2007) reported that Geldart Group B particles had a higher length of acceleration zone as compared to the smaller Group A particles. De Wilde et al. (2005) compared simulation data with experimental data using the LDA technique. They observed that solid movement to the riser is higher in the case of the aerated inlet compared to the non-aerated inlet. They observed the constant length of the acceleration zone regardless of the solid flux and inlet gas velocity. Arastoopour (2001) reported that aerated solid inlets have a more uniform solid distribution as compared to the non-aerated solid inlets, and the accumulation of solids at the bottom section is less with an aerated solid. Pantzali et al. (2015) reported solid phase velocity flow fields such as mean and RMS velocity profiles of velocity components and kinetic energy and stress profiles at the bottom section of the riser for Geldart Group A particles.

Majority of the solid phase radial profile of velocity flow fields reported in the CFB riser are for the fully-developed or middle sections. The present study attempts to investigate the solid phase velocity flow field and solid turbulence in the CFB riser at the inlet section and the fully developed section of the riser. Experiments using bigger diameter Geldart Group B particles are carried out in a laboratory-scale CFB to narrow down the experimental velocity data gap for gas-solid riser with Geldart Group B particles. Granular temperature

and Turbulence intensity are estimated in addition to the mean and RMS velocity profile to define the local and global solids mixing in the riser. The current work attempts to gather and systematically display experimental data.

3.2 Experimental Setup

The schematic diagram of the laboratory-scale cold-flow CFB experimental setup is shown in Figures 3.1 and 3.2. The CFB setup comprises a riser, two cyclone separators in series at the top, and a downer. The riser's height and internal diameter are 3 m and 0.05 m, respectively. The riser exit is a 90° elbow connected to the first cyclone separator, as shown in Figure 3.1. Downer/solid storage and riser are connected by a dipleg with varying diameters. The internal diameter of the initial part of the dipleg is 0.076 m, which is reduced to 0.038 m before it connects to the riser at the solid inlet at an angle of 60° with the vertical plane. The solid inlet is 5 cm above the primary air inlet. A high inventory cylindrical storage tank (which can hold more than 25 kg of solids) tank with an inner diameter of 0.15 m and a height of 2.2 m is used as a downer, as shown in Figure 3.1. The size of the storage tank is intentionally made bigger compared to the rise to ensure there is no starvation of solids to the riser due to any inventory shortage. Spherical glass beads ($\rho_p = 2500 \text{ kg/m}^3$, $d_p = 500 \text{ }\mu\text{m}$) are used as the solid phase. Solid inventory was obtained from India glass beads, Mumbai, India. Density of the glass beads are 2500 kg/m^3 . Mean particle diameter is $500 \text{ }\mu\text{m}$ (in the range of $450 \text{ }\mu\text{m} - 600 \text{ }\mu\text{m}$). Minimum fluidization velocity (U_{mf}) of solids is 0.31 m/s and terminal settling velocity (U_t) is 3.8 m/s. A high-capacity reciprocating compressor of 20 kW is used for both primary and secondary air (to aerate the solid storage) supply. A secondary air tank of 1500 liter is used to reduce flow fluctuation, which is caused by the pressure deviation because of compressor's auto ON/OFF settings. Two pressure regulators are attached each after the first and the second

tank to maintain constant line pressure and constant flow to the riser as shown in the Figure 3.1. The pressure in the second tank is maintained at 3.5 bar using the first pressure regulator attached at the outlet of the first tank. Line pressure of 1 bar is set after the second tank using the second pressure regulator. Solid in the storage are aerated below minimum fluidization velocity with secondary air from the bottom to facilitate the solid movement towards the riser. Both primary and secondary airflow is measured with rotameters and controlled by globe valves.

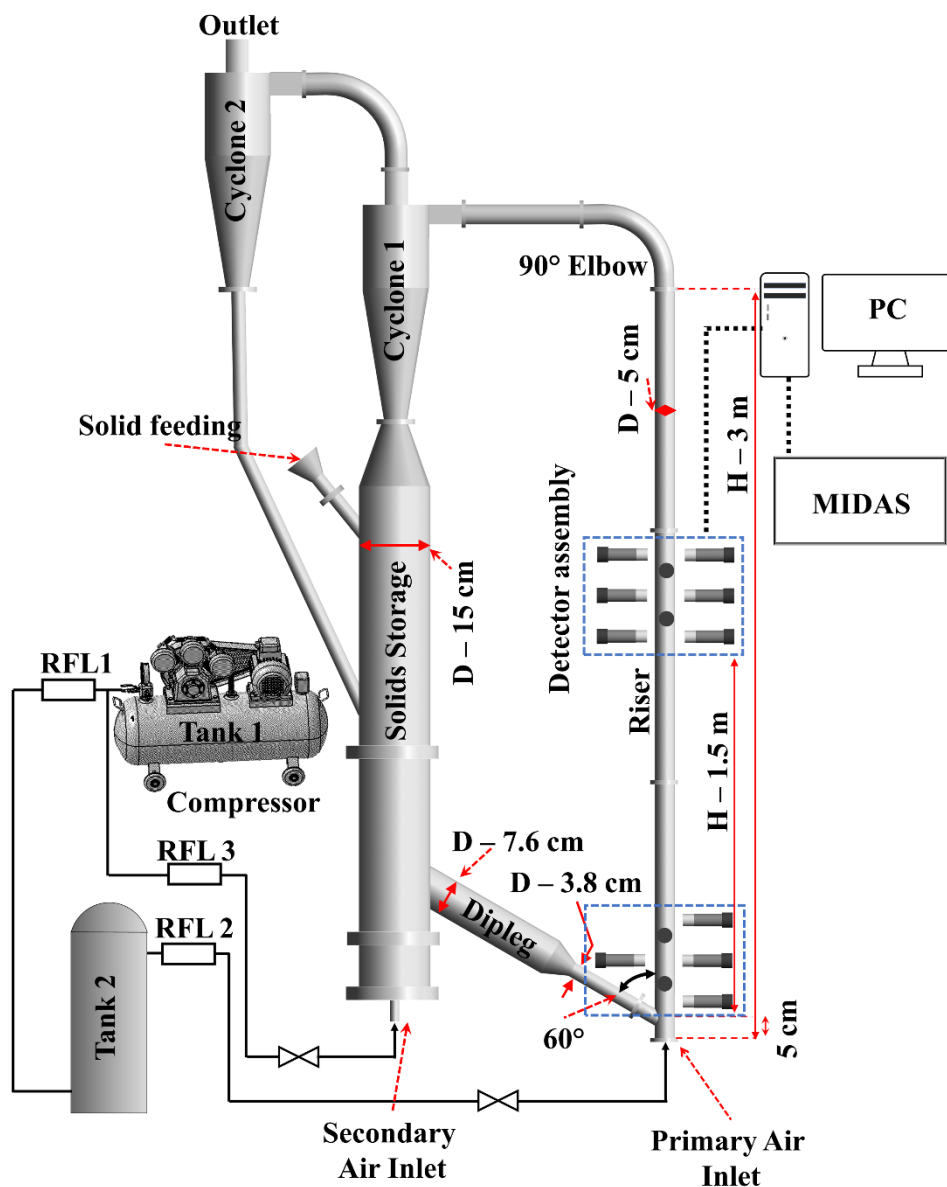


Figure 3.1: Schematic diagram of laboratory-scale cold flow CFB setup

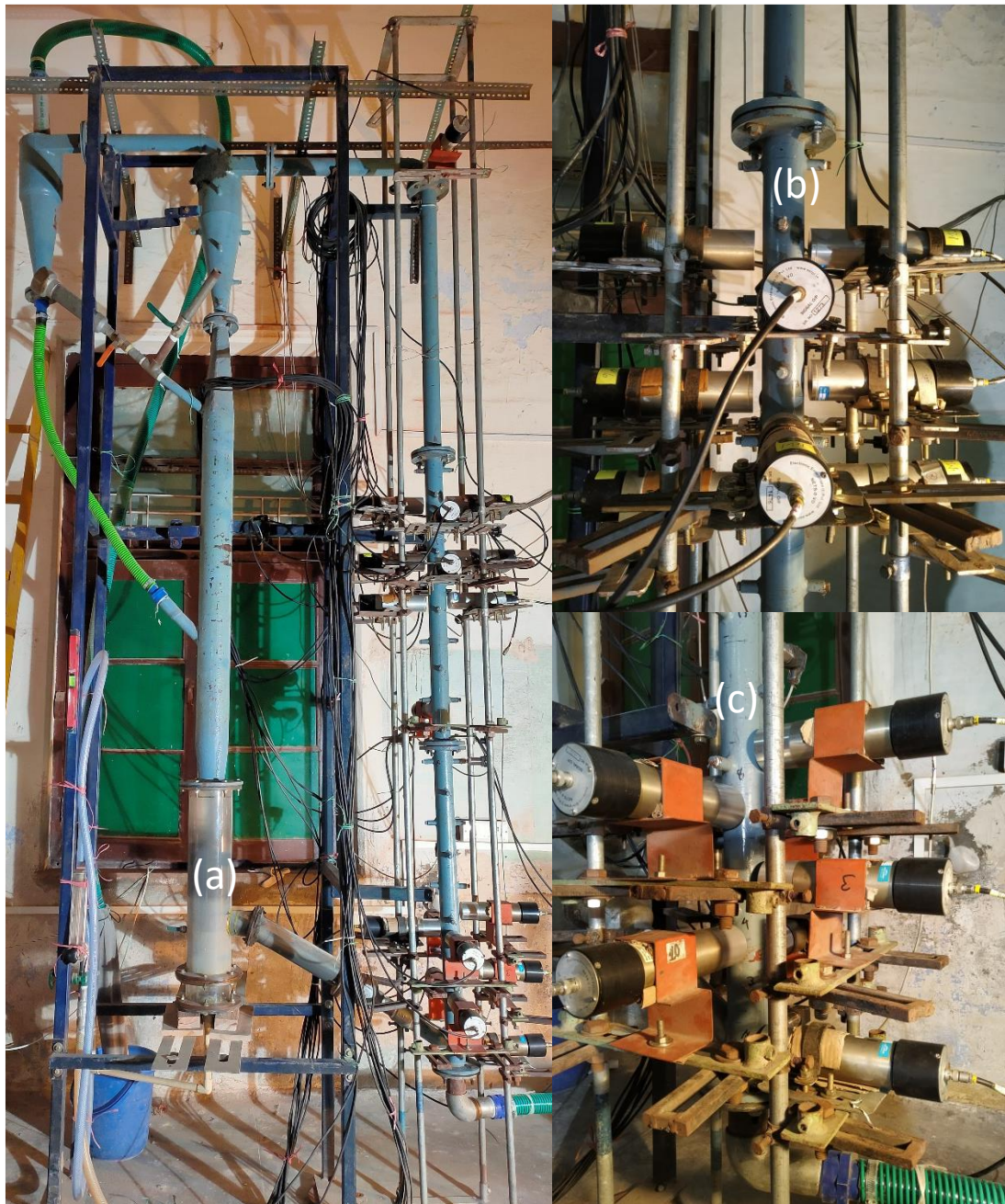


Figure 3.2: Photograph of laboratory-scale (a) overall CFB setup, (b) detector assembly at the middle section and (c) detector assembly at the bottom section

Previously, epoxy resin or aluminum powder were clotted on top of the Sc-46 particles to match the density of the tracer particle with the density of the solid particles present in the flow (Bhusarapu, 2005; Roy, 2000). This changes the surface morphology of the tracer particles, which may potentially affect the solid-solid interaction, i.e tracer particle

collisions with other solids may not result in the same collisional effect as the interaction of solid particles in the flow. This is mainly due to the change in the elasticity of both the particles (tracer and solid particles in the system). To overcome this in the current work, the surface morphology of the tracer particle is kept the same as that of the other solids present in the flow by keeping both materials the same. Hence, in the current work, Scandium powder is doped inside the glass beads (materials from which other solids are made). The method detailed by Biswal et al. (2016) is used for the same. The prepared glass beads are sent to Bhabha Atomic Research Center (BARC) for irradiation to make the tracer particle radioactive. A tracer particle of size between 450 and 600 μm is used in the current experiments. An activity of 400 to 500 μCi is used in all the experiments. It should be noted that the half-life of the tracer particle (Sc-46) is 83 days, and the experiments for each condition are performed for 2-7 days, depending on the system size and flow regime, to acquire statistically independent data. A half-life correction is used in the calibration data to account for the same.

3.3 Solid Flux Measurement

Accurate measurement of solid flux in the riser is essential when studying the solid flow field, as it is a critical parameter in CFB operations. However, measuring solid flux at the riser is challenging since solids flow in a closed-loop system. Various researchers have documented many invasive and non-invasive ways to evaluate solid flux in CFB risers in the literature (Ludlow et al., 2008; Pateence et al., 1990; Wu et al., 2001). Burkell et al., (1988) reviewed five different techniques to estimate solid circulation rate in CFB riser. Each method, however, has drawbacks of its own. They suggested that the best device for measuring the circulation rate of solids would be a modified orifice meter. Even though its range is restricted, an impact meter can provide sensitive measurements. For small setups,

the porous valve method is helpful. While using the time-of-descent approach can be tricky with tiny particles, it usually works well and gives accurate results. Although the calorimetric method needs calibration, particularly for large-scale systems, it can provide online measurements under a broad range of conditions. Roy et al. (2001a) and Bhusarapu et al. (2004) measured solid circulation rate in a two stage process at the downer section. A similar technique is implemented in the present case. Since the downer section's solid fraction is too low to be evaluated using the radiation base densitometry approach (due to the downer diameter being considerably larger than the riser), flux measurements at the downer section are not feasible. Solid flux is measured in the dipleg section of a pilot plant CFB setup as described in Chapter 4. However, due to a lack of space to place the detectors at the dipleg section, we have measured solids flux directly at the riser section in the current laboratory-scale setup. Both time of flight and solid fraction are measured at the riser section where RPT is performed. Two highly sensitive pressure probe (0-100 mbar) is placed around the PRT zone at a distance of 40 cm to measure solid hold-up from pressure difference (equation 3.3). The velocity of a tracer (v_s) is determined by dividing the distance between detectors (L_2) by the mean time of flight of the tracer in the same zone (equation 3.4). The schematic diagram of the detector assembly and pressure probes at the riser section for solids flux measurement is shown in Figure 3.3. The solid velocity v_s and solid fraction ε_s are measured to calculate the solid flux G_s by using equation 3.1

$$G_s = \frac{\rho_p \int v_s \varepsilon_s dA}{\int dA} \quad (3.1)$$

$$\langle G_s \rangle = \rho_p \langle v_s \rangle \langle \varepsilon_s \rangle A \quad (3.2)$$

$$\langle \varepsilon_s \rangle = \frac{\langle \Delta P \rangle}{\rho_s g h} \quad (3.3)$$

$$\langle v_s \rangle = \frac{L_2}{\langle \Delta t \rangle} \quad (3.4)$$

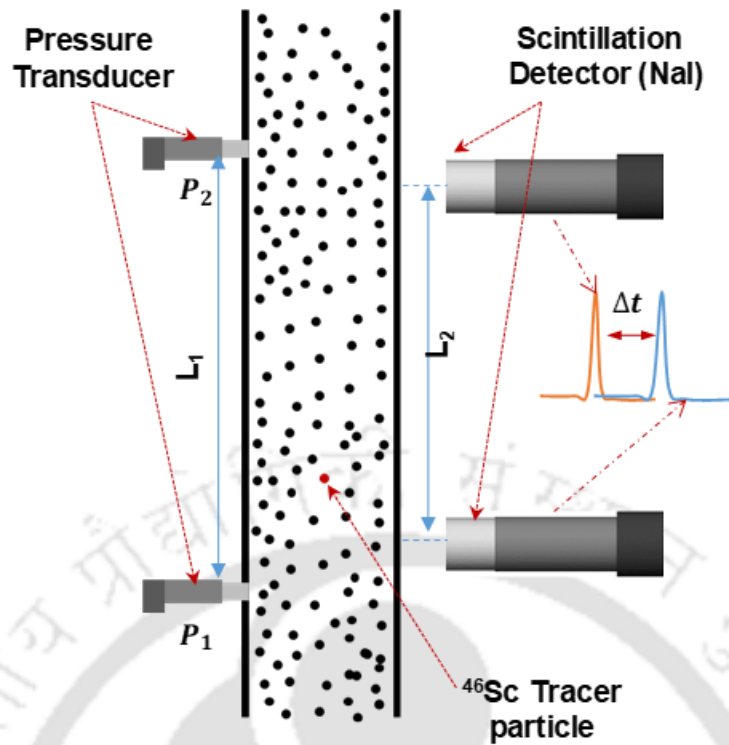


Figure 3.3: Schematic diagram of detectors and pressure probe assembly for solid flux measurement

Table 3.1 Operating condition with time solid flux measurement

Inlet gas velocity, U_g	Solids Inventory	Solid velocity, $\langle v_s \rangle$	Solid fraction, $\langle \epsilon_s \rangle$	Riser solids flux G_s
m/s	kg	(m/s)	(%)	$\text{kg/m}^2\text{s}$
6	8	0.42	3.66	40
6.5	10	0.83	3.22	60
7	8	1.5	1.51	60
7	10	1.71	1.68	75
7	14	1.82	2.32	100
8	10	2.63	1.44	100
8	14	2.67	2.04	150
8	16	2.72	2.75	200
9	10	3.11	1.20	100

3.4 Radioactive Particle Tracking (RPT) Measurements

The solid phase flow field at the developing bottom (riser height 0.1 – 0.4 m) and fully developed middle section (riser height 1.5 – 1.9 m) of the riser and is mapped using the radiation-based non-invasive RPT technique. Over an extended period of time, a single radioactive particle (high energy γ -ray emitter) is tracked as a tracer, and its motion is represented as the motion of the solid phase, assuming the system is ergodic. Tracer particle Sc-46 isotope doped in a glass bead is prepared (Biswal et al., 2016) at the BARC facility, which has approximately the same density and diameter as glass beads used as solid phase. 18 scintillation detectors (NaI) are strategically (Larachi et al., 1995; Roy et al., 2002) placed around the zone of interest (0.1-0.5 m and 1.40-1.90 m height riser from the primary air inlet) in a staggered manner, as shown in Figure 3.4. Initially, a resolution and sensitivity experiment is performed to choose the optimum detector position, which gives the lowest resolution and maximum sensitivity (Roy et al., 2002, 2001b). Because of the higher particle velocity, a data acquisition frequency of 100 Hz is used (Kamalanathan et al., 2017) to acquire data for nearly 1.5 – 2.5 days until statistically adequate (Roy et al., 2005) data is obtained. Though it is observed that nearly two thousand circulations are good enough to have statistically sufficient data for each cell, approximately three thousand circulations is recorded for each experiment. During calibration, the same radioactive tracer particle is glued to the tip of a rod and placed into different areas through the ports available on the riser wall. The count generated by detectors is then recorded for all possible positions during experiments. To obtain the discrete position vs count data directly, a tracer must be placed physically at each of the numerous points, which is both time-consuming and nearly impossible. Thus, a position vs count map is generated for every discrete position in the scan zone using the Monte Carlo method with the help of a strategically selected finite number of position vs count data sets which are recorded during calibration. Nuclear

radiation models based on Monte Carlo algorithms are well-documented (Beam et al., 1978; Kaplanis, 1978; Moens et al., 1982; Wielopolski, 1977) in nuclear physics. During the experiment, when traces pass through the scan zone, the counts are generated by the detector record with the help of the MIDAS. This time series count data is later compared with the count vs position table to generate the Lagrangian position of the tracer particle.

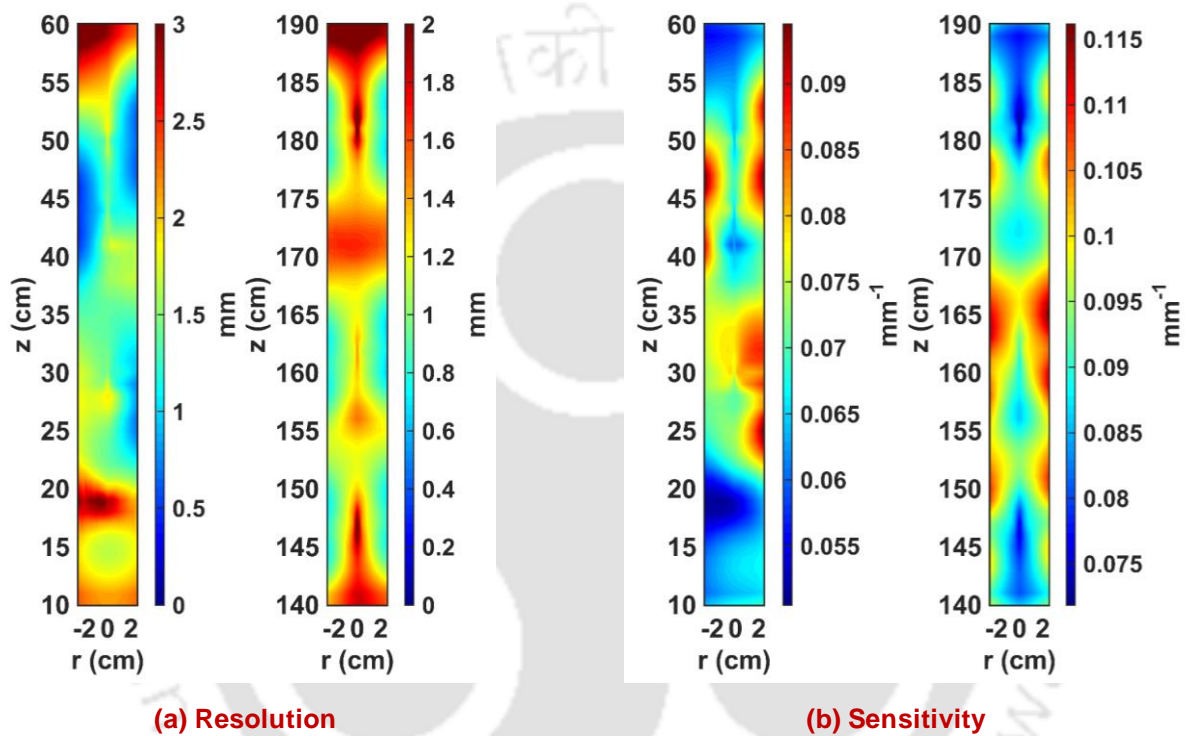


Figure 3.4: Contours of resolution and sensitivity for RPT experiments

Figure 3.5 represents one such Lagrangian track of instantaneous positions of tracer as a function of time, which can be used to extract velocity flow field information in many ways. The instantaneous Lagrangian velocity of the tracer is determined by calculating a temporal derivative of the tracer's coordinates. By using ergodicity, one tracer particle's velocity is converted into the time-averaged Eulerian velocity field, which represents the whole ensemble of particles provided that statistically sufficient number of data is acquired.

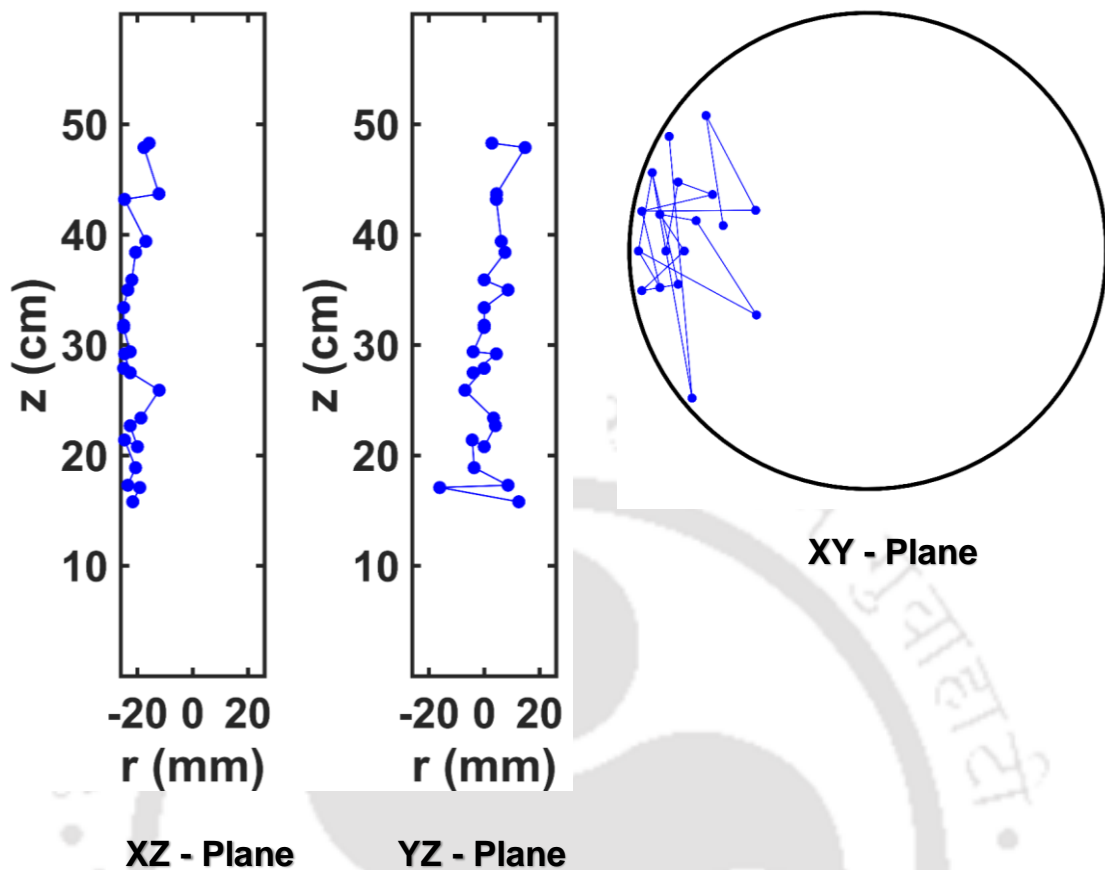


Figure 3.5: Lagrangian track of tracer in a different plane

Assuming a hypothetical grid in the riser section's 3D space allows us to transform Lagrangian velocity data into a Eulerian grid. The velocity is determined by time-differencing for any two consecutive tracer points and allocated to the grid compartments. A histogram or probability density function (PDF) of the instantaneous velocities can be produced if the tracer particle passes through each grid compartment a sufficient number of times. In the current data processing grid selected as $\Delta r = 0.5$ cm, $\Delta z = 2$ cm and $\Delta \theta$ varied in such a way that each compartment has an equal volume of approximately 1.57 cm³. It can be observed from Figure 3.5 that the instantaneous position track generated by each pass is unique, and the movement of the tracer is mainly in the axial direction . Detailed algorithms of post-processing can be found in the literature (Bhusarapu et al.,

2005; Godfroy et al., 1999; Kalo et al., 2019a; Roy et al., 2005; Upadhyay and Roy, 2010)

and equations are presented in Table 2.2.

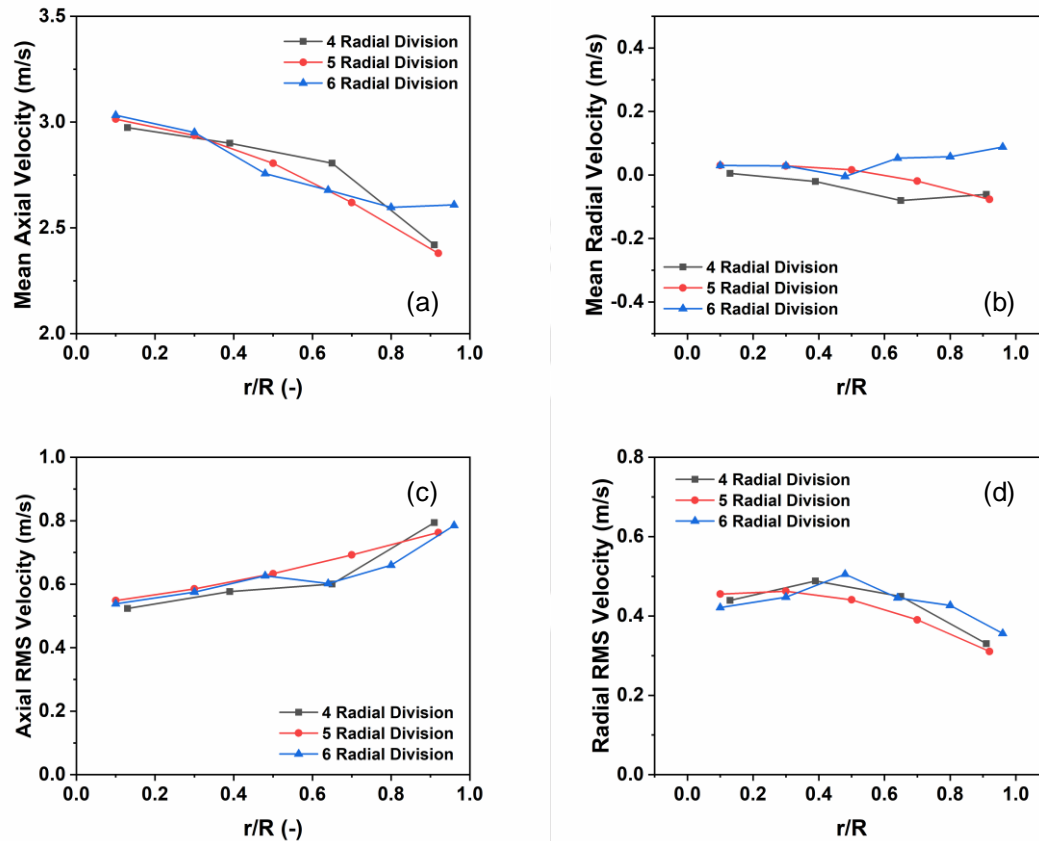


Figure 3.6: Azimuthally averaged (a) mean axial velocity, (b) mean radial velocity, (c) axial RMS velocity and (d) radial RMS velocity profiles with different grid sizes for operating condition of $G_s = 100 \text{ kg/m}^2\text{s}$ and $U_g = 8 \text{ m/s}$

In Figure 3.6, mean axial and radial velocities, axial and radial RMS velocities are presented with different grid sizes based on the number of divisions in the radial direction. It's clear that when using 4 and 5 divisions, the mean and fluctuation velocity are similar. However, with 4 divisions, some vital information near the wall is missing. On the other hand, with 6 divisions, there are notable differences in the mean and RMS velocity profiles compared to 4 and 5 divisions. Therefore, five divisions in the radial direction appear to be the best choice.

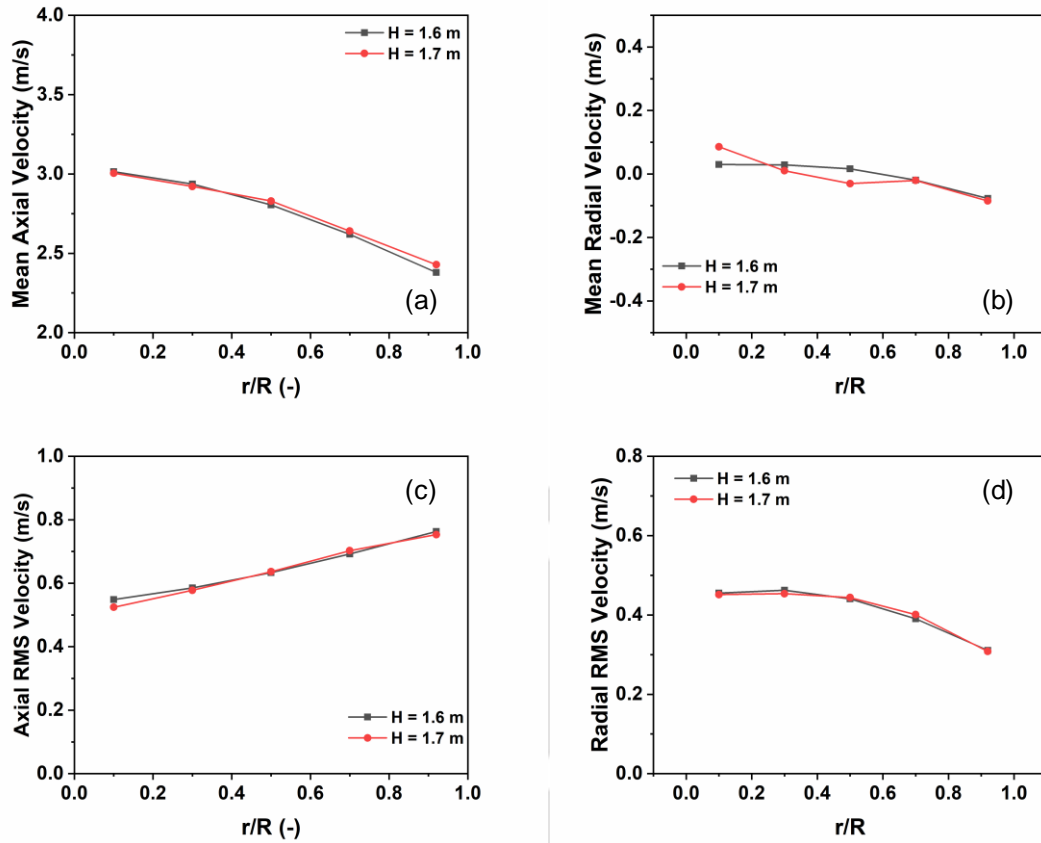


Figure 3.7: Azimuthally averaged (a) mean axial velocity, (b) mean radial velocity, (c) axial RMS velocity and (d) radial RMS velocity profiles at different heights for operating condition of $G_s = 100 \text{ kg/m}^2 \text{ s}$ and $U_g = 8 \text{ m/s}$

Figure 3.7 illustrates the effect of height on the mean and fluctuating velocity components in the middle section of the riser. Within this section, flow development is predominant, resulting in minimal changes in mean and RMS velocity. Mean axial, mean radial, axial RMS and radial RMS velocities data are presented at heights of 1.6 and 1.7 meters within the riser. Notably, the RPT scan zone for the central section spans from 1.4 to 1.9 meters. Additionally, when considering resolution and sensitivity, the contour map indicates that the 1.4–1.8 meter range offers superior accuracy. Therefore, all velocity flow profiles for the central section are presented at a height of 1.6 meters.

3.5 RPT Results and Discussion

Initially, solid flux values are measured by varying solid inventory and gas velocity at the primary and secondary inlets. For RPT experiments, the operating conditions are carefully chosen to show the effect of the solid flux and inlet gas velocity on the dynamics of the solid flow in a riser. Different types of choking velocities (Bi et al., 1993) are calculated (V_{cc} , V_{ca} , V_{mp}) to determine the fluidization regime and each of these falls under the fast fluidization regime. Classical choking velocity (V_{cc}) is obtained from the correlation given by Yousfi and Gau (1974), as mentioned in Equation 3.5. While the minimum transport velocity (V_{ca}), also called type A choking velocity and defined as the point where the uniform suspension collapses, can be calculated from the correlation (Equation 3.6) given by Bi and Fan (1991). The minimum pressure drop point denotes the transition from homogeneous dilute flow to core-annular dilute flow. Bi and Fan (1991) provide a correlation to estimate this transition velocity (V_{mp}), given as Equation 3.7. It can be observed that for current particle diameter and riser diameter, V_{mp} is lower than V_{ca} . Bi et al. (1993) mentioned that in such a situation, there would not be any core annular regime. All operating conditions and parameters used in the current work are mentioned in the regime plot presented in Figure 3.8.

$$\frac{V_{cc}}{\sqrt{gd_p}} = 32Re_t^{-0.06} \left(\frac{G_s}{\rho_G} V_{cc} \right)^{0.28} \quad (3.5)$$

$$\frac{V_{ca}}{\sqrt{gd_p}} = 21.6Ar^{0.105} \left(\frac{G_s}{\rho_G} V_{ca} \right)^{0.542} \quad (3.6)$$

$$V_{mp} = 10.1(gd_p)^{0.347} \left(\frac{G_s}{\rho_G} \right)^{0.31} \left(\frac{d_p}{D} \right)^{-0.139} Ar^{-0.021} \quad (3.7)$$

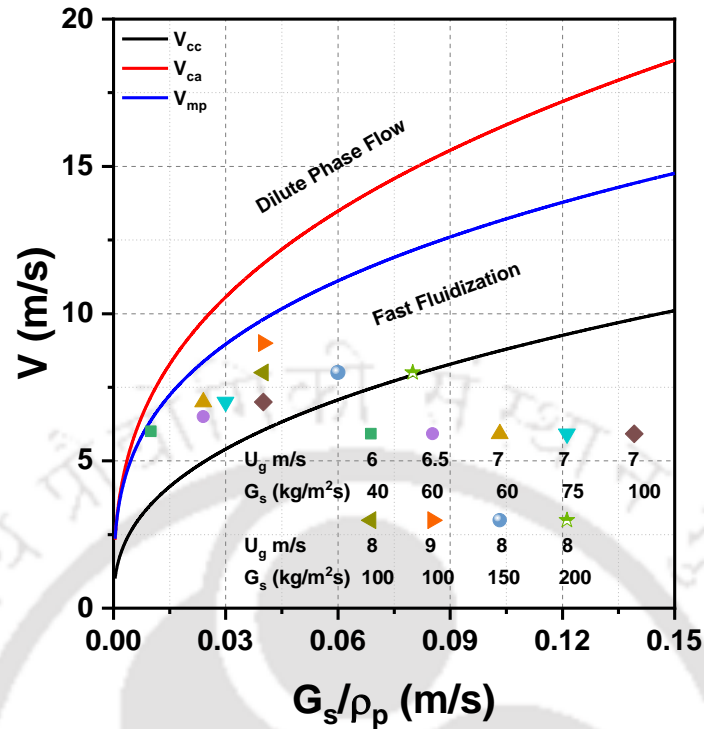


Figure 3.8: Flow regime diagram (Bi and Grace, 1995) with operating conditions

RPT is performed at the developing bottom section and the fully developed middle section of the riser. In the bottom section, seven detectors are used, and in the middle section, ten detectors are used to track the motion of the tracer. Simultaneously, one detector is placed at the exit bend of the riser to detect the exit of the tracer from the riser, and one detector is used as a detector just at the solid inlet to detect the solid entry to the riser.

In the current work, velocity flow fields are measured from RPT post-processing (Bhusarapu et al., 2006; Kalo et al., 2019a; Roy et al., 2005; Upadhyay and Roy, 2010), and the residence time distribution (RTD) of the solid phase is measured from the time of flight (Bhusarapu et al., 2004;) of the tracer between different detectors. Azimuthal averaged radial profiles for velocity flow parameters are presented at the bottom and middle sections, and solid phase RTD is presented zone-wise. For the bottom section, a radial profile of the However, velocity flow field parameters are presented for two different

heights (0.2 and 0.4 m). However, for the middle section, which is a fully developed section with minimal velocity changes, the radial profile of velocity flow fields are presented only at 1.6 m height from the primary gas inlet.

3.5.1 Lagrangian Track of Particle Position

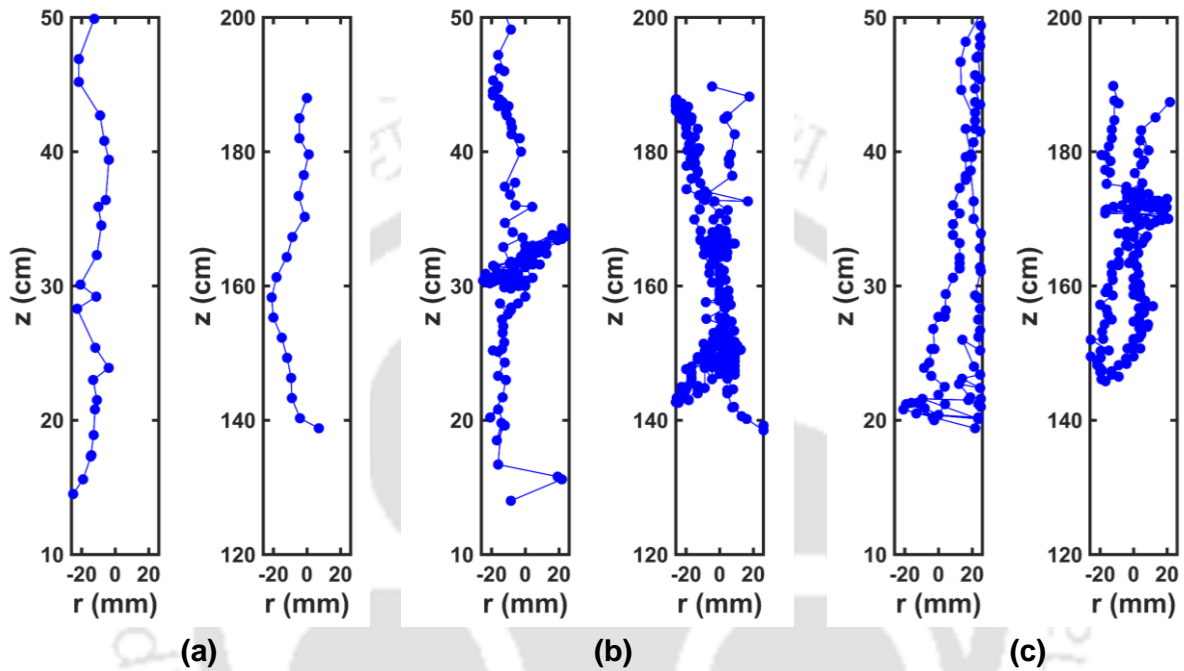


Figure 3.9: Tracer particle motion for a track (a) without back mixing, (b) with back mixing and (c) internal recirculation

In an RPT experiment, the location of the single radioactive tracer particle in three-dimensional space is reconstructed at every instance. The presented tracer trajectories in Figure 3.9 demonstrate this clear pattern of axial dominance within each track of the solid. However, radial motions are observed, although they are generally less significant and more dispersive than the predominant axial movement. The Lagrangian tracks can be categorized into three distinct groupings, each characterized by its own unique collection of flow patterns: (a) particle tracks without back mixing; (b) particle tracks with back mixing; and (c) particle tracks with internal recirculation. Irrespective of operational conditions, particle tracking without mixing remains predominant. Particle track with back

mixing becomes apparent at both lower (6, 6.5, and 8 m/s) and higher (8 and 9 m/s) gas velocities. It's important to note that back mixing occurs much less frequently at 9 m/s than it does under lower gas velocity conditions. When a particle track shows internal recirculation, it means that tracer particles occasionally cross the scan zone before returning to it. Only at lower gas velocities of 6 and 6.6 m/s are tracks demonstrating internal recirculation visible, with occasional appearances at 7 m/s. Notably, higher gas velocity like 8 or 9 m/s do not exhibit these recirculation patterns. Instantaneous velocity is calculated from the time difference between these instantaneous positions and stored in the corresponding cells, which are later used to generate PDF at different positions. The distribution of instantaneous velocity provides valuable insights into the dynamic behavior of solid motion in a fluid medium. While the mean velocity profile of the solid phase is widely presented and discussed in the literature, there is not much literature (Bhusarapu et al., 2006; Fiedler et al., 1997; Tartan and Gidaspow, 2004) available on the instantaneous velocity distribution of the solid phase in a gas-solid CFB riser.

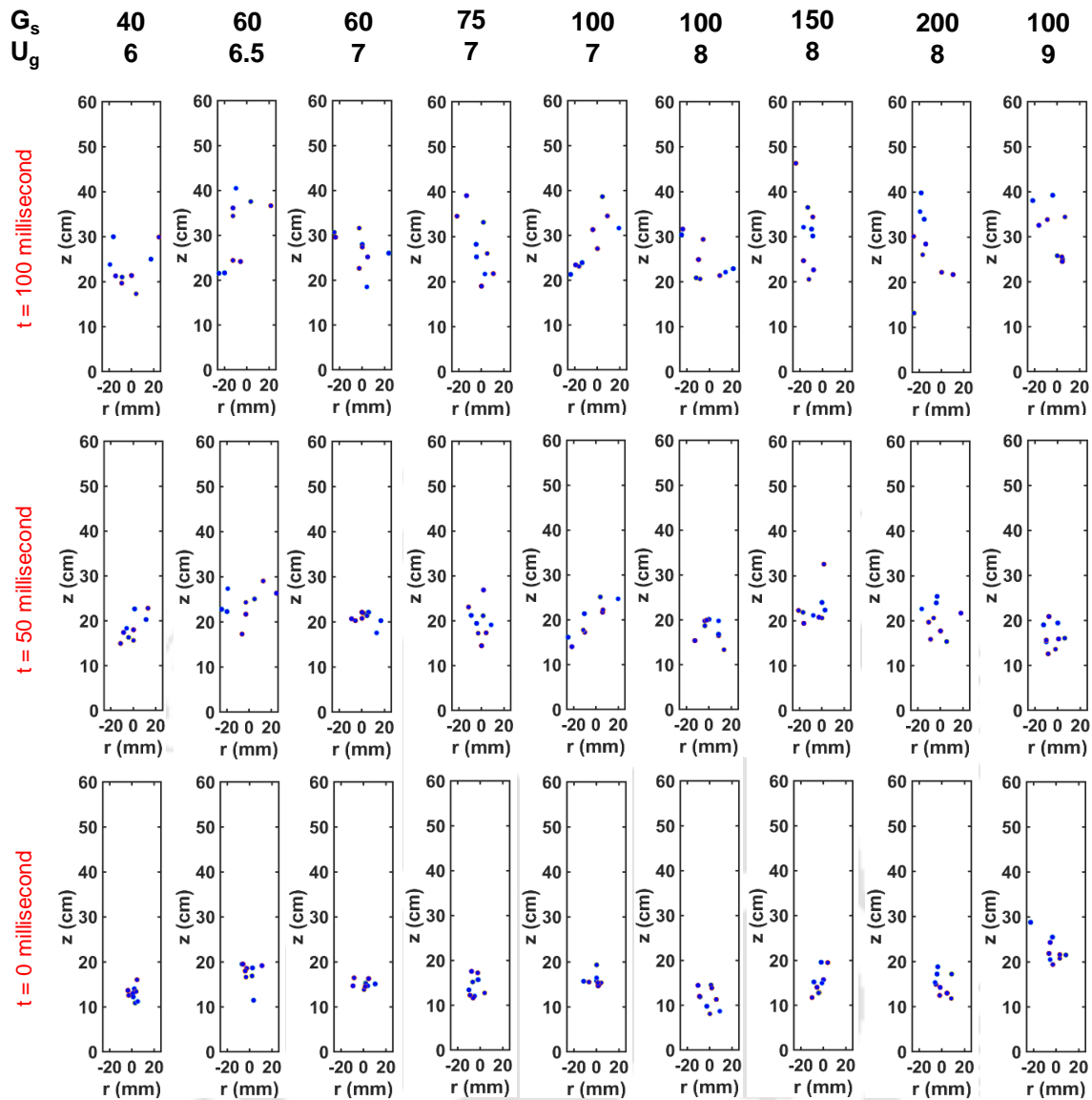


Figure 3.10: Particle position after 50 and 100 milliseconds when the tracer enters the scan zone from the center

Figure 3.10 - 3.12 illustrates the movement of a group of particles within the lower section of the riser over a defined time frame. In each case, track 10 particles are selected to represent their collective motion. These particles originate near the solid inlet wall, whether they enter from the central or wall-side inlet. Notably, as depicted in Figure 3.11, regardless of the entry point, these particles tend to remain within their initial zone. The figures depict particle positions at 50 and 100 milliseconds after entering the riser. After 50 milliseconds

of entry into the scanning zone, the particles begin to disperse, and by the 100-millisecond mark, they are distributed across various radial positions.

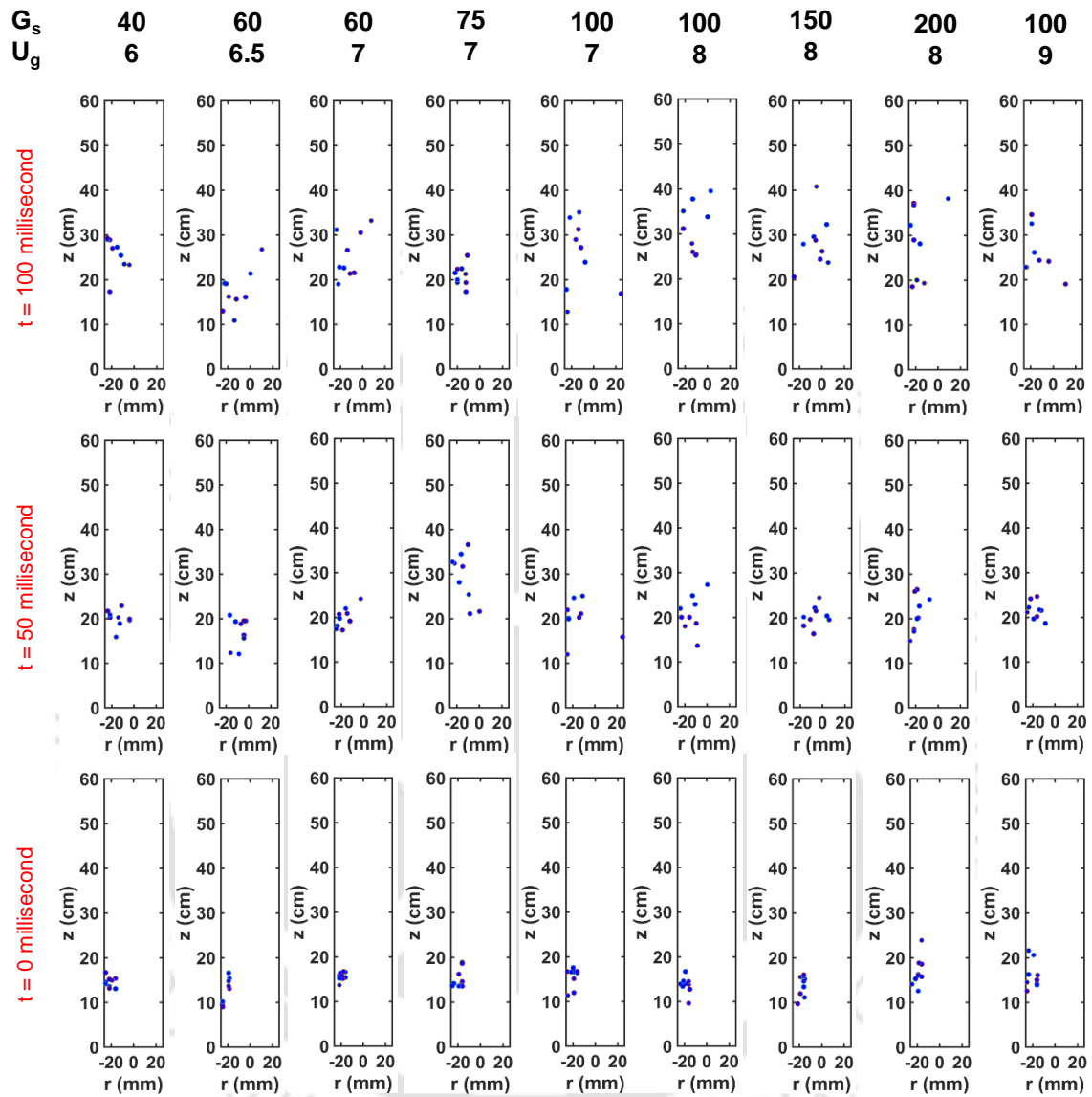


Figure 3.11: Particle position after 50 and 100 milliseconds when the tracer enters the scan zone from the wall region (solid inlet side)

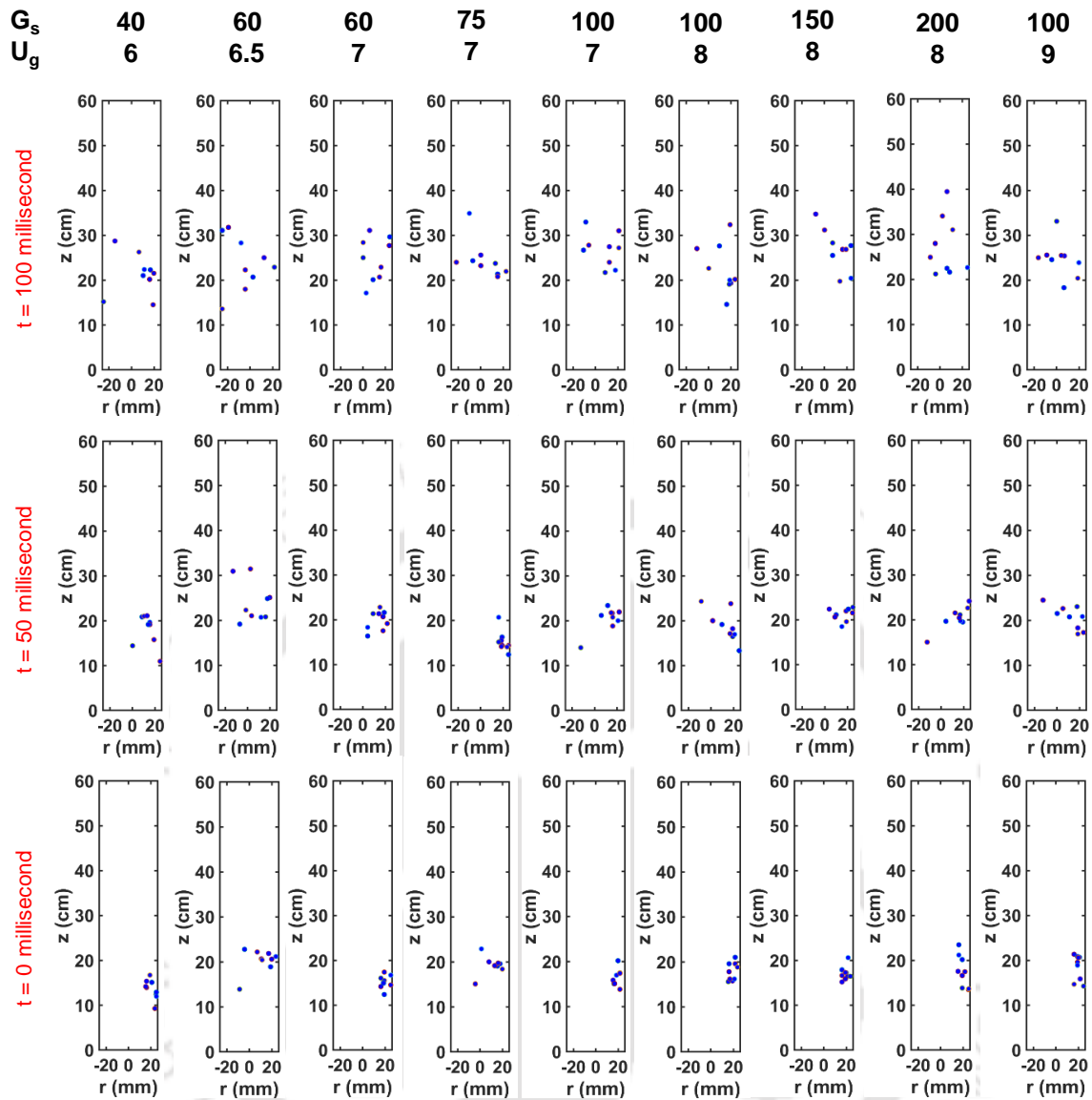


Figure 3.12: Particle position after 50 and 100 milliseconds when the tracer enters the scan zone from the wall region (Opposite of solid inlet side)

This observation highlights that particles, regardless of their entry point, eventually explore different radial positions, deviating from their initial zone. It underscores the variation in particle movement over time, with some particles traversing more complex paths compared to others. This diversity in motion arises from intricate particle-particle and particle-wall interactions, resulting in varying degrees of tortuosity in their trajectories. Particles following relatively straight paths cover greater distances compared to those with more tortuous trajectories. As the flow develops in the lower section, Figures 3.10, 3.11, and 3.12

show that particle movements remain largely similar in the initial 50 milliseconds after entering the riser, regardless of the operating conditions. However, after 100 milliseconds, it becomes evident that variations in particle elevation occur under various operating conditions. In comparison to 6 m/s and 7 m/s, particles travel a greater distance when the inlet gas velocity is 8 and 9 m/s. However, there are no noticeable differences in particle height with varying solid flux.

Figure 3.13 depicts the cross-sectionally normalized number of occurrence contour (NOC) map for the tracer at varying heights within the bottom section. NOC plot visualizes the spatial distribution of detected radioactive particles by representing the density or intensity of particle occurrences across a region. During the reconstruction, the instantaneous position of the tracer particle is generated, and position data is stored in each cell. In the current work, the NOC plot is presented by normalizing the number of occurrences in each cell on different planes. This type of plot helps in understanding where solids are concentrated or dispersed. The contour plot allows analysts to identify hotspots or areas of high particle concentration as well as regions with lower particle densities. These contour plots offer valuable insights into the fluid dynamics, revealing the locations of particle concentrations and the paths particles follow. However, converting the contour map directly into a concentration plot is challenging due to the additional influence of local velocity.

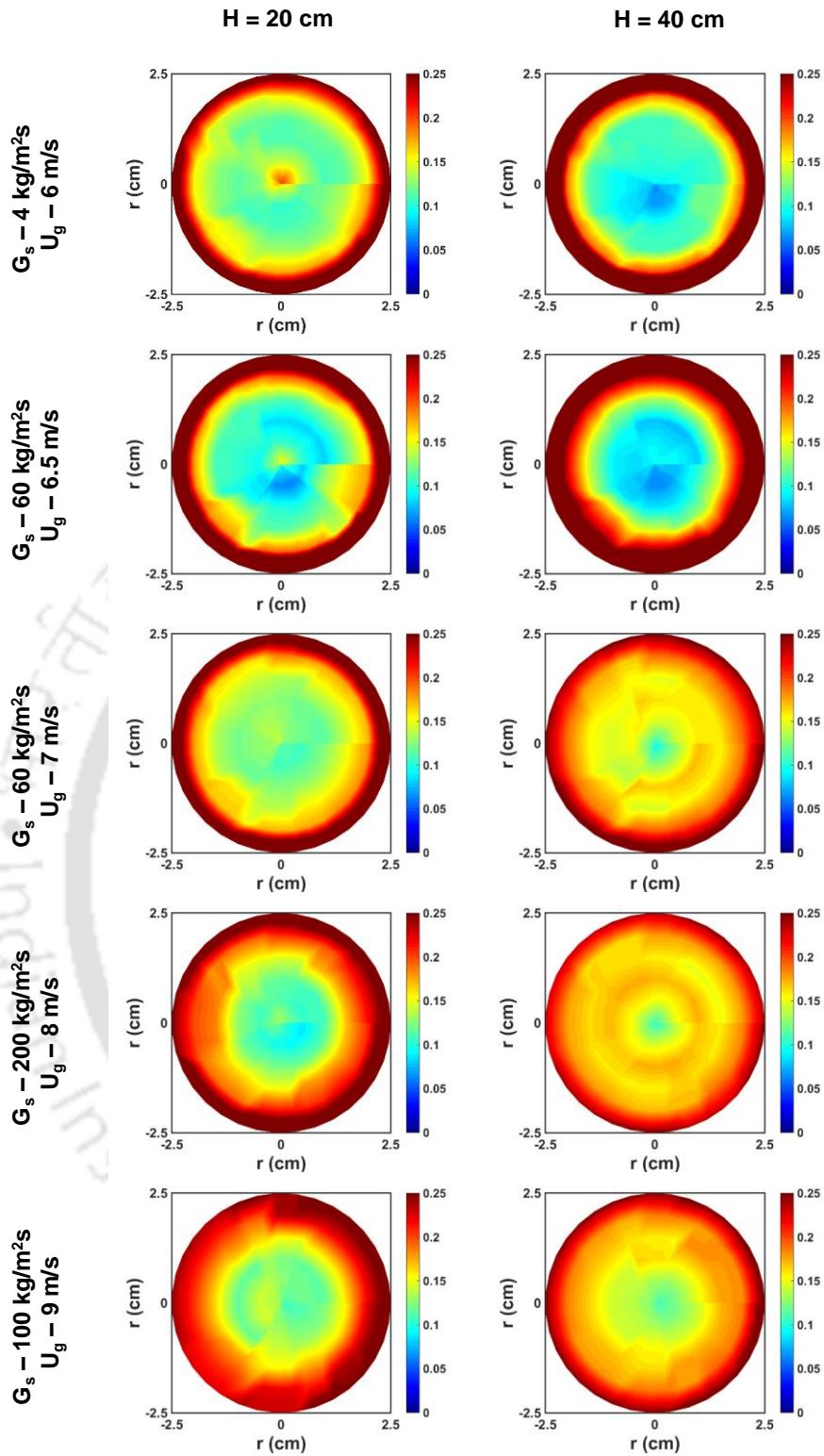


Figure 3.13: Normalized number of occurrence contour plots at different heights and operating conditions at the bottom section

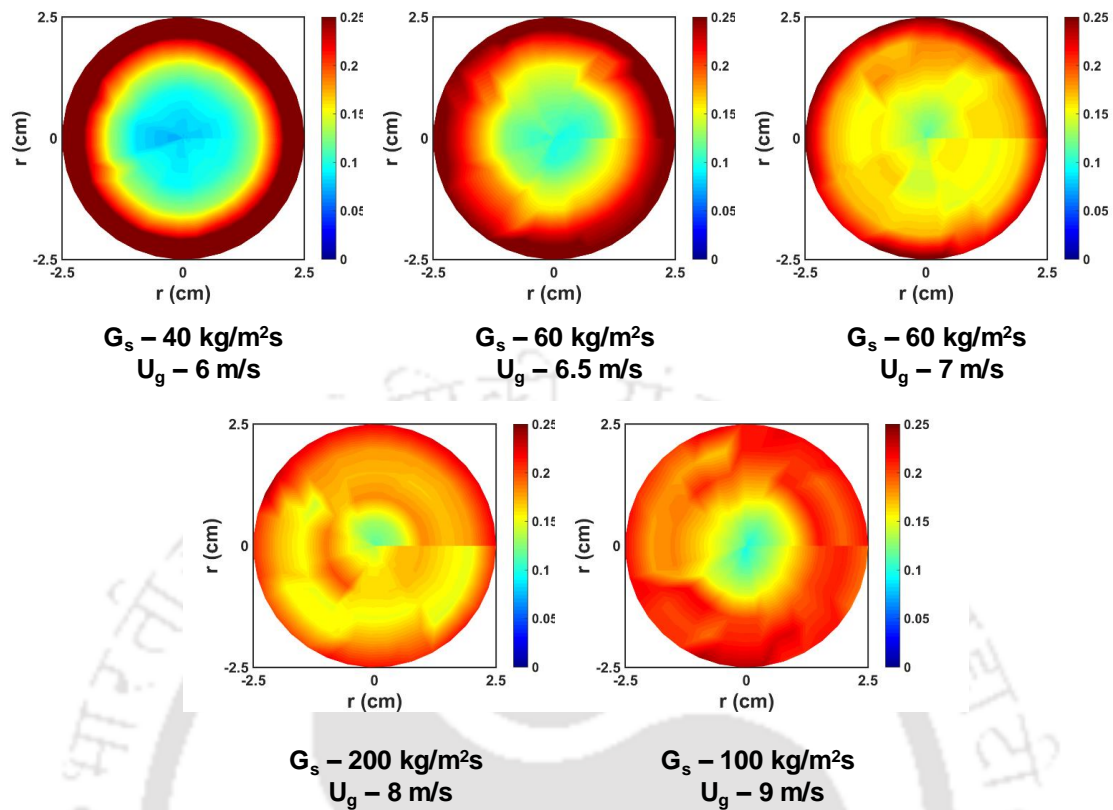


Figure 3.14: Normalized number of occurrence contour plots at different operating conditions at the middle section

In instances where the tracer passes through low-velocity zones, it moves more slowly, leading to an increase in occurrence detections. Separating the effects of concentration and velocity on occurrence is a complex task. It's noteworthy that, regardless of height or operating conditions, the NOC remains low at the central region and increases towards the wall. This trend serves as a reliable indicator of higher solid concentration near the wall. In Figure 3.14, a normalized NOC map for the middle section of the riser is presented. At higher gas velocities (9 m/s), the NOC distribution appears relatively uniform, signifying an even dispersion of solids. Conversely, when gas velocities are lower (6 and 6.5 m/s), a noticeable shift in NOC near the wall indicates a higher solid holdup in that region.

3.5.2 PDF of Instantaneous Velocity

Velocity distribution can be determined by continuously monitoring velocity at a specific point in the riser. To comprehend and forecast reactor behavior, understanding velocity distribution is essential (Levenspiel, 1999). However, most existing techniques do not provide this distribution. RPT is a versatile method that can obtain velocity distribution at every spatial point. Velocity distribution is obtained as follows: Lagrangian velocity vector is calculated from two consecutive positions, as previously explained. This vector is then assigned to the compartment containing its midpoint. Velocity distributions are obtained by repeating this process within the compartment. In our study, experiments were conducted over an extended period to collect statistically sufficient data. It is important to note that the stationarity condition ensures no further changes in the distribution. Probability distribution function (PDF) plot is generated by normalizing the histogram diagram of instantaneous velocity data stored in each cell.

It is clearly visible from the PDF diagrams (Figures 3.15–3.20) that irrespective of operating conditions and radial position, all diagrams are unimodal. Bhusarapu et al. (2006) reported bimodal distribution with Geldart Group B particles for a larger diameter riser. No such PDF with bimodal distribution is found even at the bottom section of the riser (Figures 3.15–3.18). Bhusarapu et al. (2006) employed smaller-sized Geldart Group B particles and a wider riser, leading to the clustering phenomenon and resulting in a bimodal velocity distribution. In Figures 3.15–3.20, the PDF diagrams of instantaneous axial velocity are represented at the riser center ($r/R = 0$), the annular region ($r/R = 0.48$) and near the wall region ($r/R = 0.88$).

Figures 3.16–3.17 show the PDF diagram at a height of 0.2 m from the riser bottom. It is just above the solid inlet and the solid velocity is lower. It is visible that negative

instantaneous velocity exists all over the radial position, even at higher gas velocities (8 and 9 m/s). And at the same time, the PDFs are comparatively wider than the PDFs of 0.4 m (Figures 3.17–3.18) and 1.6 m (Figures 3.19 –3.20). It indicates that at this zone, the solid back mixing is much intense.

In the PDFs of instantaneous velocity at a height of 0.4 m (Figures 3.17–3.18), negative instantaneous velocity is evident across all gas velocities and radial positions. However, at higher gas velocities (8 and 9 m/s), negative velocity exists but is barely noticeable in the center region.

Figures 3.19 show that in some instances, negative velocity is observed, although the occurrence and magnitude of negative instantaneous velocities are very low. There are very few instances of negative velocities that can be observed for gas velocities of 6 and 6.5 m/s in the center region. However, at the annular region and near the wall region, downward motions are noticeable. There is no downward motion of solids observed at gas velocity of 7 m/s at the center and annular regions except near the wall region. Figure 3.20 shows that at gas velocities of 8 and 9 m/s there is no negative velocity at any reading position. It is worth noting that the mean velocity, remains consistently positive irrespective of height, radial positions, and operating conditions. At lower gas velocities, the downward motion of tracer particles is more noticeable compared to higher gas velocities.

Regardless of operating conditions and radial positions, the occurrence of negative velocities decreases with height. It confirms that at the bottom section near the solid inlet, there is an intense particle-particle interaction that hinders solid motion, resulting in solid back mixing and internal circulation. In the middle section, flow is developed, and the solid fraction is lower compared to the bottom section; thus, there is less possibility for the

particles to move downward. Only at low gas velocity and near the wall region (where gas velocity is also low), particles move downward in certain instances.

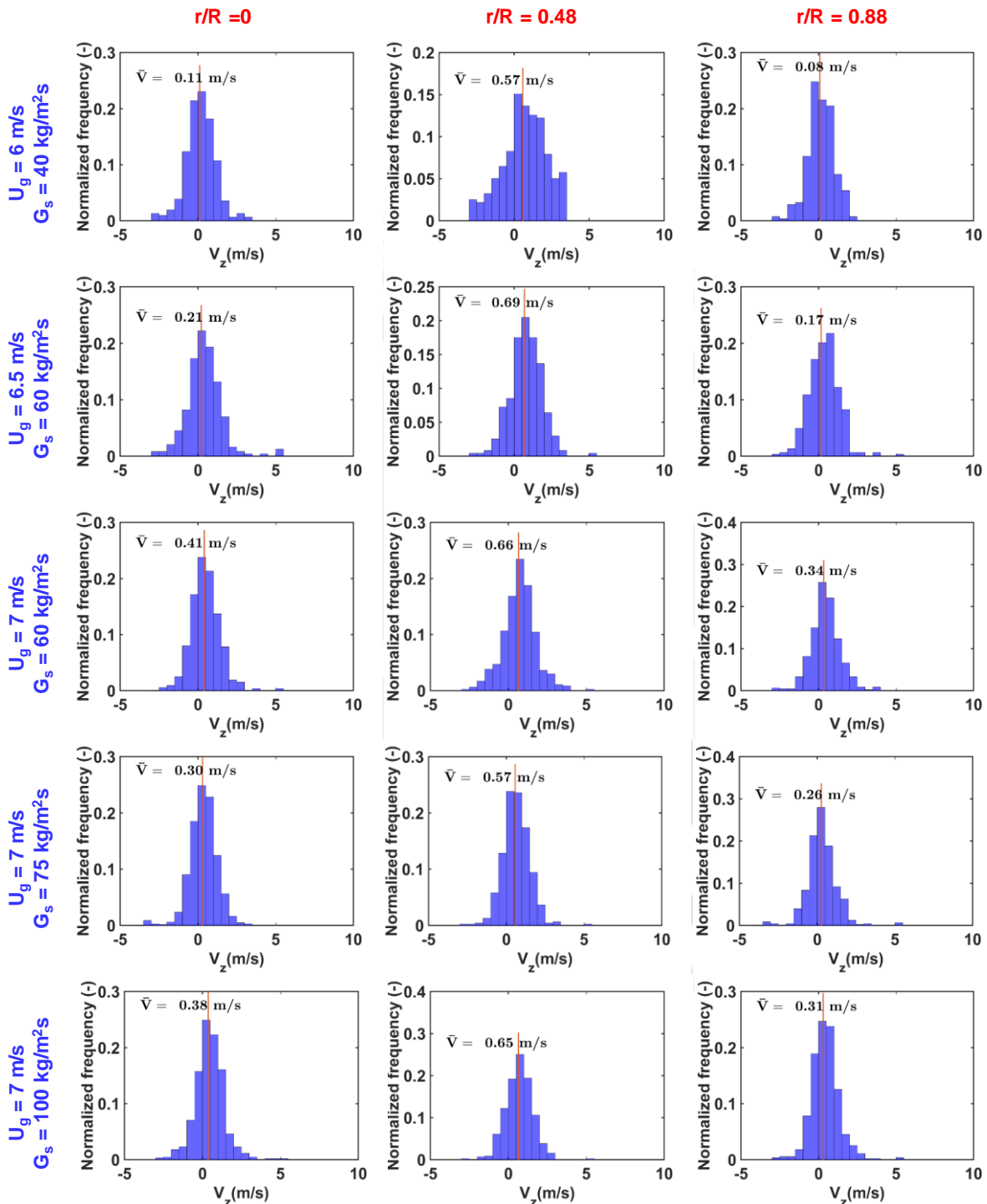


Figure 3.15: Normalized histogram diagram of instantaneous velocity at three radial locations for the bottom section ($h = 0.2$ m) of the riser for lower gas velocities

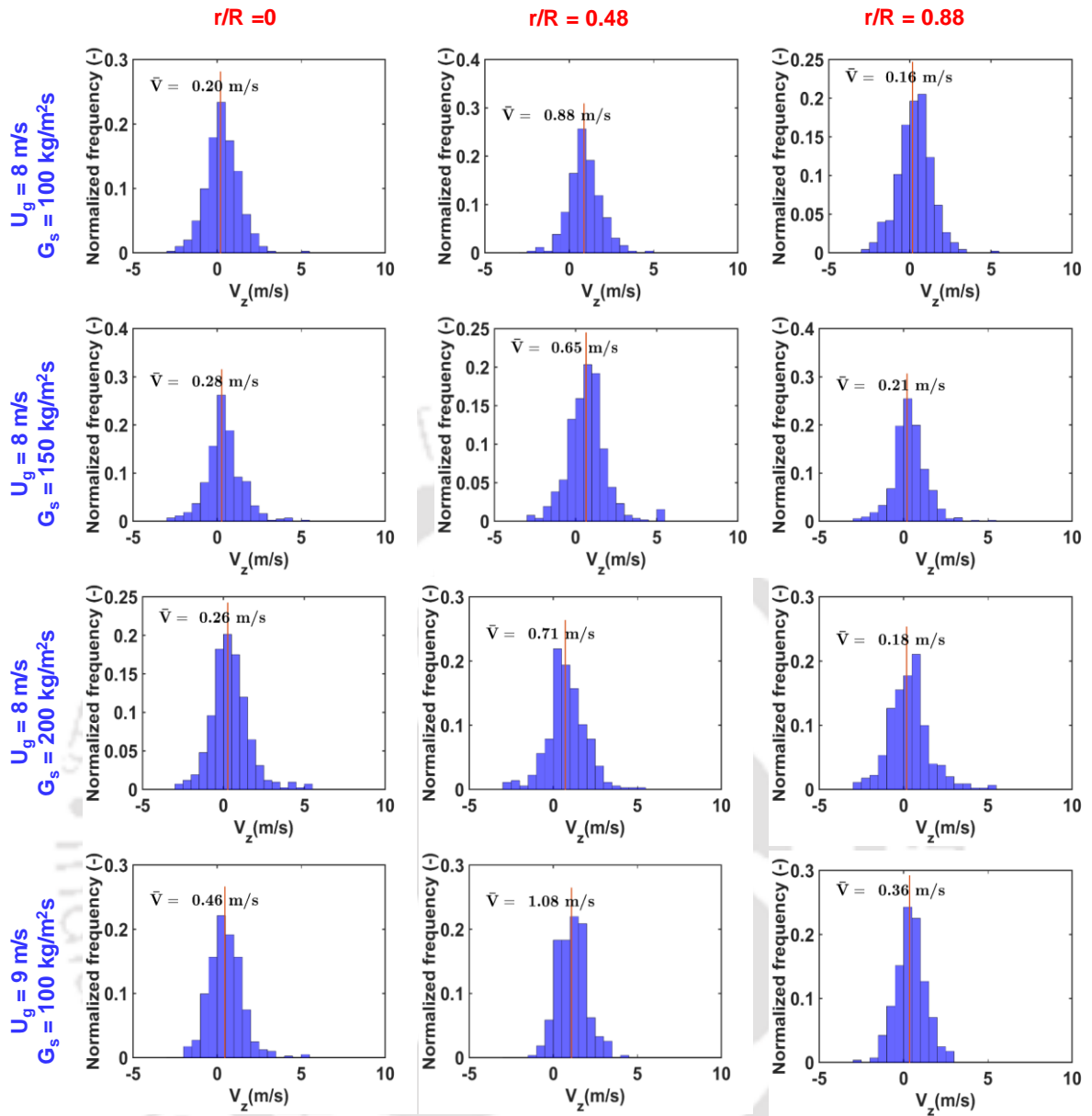


Figure 3.16: Normalized histogram diagram of instantaneous velocity at three radial locations for bottom section ($h = 0.2 \text{ m}$) of the riser for higher gas velocities

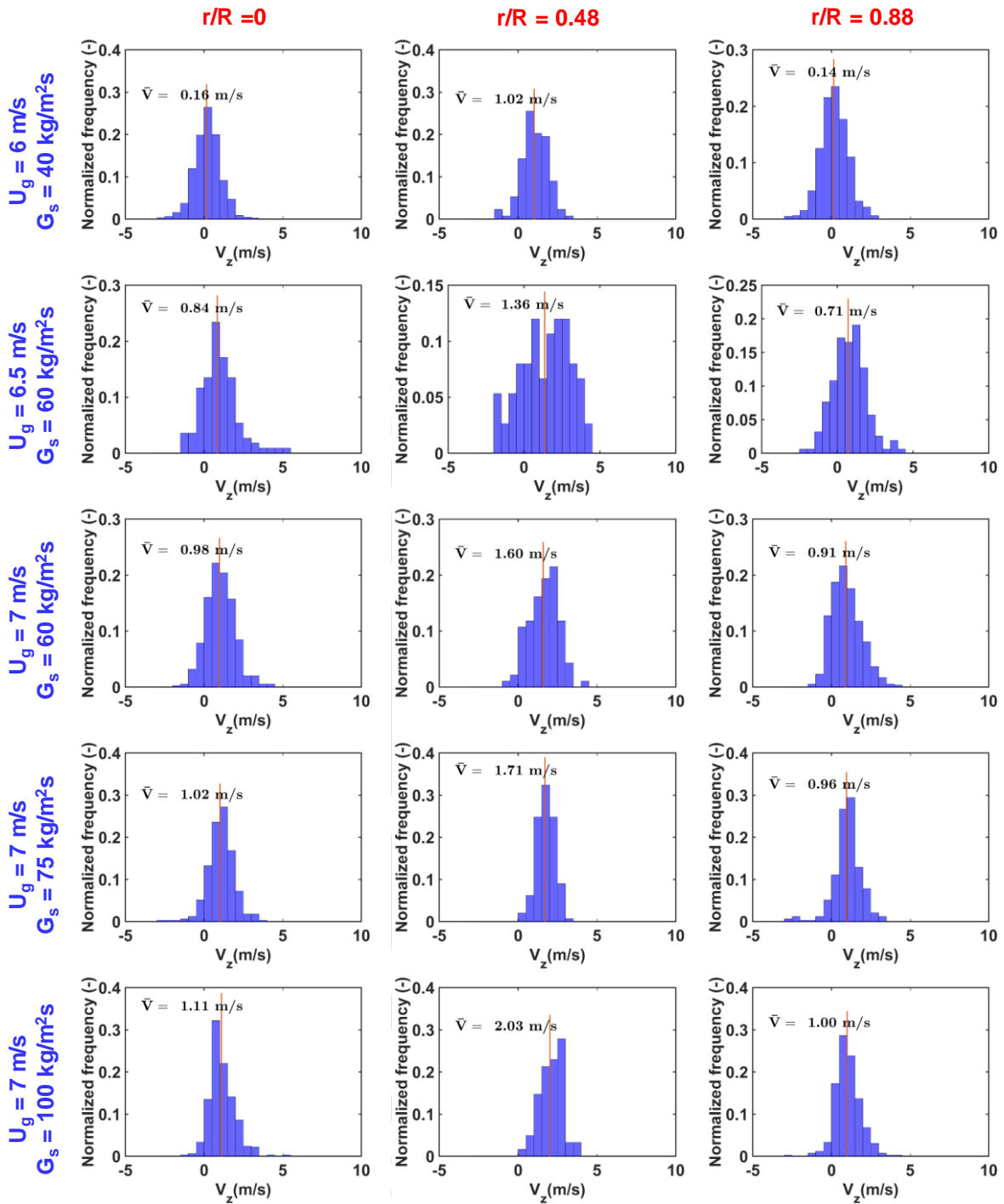


Figure 3.17: Normalized histogram diagram of instantaneous velocity at three radial locations for the bottom section ($h = 0.4$ m) of the riser for lower gas velocities

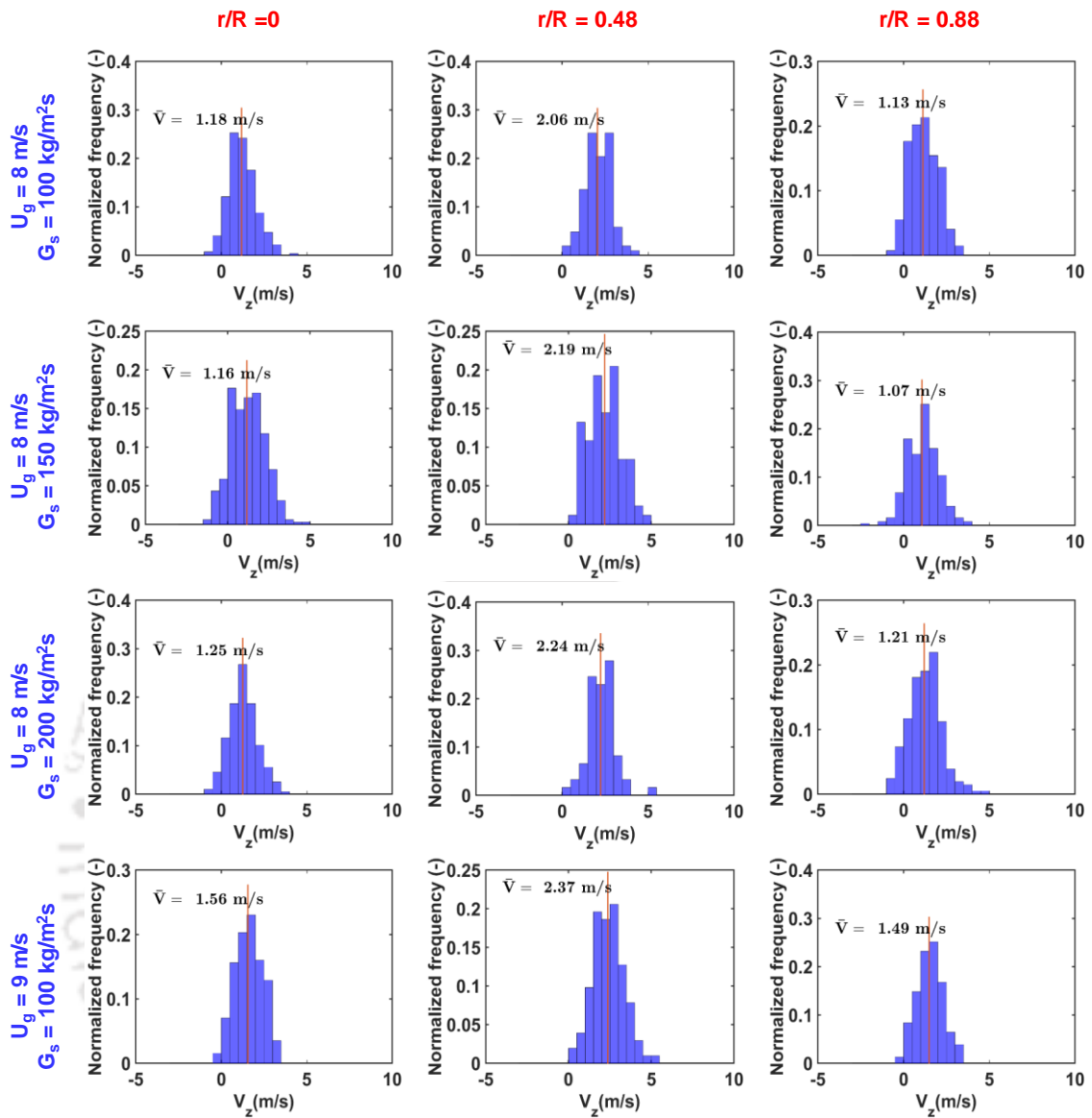


Figure 3.18: Normalized histogram diagram of instantaneous velocity at three radial locations for the bottom section ($h = 0.4$ m) of the riser for higher gas velocities

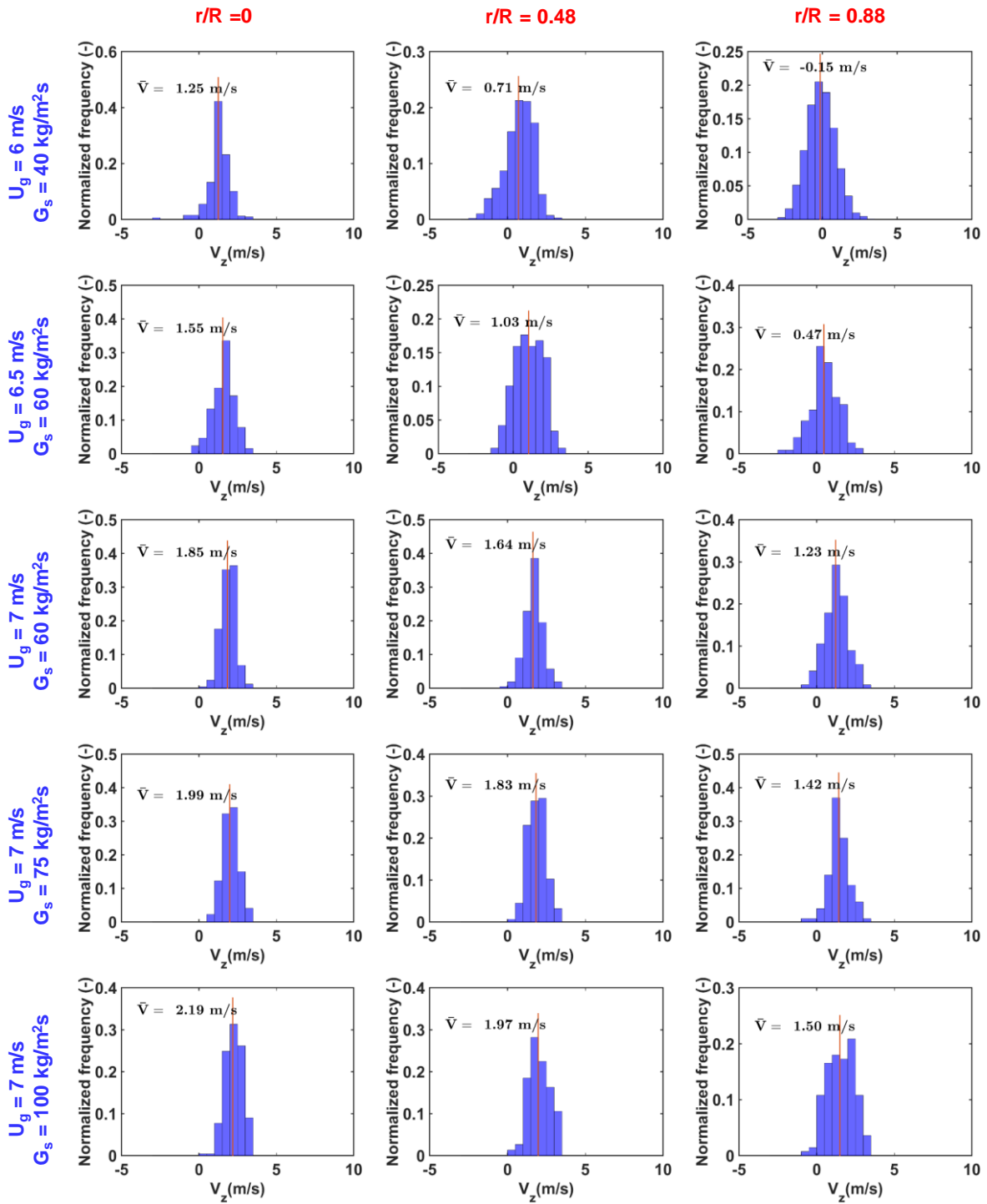


Figure 3.19: Normalized histogram diagram of instantaneous velocity at three radial locations for the middle section ($h = 1.6$ m) of the riser for lower gas velocities

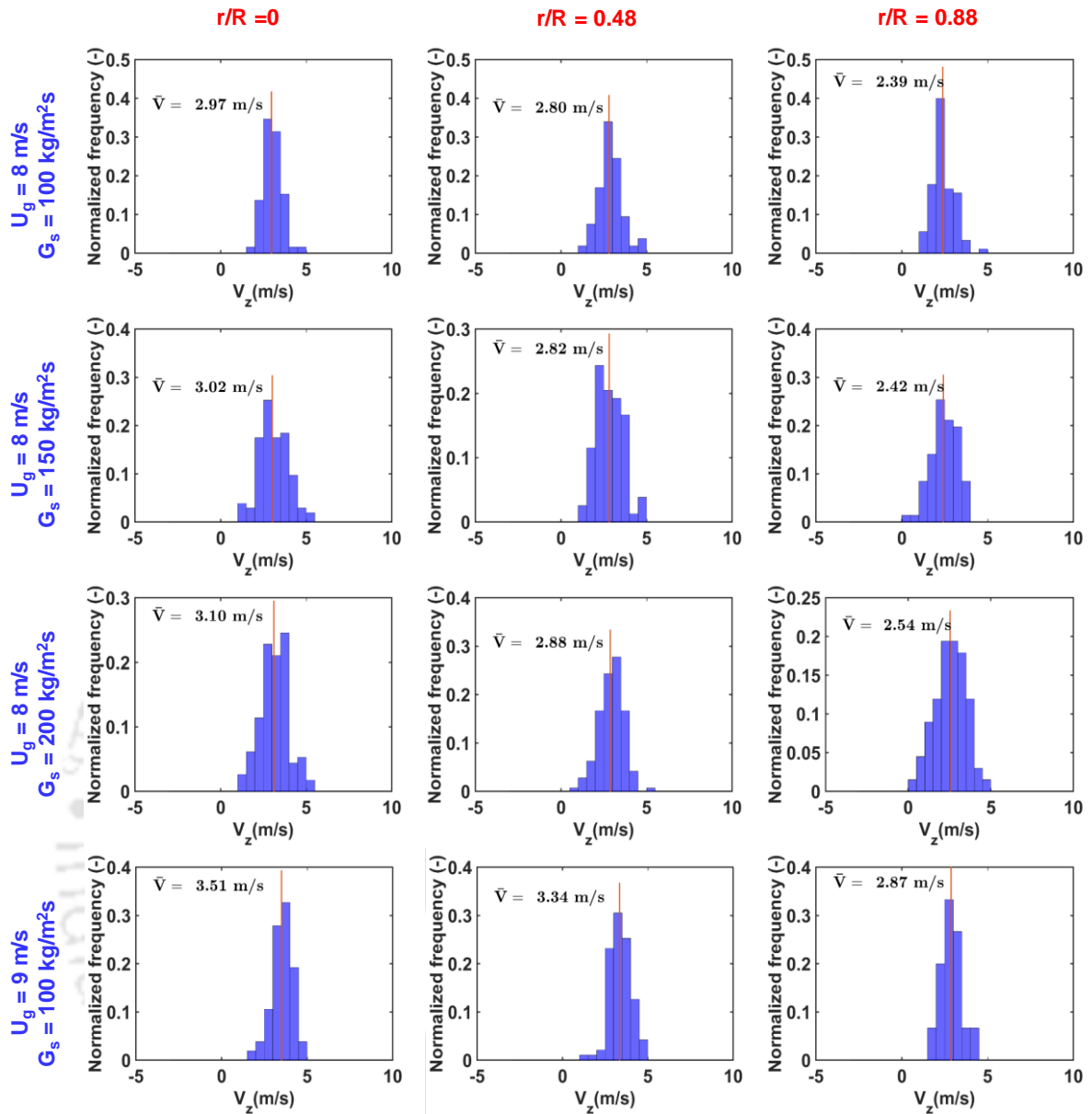


Figure 3.20: Normalized histogram diagram of instantaneous velocity at three radial locations for the middle section ($h = 1.6$ m) of the riser for higher gas velocities

3.5.3 Velocity Vector Plots

Figures 3.21 and 3.22 display the velocity vector in the lower and middle sections of the riser, respectively. These visuals provide important insights into the riser's flow patterns. The lower section shows a noticeable trend: the average velocity increases with elevation. Despite the relatively low velocity at the solid inlet, no consistent downward motion is observed under any operating conditions. Both sections depict velocity within a 0-180

degree range, and despite solids entering from one side, their velocity distribution remains largely symmetrical. When examining the instantaneous position trace and the PDF diagram of instantaneous velocity, downward motion can be observed. However, when looking at the overall velocity vector, there is generally no internal circulation, and the mean velocity predominantly points upward.

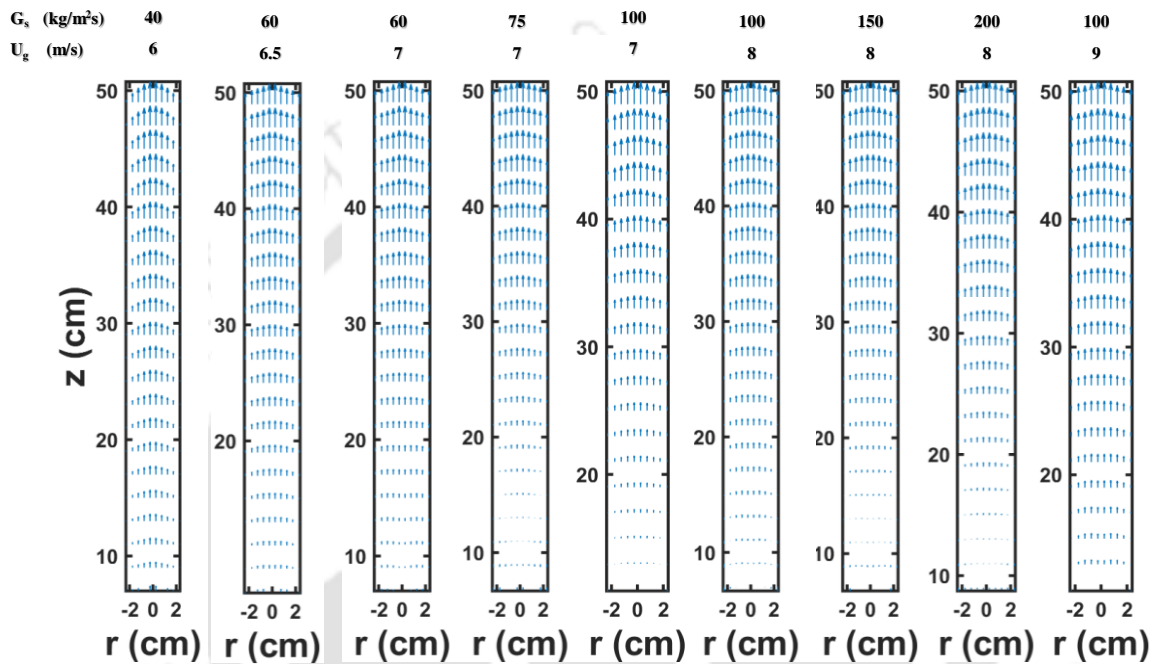


Figure 3.21: Velocity vector plot at the bottom section for different operating conditions

The axial velocity vectors for the lower section and middle section of the riser are presented in Figure 3.21 and Figure 3.22, respectively. During post-processing, after position reconstruction, velocity data stored in the Eulerian cell is utilized to generate a velocity vector. It is evident that in both the lower and middle sections, velocity is low near the wall and higher at the center of the riser. In the lower section, velocity increases with height from the inlet to the exit section of the lower scan zone, while in the middle section, velocity remains relatively constant, regardless of the height.

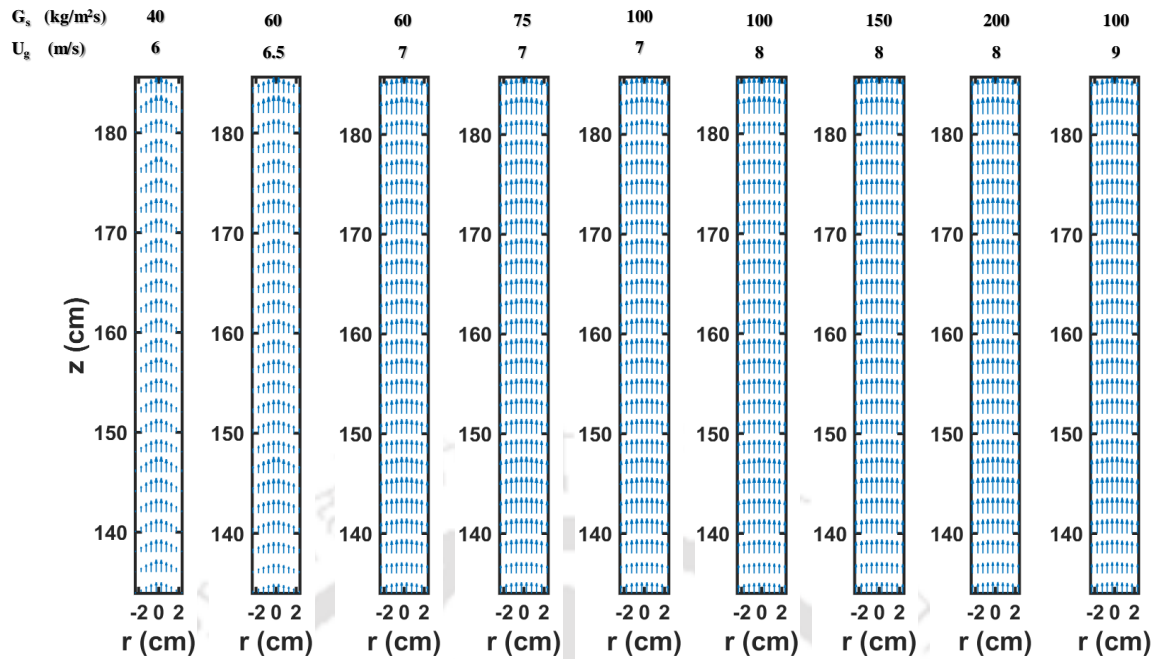


Figure 3.22: Velocity vector plot for the middle section for different operating conditions

3.5.4 Ensemble Averaged Velocity

Figures 3.23 and 2.24 show the radial velocity profile of the mean axial velocity for the bottom section at 0.2 m and 0.4 m, respectively. Detailed mean velocity calculations from instantaneous positions are given in the table 2.2 in Chapter 2. It can be observed that in both cases, the solid phase mean velocity is lowest near the wall and highest near the center. The mean velocity of the solid at the center of the riser can be attributed to many reasons. The no-slip boundary of the gas phase is one of the main reasons. Like solid phase gas velocity, it is not uniform through the radial position. Due to the lower gas velocity near the wall, the drag force acting on the solid phase is also lower, which causes a lower solid velocity. Solid concentration is not uniform around the radial portion; it is typically lower at the center. In most cases, the solid concentration is higher near the wall due to the inherent outward migration of particles in the riser. Particle-wall interaction and a higher degree of particle-particle collision create hindrances to solid movement near the wall. The mean axial velocity is high at the center, irrespective of height and operating condition.

Pantzali et al., 2015) reported similar velocity profile at the bottom section of the riser with Geldart Group A particles. Also, a similar phenomenon is observed for the Geldart Group B particles at the bottom section of a pilot scale riser as mentioned in Chapter 4.

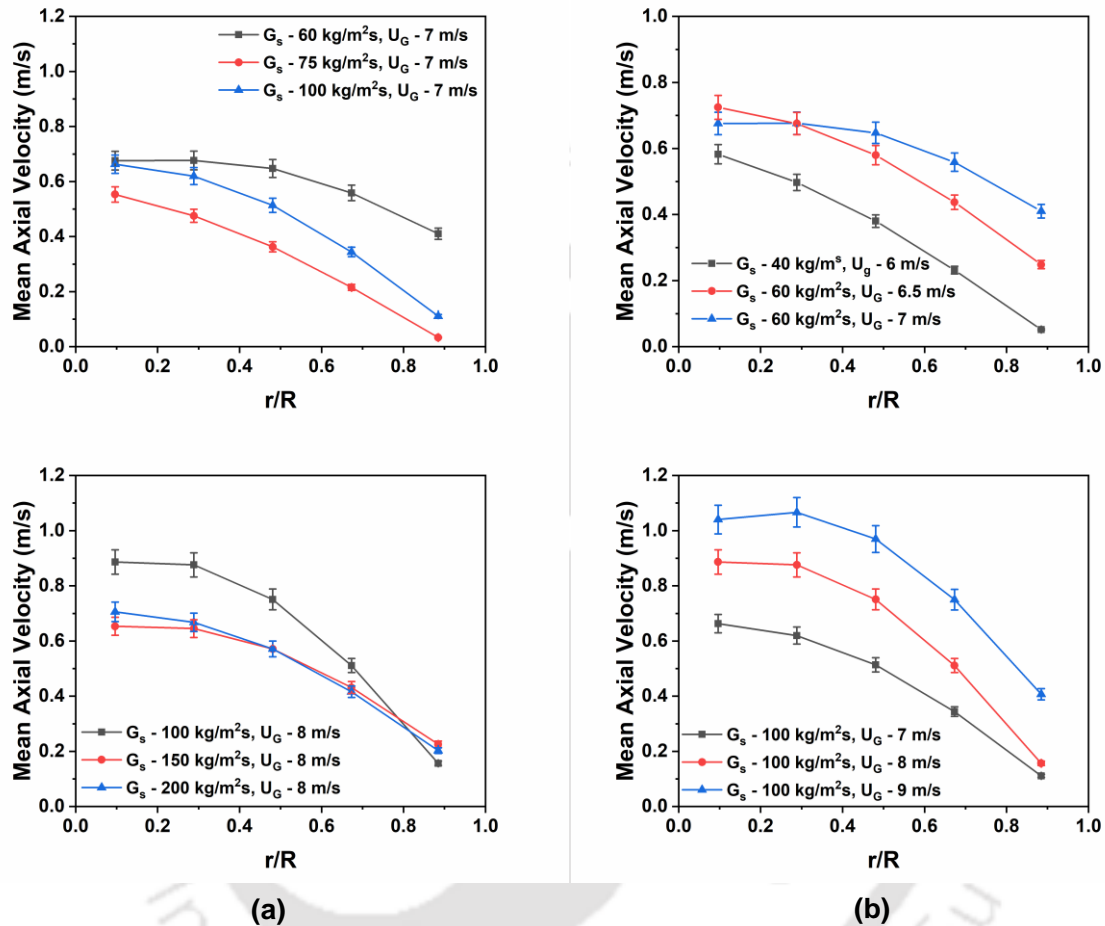


Figure 3.23: Radial variation of azimuthally averaged mean axial velocity profile at the bottom section ($h = 0.2$ m) (a) effect of solid flux and (b) effect of inlet gas velocity

The hydrodynamics of CFB is complex in nature. Solid particles travel through a continuous acceleration and de-acceleration process due to the complex solid-fluid interaction, solid-solid interaction, and solid-wall interaction. The bottom section of the riser is called the acceleration zone or developing zone, where solid particles go through vigorous interactions. The momentum transfer from fluid to particles caused acceleration and resulted in an increasing mean solid velocity. Typically, the solid concentration

decreased with height at the bottom section. Reduced solid concentrations allow the fluidizing medium to flow more freely, increasing its velocity. However, after a certain height of the riser, the mean solid velocity remains almost constant, which is called a fully developed zone.

Figure 3.23(a) shows that in the case of increasing solid flux, the mean axial velocity increment is not proportional. It can be observed that at both inlet gas velocities of 7 and 8 m/s, at lower solid flux, the mean axial velocity is higher, then decreases again with the increase in solid flux, then increases marginally again. A similar observation is made for the bottom section of pilot scale riser as described in the Chapter 4. Solids can move relatively freely and unhindered at lower solid flux, where the solid fraction is relatively low. The solid fraction increases with an increase in solid flux, which causes more hindrance in the solid movement resulting in lower mean solid velocity. However, after a certain solid flux, solid slip velocity increases due to the increase in velocity. However, this phenomenon is only visible near the entry section of the riser, and it disappeared at the height of 40 cm. The jet-like structure reported in the literature (De Wilde et al., 2005; Pantzali et al., 2015) at the solid inlet section of the riser disappeared within a few distances from the solid inlet. Figure 3.23(b) shows the mean axial velocity of solids increasing with the increase in gas velocity. It is expected that as gas velocity increases, momentum transfer to solids increases as well, resulting in an increase in axial velocity. However, the mean velocity profile at 40 cm height on the riser, when solid flux remains unchanged (Figure 3.24(b)), increases in inlet gas velocity also result in an increase in mean axial velocity. It can also be observed that the mean velocity also increases. Figures 3.23 and 3.24 confirm that inlet gas velocity has a more significant effect on mean axial velocity than mean solid flux until the solid fraction reaches a critical point.

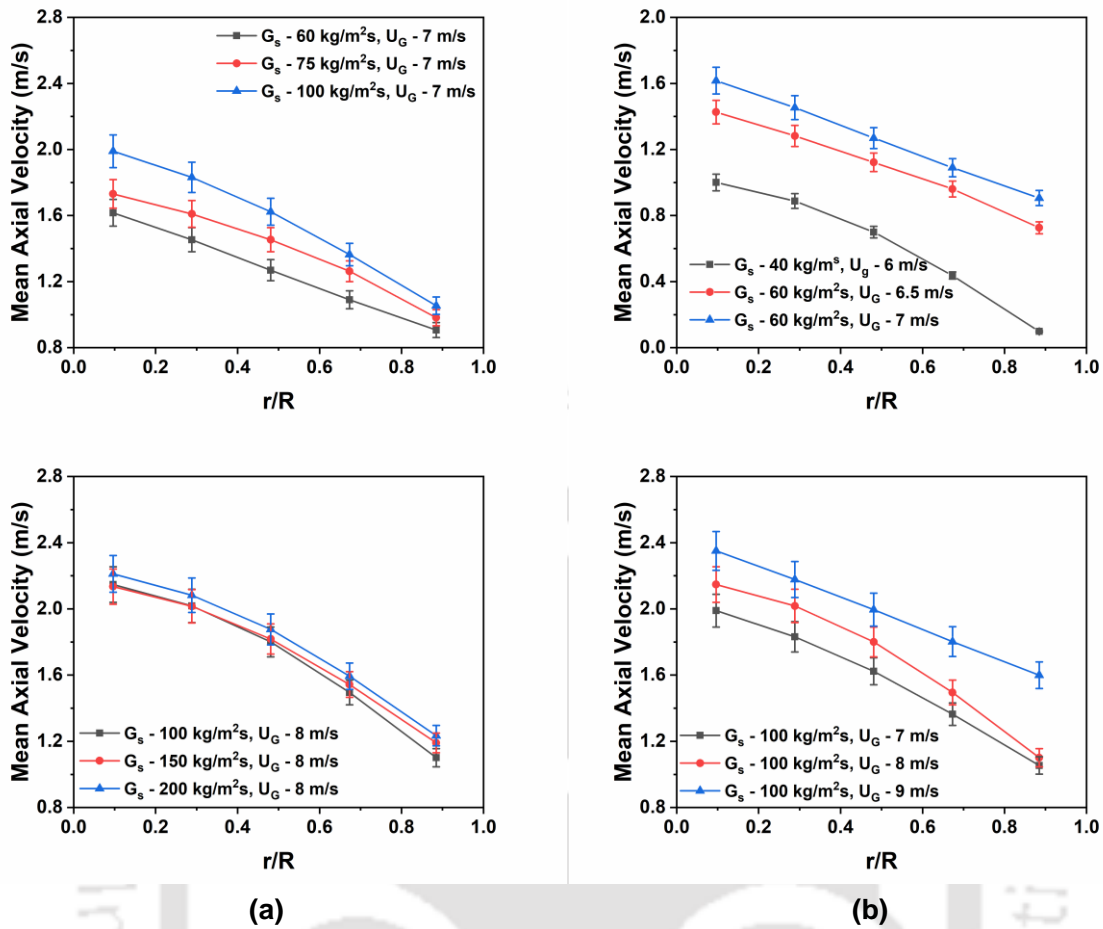


Figure 3.24: Radial variation of azimuthally averaged mean axial velocity profile at the bottom section ($h = 0.4$ m) (a) effect of solid flux and (b) effect of inlet gas velocity

Figure 3.25 shows the effect of solid flux and inlet gas velocity on the mean axial velocity for the middle section of the riser. The velocity at the center is highest irrespective of solid flux, and the operating condition gradually decreases towards the wall. However, no negative mean velocity was observed, apart from the gas velocity condition of 6 m/s. The mean axial velocity profile in the current work is flat compared to the axial velocity profiles reported at similar operating conditions and particle size in a pilot scale riser, as reported in Chapter 4. On the one hand, the gas velocity is lower near the wall due to the no-slip boundary condition. On the other hand, in the riser, particles are pushed toward the riser wall while traveling upward, causing solid distribution higher towards the wall.

Combination two caused lower velocity near the wall. The effect becomes more significant for a larger diameter riser than the small diameter column. The shape of the profile presented by Bader et al., (1988), Godfroy et al., (1999) and Bhusarapu et al., (2006, 2005) are more parabolic than the findings with current work, as the riser diameter is comparatively much smaller

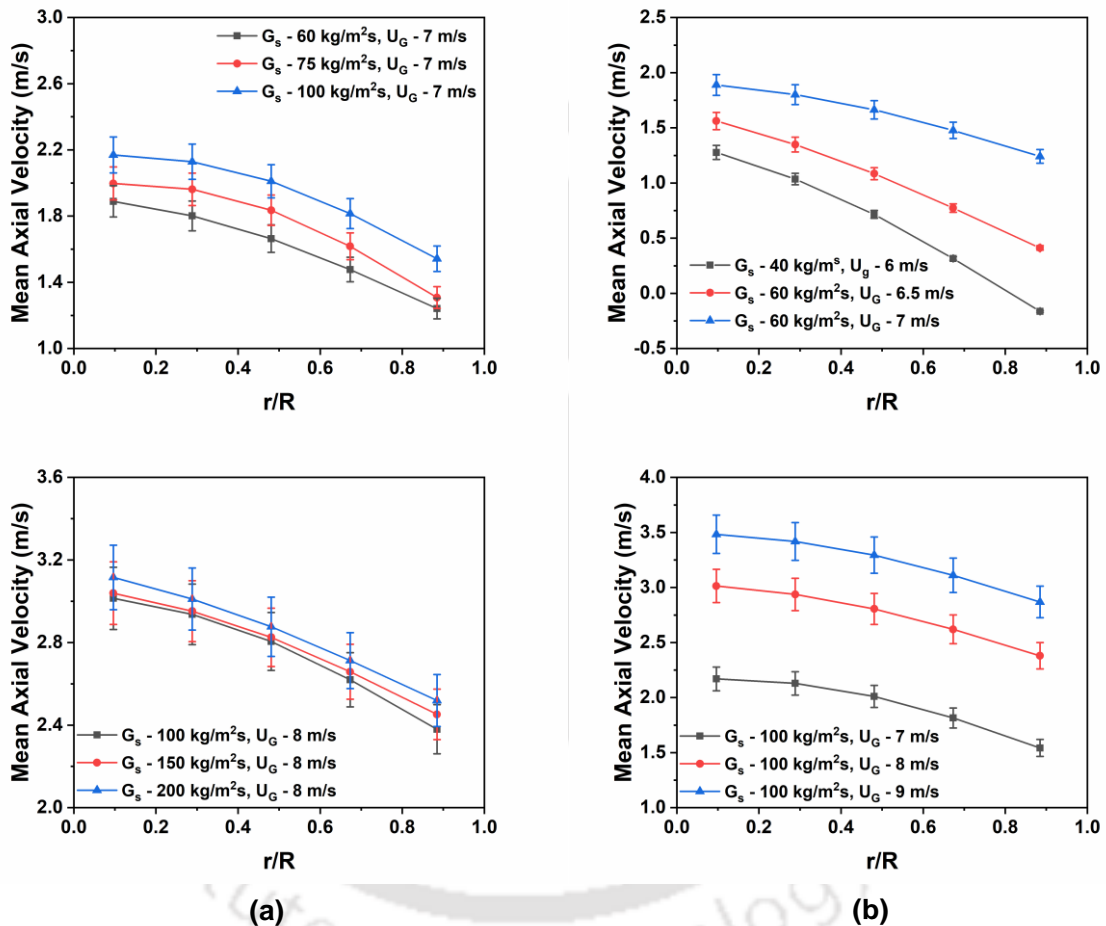


Figure 3.25: Radial variation of azimuthally averaged mean axial velocity profile at the middle section ($h = 1.6$ m) (a) effect of solid flux and (b) effect of inlet gas velocity

The increase in solid flux clearly increases the mean axial velocity; however, this increment is very small when compared to the mean velocity increment due to inlet gas velocity when the solid flux is unchanged. For inlet gas velocity of 7 m/s, mean axial velocity increases with an increase in solid flux, however this increment is comparatively less at inlet gas

velocity of 8 m/s. At low velocity, the solid fraction is higher, and an increase in solid flux increases the solid fraction even more, resulting in an increase in mean axial velocity. This effect is less pronounced with an inlet gas velocity of 8 m/s because the solid fraction itself is lower at a higher velocity.

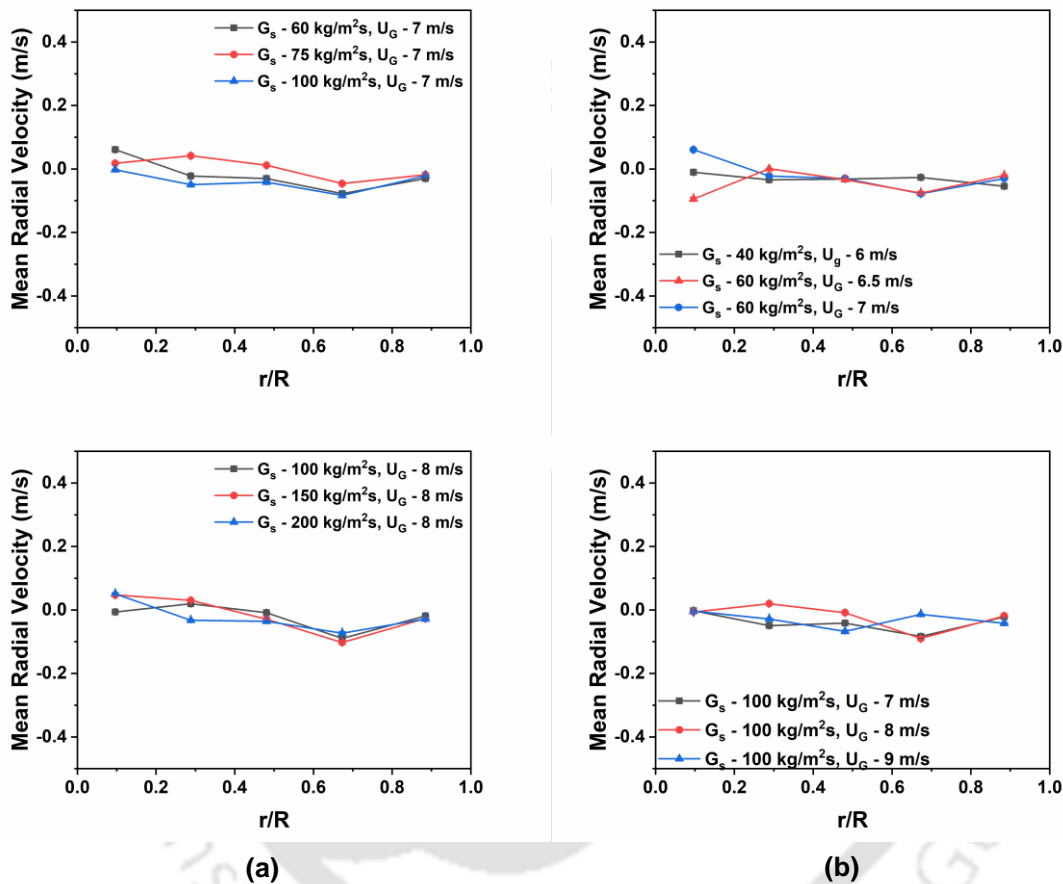


Figure 3.26: Radial variation of azimuthally averaged mean radial velocity profile at the bottom section ($h = 0.2$ m) (a) effect of solid flux and (b) effect of inlet gas velocity

The average radial velocities of the bottom and middle sections are depicted in Figures 3.26, 3.27 and 3.28 respectively. Regardless of the setup or riser height, a consistent range of -0.1 to 0.1 is maintained by the average radial velocity. Negative radial velocity signifies particle movement towards the wall, while positive axial velocity indicates motion towards the riser center. In the current experiments, all recorded average radial velocity values are below 0.1, signifying minimal radial motion. It's worth noting that achieving a precise

velocity of zero is a significant challenge due to the inherent limitations of measurement techniques. Hence, a small value for the mean radial velocity was recorded by RPT.

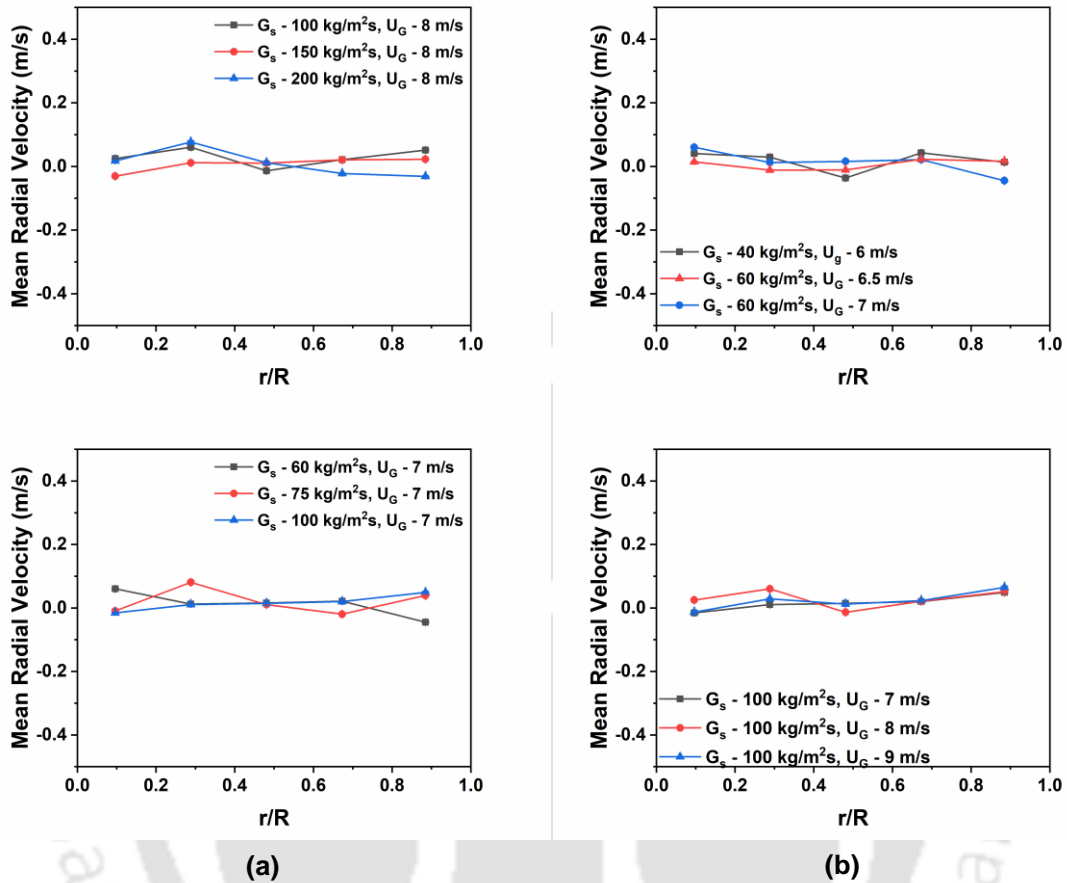


Figure 3.27: Radial variation of azimuthally averaged mean radial velocity profile at the bottom section ($h = 0.4$ m) (a) effect of solid flux and (b) effect of inlet gas velocity

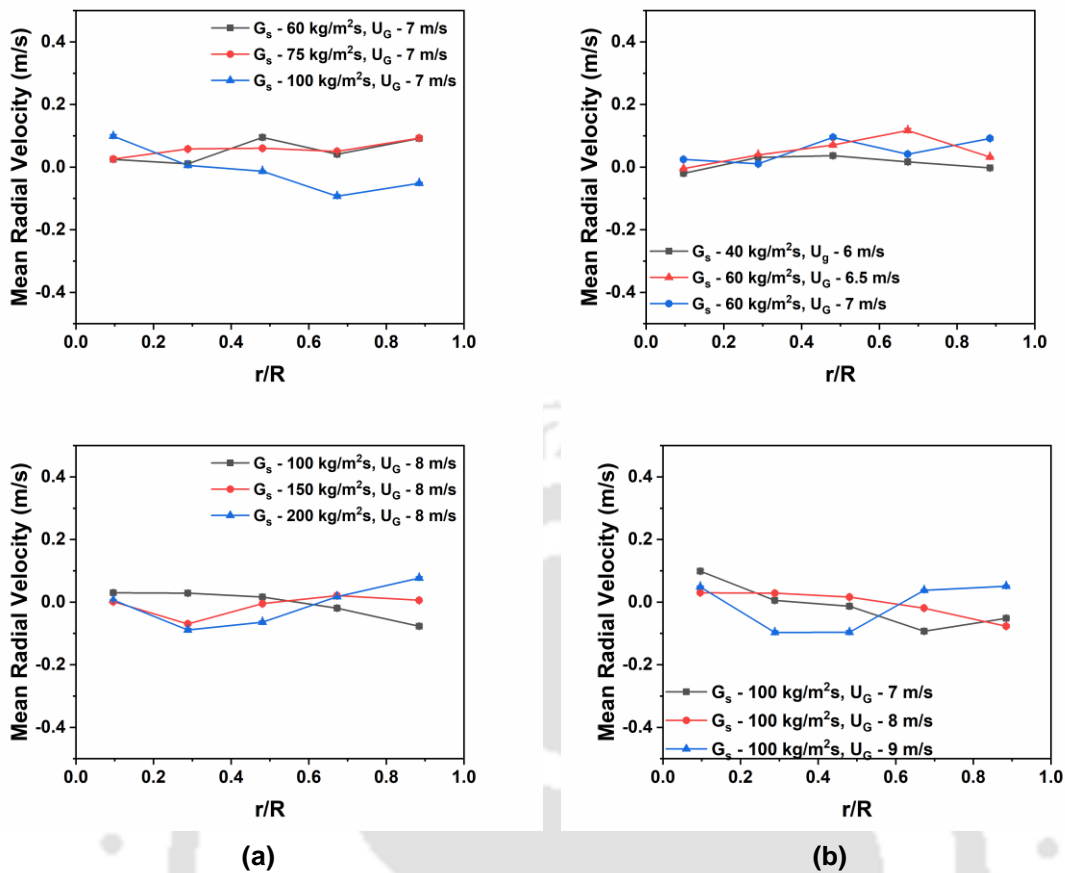


Figure 3.28: Radial variation of azimuthally averaged mean radial velocity profile at the bottom section ($h = 1.6$ m) (a) effect of solid flux and (b) effect of inlet gas velocity

3.5.5 Solid Velocity Fluctuations

Figures 3.29, 3.30 and 3.31 show the radial profile of axial velocity fluctuation (axial RMS velocity) for different gas inlet velocities and solid fluxes for heights of 0.2 m, 0.4 m and 1.6 m. It is clearly visible from this picture in Figures 3.29, 3.30 and 3.31 that velocity fluctuation is higher at the bottom, and with increasing height, axial RMS velocity decreases. The axial velocity profile also changes with increasing height. At the bottom section, just above the solid inlet (0.2 m from the air inlet), axial RMS velocity is higher at the center and decreases toward the wall. However, the change in magnitude is not significant compared to 0.4 m or 1.6 m height. Both particle-particle, particle-wall collisions and the mean free path between collisions play a considerable role in velocity

fluctuation. Typically, the riser bottom section has a higher solid holdup than the fully developed section, which causes more particle-particle collision, resulting in higher axial RMS velocity. Similarly, the typical profile of a CFB riser's solid holdup increases toward the wall. At the bottom section, where the solid holdup is already high, the mean free path plays a dominant role at the center of the riser where the solid fraction is comparatively less and the solid can move freely without restriction, causing a higher magnitude of axial velocity as well as axial RMS velocity. As height increases, solid holdup decreases so does particle-particle collision. As a result, axial RMS velocity decreases with height, as observed in Figures 3.29 and 3.30. The shape of the radial variation of axial RMS velocity also changes with height. In Figures 3.24 and 3.25, it can be observed that near the wall region, the magnitude of axial velocity has not changed much from 0.2 m to 0.4 m. however, at the center, there is a drastic change in axial RMS velocity. It further continues to a fully-developed section where axial RMS velocity is low at the center and gradually increases towards the wall.

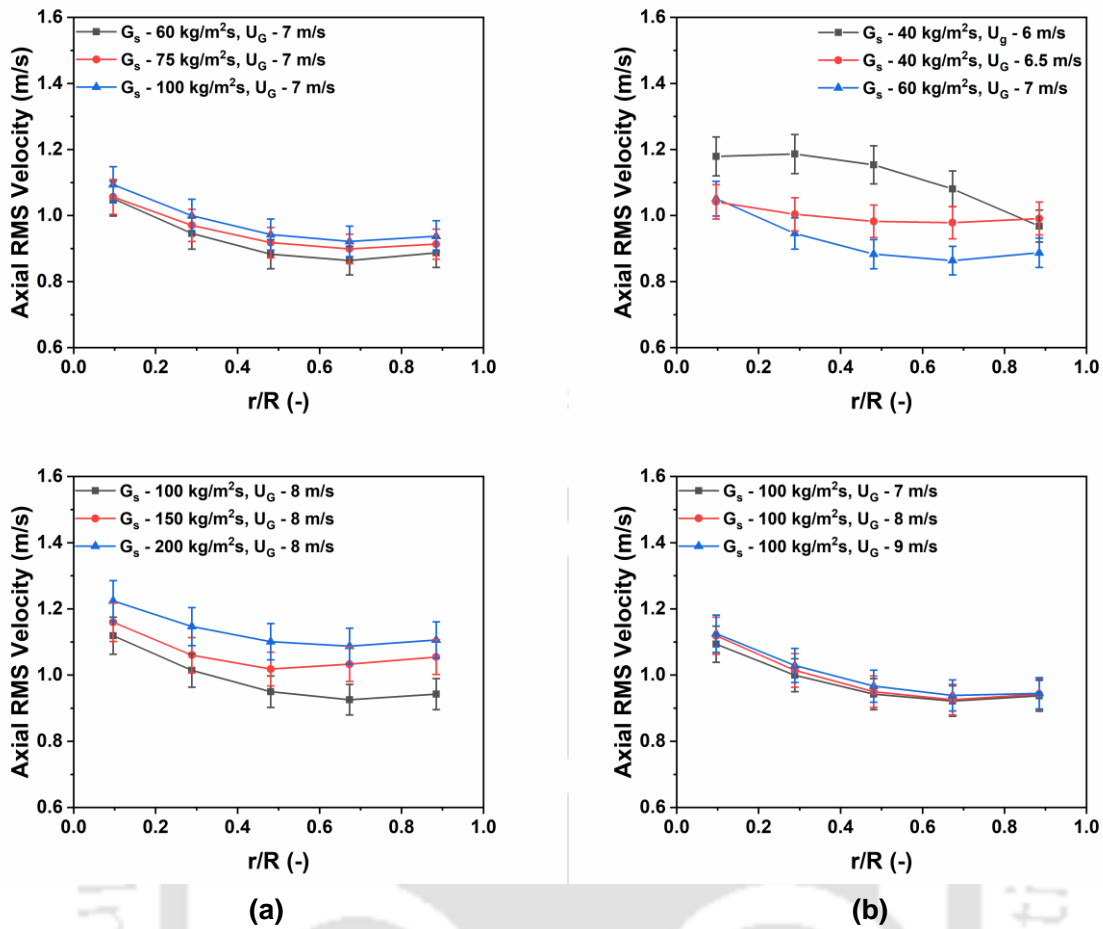


Figure 3.29: Radial variation of azimuthally averaged axial RMS velocity profile at the bottom section ($h = 0.2$ m) (a) effect of solid flux and (b) effect of inlet gas velocity

Figure 3.29(b) shows that the axial RMS velocity increment is a very minimal increase with the gas velocity at the solid flux of $100 \text{ kg/m}^2\text{s}$. However, a significant variation of axial RMS velocity can be observed at lower gas velocity at even similar solid flux. It can be observed from the tracer track and histogram diagram that velocity fluctuation and variation are much higher in the case of the gas velocity of 6 m/s and 6.5 m/s . Solid motion changes dramatically as gas velocity increases from 6 m/s to 6.5 m/s . It can be observed from the PDFs of instantaneous axial velocity data and as well mean axial velocity profiles. For the same reason, axial RMS velocity is also relatively high at 6 m/s . It is essential to note that the profile of axial RMS velocity for 6 m/s is different for other operating conditions. With

increase in gas velocity, solids mean velocity magnitude increases resulting in increased velocity fluctuation. In the case of an increase in solid flux, axial RMS velocity increases as a result of an increase in particle-particle interaction. However, for different solid fluxes at an inlet gas velocity of 8 m/s, the increase in axial RMS velocity is much smaller than the magnitude increase at inlet gas velocity of 7 m/s.

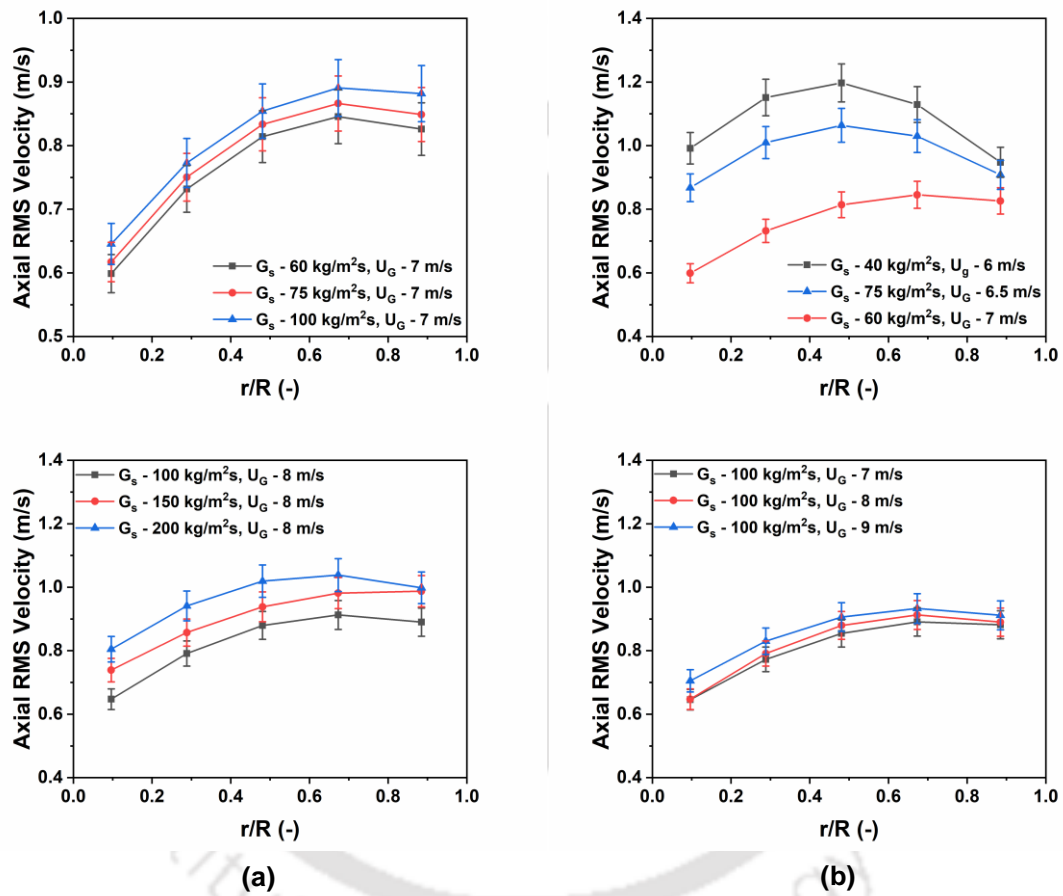


Figure 3.30: Radial variation of azimuthally averaged axial RMS velocity profile at the bottom section ($h = 0.4$ m) (a) effect of solid flux and (b) effect of inlet gas velocity

From Figures 3.30(a) and 3.30(b), it can be observed that the axial RMS velocity profile becomes comparatively much clear compared to axial RMS velocity profile at 0.2 m height. With the increase in solid flux axial RMS velocity increases and with increases because of high particle-particle collision. Though, with an increase in inlet gas velocity solid fraction

decreases while solid flux is constant axial RMS velocity increases due to increase in velocity magnitude.

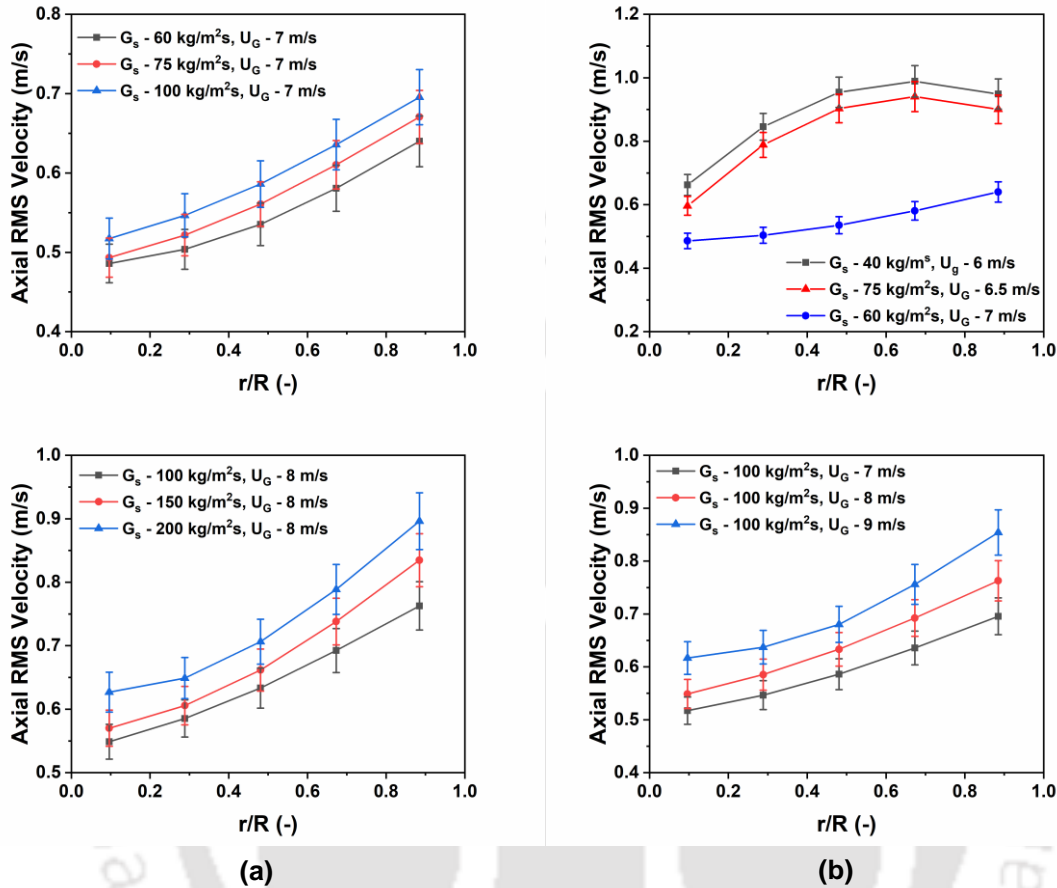


Figure 3.31: Radial variation of azimuthally averaged axial RMS velocity profile at the middle section ($h = 1.6$ m) (a) effect of solid flux and (b) effect of inlet gas velocity

Figure 3.31 shows a clearer trend than Figures 3.29 and 3.30. Increase in gas velocity, axial velocity increases while solid flux is constant. With increased solid flux at constant inlet gas velocity also increases axial RMS velocity. Bhusarapu et al. (2006) and Pantzali et al. (2013) also reported similar trend with respect to gas velocity and solid flux. However Godfroy et al. (1999) reported decrease in axial velocity fluctuation with increase in gas velocity. The magnitude of axial RMS velocity reported by Bhusarapu et al. (2005) is much higher than the current finding. With increasing riser diameter, particles get more space to

move freely, causing a higher degree of velocity fluctuation. Even with similar operating conditions in the pilot scale riser (Chapter 4) axial RMS velocity was much higher compared to the laboratory scale riser.

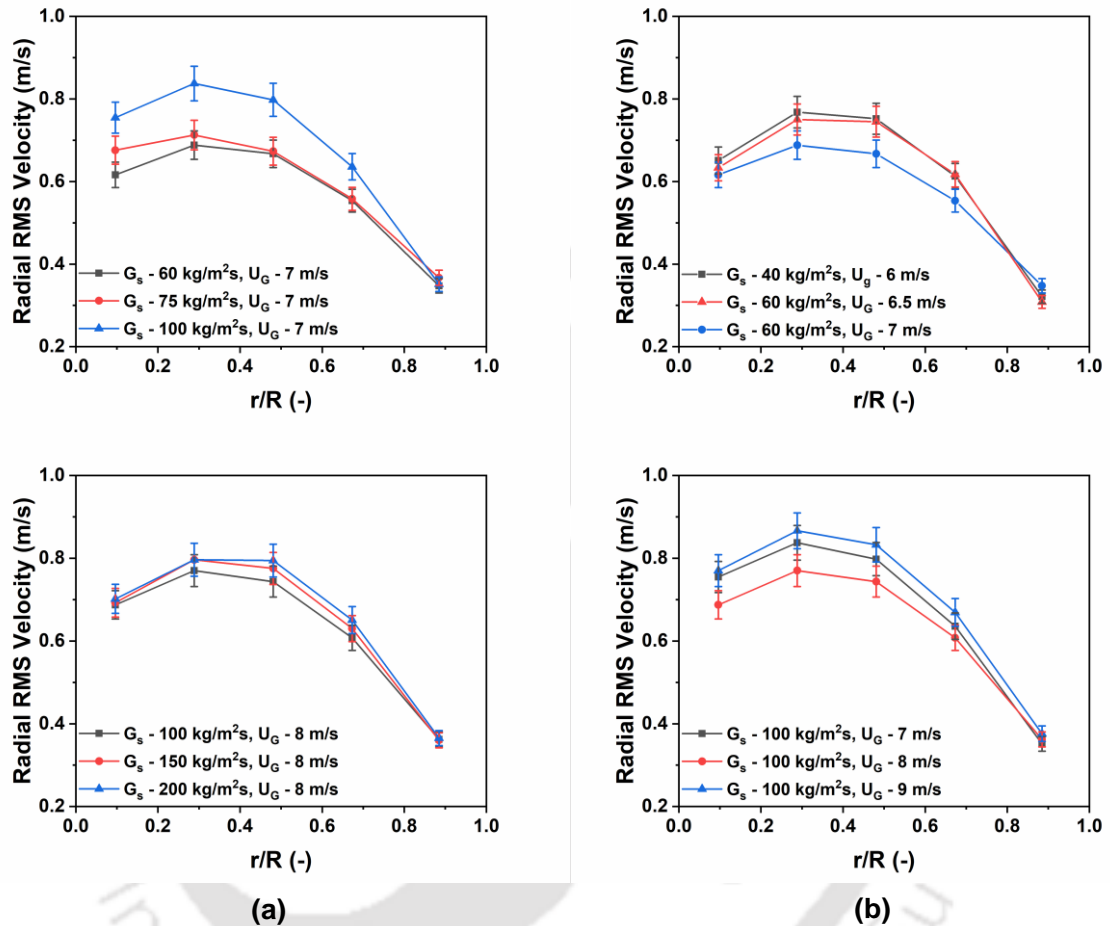


Figure 3.32: Radial variation of azimuthally averaged radial RMS velocity profile at the bottom section ($h = 0.2$ m) (a) effect of solid flux and (b) effect of inlet gas velocity

Figures 3.32, 3.33 and 3.34 show the radial velocity fluctuation or radial RMS velocity. Although mean radial velocity is minimal and negligible, radial RMS velocity is clearly observable. Radial RMS velocity is lower than axial velocity, irrespective of operating condition and height. Particles predominantly move upward, and the velocity magnitude is much higher in the axial direction. Radial movement of the particle is limited due to restricted geometry as the riser diameter is smaller. Also, the particle moves equally inward

and outward, which makes the mean radial velocity almost zero. However, radial RMS velocity is significant. As solid particles mostly move in an axial direction, instantaneous axial velocity is much higher than instantaneous radial velocity. as a result, radial RMS velocity is lower than axial RMS velocity.

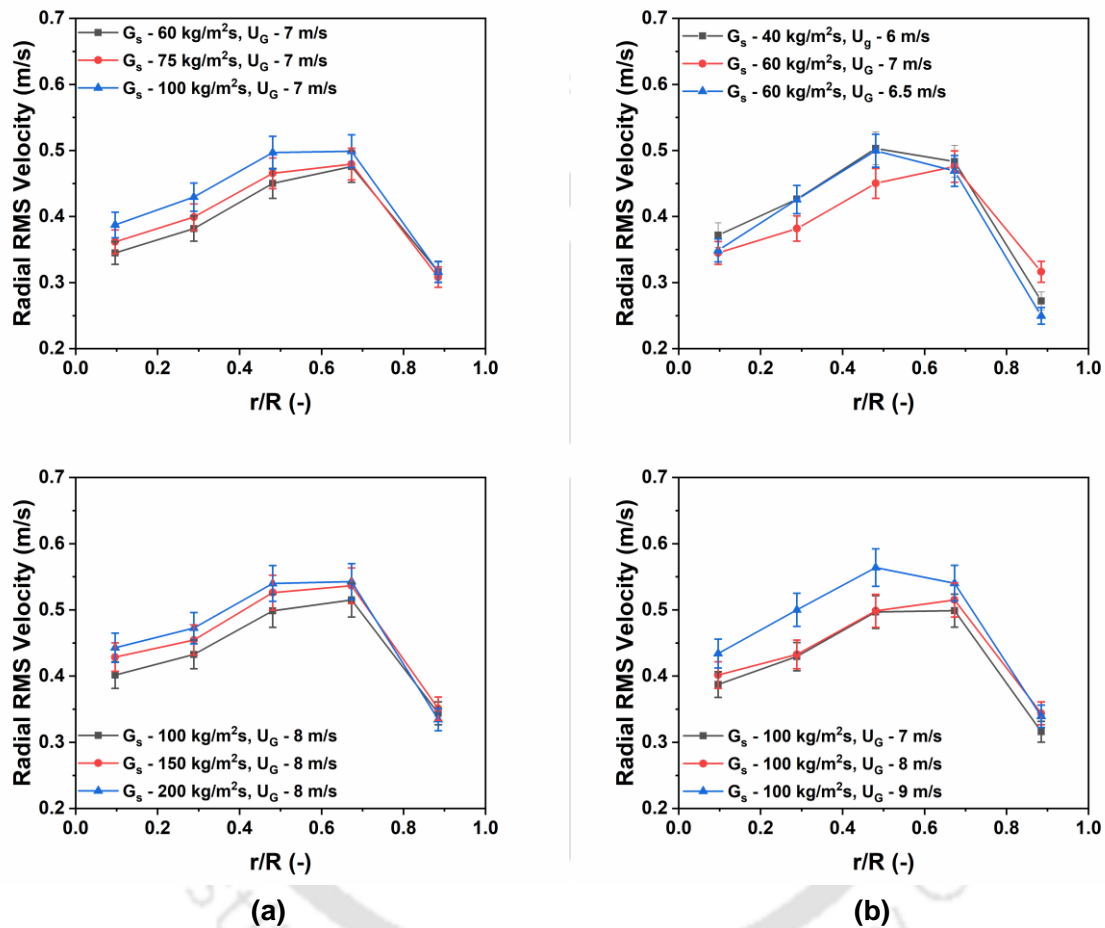


Figure 3.33: Radial variation of azimuthally averaged radial RMS velocity profile at the bottom section ($h = 0.4$ m) (a) effect of solid flux and (b) effect of inlet gas velocity

It can be observed from Figure 3.32a that with increasing solid flux maintaining the same gas velocity, radial RMS velocity increases. With the increase in solid flux, particle-particle collision increases, due to which radial RMS velocity increases. In the case of increasing inlet gas velocity (Figure 3.32(b)) at constant solid flux RMS velocity increases due to an increase in magnitude in velocity. Figures 3.33 and 3.34 also show similar phenomena in

relation to the effect of solid flux and inlet gas velocity. It can be observed clearly from Figure 3.32 that velocity fluctuations are much narrower in the laboratory scale riser compared to the larger diameter riser (Chapter 4).

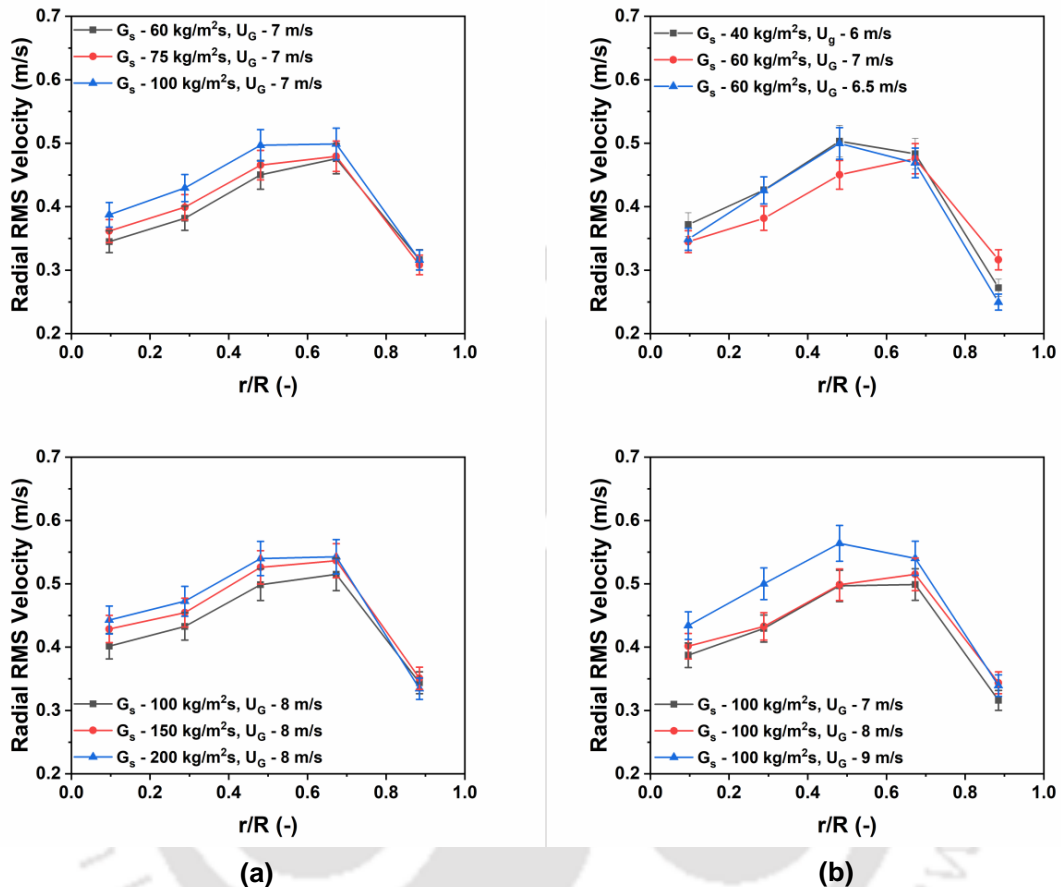


Figure 3.34: Radial variation of azimuthally averaged radial RMS velocity profile at the middle section ($h = 1.6$ m) (a) effect of solid flux and (b) effect of inlet gas velocity

3.5.6 Granular Temperature

Granular temperature is analogous to thermal temperature in the kinetic theory of granular flow. In thermodynamics, the temperature can be measured; it is proportional to the variance of the molecular velocity distribution. In the kinetic theory of granular flow, the granular temperature is proportional to the variance of the particle's velocity distribution. Granular temperature serves as a crucial indicator of particle mixing and segregation in

CFB risers. Higher granular temperatures indicate greater particle mixing, fostering uniform fluidization and heat transfer. Higher granular temperatures also indicate more effective particle collisions, improving heat transfer between the fluidizing gas and solid particles. This is particularly significant for processes like combustion or chemical reactions within the riser, where efficient heat transfer is vital for optimal performance. Granular temperature is crucial in CFB riser design, affecting fluidization behavior and heat transfer efficiency. Thus, understanding and controlling granular temperature is essential for achieving desired operating conditions and maximizing the efficiency of CFB processes.

Granular temperature cannot be measured directly like thermodynamic temperature. Granular temperature can be calculated by detailed measurement of the particle velocity experimentally or numerically (Goldhirsch, 2008). Granular temperature gives the idea of random oscillation of particles, which is the average of the variances of the instantaneous velocities' components of the particles. It defines as, particles dissipating energy due to inelastic collisions and drag between the fluid and particles. The granular temperature was first measured by Cody et al. (1996) in a bubbling fluidized bed using a vibration meter. Wildman and Huntley (2000) used a video camera to estimate the granular temperature in a binary fluidized bed. Tartan and Gidaspow (2004) and Jung et al. (2005) presented a detailed measurement technique to estimate the granular temperature using CCD camera. They measured instantaneous velocity with the help of CCD camera and then calculated granular temperature. In current work, detailed solid velocity measurement is done with the help of radioactive particle tracking. From the detailed velocity flow filed, the granular temperature is calculated. The same equation is used in the current work presented by Tartan and Gidaspow (2004). Detailed granular temperature estimation methods from the radioactive particle technique can be found in the literature (Kalo et al., 2020, 2019b).

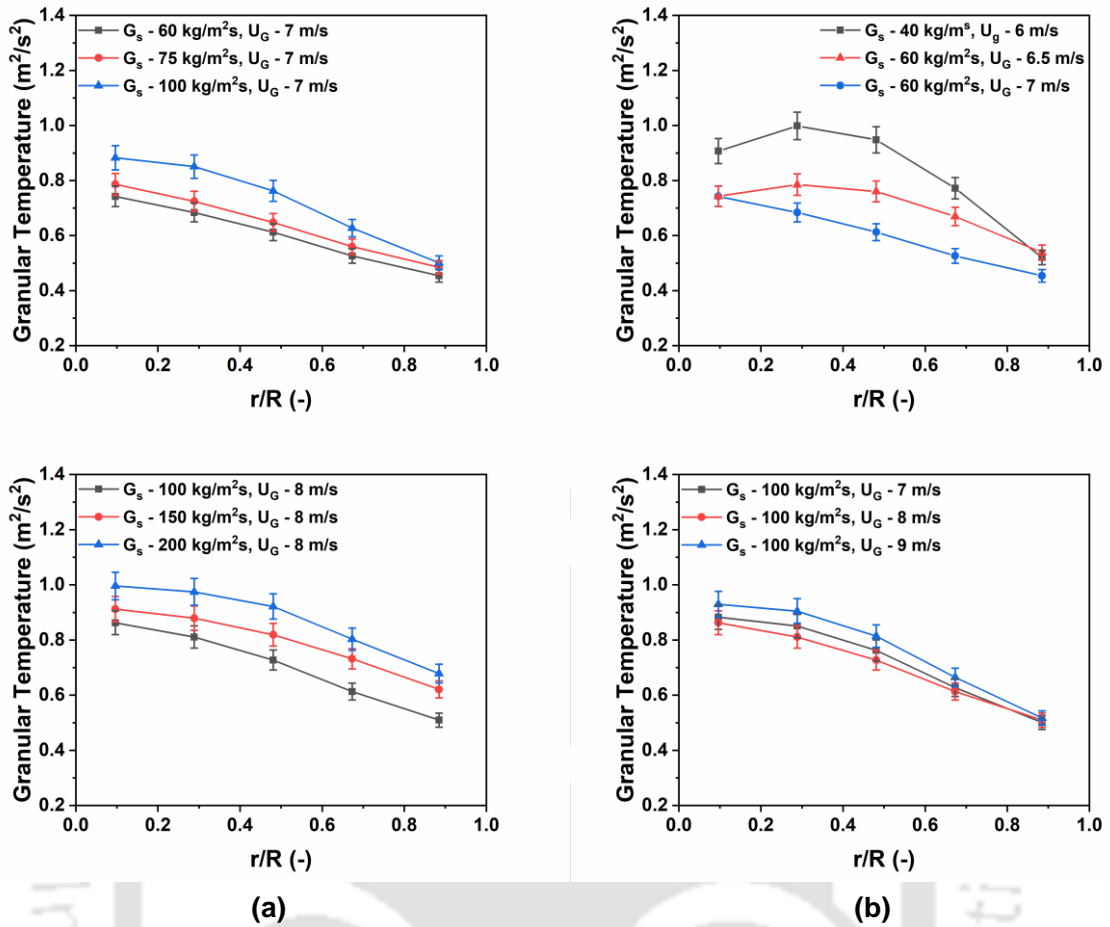


Figure 3.35: Radial variation of azimuthally averaged granular temperature profile at the bottom section ($h = 0.2$ m) (a) effect of solid flux and (b) effect of inlet gas velocity

The radial profile of granular temperature is presented in Figures 3.35, 3.36 and 3.37 for a riser height of 0.2 m, 0.40 m at the bottom section, and 1.6 m at the middle section. It is clearly visible that the granular temperature decreases with height. In the case of axial and radial RMS velocities, the axial RMS velocities also decrease with height. As the granular temperature is calculated from RMS velocity components, it shows similar trends with increasing height. At the bottom section, the solid fraction is higher, and with increasing height, the solid fraction decreases. Due to higher particle-particle collisions at the bottom section of the riser, granular temperatures are higher compared to the middle section. A

similar observation was reported by Pantzali et al. (2015) with Geldart Group A particles in a riser in a dilute phase condition.

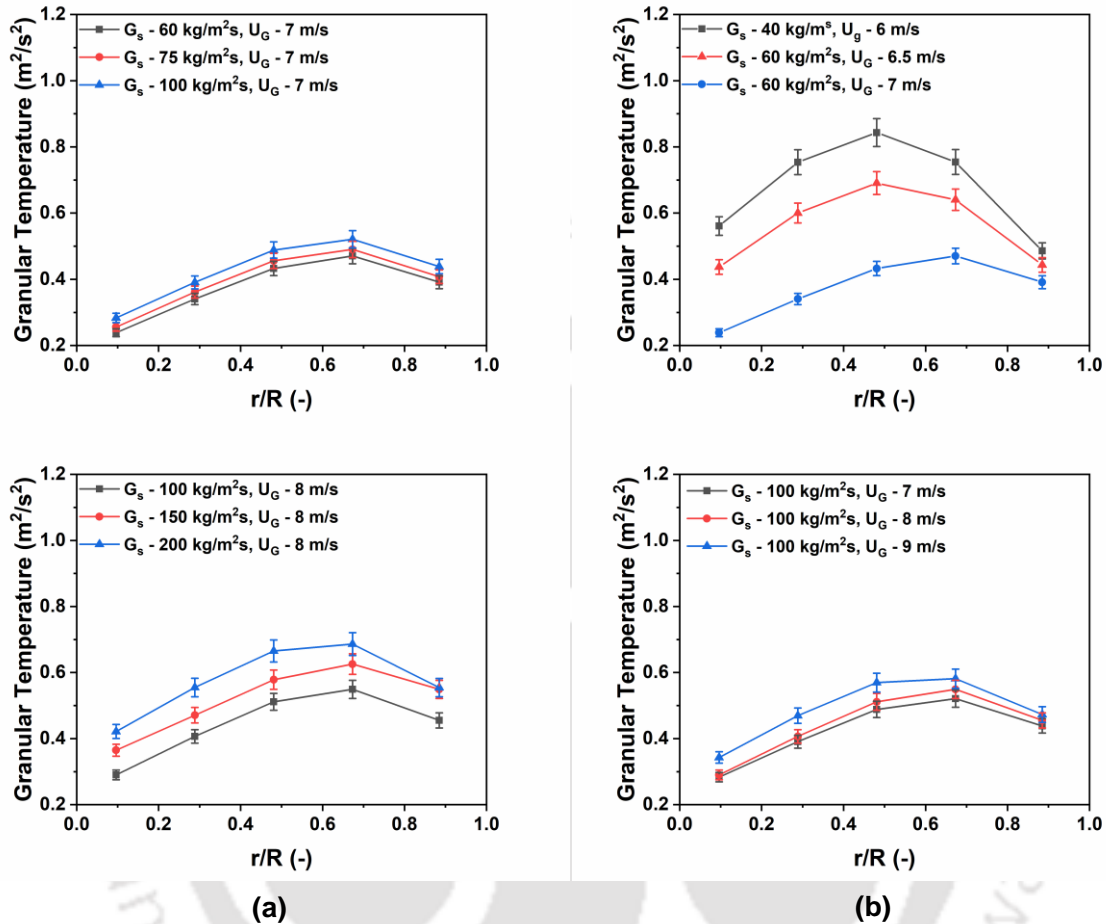
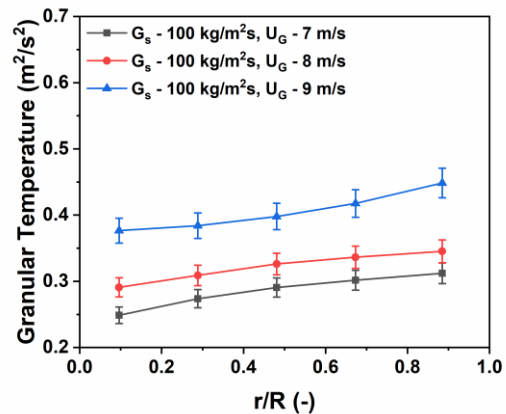
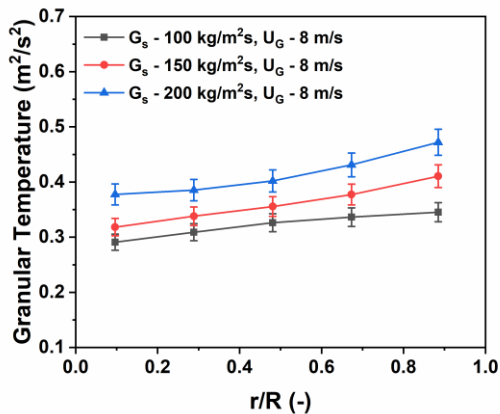
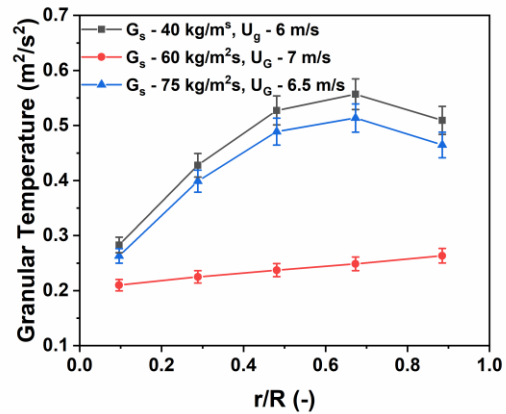
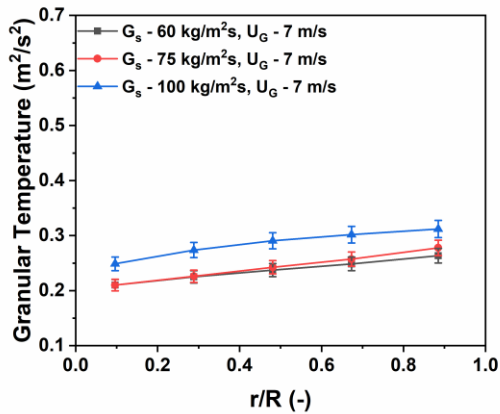


Figure 3.36: Radial variation of azimuthally averaged granular temperature profile at the bottom section ($h = 0.4$ m) (a) effect of solid flux and (b) effect of inlet gas velocity

Figure 3.35 shows that the granular temperature is higher at the center and decreases toward the wall. It is just above the solid inlet, and the mean velocity profile at the center of the column is higher compared to the wall. Because of the higher solid velocity at the center of the column, the granular temperature is higher at the center. It is clearly visible that with the increase in gas velocity, the solid granular temperature is also increasing. However, at lower gas velocities (6 m/s and 6.5 m/s), the trend is different. As discussed in the instantaneous position track and instantaneous velocity PDF sections, solid particles have

internal recirculation at gas velocities of 6 or 6.5 m/s. When solid particles recirculate internally, certain ones descend and others ascend in the riser. The interaction between particles moving upward and those moving downward is markedly more intense than that between particles solely moving upward. Such intense interaction causes high velocity flocculation and a higher granular temperature.

The radial variation in granular temperature profiles changes with the height. Figure 3.36 shows that the granular temperature is at the center and increases toward the annular region. It is a well-established phenomenon for the riser to have a higher solid fraction in the annular and wall region. Due to the increase in inter-particle collision, the granular temperature is higher toward the wall. However, next to the wall region, a dip in granular temperature can be observed. From Figure 3.24, it is visible that the axial velocity next to the wall is very low. Due to the low velocity near the wall at a height of 0.4 m, the magnitude of the granular temperature is also low. It is clearly visible from Figure 3.36(a) that with an increase in solid flux, granular temperature increases as higher solid flux causes partial interference. Similarly, in the case of increasing inlet velocity (Figure 3.36(b)), granular temperature increases due to a higher magnitude of solid velocity. However, at lower gas velocities (6 and 6.5 m/s), granular temperature increases with decreasing gas velocity due to the intense interaction between falling particles and particles moving upward.



(a)

(b)

Figure 3.37: Radial variation of azimuthally averaged granular temperature profile at the middle section ($h = 1.6$ m) (a) effect of solid flux and (b) effect of inlet gas velocity

Figure 3.37 shows the Granular temperature profile of the fully developed middle section of the riser. It is clearly visible that with the increase of solid flux granular temperature increases. The increment is clearly visible compared to the bottom section of the riser. With the increase in inlet gas velocity, the granular temperature also increases. Although the effect of solid flux and gas velocity is similar to the larger diameter riser reported in Chapter 4, the radial profile is not the same. Bhusarapu, (2005) reported a similar quantity in terms of turbulent kinetic energy, which is way higher than the current finding. In current work, granular temperature is lower at the center and highest near the wall. In larger diameter riser, the granular temperature is highest at the core annular region. This difference is

mostly related to the mean velocity profile. In a smaller diameter riser, the mean velocity profile is flat compared to the larger diameter riser. Thus, the mean velocity near the wall is quite high compared to the larger diameter riser, unlike the larger diameter riser.

3.5.7 Solid Stress

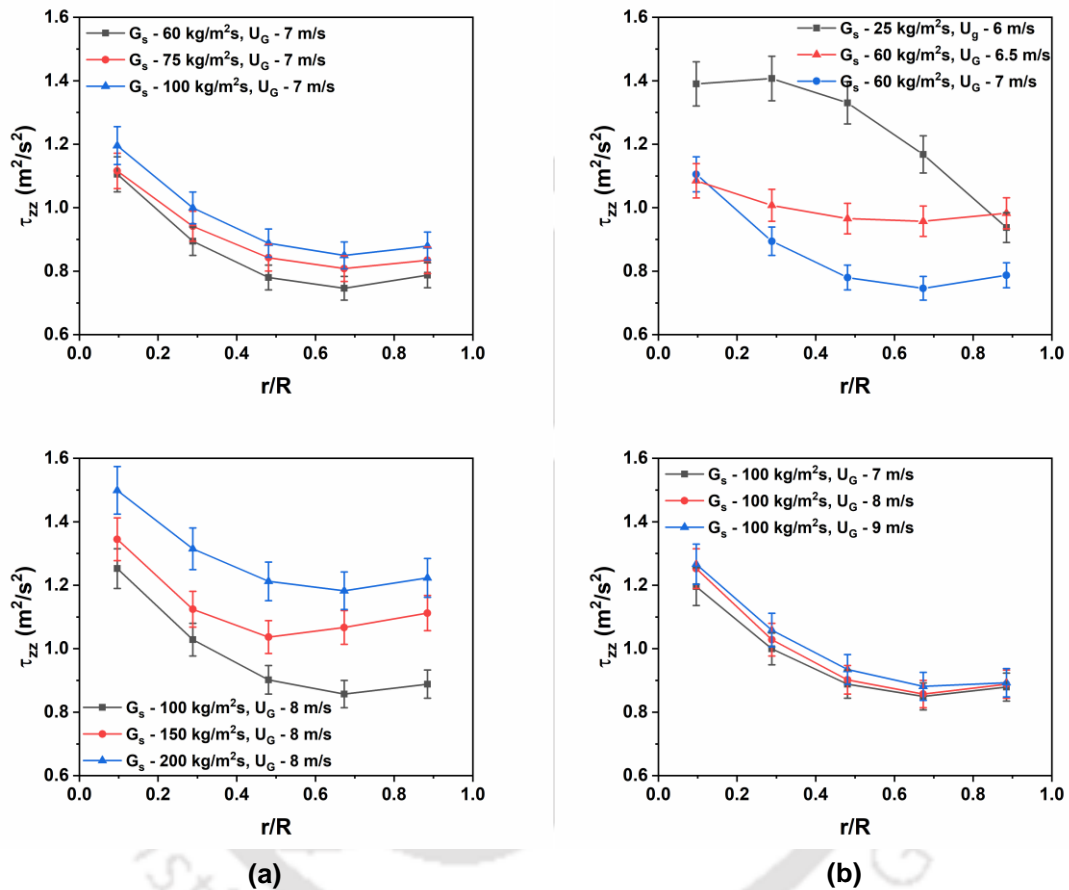


Figure 3.38: Radial variation of azimuthally averaged normal stress profile at the bottom section ($h = 0.2 \text{ m}$) (a) effect of solid flux and (b) effect of inlet gas velocity

Solid stress refers to the mechanical forces exerted by the solid particles on each other and on the walls of the container or reactor. Solid normal stress in a fluidized bed refers to the force that solid particles exert on the reactor vessel walls or on neighboring particles within the bed, acting perpendicular to their surfaces. This stress is governed by various factors, including particle weight, hydrodynamic interactions, and bed structure. Solid shear stress

arises from the sliding motion of solid particles past each other. This can occur during particle rearrangement, mixing, or due to the drag forces exerted by the fluidizing gas.

Figures 3.38, 3.39 and 3.40 show the azimuthally averaged solid phase axial normal stress with height for different solid flux and gas velocities at the heights of 0.2 m, 0.4 m, and 1.6 m, respectively for the bottom section and middle section of the riser. Figures 3.41, 3.42 and 3.43 show the azimuthally averaged axial solid phase shear stress with height for different solid flux and gas velocities at the heights of 0.2 m, 0.4 m, and 1.6 m, respectively, for the bottom section and middle section of the riser. Fluctuating velocity variances in both axial and radial directions are derived from instantaneous velocity measurements. These variances, often referred to as RMS velocity, are essential for computing normal and shear stress. Tartan and Gidaspow (2004) conducted a study measuring shear and normal stress based on the fluctuating velocity with the help of CCD camera. by Pantzali et al. (2015, 2013) and Bhusarapu et al. (2006) used a similar approach to stress calculations from velocity fluctuations.

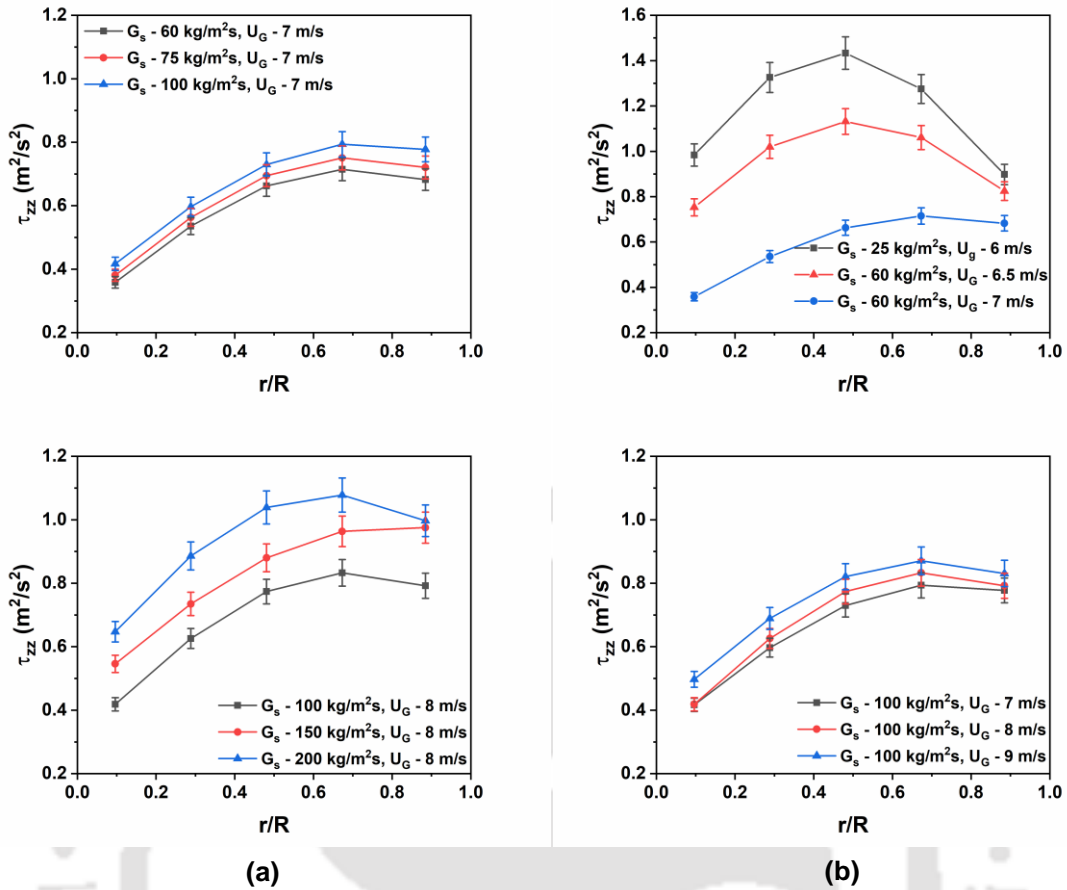


Figure 3.39: Radial variation of azimuthally averaged normal stress profile at the bottom section ($h = 0.4$ m) (a) effect of solid flux and (b) effect of inlet gas velocity

It can be observed from Figures 3.38–3.43 that the axial normal stress is higher than the shear stress for all the cases in the bottom section. Similar observations may also be obtained in the middle region. The axial normal stress is lower in the core region at a height of 0.2 m. As height increases, the stress within the core decreases significantly, while changes in stress near the wall region are minimal. In the middle section, normal stress is lower than in the bottom section as particle-particle interaction is much higher at the bottom section compared to the middle section. The core of the riser has lower normal stress compared to the wall section. It can be observed that lower gas velocities of 6 and 6.5 m/s have much higher normal stress compared to higher gas velocities. It is apparent from the PDF diagrams of instantaneous velocities and RTD measurements presented in subsequent

sections of this chapter that the back mixing exhibits a significant increase when the inlet gas velocities are 6 and 6.5 m/s. It causes increased normal stress when gas velocities are low.

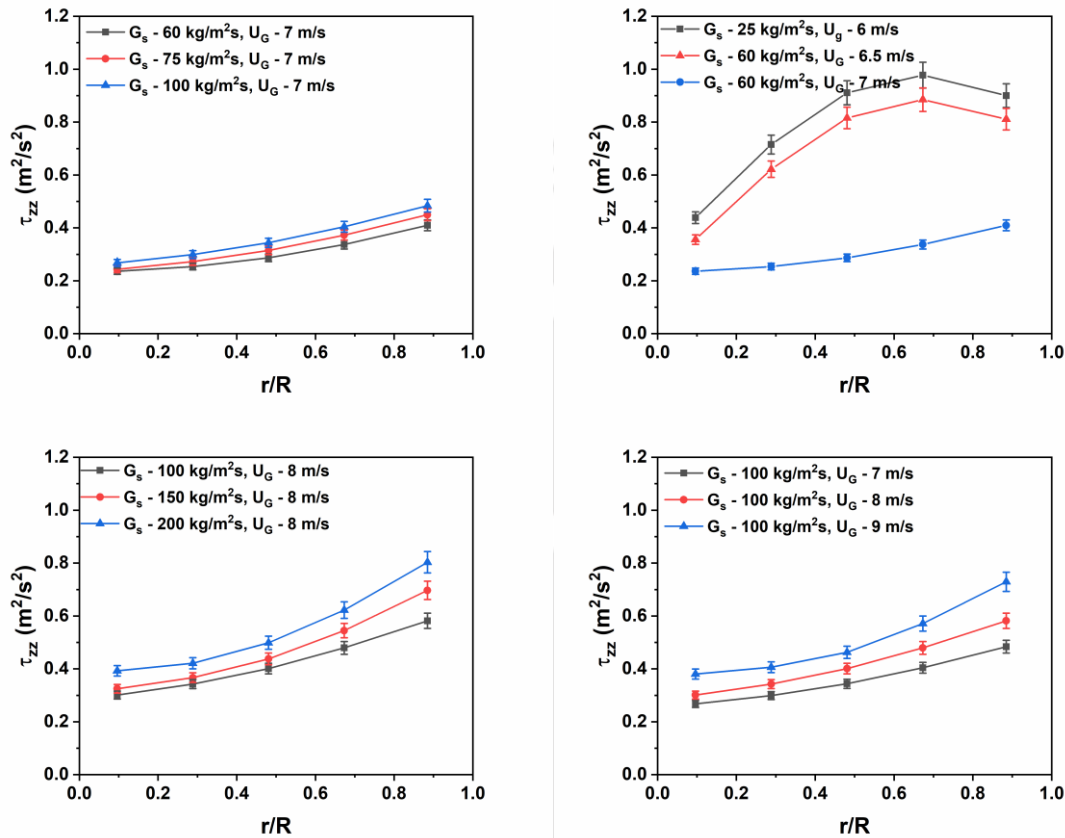


Figure 3.40: Radial variation of azimuthally averaged normal stress profile at the middle section ($h = 1.6$ m) (a) effect of solid flux and (b) effect of inlet gas velocity

The solid shear stress is the force per unit area that acts tangentially on the solid particles as they move relative to each other within the bed. It results from the frictional interaction between neighboring particles and the drag force exerted by the gas on the particles. Figures 3.41, 3.42 and 3.43 show the solid shear stress profile at 0.2, 0.4 and 1.6 m. It can be observed that the profile is different from a normal stress profile. Shear stress decreases with weight. At the height of 0.2 m, shear stress is higher at the center and reduces toward the wall. However, at the height of 0.4 m and 1.6 m, the shear stress value at the center is lower and increases towards the wall. It can also be observed that shear stress is higher than

normal at any height or radial position. Near the wall, the solid fluctuation reduces due to the hindrance created because of the wall and low gas velocity near the wall region. The value reported by Pantzali et al. (2015, 2013) and Tartan and Gidaspow (2004) is much lower compared to the value observed for the current set of experiments. Bhusarapu et al. (2006, 2005) reported a much higher value in magnitude for both normal and shear stress as in all the above cases, solid flux was very low and hence the fluctuation was higher.

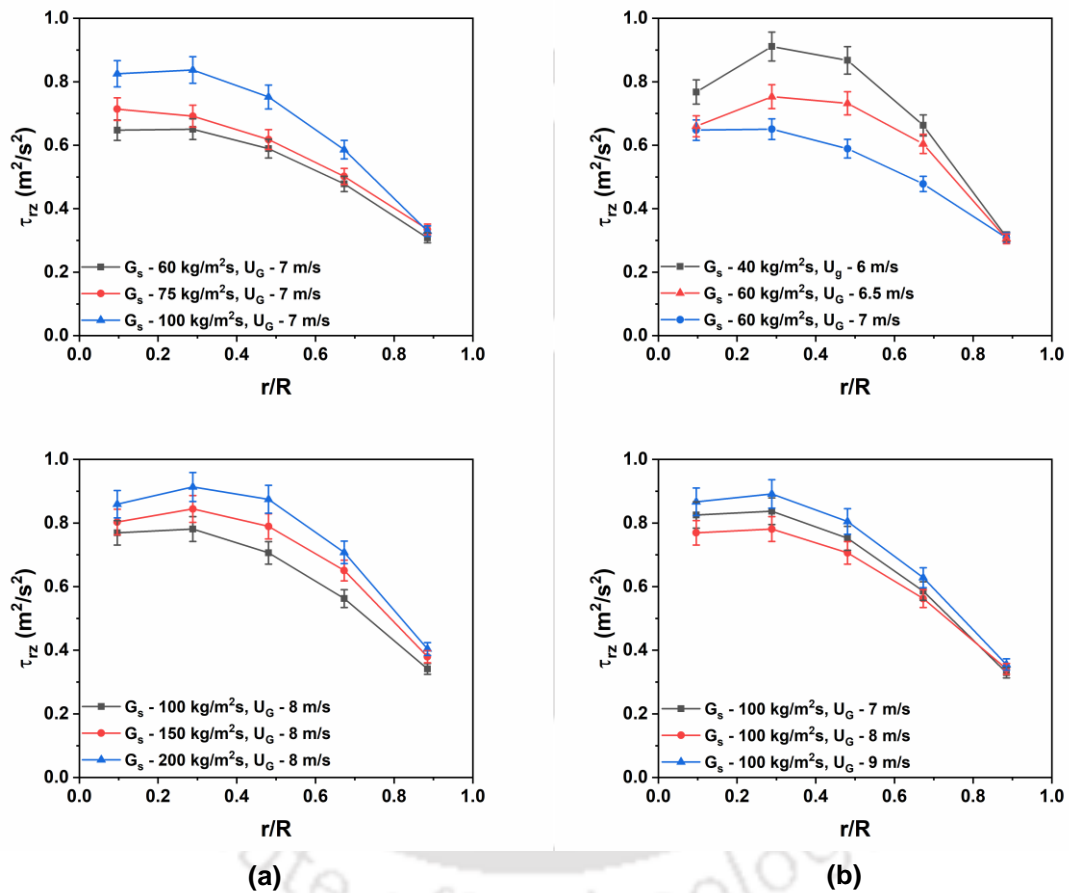


Figure 3.41: Radial variation of azimuthally averaged shear stress at the bottom section ($h = 0.2$ m) (a) effect of solid flux and (b) effect of inlet gas velocity

Figures 3.41(a), 3.42(a) and 3.43(a) illustrate the impact of solid flux on shear stress at heights of 0.2 m, 0.4 m and 1.6 m. It is apparent that an increase in solid flux at a constant gas velocity leads to a rise in shear stress. This increase in solid flux, while maintaining a constant gas velocity, results in a higher solid fraction. Consequently, there is an increase

in particle-particle collisions, thereby elevating the solid's shear stress. Figures 3.41(b), 3.42(b) and 3.43(b) illustrate the impact of gas velocity on shear stress. It is noteworthy to observe that at lower solid flux, higher gas velocity has lower shear stress, whereas at higher solid flux, the effect is different. At lower gas velocities (6 and 6.5 m/s), downward motion is significant; thus, it causes hindrance to solid movements, resulting in higher shear stress. However, at a solid flux of 60 kg/m²s and gas velocity of 7 m/s, the downward motion of solids is much less prominent compared to at gas velocities of 6 and 6.5 m/s. Thus, shear stress is less. However, with a solid flux of 100 kg/m²s, shear stress is higher at a gas velocity of 9 m/s compared to gas velocities of 7 and 8 m/s. Despite the decrease in particle collisions at higher gas velocities, the magnitude of mean velocity increases, leading to higher shear stress.

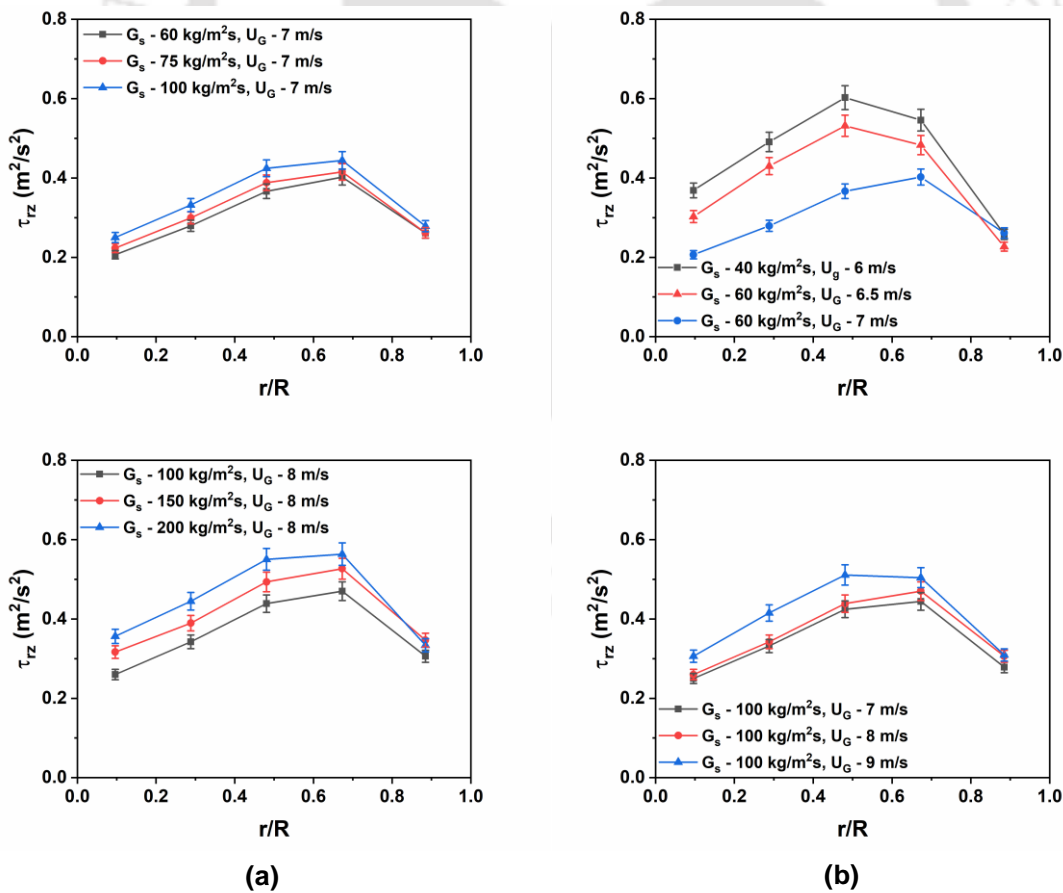


Figure 3.42: Radial variation of azimuthally averaged shear stress at the bottom section ($h = 0.4$ m) (a) effect of solid flux and (b) effect of inlet gas velocity.

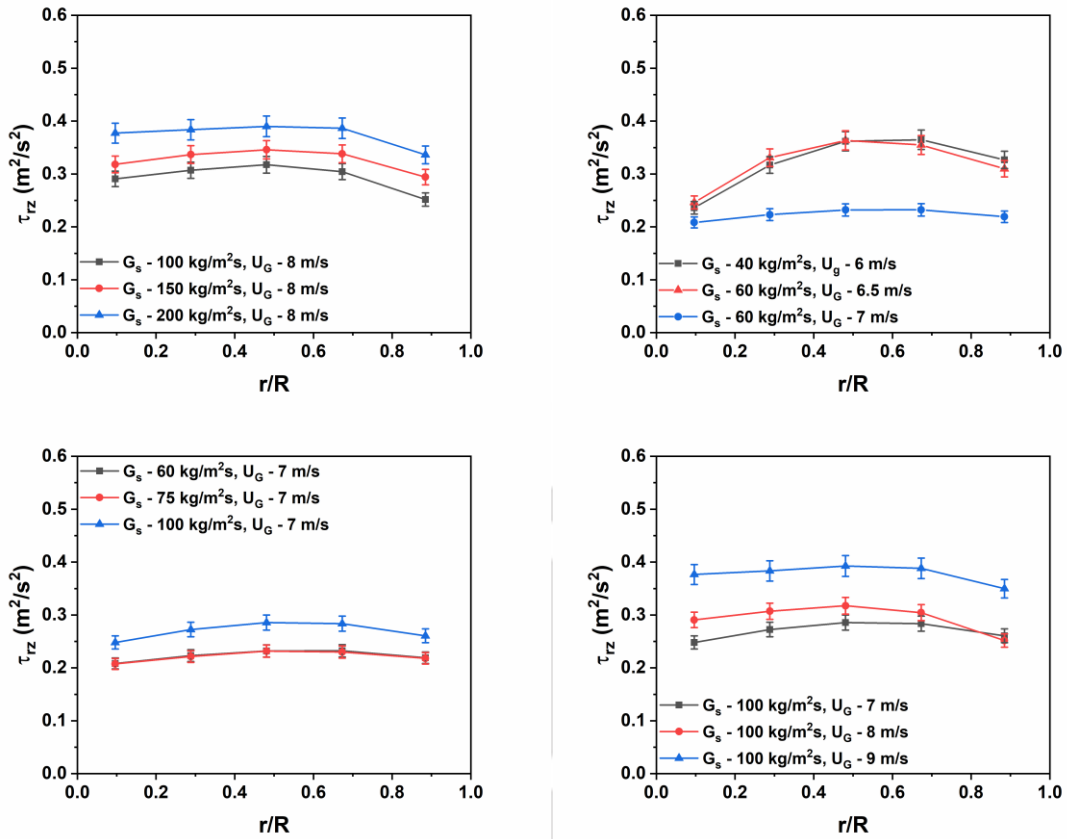


Figure 3.43: Radial variation of azimuthally averaged shear stress at the middle section ($h = 1.6$ m) (a) effect of solid flux and (b) effect of inlet gas velocity.

3.5.8 Turbulence Intensity

Figures 3.44, 3.45 and 3.46 show the radial profile of turbulent intensity at the bottom section (0.2 m and 0.4 m) and middle section (1.6 m). Axial and radial RMS velocity and granular temperature offer valuable insights into the complex nature of velocity fluctuation. However, it becomes clear from further analysis that it is highly dependent on gas velocity. Though the magnitude of turbulent fluctuations enables us to understand this dynamic interaction, it does not explicitly reveal the precise level of turbulence present in the system. Turbulence intensity gives us a complete representation of the degree of turbulence in the suspension by normalizing velocity fluctuation with respect to mean velocity. Turbulence intensity is higher near the wall and it decreases towards the center

irrespective of gas velocity and solid flux. Particle-particle interaction near the wall is higher due to the proximity of particles near the wall. At the same time, the mean velocity near the wall is lower. Due to substantial differences in velocity, turbulence intensity near the wall region is higher compared to the column center. A similar observation is reported by Pantzali et al. (2013) with Geldart Group A particles.

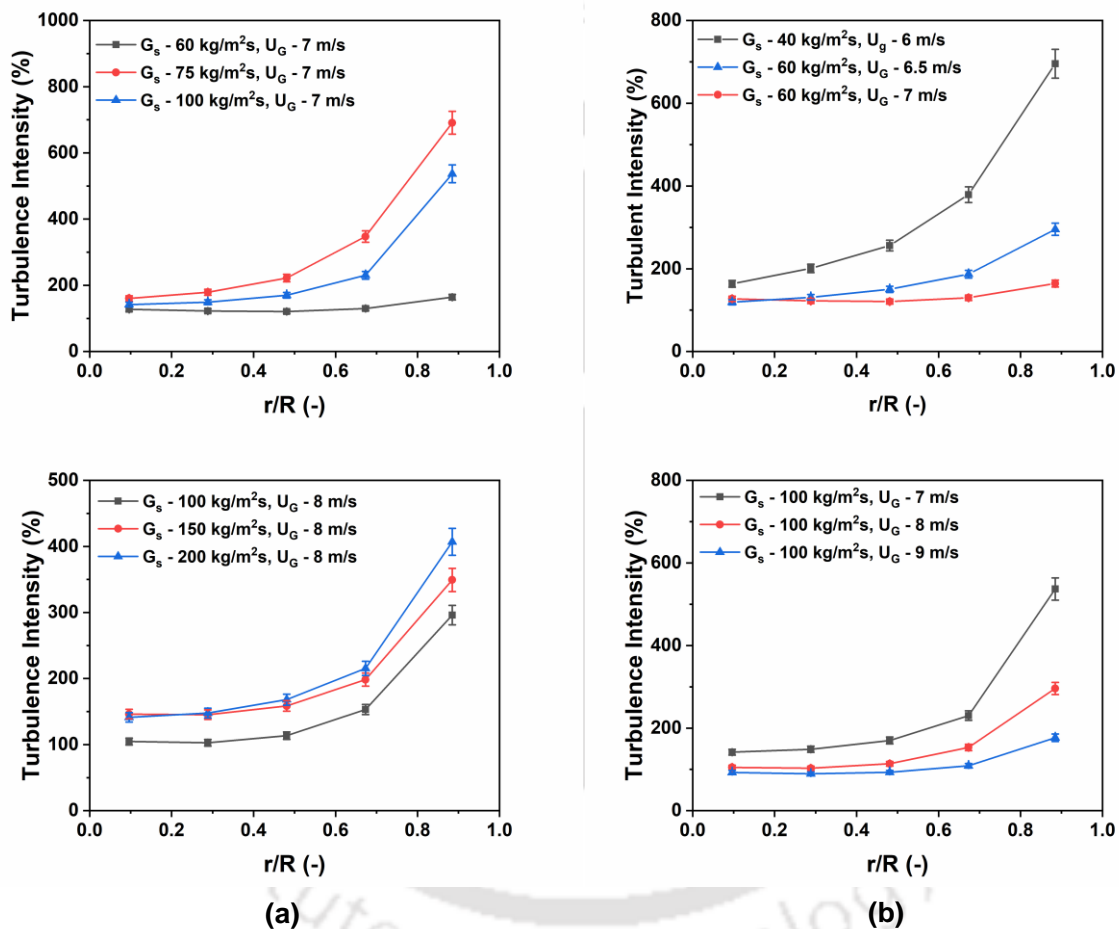


Figure 3.44: Radial variation of azimuthally averaged turbulence intensity at the bottom section ($h = 0.2$ m) (a) effect of solid flux and (b) effect of inlet gas velocity

Figure 3.44 depicts turbulence intensity at a height of 0.2 m of the riser. It is clear that turbulence intensity decreases with increasing gas velocity while maintaining the same solid flux. Although solid velocity flocculation increases with increasing gas velocity, the increment in mean axial velocity is much higher, which leads to lower turbulence intensity.

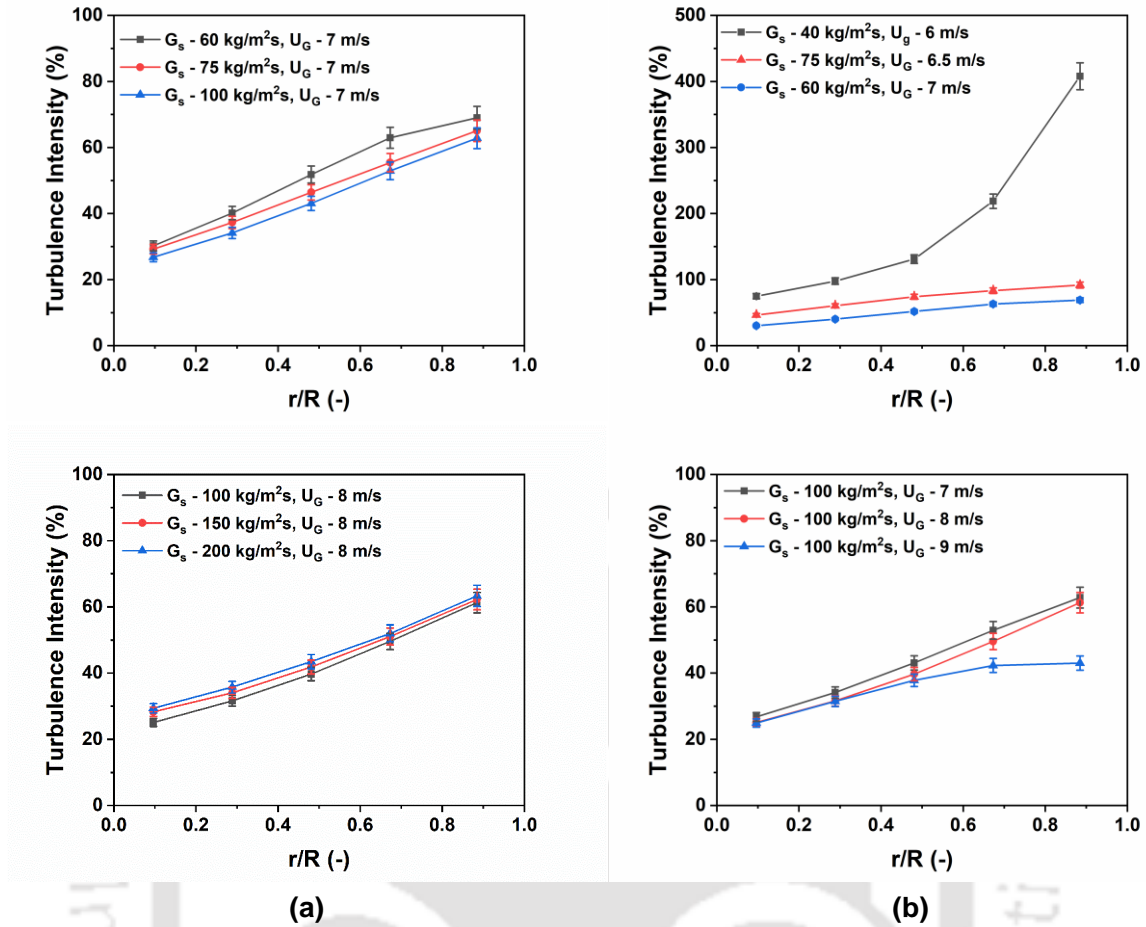


Figure 3.45: Radial variation of azimuthally averaged turbulence intensity at the bottom section ($h = 0.4$ m) (a) effect of solid flux and (b) effect of inlet gas velocity

Comparing Figures 3.44, 3.45 and 3.46, it can be observed that turbulence intensity decreases with increasing height. With increasing height, solid velocity fluctuations decrease and mean solid velocity increases, which leads to a decrease in turbulence intensity. Solid hold-up decreases with height and particle-particle interaction decreases at the same time.

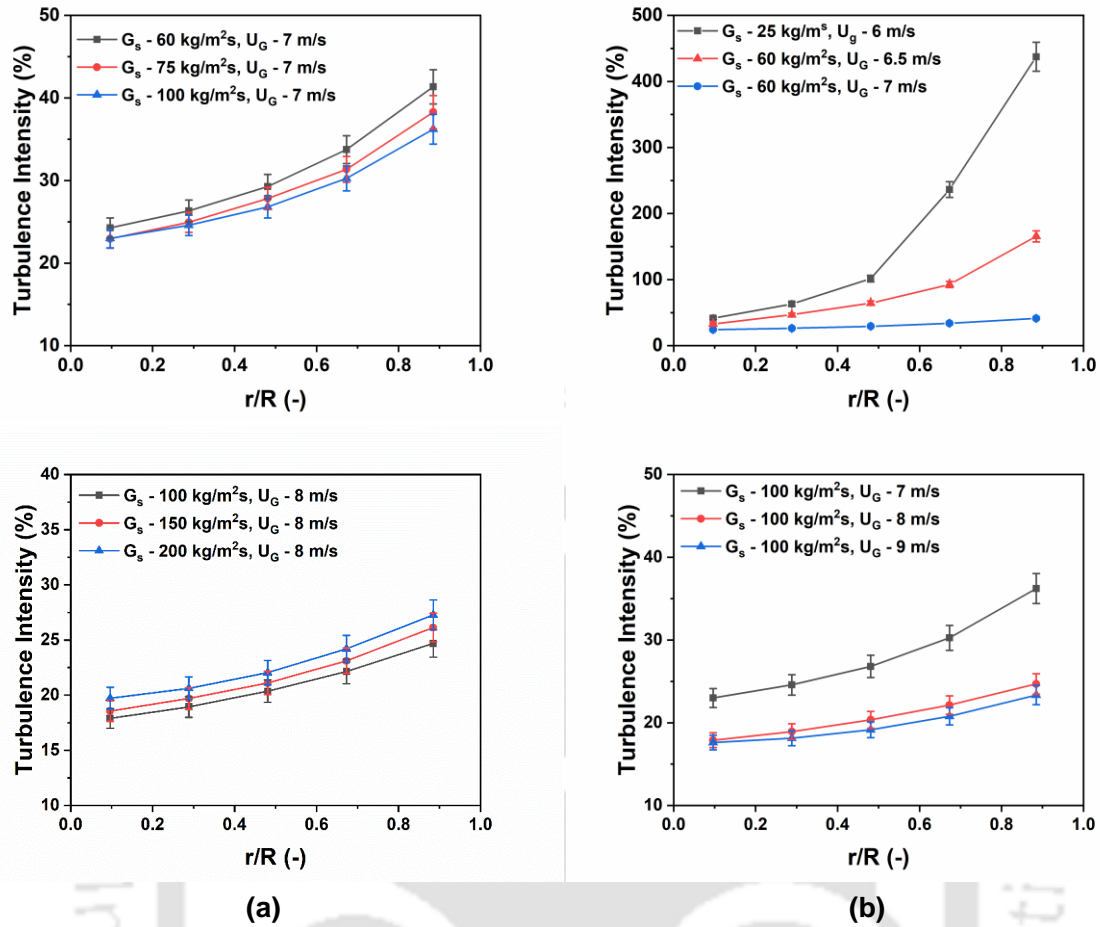
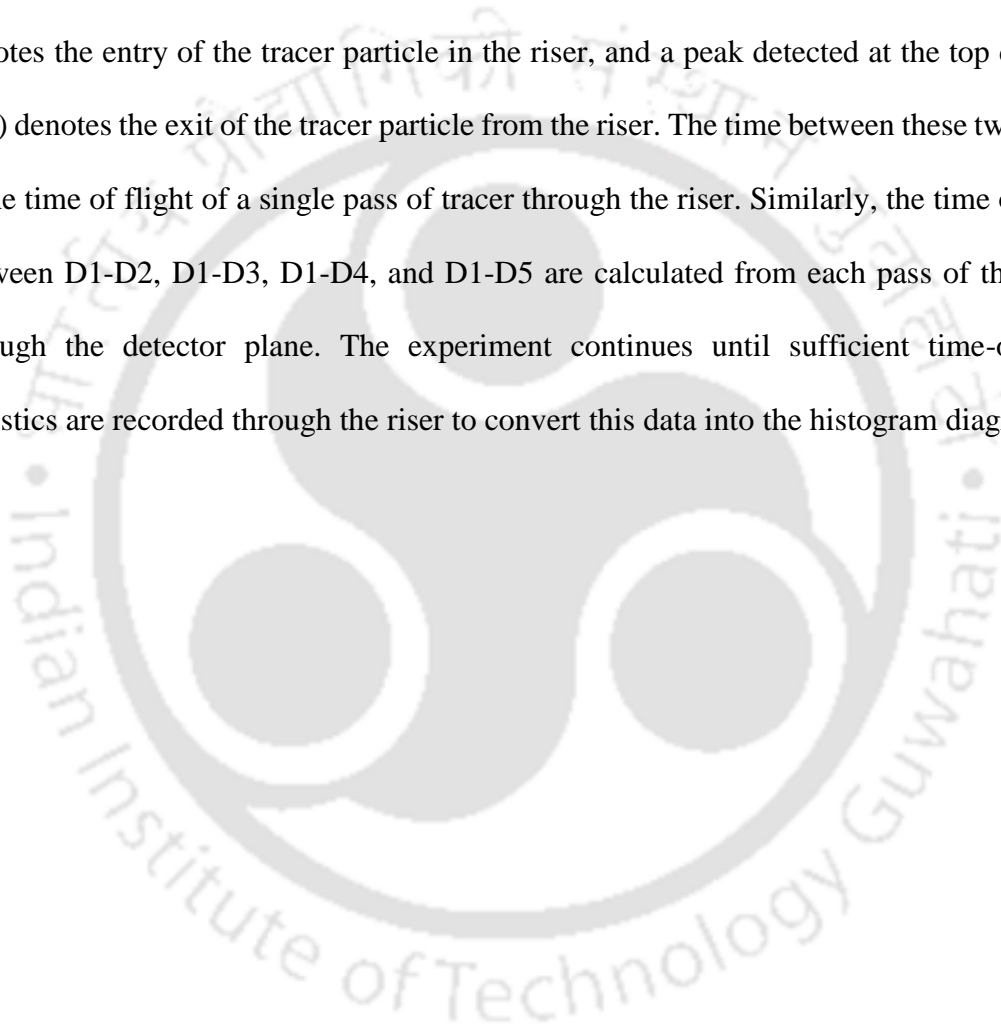


Figure 3.46: Radial variation of azimuthally averaged turbulence intensity at the middle section ($h = 1.6$ m) (a) effect of solid flux and (b) effect of inlet gas velocity

3.6 Solids Mixing in Laboratory Scale Setup

The RPT experiments at the bottom and middle section and RTD experiments at different zones are performed simultaneously. Experiments are performed at different operating conditions (gas inlet velocity and solid flux) to decipher the effect of gas inlet velocity and solid flux on mixing characteristics. Five detectors (D1–D5) are utilized for the RTD study, as depicted in Figure 3.47. The first detector (D1) is precisely placed at the solid inlet plane. As the tracer particle passes through the detector plane, it gives a sharp peak at the detector, as shown in Figure 3.48. The peak at detector D1 indicates the entry of the tracer particle in the riser section. The detectors are carefully arranged to measure the RTD with an

increasing riser height. D1-D2 are used for bottom section RTD measurements. Similarly, D1-D3, and D1-D4 are used for RTD measurement from the inlet to the start and end middle sections, respectively. D1-D5 are used to measure the overall RTD of the CFB riser. As only a single tracer particle is used in the current experiment, the count peak (intensity of radiation emitted by the tracer particle) recorded by the detector is unique and represents the presence of the tracer particle at the detector plane. For example, a peak detected at D1 denotes the entry of the tracer particle in the riser, and a peak detected at the top detector (D5) denotes the exit of the tracer particle from the riser. The time between these two peaks is the time of flight of a single pass of tracer through the riser. Similarly, the time of flight between D1-D2, D1-D3, D1-D4, and D1-D5 are calculated from each pass of the tracer through the detector plane. The experiment continues until sufficient time-of-flight statistics are recorded through the riser to convert this data into the histogram diagram.



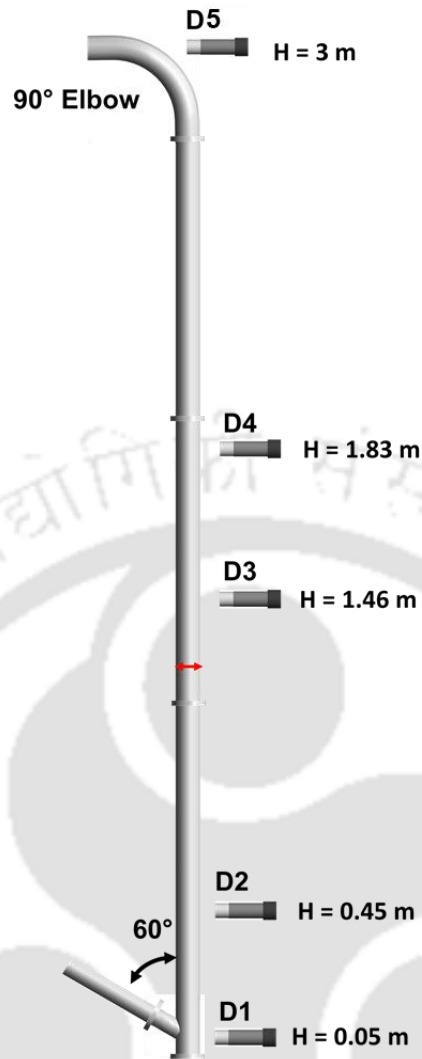


Figure 3.47: Detector arrangement for RTD experiment for laboratory scale riser

Although it appears the same, the residence time distribution curve is not directly represented in the time of flight histogram diagram from single-particle data. In principle, the RTD curve for a mass tracer is established, and data on concentration against time is shown. The area under the concentration vs. time curve is calculated by dividing the concentration data by the mass of the tracer, and the resulting E curve (exit age distribution or RTD curve) is obtained. The mass conservation of the tracer is essential for obtaining an RTD curve. In addition to this, the mass conservation of the tracer reveals when it is appropriate to end the experiment. In a single tracer time of flight experiment, however, mass conservation is not possible, so the histogram of time of flight cannot be used directly

as an RTD curve. In the single tracer RTD experiment, multiple tracer passes are recorded, which effectively represents the detection of a group of particles injected at the inlet, assuming the system is 'ergodic'. A histogram of multiple times of flights represents frequency vs. time (as shown in Figure 3.49a). This histogram diagram can be normalized by calculating the E curve from the area under the histogram curve (as shown in Figure 3.49 b), which corresponds to the E curve from the concentration profile. This normalized frequency curve is fitted by using the axial dispersion model (ADM), which is one of the most commonly used expression to model such bed, as shown in Figure 3.49 c. The value of the dispersion number, which fitted the experimental data well, is used to calculate the Peclet number and dispersion coefficient. A MATLAB code is written to obtain the optimized dispersion number for each histogram.

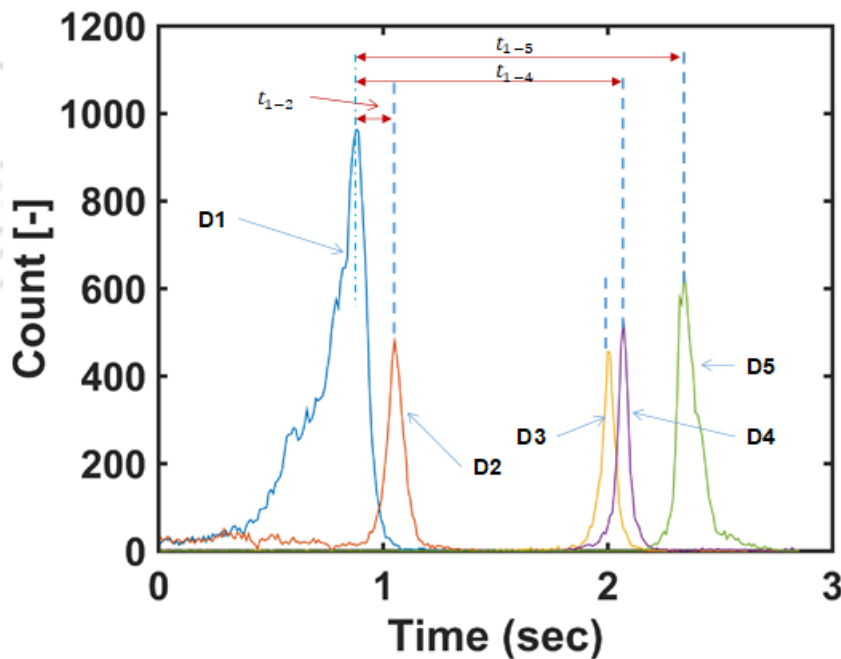


Figure 3.48: Count vs time data obtained at different detectors to find residence time of the particle in a particular zone

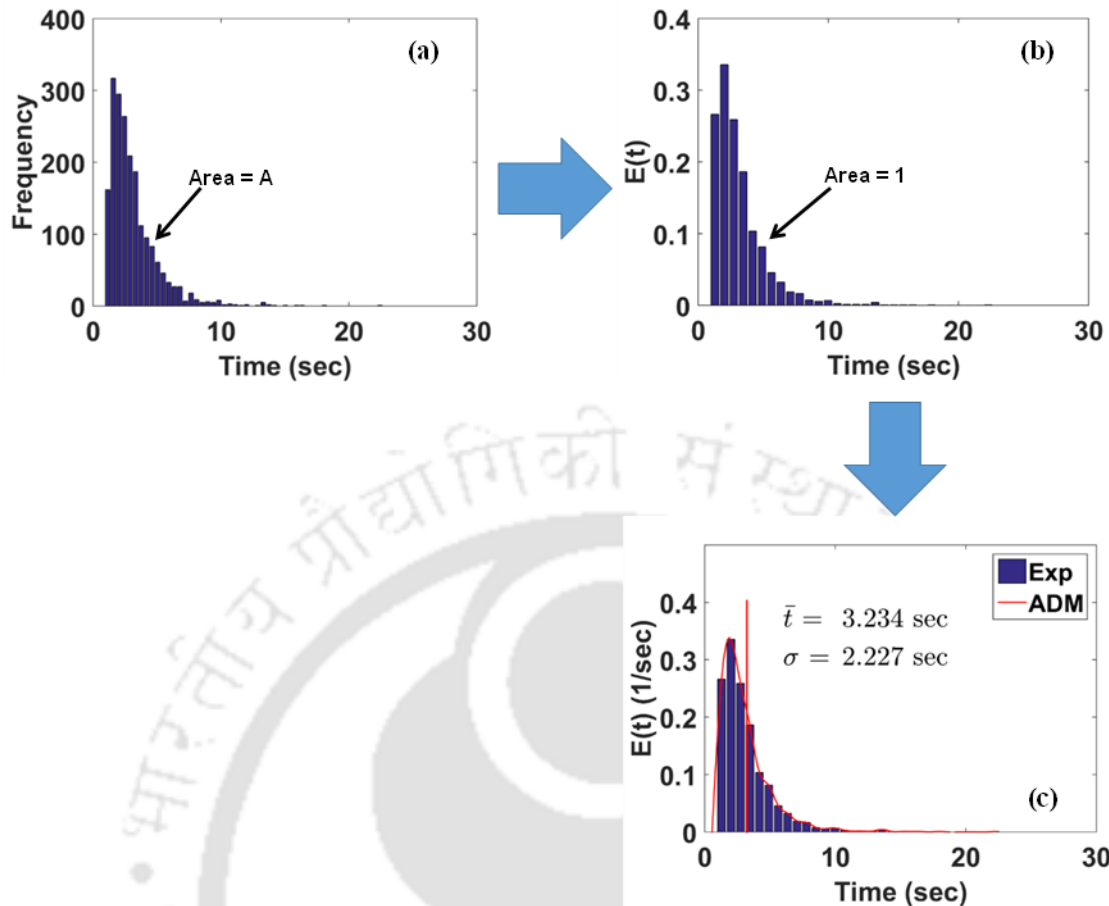


Figure 3.49: Flowchart to obtain the RTD curve from single particle tracking data: (a) histogram of time of flight, (b) normalized histogram and (c) E curve and Axial dispersion model fitting

3.6.1 Residence Time Distribution

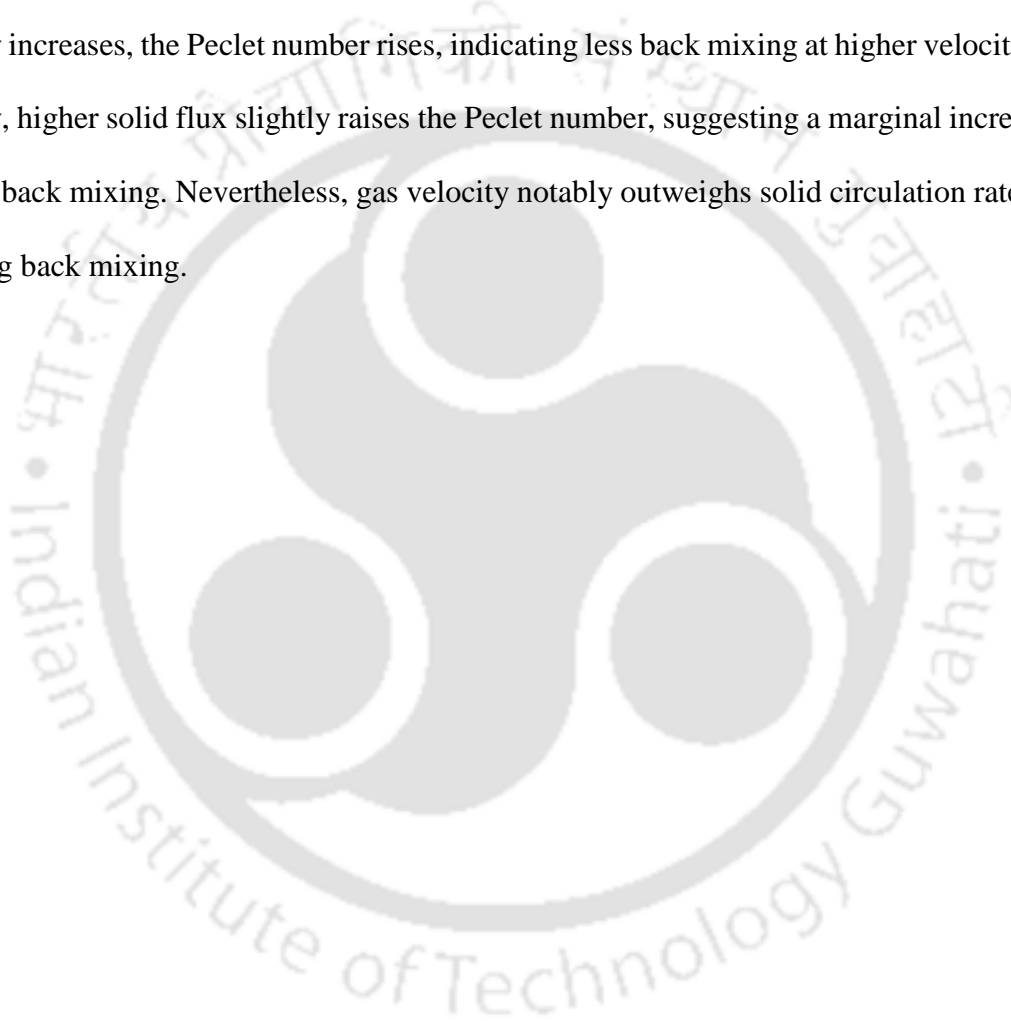
the probability distribution function (PDF) of the residence time of the tracer particle inside the riser at different sections for different operating conditions are presented in Figures 3.50, 3.51 and 3.52. D1-D2, which represents the bottom section of the riser, has a comparatively longer tail than other sections (D1-D3 and D1-D4 or D1-D5). It shows that the back mixing is higher at the bottom section of the column. Solids enter the riser through the solid inlet, a bottom section where the solid velocity is low and the solid fraction is high. Due to the high solid fraction, it behaves like a bubbling bed. Consequently, the level of back mixing in this area is notably higher compared to the other sections of the riser.

The solid's velocity increases as it rises in the riser. As a result, the velocity is slower at the bottom compared to the middle, causing a broader range of residence time in the lower section. In Figures 3.50, 3.51 and 3.52, the RTD distribution tracer labeled D1–D3 represents RTD from the inlet section to the start of the middle section. It is clear from the histogram diagram that with a higher mean residence time, the distribution is relatively lower than the bottom section. Similarly, D1–D4 represents the inlet section at the top of the middle section. In D1-D4 plots, it can be observed that the mean residence time is higher than in D1-D3, as expected, but the relative distribution is significantly lower. D1–D5 represents the solid RTD for the solid inlet–outlet section vs. the overall RTD.

It is evident that the RTD distribution is wider at lower gas velocities and narrows as gas velocities increase. It's interesting to note that the distribution is significantly wider at a gas velocity of 6 m/s (Figure 3.50) than it is at a higher gas velocity. It confirms previous findings from instantaneous position track plots about the internal recirculation of particles as observed in tracer track plots. With a gas velocity of 6.5 m/s, the mean RTD changes rapidly from a gas velocity of 6 m/s. At higher gas velocities of 7, 8, and 9 m/s, it is observed that the distribution was much narrower. RTD data for all the operating conditions are summarized in Table 3.2. With the increase in gas velocity, the mean residence time decreases, as expected. The Peclet number for each operating condition is calculated to analyze the mixing behavior. The Peclet number for an ideal mixed flow system tends to zero, and the Peclet number for a perfect plug flow system tends to infinity.

The results indicate that, in all conditions, the Peclet number is lower at the bottom and rises with height. This suggests that regardless of the operating condition, back mixing is consistently more pronounced in the bottom section. However, these values are significantly greater than zero. Hence, even though back mixing is observed at the bottom section, it does not behave like a mixed flow reactor. With increasing height, the Peclet

number increases, and flow patterns trend toward plug flow reactors. It also indicates that the back mixing decreases with increasing height. Despite the fact that no reactor is ideal for plug flow, reactors are considered near plug flow when the Peclet number (Wei and Zhu, 1996) height is more significant than 100. In the current work, the Peclet Number is higher than 100. For a gas velocity of 9 m/s, the Peclet number of the overall reactor is more than 50. At a gas velocity of 9 m/s, the reactor's Peclet number exceeds 50. As gas velocity increases, the Peclet number rises, indicating less back mixing at higher velocities. Notably, higher solid flux slightly raises the Peclet number, suggesting a marginal increase in solid back mixing. Nevertheless, gas velocity notably outweighs solid circulation rate in affecting back mixing.



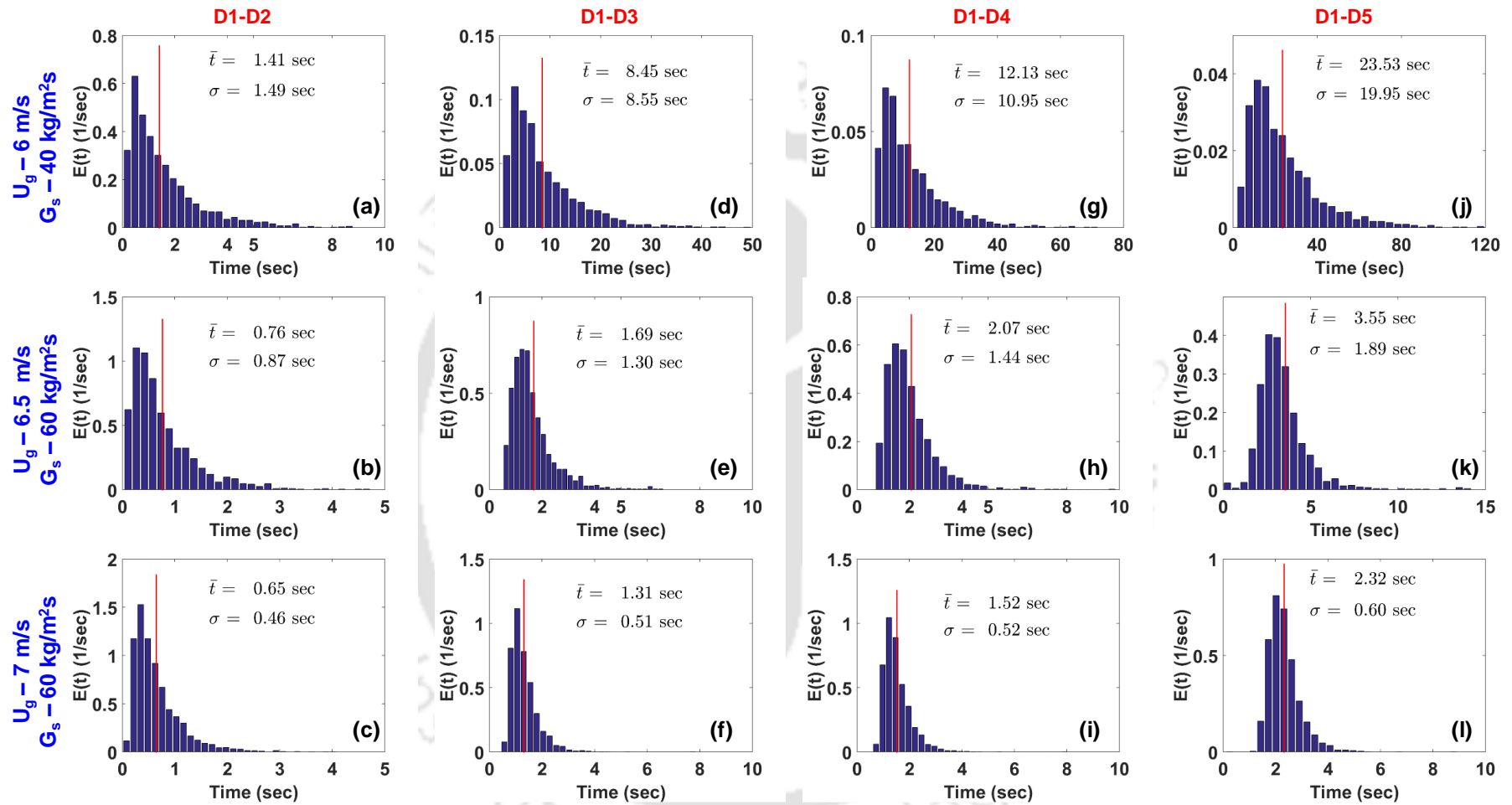


Figure 3.50: RTD for (a,b,c) inlet section, (d,e,f) inlet to the middle section, (g,h,i) inlet to end of the middle section and (j,k,l) overall section of the riser

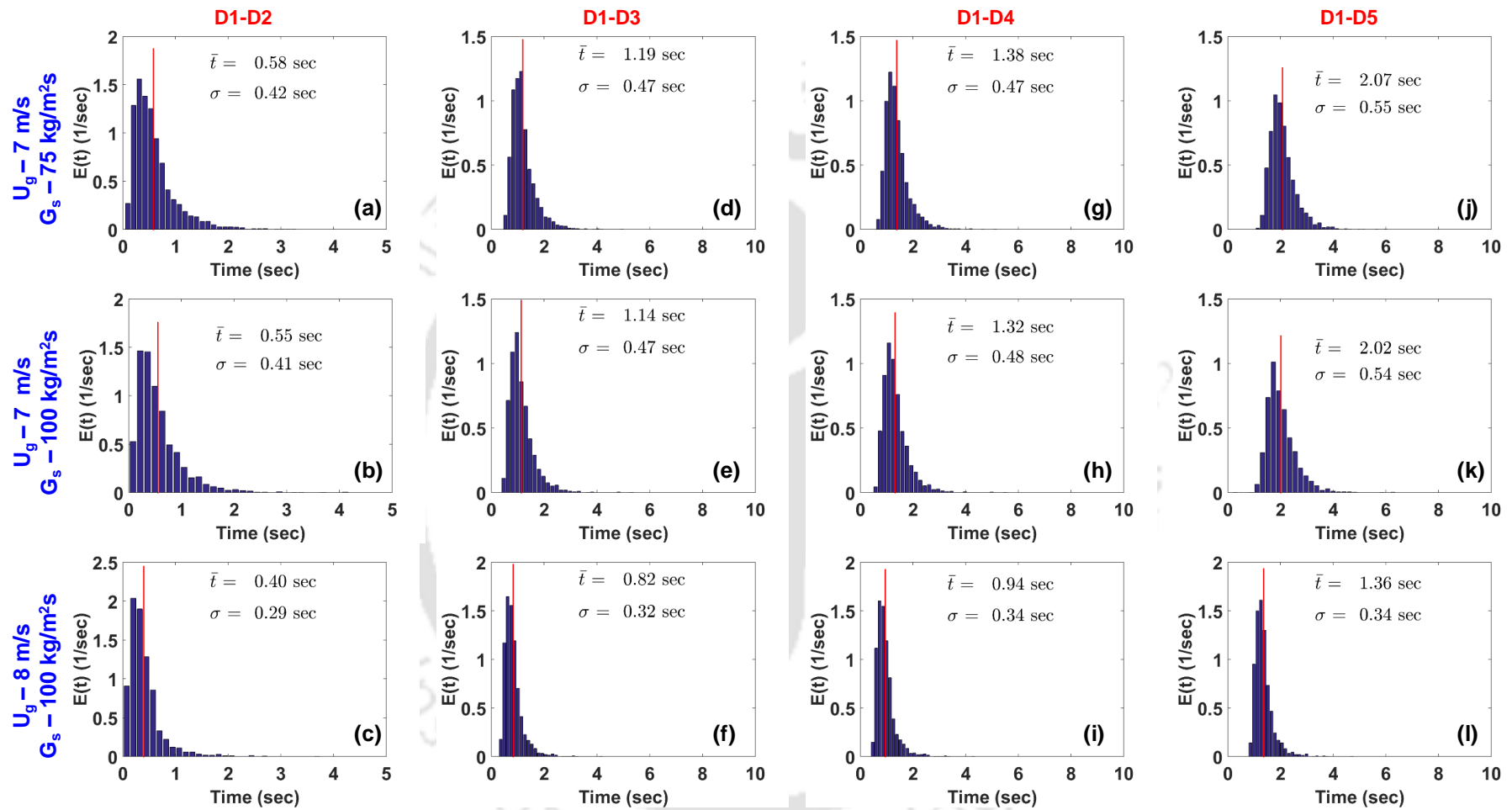


Figure 3.51: RTD for (a,b,c) inlet section, (d,e,f) inlet to start of the middle section, (g,h,i) inlet to end of the middle section and (j,k,l) overall section of the riser

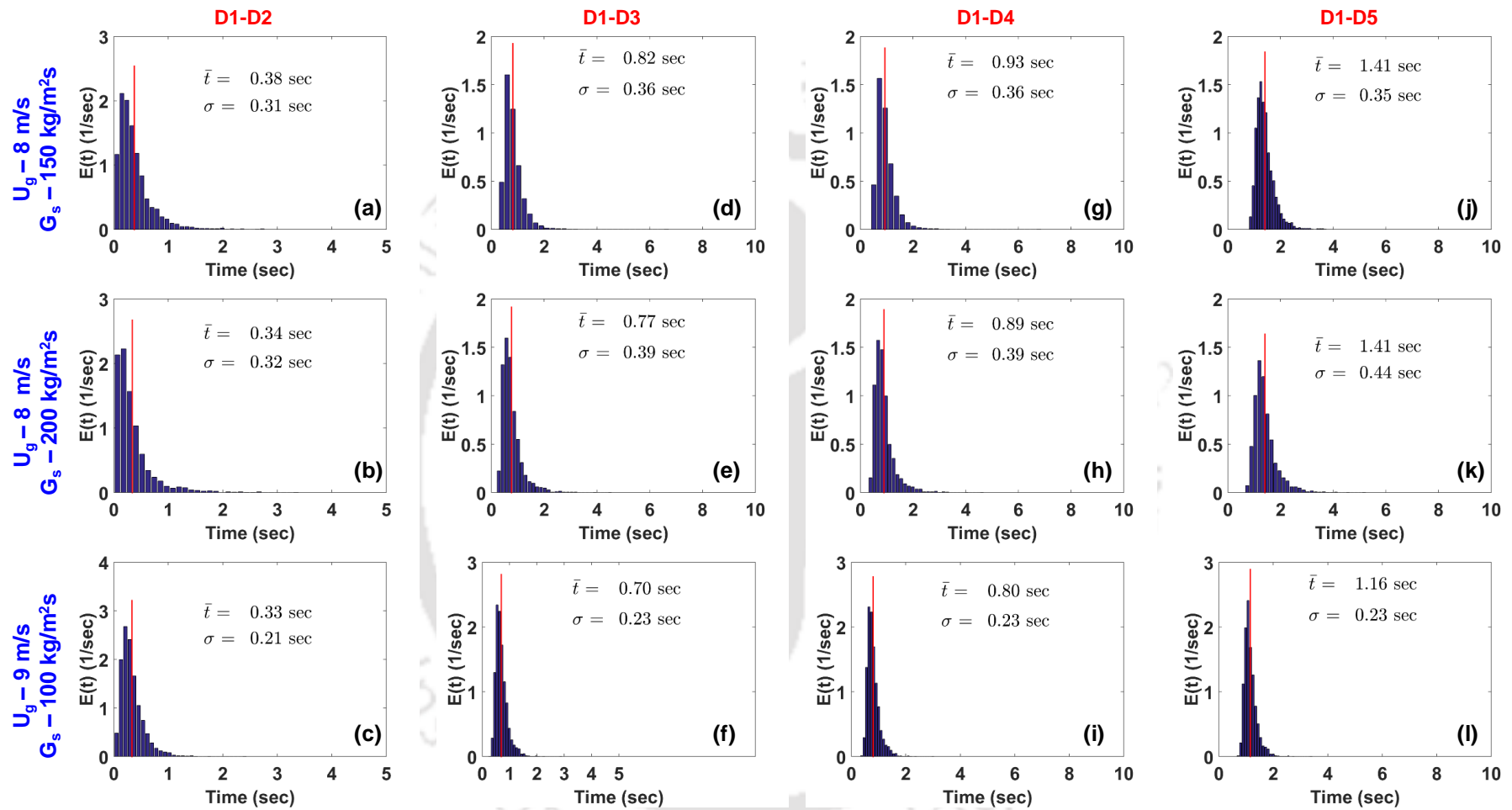


Figure 3.52: RTD for (a,b,c) inlet section, (d,e,f) inlet to start of the middle section, (g,h,i) inlet to end of the middle section and (j,k,l) overall section of the riser

Table 3.2: Residence time distribution and Peclet number

U_g (m/s)	G_s (kg/m ² s)		D1-D2	D1-D3	D1-4	D1-D5
6	40	\bar{t}	1.412	8.454	12.137	23.533
		σ^2/\bar{t}^2	1.119	1.024	0.813	0.673
		Pe	3.713	3.937	4.598	5.240
6.5	60	\bar{t}	0.764	1.690	2.067	3.553
		σ^2/\bar{t}^2	1.309	0.591	0.484	0.281
		Pe	3.352	5.742	6.628	9.960
7	60	\bar{t}	0.645	1.311	1.519	2.323
		σ^2/\bar{t}^2	0.511	0.149	0.119	0.067
		Pe	6.373	16.689	20.171	33.617
7	75	\bar{t}	0.581	1.190	1.377	2.073
		σ^2/\bar{t}^2	0.517	0.154	0.119	0.071
		Pe	6.320	16.159	20.182	31.570
7	100	\bar{t}	0.554	1.135	1.318	2.015
		σ^2/\bar{t}^2	0.552	0.169	0.134	0.073
		Pe	6.028	15.019	18.199	30.984
8	100	\bar{t}	0.397	0.823	0.944	1.455
		σ^2/\bar{t}^2	0.536	0.155	0.126	0.055
		Pe	6.152	16.127	19.175	40.312
8	150	\bar{t}	0.375	0.816	0.930	1.412
		σ^2/\bar{t}^2	0.692	0.192	0.149	0.063
		Pe	5.139	13.522	16.665	35.469
8	200	\bar{t}	0.339	0.768	0.893	1.408
		σ^2/\bar{t}^2	0.907	0.253	0.190	0.097
		Pe	4.269	10.822	13.612	23.961
9	100	\bar{t}	0.333	0.698	0.803	1.156
		σ^2/\bar{t}^2	0.382	0.105	0.080	0.041
		Pe	7.891	22.358	28.376	53.027

3.6.2 Trajectory Length Distribution (TLD)

RPT experiments were carried out in different conditions, covering both the bottom and middle sections, as mentioned earlier. Figure 3.53 displays a typical Lagrangian track from

RPT experiments, illustrating the path of a tracer particle through the bottom section. Extensive sets of trajectories were generated for both sections, providing data on each particle's path length before exiting the area of interest. These independent trajectories were used to create histograms, which, in turn, allowed for the calculation of the macromixing index (M). According to Villermaux (1996) Macromixing index quantifies the degree of back mixing by comparing the average path length of the tracer particle to the actual distance between the inlet and outlet.

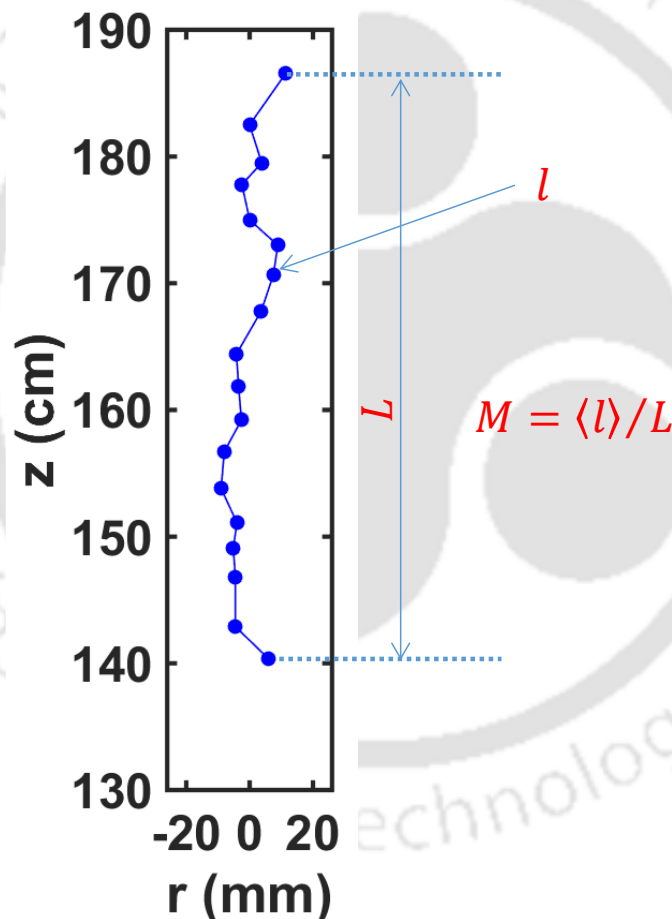


Figure 3.53: Tracer trajectory for a single pass in the scan zone

In this context, L is defined as the distance between the start and end point of the zone of interest, and l represents the actual path traveled by the tracer particle within a specific scan zone. A high M value indicates effective macromixing, with particle elements traveling a

significant distance before leaving the zone of interest. In an ideal plug flow system, M equals one, while in an ideal mixed flow system, M approaches infinity. Interestingly, the trajectory length distribution (TLD) curve is akin to the residence time distribution (RTD) curve, as both can be analyzed to gain insights into the reactor's macromixing behavior.

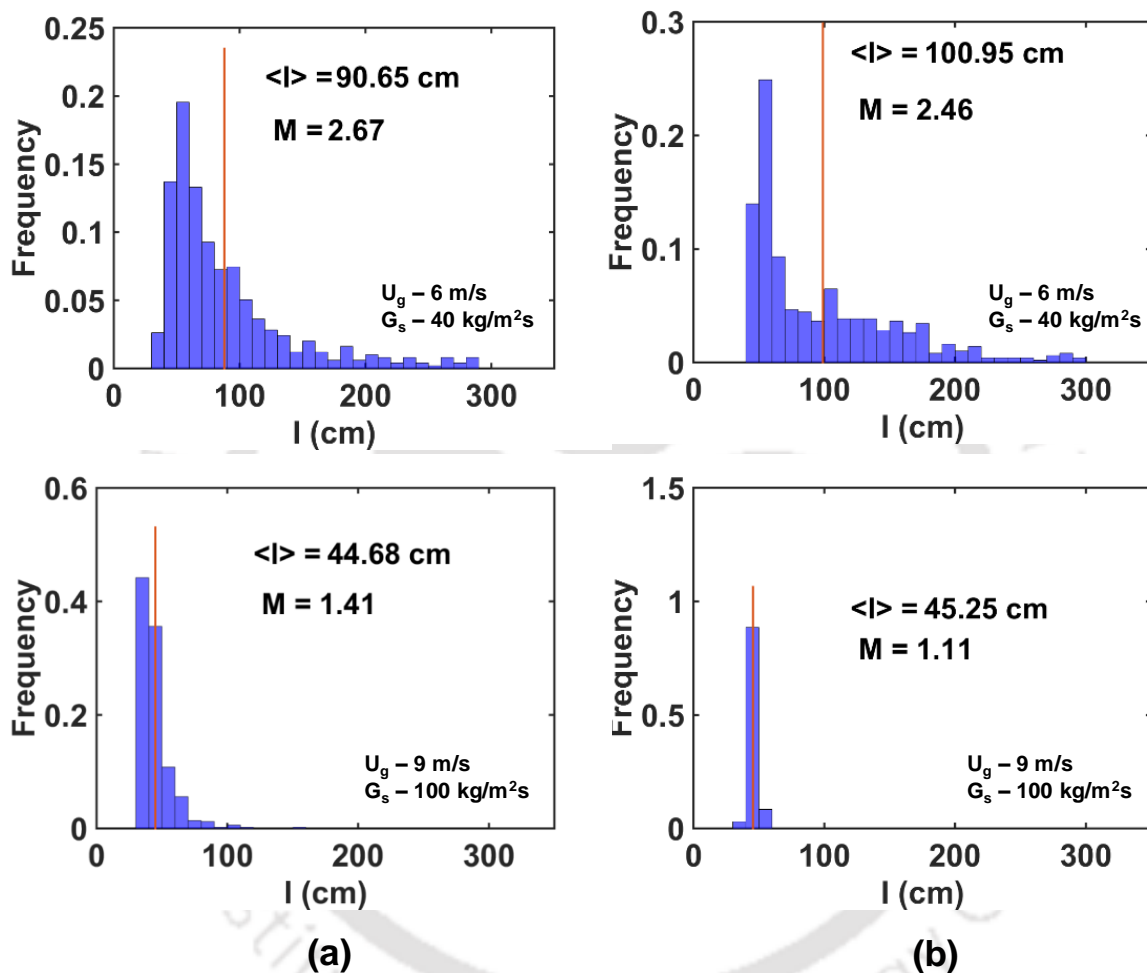


Figure 3.54: Trajectory length distribution at (a) bottom section and (b) middle section.

Figure 3.54 depicts the diagram of the trajectory length distribution of the gas velocity of 6 m/s and 9 m/s. A long tail can be observed of trajectory length in the case of gas velocity of 6 m/s, which is missing in the case of the gas velocity of 9 m/s. Also, the tail is longer in the bottom section compared to the middle section of the riser. This indicates that the average path traveled by the tracer is much more tortuous compared to the the bottom

section. The macromixing index (M) and mean trajectory lengths ($\langle l \rangle$) are presented in Table 3.3 for both the bottom and middle sections. So, for all the cases, the value of M is higher at the bottom section compared to the top section. It confirms that the middle section tracer traveled a comparatively straight path compared to the bottom section. It can be observed that the M value decreases as the gas velocity increases because the particles move comparatively straight in the axial direction and very little in the radial direction. When the solid flux increases at the same gas velocity, an increase in M value is observed as the movement of particles is relatively more tortuous at higher solid flux. However, the increment in M value due to a change in solid flux is much less significant. So, the solid flux has a lesser effect on the Micromixing Index compared to gas velocity.

Table 3.3: Trajectory length distribution of the bottom and middle section of the riser

U_g (m/s)	G_s kg/m ² s	Bottom Section		Middle Section	
		$\langle l \rangle$ cm	M (-)	$\langle l \rangle$ cm	M (-)
6	40	90.65	2.67	100.95	2.46
6.5	60	68.23	2.11	66.86	1.67
7	60	50.34	1.51	48.97	1.22
7	75	52.92	1.64	49.13	1.23
7	100	56.63	1.74	50.60	1.26
8	100	48.84	1.51	46.65	1.13
8	150	50.64	1.58	47.07	1.14
8	200	50.70	1.60	46.86	1.16
9	100	44.68	1.41	45.25	1.11

3.7 Summary

To understand solid motion in the riser of a gas-solid cold flow circulating fluidized bed, a radiation-based non-invasive RPT technique is implemented at the bottom and middle sections of the riser. The experiments are conducted with Geldart Group B particles. A wide range of instantaneous and time-averaged flow field data are obtained for the solid phase. Lagrangian tracks of tracer particles at both the bottom and middle sections show that each path of the tracer is unique, but tracks can be classified based on back mixing and internal recirculation characteristics. The probability distribution function of instantaneous axial velocity data shows that in certain instances, at low gas velocity, particles can have negative velocity, but overall, solid motion is always positive. Especially in the cases of 6 and 6.5 m/s, internal recirculation is clearly visible. It causes intense particle-particle interaction. Hence, axial velocity fluctuation, granular temperature, and turbulence intensity are much higher at 6 m/s and 6.5 m/s. The RTD E curve shows wider distributions and long tails at lower gas velocities. RTD confirms that solid back mixing is higher in the bottom section of the riser, irrespective of operating conditions and solid back mixing decreases with increasing height. Peclet numbers confirm that back mixing is highly dependent on gas velocity compared to solid flux. With a rise in solid flux, the Peclet number experiences a slight reduction, signifying enhanced mixing at elevated solid flux levels. However, these changes remain quite marginal. Conversely, as gas velocity increases, the Peclet number demonstrates a swift increase, highlighting a corresponding rapid decline in solid back mixing. Trajectory length distribution (TLD) results reveal solid mixing phenomena akin to RTD. Solid mixing is more pronounced in the lower section than in the middle section. This enhanced mixing occurs at lower gas velocity levels as opposed to higher gas velocities, and solid flux exerts only a minimal impact on the overall solid mixing process.

Notations

A	Column cross section area,	$[m^2]$
Ar	Archimedes number	$[-]$
D	Riser diameter	$[m]$
G_s	Solid flux	$[kg/m^2s]$
L	Distance between start and end point of a tracer particle track	$[cm]$
l	Actual path traveled by tracer particle	$[cm]$
M	Macromixing index	$[-]$
ΔP	Pressure drop	Pa
U_{mf}	Minimum fluidization velocity	$[m/s]$
U_t	Terminal settling velocity	$[m/s]$
V_{ca}	Transition velocity between fast fluidization and core-annular dilute phase flow (Type A choking velocity)	$[m/s]$
V_{cc}	Classical choking velocity	$[m/s]$
V_{mp}	Transition from homogeneous dilute flow to core-annular dilute flow (minimum pressure drop point)	$[m/s]$
v_s	Solid velocity	$[m/s]$
ϵ_s	Solid fraction	$[-]$
ρ_G	Gas density	$[kg/m^3]$
ρ_p	Particle density	$[kg/m^3]$

References

- Anantharaman, A., Issangya, A., Karri, S.B.R., Findlay, J., Hrenya, C.M., Cocco, R.A., Chew, J.W., 2017. Annulus flow behavior of Geldart Group B particles in a pilot-scale CFB riser. *Powder Technol.* 305, 816–828.
- Arastoopour, H., 2001. Numerical simulation and experimental analysis of gas/solid flow systems: 1999 Fluor-Daniel plenary lecture. *Powder Technol.* 119, 59–67.
- Bader, R., Findlay, J., Knowlton, T.M., 1988. Gas/Solids Flow Patterns in a 30.5-Cm-Diameter Circulating Fluidized Bed, in: Basu, P., Large, J.F.B.T.-C.F.B.T. (Eds.), *Circulating Fluidized Bed Technology*. Pergamon, pp. 123–137.
- Beam, G.B., Wielopolski, L., Gardner, R.P., Verghese, K., 1978. Monte Carlo calculation of efficiencies of right-circular cylindrical NaI detectors for arbitrarily located point sources. *Nucl. Instruments Methods* 154, 501–508.
- Berruti, F., Chaouki, J., Godfroy, L., Pugsley, T.S., Patience, G.S., 1995. Hydrodynamics of Circulating Fluidized Bed Risers : A Review. *Can. J. Chem. Eng.* 73, 579–602.
- Bhusarapu, Satish, Al-Dahhan, M., Dudukovic, M.P., 2004. Quantification of solids flow in a gas-solid riser: Single radioactive particle tracking. *Chem. Eng. Sci.* 59, 5381–5386.
- Bhusarapu, S., Al-Dahhan, M.H., Duduković, M.P., 2006. Solids flow mapping in a gas-solid riser: Mean holdup and velocity fields. *Powder Technol.* 163, 98–123.
- Bhusarapu, S., Al-Dahhan, M.H., Duduković, M.P., Trujillo, S., O'Hern, T.J., 2005. Experimental study of the solids velocity field in gas-solid risers. *Ind. Eng. Chem. Res.* 44, 9739–9749.
- Bhusarapu, S., Fongarland, P., Al-Dahhan, M.H., Duduković, M.P., 2004. Measurement of overall solids mass flux in a gas-solid Circulating Fluidized Bed. *Powder Technol.* 148, 158–171.

- Bhusarapu, S.B., 2005. Solids Flow Mapping In Gas-Solid Risers. D.Sc Thesis, Washington University, Saint Louis, Missouri, USA.
- Bi, H.T., Fan, J., 1991. Regime transitions in gas-solid circulating fluidized beds, in: AIChE Annual Meeting. Los Angeles, 17–22 November.
- Bi, H.T., Grace, J.R., Zhu, J.X., 1993. Types of choking in vertical pneumatic systems. *Int. J. Multiph. Flow* 19, 1077–1092.
- Biswal, J., Joseph, A., Shah, J.G., Pant, H.J., Dash, A., 2016. Preparation of 46Sc glass microspheres by combined melt-quenching and microwave methods for applications in radioactive particle tracking experiments. *J. Radioanal. Nucl. Chem.* 308, 335–340.
- Burkell, J.J., Grace, J.R., Zhao, J., Lim, C.J., 1988. Measurement of Solids Circulation Rates in Circulating Fluidized Beds, in: *Circulating Fluidized Bed Technology II*. Pergamon Press plc, pp. 501–509.
- Chan, C.W., Seville, J., Yang, Z., Baeyens, J., 2009. Particle motion in the CFB riser with special emphasis on PEPT-imaging of the bottom section. *Powder Technol.* 196, 318–325.
- Cheng, Y., Fei, W., Yang, G., Yong, J., 1998. Inlet and outlet effects on flow patterns in gas-solid risers. *Powder Technol.* 98, 151–156.
- Chew, J.W., Hays, R., Findlay, J.G., Knowlton, T.M., Reddy Karri, S.B., Cocco, R.A., Hrenya, C.M., 2012. Cluster characteristics of Geldart Group B particles in a pilot-scale CFB riser. I. Monodisperse systems. *Chem. Eng. Sci.* 68, 72–81.
- Chew, J.W., LaMarche, W.C.Q., Cocco, R.A., 2022. 100 Years of Scaling Up Fluidized Bed and Circulating Fluidized Bed Reactors. *Powder Technol.* 409, 117813.
- Cody, G.D., Goldfarb, D.J., Storch, G. V., Norris, A.N., 1996. Particle granular temperature in gas fluidized beds. *Powder Technol.* 87, 211–232.

- De Wilde, J., Van Engelandt, G., Heynderickx, G.J., Marin, G.B., 2005. Gas-solids mixing in the inlet zone of a dilute circulating fluidized bed. *Powder Technol.* 151, 96–116.
- Fiedler, O., Werther, J., Labahn, N., Kumpart, J., Christofori, K., 1997. Measurement of local particle velocities and velocity distributions in gas-solid flows by means of the spatial filter method. *Powder Technol.* 94, 51–57.
- Godfroy, L., Larachi, F., Chaouki, J., 1999. Position and velocity of a large particle in a gas/solid riser using the radioactive particle tracking technique. *Can. J. Chem. Eng.* 77, 253–261.
- Goldhirsch, I., 2008. Introduction to granular temperature. *Powder Technol.* 182, 130–136.
- Jung, J., Gidaspow, D., Gamwo, I.K., 2005. Measurement of two kinds of granular temperatures, stresses, and dispersion in bubbling beds. *Ind. Eng. Chem. Res.* 44, 1329–1341.
- Kalo, L., Kamalanathan, P., Pant, H.J., Cassanello, M.C., Upadhyay, R.K., 2019a. Mixing and regime transition analysis of liquid-solid conical fluidized bed through RPT technique. *Chem. Eng. Sci.* 207, 702–712.
- Kalo, L., Pant, H.J., Cassanello, M.C., Upadhyay, R.K., 2019b. Time series analysis of a binary gas-solid conical fluidized bed using radioactive particle tracking (RPT) technique data. *Chem. Eng. J.* 377, 1385–8947.
- Kalo, L., Pant, H.J., Upadhyay, R.K., 2020. Validation of the Glicksman Scaling Law for Gas-Solid Conical Fluidized Beds Using the Radioactive Particle Tracking Technique. *Ind. Eng. Chem. Res.* 59, 20943–20952.
- Kamalanathan, P., Kalo, L., Pant, H.J., Upadhyay, R.K., 2017. Effect of dynamic bias on accuracy of radioactive particle tracking (RPT) technique at different data

- acquisition frequencies. *Appl. Radiat. Isot.* 128, 13–21.
- Kaplanis, S.N., 1978. Efficiency variations of cylindrical detectors for non-axial point-sources. *Int. J. Appl. Radiat. Isot.* 29, 543–544.
- Larachi, F., Chaouki, J., Kennedy, G., 1995. 3-D mapping of solids flow fields in multiphase reactors with RPT. *AIChE J.* 41, 439–443.
- Levenspiel, O., 1999. Chemical reaction engineering. *Ind. Eng. Chem. Res.* 38, 4140–4143.
- Ludlow, J.C., Monazam, E.R., Shadle, L.J., 2008. Improvement of continuous solid circulation rate measurement in a cold flow circulating fluidized bed. *Powder Technol.* 182, 379–387.
- Manyele, S. V., Khayat, R.E., Zhu, J., 2002. Investigation of the dynamics of a high-flux CFB riser using chaos analysis of pressure fluctuations. *Chem. Eng. Technol.* 25, 801–810.
- Moens, L., De Corte, F., Simonits, A., Xilei, L., De Wispelaere, A., De Donder, J., Hoste, J., 1982. Calculation of the absolute peak efficiency of Ge and Ge(Li) detectors for different counting geometries. *J. Radioanal. Chem.* 70, 539–550.
- Pantzali, M.N., De Ceuster, B., Marin, G.B., Heynderickx, G.J., 2015. Three-component particle velocity measurements in the bottom section of a riser. *Int. J. Multiph. Flow* 72, 145–154.
- Pantzali, M.N., Lozano Bayón, N., Heynderickx, G.J., Marin, G.B., 2013. Three-component solids velocity measurements in the middle section of a riser. *Chem. Eng. Sci.* 101, 412–423.
- Pateence, G.S., Chaouki, J., Grandjean, B.P.A., 1990. Solids flow metering from pressure drop measurement in circulating fluidized beds. *Powder Technol.* 61, 95–99.
- Rhodes, M., Mineo, H., HIRAMA, T., 1992. Particle motion at the wall of a circulating

- fluidized bed. *Powder Technol.* 70, 207–214.
- Roy, S., 2000. Quantification of two phase flow in liquid solid riser(Ph.D. Thesis). Saint Louis, Missuri. USA, Washington University.
- Roy, S., Kemoun, A., Al-Dahhan, M., Dudukovic, M.P., 2001a. A method for estimating the solids circulation rate in a closed-loop circulating fluidized bed. *Powder Technol.* 121, 213–222.
- Roy, S., Kemoun, A., Al-Dahhan, M.H., Dudukovic, M.P., 2005. Experimental investigation of the hydrodynamics in a liquid-solid riser. *AIChE J.* 51, 802–835.
- Roy, S., Larachi, F., Al-Dahhan, M.H., Dudukovic, M.P., 2001b. Resolution and sensitivity in computer-automated radioactive particle tracking (CARPT). *Process Imaging Autom. Control* 4188, 122.
- Roy, S., Larachi, F., Al-Dahhan, M.H., Duduković, M.P., 2002. Optimal design of radioactive particle tracking experiments for flow mapping in opaque multiphase reactors. *Appl. Radiat. Isot.* 56, 485–503.
- Stellema, C.S., 1988. Radiotracers for gas/solids flows in (Interconnected) fluidized beds. Ph.D Dissertation, Delft University of Technology, Delft, Netherlands.
- Tartan, M., Gidaspow, D., 2004. Measurement of granular temperature and stresses in risers. *AIChE J.* 50, 1760–1775.
- Tribedi, T., Pillajetti, P., Kumari, R., Pant, H.J., Tiwari, P., Upadhyay, R.K., 2022. Measurements of Solid Velocity in a Pilot-Scale Geldart’s Group B Circulating Fluidized Bed Using a Radioactive Particle Tracking Technique. *Ind. Eng. Chem. Res.* 61, 9110–9121.
- Tribedi, T., Tiwari, P., Pant, H.J., Upadhyay, R.K., 2023a. Solid Phase Macromixing Study in a Pilot-Scale Geldart Group B Circulating Fluidized Bed Riser Using Single Particle RTD and RPT Measurements. *ACS Eng. Au* 3, 165–172.

- Tribedi, T., Tiwari, P., Pant, H.J., Upadhyay, R.K., 2023b. Solid Flow Mapping at the Bottom Section of a Pilot-Plant Scale Riser with the Help of a Radioactive Particle Tracking Technique. *Ind. Eng. Chem. Res.* 62, 19133–19144.
- Upadhyay, R.K., Roy, S., 2010. Investigation of hydrodynamics of binary fluidized beds via radioactive particle tracking and dual-source densitometry. *Can. J. Chem. Eng.* 88, 601–610.
- Van engelandt, G., De Wilde, J., Heynderickx, G.J., Marin, G.B., 2007. Experimental study of inlet phenomena of 35 ° inclined non-aerated and aerated inlets in a dilute cold-flow riser. *Chem. Eng. Sci.* 62, 339–355.
- Villiermaux, J., 1996. Trajectory length distribution (TLD), a novel concept to characterize mixing in flow systems. *Chem. Eng. Sci.* 51, 1939–1946.
- Wei, F., Zhu, J.X., 1996. Effect of flow direction on axial solid dispersion in gas-solids cocurrent upflow and downflow systems. *Chem. Eng. J. Biochem. Eng. J.* 64, 345–352.
- Wielopolski, L., 1977. The Monte Carlo calculation of the average solid angle subtended by a right circular cylinder from distributed sources. *Nucl. Instruments Methods* 143, 577–581.
- Wildman, R.D., Huntley, J.M., 2000. Novel method for measurement of granular temperature distributions in two-dimensional vibro-fluidised beds. *Powder Technol.* 113, 14–22.
- Wilhelm, R.H., Kwauk, M., 1948. Fluidization of solid particles. *Chem. Eng. Prog.* 44, 201–218.
- Wu, W., Gerhart, A.L., Chen, Z., Dellenback, P.A., Agarwal, P.K., 2001. A device for measuring solids flowrate in a circulating fluidized bed. *Powder Technol.* 120, 151–158.

Yerushalmi, J., Turner, D.H., Squires, A.M., 1976. The Fast Fluidized Bed. Ind. Eng. Chem. Process Des. Dev. 15, 47–53.

Yousfi, Y., Gau, G., 1974. Aerodynamique de l'écoulement vertical de suspensions concentrees gaz-solides-I. Regimes d'écoulement et stabilite aerodynamique. Chem. Eng. Sci. 29, 1939–1946.

Zhou, J., Grace, J.R., Lim, C.J., Brereton, C.M.H., 1995. Particle velocity profiles in a circulating fluidized bed riser of square cross-section. Chem. Eng. Sci. 50, 237–244.



CHAPTER 4

Experimental Investigation on a Pilot-Scale CFB Riser: Solid-phase Flow Fields and Mixing Characteristics

Scope

In this chapter, the solid phase velocity flow field at the bottom and middle sections of the pilot scale CFB riser is discussed. Section-wise solid phase residence time distribution investigations are presented, and solid mixing behavior is discussed. A comparative study of laboratory scale and pilot scale results is outlined. The study of hydrodynamic similarities is discussed. Empirical correlation is developed in the current study to predict solid velocity based on operating conditions.

4.1 Introduction

Circulating fluidized bed (CFB) is widely used in petrochemical, chemical, fine chemical, metallurgical, and power industries due to its effective heat and mass transfer properties, higher throughput, and operational flexibility (Berruti et al., 1995). The various applications of CFBs differ in their capacity to handle solid fluxes. Low-solid-flux CFBs have applications in drying, alumina calcination, iron ore reduction, and so forth, while high-solid-flux CFBs are often used in fluid catalytic cracking (FCC), maleic anhydride production, coal and biomass combustion/gasification, chemical looping combustion, and so forth (Berruti et al., 1995; Chang et al., 2016; Zhu and Bi, 1995). Nowadays, the utilization of low-rank coal (with high ash and/or moisture content) poses a significant problem. The high-flux CFBs can play a vital role in the combustion or gasification of such low-rank coal and can be operated at both high gas velocity and solid circulation rates,

leading to better heat and mass transfer and solid mixing. However, in view of the lack of data related to high-flux CFBs, the design and scale-up strategies of such a system are still not completely understood. The complex dynamics of gas–solid flow and their interaction at different lengths and timescales make it even more intricate to understand the behaviour of such systems.

Scale-up of circulating fluidized beds is a continuing activity in the chemical process industry for more than half a century (Matsen, 1997). Despite that, there is always a certain uncertainty remaining for CFB scale-up. The hydrodynamic scaling law is a key tool for successfully scaling up circulating fluidized beds. In a circulating fluidized bed reactor, sub processes like gas-solid contact, heat and mass transfer, and chemical reactions happen, and these sub processes influence each other (Horio, 1997). Therefore, scale-up involves establishing a balance among these sub processes to ensure the overall output meets the output demands at a larger scale, maintaining the efficiency already established in small-scale test plants. Hydrodynamics, heat transfer, mass transfer, and reaction kinetics are individually investigated prior to scale-up to obtain as much information as possible. These data are then used to create models that predict reactor design.

4.2 Experimental Setup

Pilot scale CFB is designed so that the diameter and height of the riser are twice the laboratory scale CFB. The schematic diagram of the pilot-plant scale cold-flow model of the CFB used in this study is shown in Figure 4.1. The experimental setup consists of a riser section, a downer section, two cyclone separators connected in series, and a solid storage tank. The internal diameter of the riser is 0.10 m, and the height is 6.5 m. The top of the riser is connected with a primary cyclone with 90° elbow. There are two inlets in the riser section: one at the bottom and another one at 0.15 m above the bottom inlet, inclined

at 60° with the vertical plane. Air enters the riser from the bottom inlet at ambient temperature, and solids enter through the side inlet, which is connected to solid storage with a dipleg of an internal diameter of 0.076 m. A high-inventory storage tank with an inner diameter of 0.4 m and a height of 0.6 m with a conical bottom is used that can hold more than 100 kg of solids. The shape of the storage tank is conical at the bottom and cylindrical at the top, as shown in Figure 4.1. This storage is aerated with compressed air much below the minimum fluidization velocity to prevent choking of solids and facilitate solid movement toward the dipleg, which is connected to the riser. The dipleg is attached at the side of the conical section. Gas and solids flow upward through the riser and are separated through primary and secondary cyclones connected in series at the top. One feeding valve on the upper side of the storage tank serves as a solid feeding inlet for the CFB system. This valve remains closed during CFB operation. A bag filter is also provided at the outlet of the secondary cyclone to capture the carryover of the solids if any. Primary and secondary cyclone bottoms connect with the storage tank via diplegs of diameter 0.10 m and 0.05 m, respectively. A lobe-type blower of 20 kW is used to supply primary air which is regulated by a gate valve. The storage tank is supplied with compressed air from a 10 kW compressor and the line pressure is maintained at 1 bar with a pressure regulator. Both primary and secondary air flow are measured with the sets of rotameters. Glass beads with a mean diameter of $500\ \mu\text{m}$ and a density of $2500\ \text{kg/m}^3$ (Geldart Group B) are used as the solid phase, same as the laboratory scale.

An identical radioactive tracer particle is used in both laboratory and pilot scale experiments. To ensure a consistent measurement accuracy, pilot scale experiments use the same data acquisition system (MIDAS) and detectors. Moreover, the data acquisition frequency is kept the same for pilot-scale experiments as for laboratory-scale experiments.

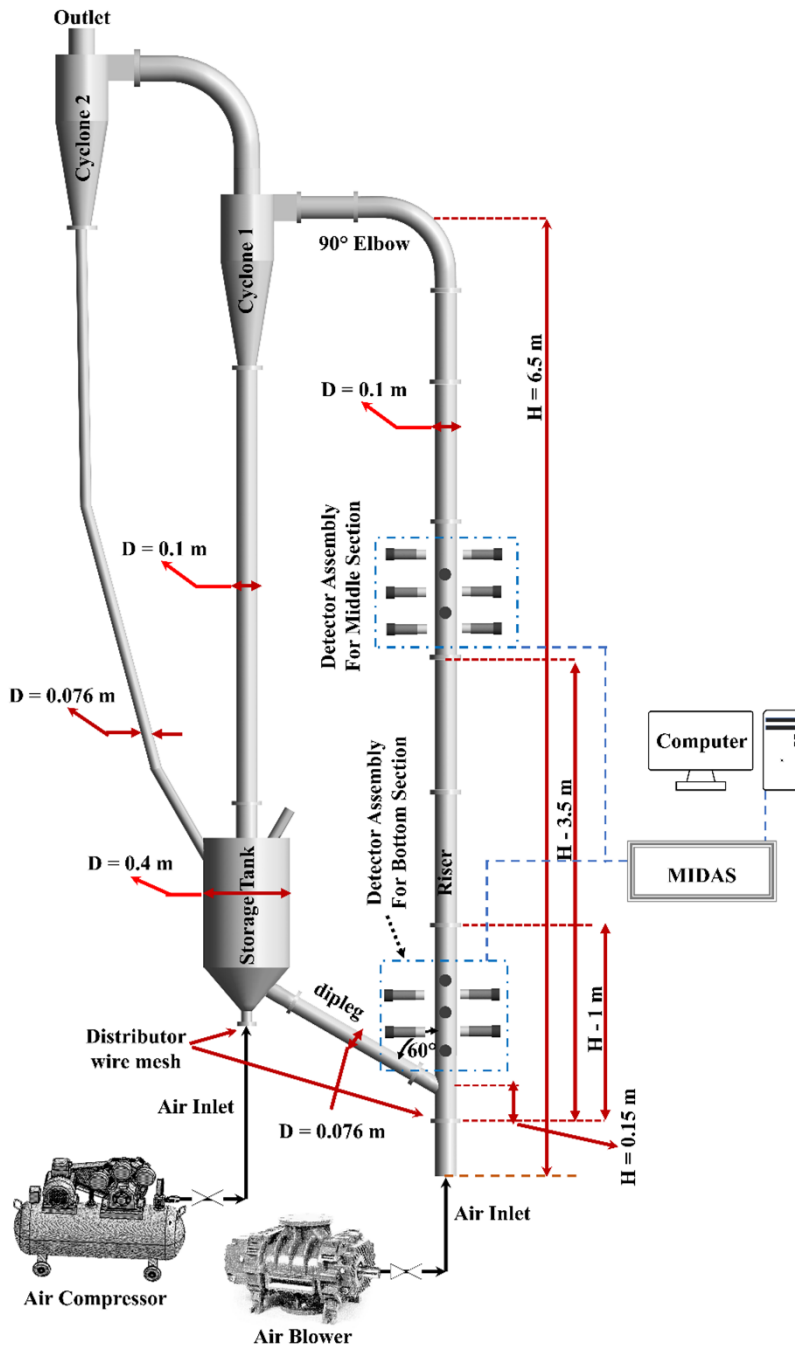


Figure 4.1: Schematic diagram of the experimental setup with detector assembly

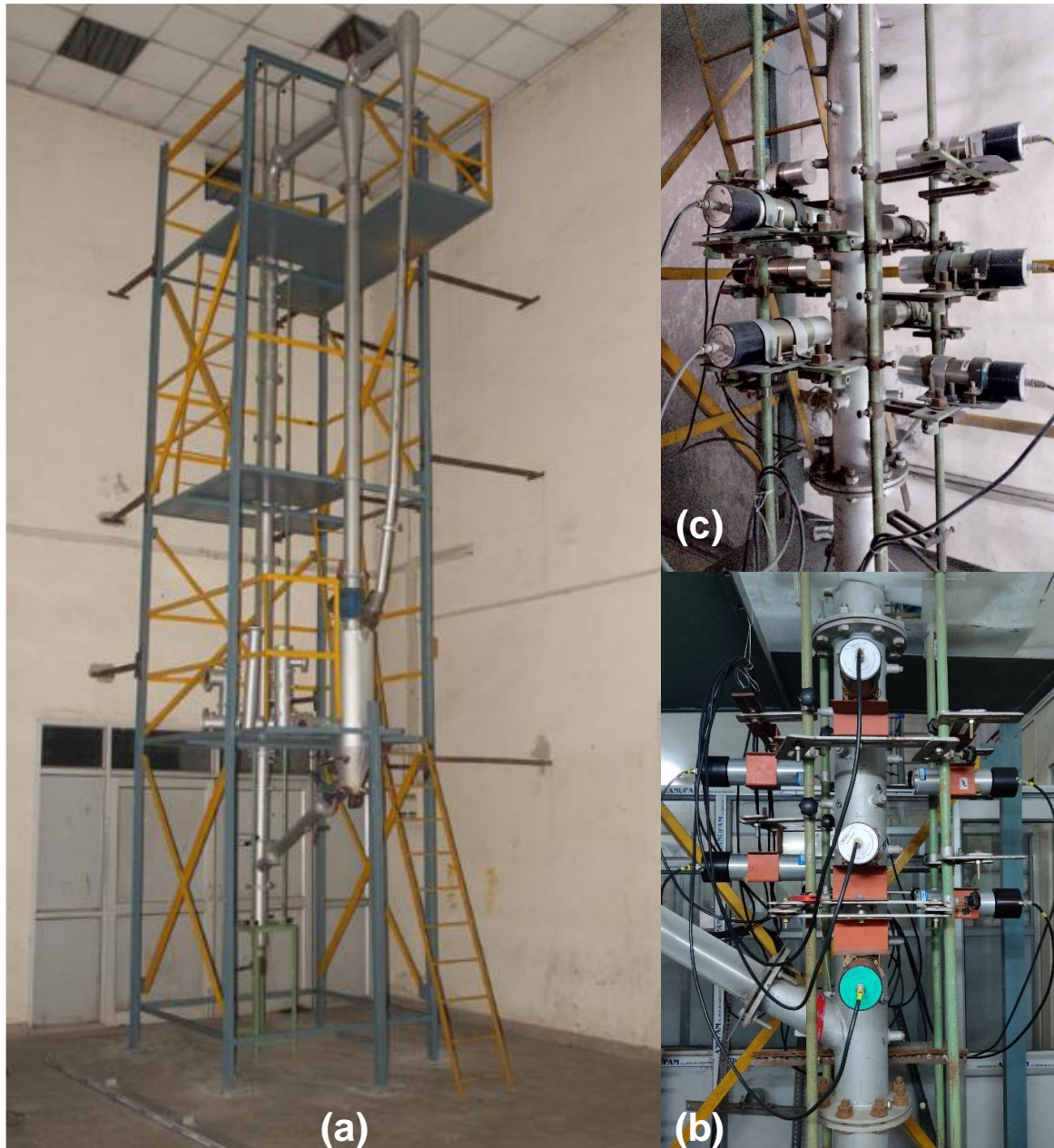


Figure 4.2: Photograph of (a) pilot scale circulating fluidized bed, (b) bottom section with detector assembly and (c) middle section with detector assembly

4.3 Solid Flux Measurement

Solid flux is a critical parameter for any CFB operation; thus, the accurate measurement of solid flux is crucial to analyze the behavior of CFB. However, it is not easy to accurately measure the solid flux in a CFB riser as solids circulate in a closed loop. To measure the solid flux, solid particle detection is necessary. It can be achieved through mechanical,

optical, or electrical methods or through heat and/or mass transfer. Mechanical methods are based on principles of flow separation such as the particle sampling probe or determination of measurement with differential pressure using the pitot tube. In the literature, many invasive and non-invasive methods have been described by various researchers to measure the solid flux in CFB risers. Burkell et al. (1988) reviewed five techniques: impact flow meter, permeable butterfly valve, time-of-descent technique, modified orifice meter, and calorimetric method for determining the solid circulation rates in CFBs. However, each of these methods has its own set of drawbacks. Wu et al. (2001) developed a solid flow meter based on the impact meter, which measures the force of the collision with solids at the downer section that effectively does not interfere with the riser flow. Ludlow et al. (2008) designed a device based on a rotating spiral vane to measure the solid circulation rate. All of these invasive methods have their own set of limitations and questionable accuracy. Pateence et al. (1990) found the solid circulation rate by measuring the pressure drop between the riser exit and cyclone inlet points and then clubbed it with the gas velocity. This non-invasive technique does not interfere with solid flow but requires pre-calibration of flux measurement by estimating the solid mass flux independently from the time-of-descent method. Roy et al. (2001) used a radioisotope-based non-invasive technique to measure the solid flux in liquid–solid CFBs. They measured the solid fraction and solid residence time in the downer section. The downer section of the liquid–solid CFB has a measurable fraction of the solids, which is not the case for gas–solid CFBs. Therefore, in the current work, the velocity and solid fraction are measured in a dipleg, where the solid fraction is sufficiently high that it can be measured accurately. The solid velocity v_s and solid fraction ε_s are measured to calculate the solid flux G_s by using equation 4.1.

$$G_s = \frac{\rho_p \int v_s \varepsilon_s dA}{\int dA} \quad (4.1)$$

$$\langle G_s \rangle = \rho_p \langle v_s \rangle \langle \varepsilon_s \rangle A \quad (4.2)$$

The time-average solid flux is then calculated by using equation 4.2. In current work, solid flux is measured at the dipleg section, and then it is converted to riser solid flux based on mass balance across the dipleg and riser.

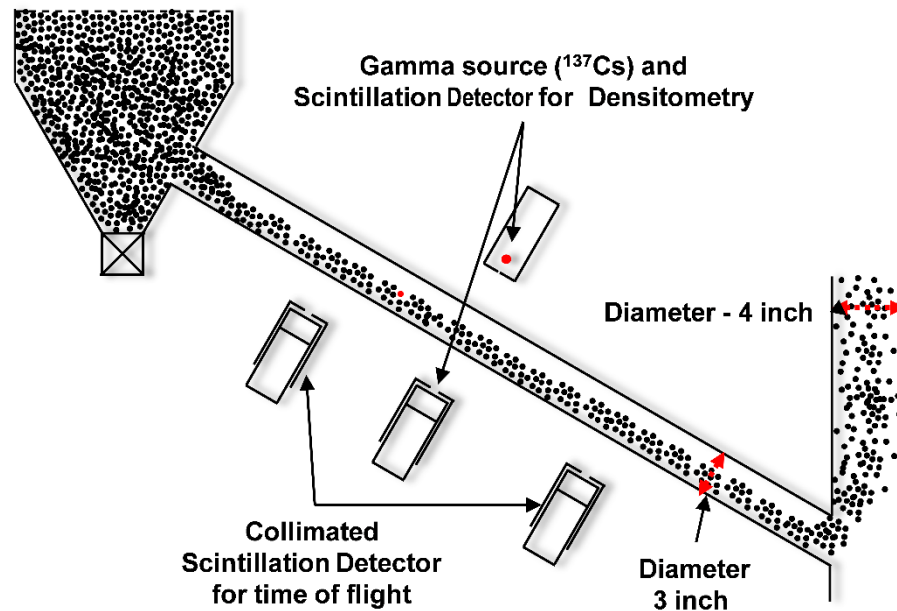


Figure 4.3: Detector assembly at the dipleg to measure the solid flux

In the current work, the solid fraction is measured by the γ -ray densitometry technique (Upadhyay et al., 2009; Upadhyay and Roy, 2010) and the mean solid velocity is measured by measuring the time of flight (mean residence time) (Bhusarapu et al., 2004; Roy et al., 2001a) of the solid phase between two known positions in the dipleg. Figure 4.3 shows the schematic diagram of both the measurements performed in the dipleg. For measuring the solid fraction, one collimated γ -ray source (^{137}Cs) and collimated scintillation detectors are placed 180° apart in the same plane. Initially, the count intensity recorded on the detector is measured (I_0) when the dipleg is empty (no solid flow condition). Thereafter, for the given flow condition (I_{exp}), the change in the photon count (due to the solid flow) on the detector is recorded. Beer–Lambert’s law is then used to calculate the solid fraction by using the above two data (Upadhyay and Roy, 2010). The data are acquired for a long time

to get a time-averaged solid fraction value. Equations 4.3, 4.4 and 4.5 is used to calculate solid fraction based on mass attenuation property of materials.

$$I_{exp} = I_0 e^{-\mu_{exp} D} \quad (4.3)$$

$$\varepsilon_{exp} = \varepsilon_a * \mu_a + \varepsilon_s * \mu_s \quad (4.4)$$

$$\varepsilon_a + \varepsilon_s = 1 \quad (4.5)$$

For velocity measurement, the radioactive tracer technique is used. However, in the current method, a single radioactive tracer particle (same as in the RPT experiment) is used to track the motion of the solid between the two fixed positions. Two collimated scintillation detectors are placed at two different locations outside the dipleg (as shown in Figure 4.3) so that they can record the photon counts only when the tracer comes in the detector plane. The distance between the two scintillation detectors is fixed (0.46 m) to measure the time of flight of the tracer particle. Whenever the tracer passes in front of the detector, a peak is observed in the recorded photon count. The time interval between the peak generated on both the detectors is measured from the experiments. Multiple passes are recorded until statistically sufficient information is obtained. The mean velocity of the solid is then calculated by dividing the distance between the detectors, ΔL , by the mean residence time $\langle t \rangle$ obtained from the time-of-flight experiments. The solid flux is controlled by adjusting the solid inventory and the compressed air supply to the storage tank. The solid flux has been quantified by varying both the solid inventory and the compressed air supply with different gas velocities. Numerous experimental flux studies were conducted, involving alterations in inventory, secondary and primary air flow rates. Subsequently, operational parameters for the current study (RPT experiment) were strategically chosen in such a way that they enabled a comprehensive analysis of the impact of solid flux and inlet gas velocity. The mean time of flight and the solid fraction is presented in Table 4.1 for operating conditions used for experiments.

Table 4.1 Operating condition with time solid flux measurement

Inlet gas velocity, U_g	Solids Inventory	Air to storage tank	time of flight, $\langle t \rangle$	Solid fraction, $\langle \varepsilon_s \rangle$	Riser solids flux G_s
m/s	kg	LPM	(sec)	(-)	kg/m ² s
8.2	50	200	2.93	0.47	100
7.6	50	400	2.64	0.58	150
8.2	80	200	2.50	0.56	150
9.2	80	200	2.11	0.50	150
8.2	80	400	1.80	0.56	200

4.4 Radioactive Particle Tacking (RPT) Measurements:

The solids flow field for different inlet gas velocities and solids fluxes are mapped by using the radioactive particle tracking (RPT) technique. Detailed of RPT technique is already explained in the Chapter 2 and Chapter 3. High energy isotope Sc-46 doped in a glass bead (Biswal et al., 2016) of approximately the same size (500 μm) is used as a tracer particle in the current experiment. This keeps the surface property of the tracer particle and other solids used in the experiments same. The RPT measurements are performed at the bottom section and fully developed region (middle section) of the CFB. Ten units of NaI (TI) scintillation detectors are assembled strategically at the bottom section (0.2-1 m) and middle section (3.5 - 4.5 m height from the bottom) of the riser to track the motion of the tracer particle as shown in Figures 4.1 and 4.2 The values of resolution and sensitivity (Roy et al., 2002; Upadhyay and Roy, 2010) are calculated for different detector positioning. The detector arrangement which yielded maximum values of resolution and sensitivity, is

considered for the measurements. Resolution and sensitivity contours is presented in Figure 4.4 for the detector arrangement used for the RPT experiment. The data is acquired (Kamalanathan et al., 2017) with 100 Hz frequency for around 4-6 days continuously to get sufficient statistics. Prior to the main experiment, calibration is performed to determine the relationship between photon count detected on each detector and the distance between the tracer particle and each detector (Beam et al., 1978; Dubé et al., 2014; Khane and Al-Dahhan, 2017; Larachi et al., 1995, 1994; Roy et al., 2002) For calibration, tracer particle is pasted on the tip of a pointed needle of a 6 mm diameter threaded rod. The rod is inserted inside the riser through the different calibration ports provided at different θ and z directions on the riser wall shown in Figures 4.2(b) and 4.2(c). In each plane, 3 ports are provided at 120° apart. Each plane of ports is 10 cm apart. Thus, all three r , θ , and z positions of the tracer particle are changed and the counts on each detector are recorded for all the positions of the tracer particle. Calibration was done at in situ conditions. The distance-count map generated by the calibration is used to reconstruct the position of the tracer particle by using suitable reconstruction algorithm (Upadhyay and Roy, 2010). Solid tracers circulate in loops, imitating other solid particles in the system. Counts recorded when tracers move through the scan zone are used to build the time series of instantaneous position data, which is basically the Lagrangian motion of particles (as shown in the Figure 4.5). Essentially, this trajectory shows how solids move inside the riser. Each circulation is unique. This Lagrangian position time series data is further used to calculate the different flow quantities like instantaneous, mean velocities and root mean square (RMS) velocities, granular temperature and turbulent quantities. The details of the post-processing methodologies and algorithms are reported in Chapter 2. The RPT measurements are performed for different operating condition as listed in Table 4.1. The effects of these two parameters on the solid flow field are investigated in the current work.

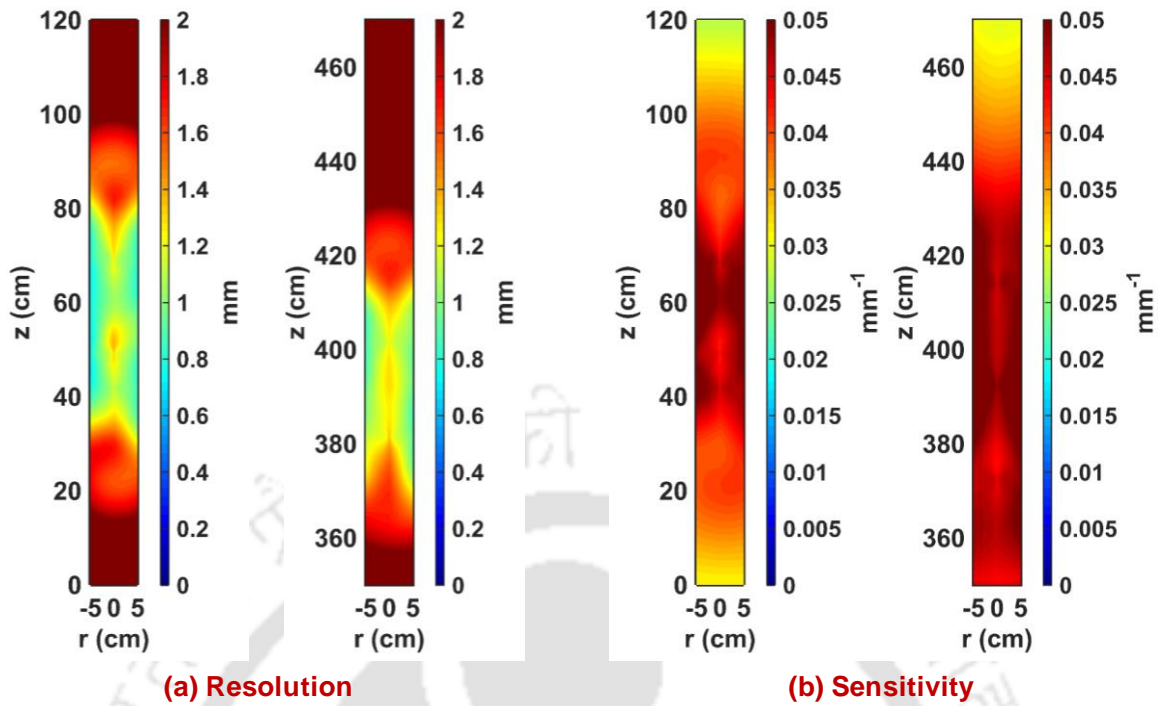


Figure 4.4: Contours of resolution and sensitivity for RPT experiments

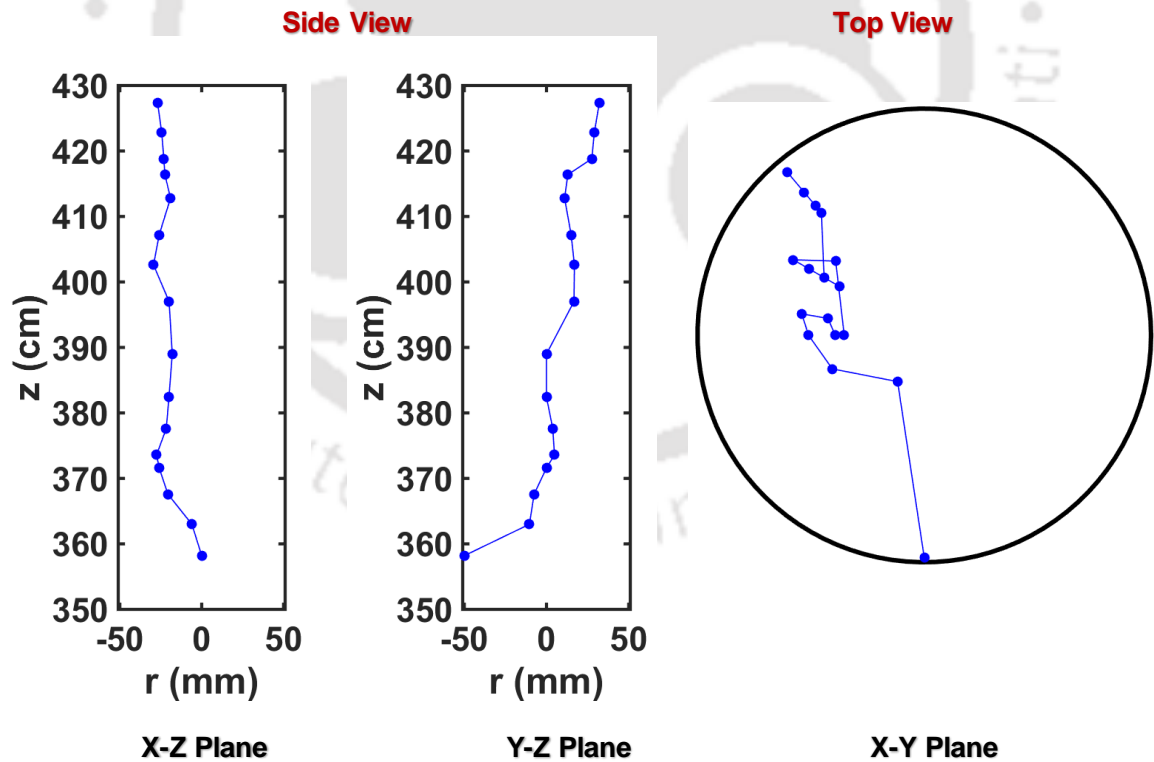


Figure 4.5: Lagrangian track of tracer in a different plane

It should be noted that solid motion differs according to the operating conditions, following were observed in all the conditions. Most of the observations are similar to the laboratory scale setup. From the position time series, instantaneous Lagrangian velocities are obtained by time differentiation. Eulerian velocities are obtained by forming virtual grid and assigning the velocities according to the midpoint of the velocity vector. An optimal grid is necessary as explained in the section previous chapter.

It is important to acknowledge that the dynamics of solid motion exhibit variations depending on the operational conditions. The entirety of solid motion is consistent and closely resembles those with laboratory-scale setups. The process of deducing instantaneous Lagrangian velocities from the time series Lagrangian position involves temporal differentiation of the Lagrangian position. On the other hand, figuring out Eulerian velocities requires setting up a virtual grid where velocities are carefully assigned based on the midpoint of the velocity vectors. The necessity for an optimized grid becomes evident, a topic that received comprehensive elucidation in the previous chapter. Different grids were tried. In Figure 4.6, different grid sizes based on the number of divisions in the radial section is presented. It's clear that when using 7 and 9 divisions, the mean and fluctuation velocity are similar. However, with 5 divisions, some vital information near the wall is missing. On the other hand, with 9 divisions, there are notable differences in the mean and RMS velocity profiles compared to 4 and 5 divisions. Therefore, five divisions in the radial direction appear to be the best choice.

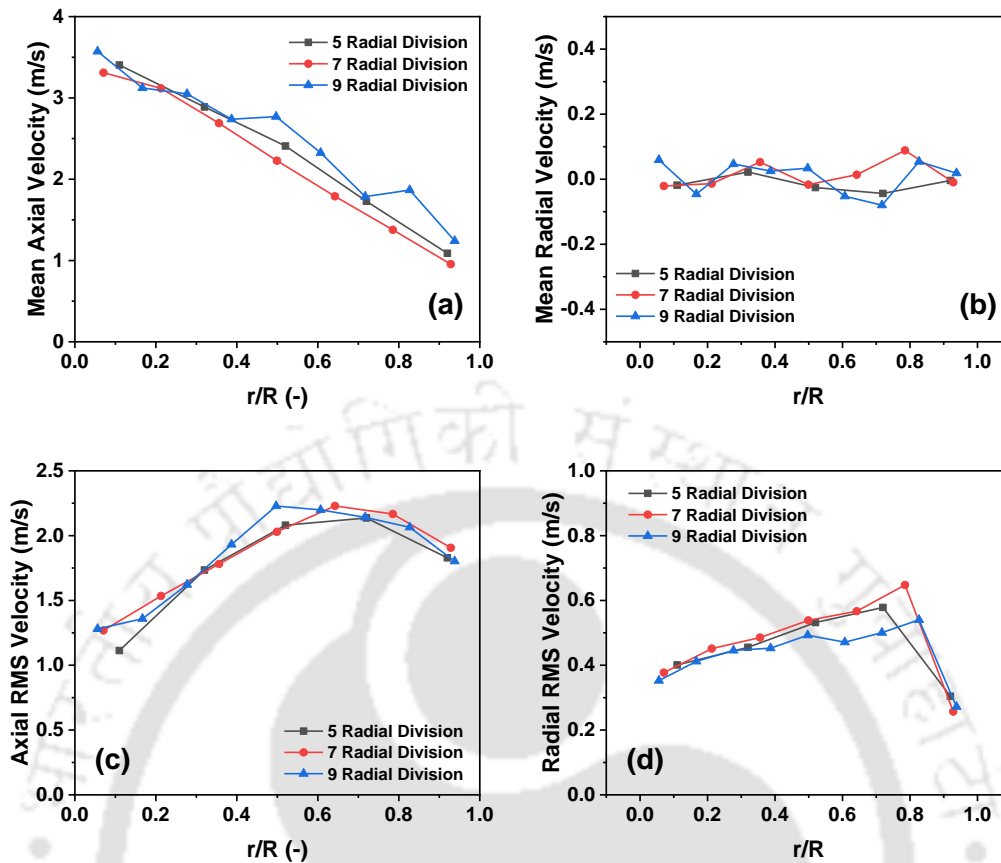


Figure 4.6: Azimuthally averaged (a) mean axial velocity, (b) mean radial velocity, (c) axial RMS velocity and (d) radial RMS velocity profiles with different grid sizes for operating condition of $G_s = 150 \text{ kg/m}^2\text{s}$ and $U_g = 7.6 \text{ m/s}$

Figure 4.7 shows the effect of height on the mean and fluctuating velocity components at the middle section of the riser. In the middle section, flow is developed, mean and RMS velocity are almost constant. The mean axial, mean radial, axial RMS, and radial RMS velocities are presented for the heights of 3.7, 3.9, and 4.1 m of the riser. It is important to note that 3.5 – 4.5 m represent the RPT scan zone for the middle section of the riser. Furthermore, in terms of resolution and sensitivity, the contour map shows that the 3.6 – 4.2 m region offers better accuracy. Therefore, for the middle section, all velocity flow profiles are presented at 3.9 m height.

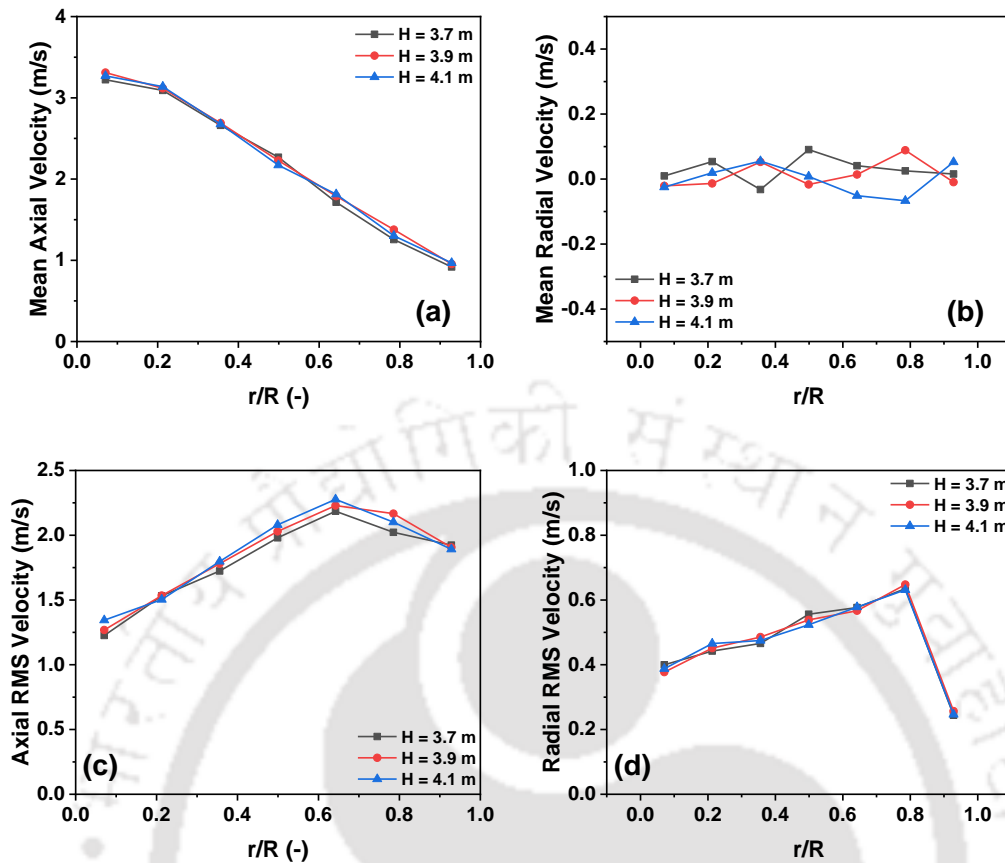


Figure 4.7: Azimuthally averaged (a) mean axial velocity, (b) mean radial velocity, (c) axial RMS velocity and (d) radial RMS velocity profiles at different heights for operating condition of $G_s = 150 \text{ kg/m}^2\text{s}$ and $U_g = 7.6 \text{ m/s}$

4.5 RPT Results and Discussion

In the present work, experiments are carried out in a CFB riser bottom and middle sections to analyze solid flow in the riser. Operating parameters are carefully chosen to allow systematic analysis of the impact of solid flux and inlet gas velocity in a high-flux riser with Geldart Group B particles. Different choking velocities (Bi and Grace, 1995) are calculated as by using equations 3.5, 3.6, and 3.7. Prior to the experiment, it is ensured that all operating conditions fell under the fast fluidized bed regime. Detailed choking velocities are presented in the previous chapter. It can be observed from Figure 4.8 that the current

riser diameter and solid particle size V_{mp} is lower than V_{ca} , which indicates the absence of core-annular regime irrespective of operating condition.

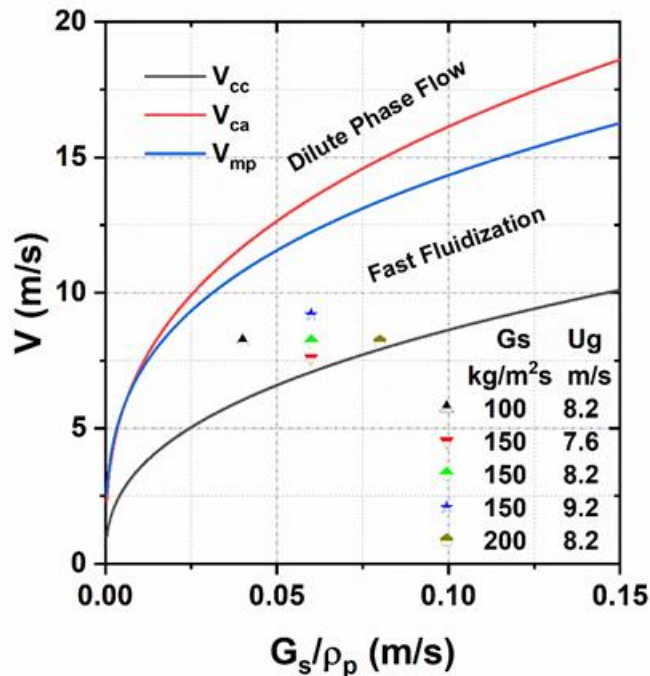


Figure 4.8: Flow regime diagram (Bi and Grace, 1995) with operating conditions

4.5.1 Lagrangian Track of Particle Position

Figure 4.9 shows some examples of the tracer particle trajectories at different time instances at the bottom (inlet of tracer particle in the riser to 1m height) and middle section for gas inlet velocity of 7.6 m/s and solid flux of 150 kg/m²s. Independent trajectories are found in each pass of tracer particle through the riser. It is clearly visible that in each track solid is predominantly moving in axial direction. Though some lateral motion (radial and tangential) is observed, however they are mostly dispersive and less significant than axial movement. These lagrangian tracks can be classified into two categories: particle track with back mixing and without back mixing. However, regardless of the operating conditions, it is found that the first type of trajectories (without back mixing) predominate. At lower inlet gas velocities (7.6 m/s), a significant number of tracks with back mixing are observed

(Figure 4.9b). At higher velocity such tracks are minimal. For all the conditions the distance moved by the tracer particle between the constant time interval (frequency at which data is acquired) is not the same. This shows that independent of the tracer particle trajectory (with or without back mixing), the tracer particle sometimes accelerates and sometimes decelerates during its path.

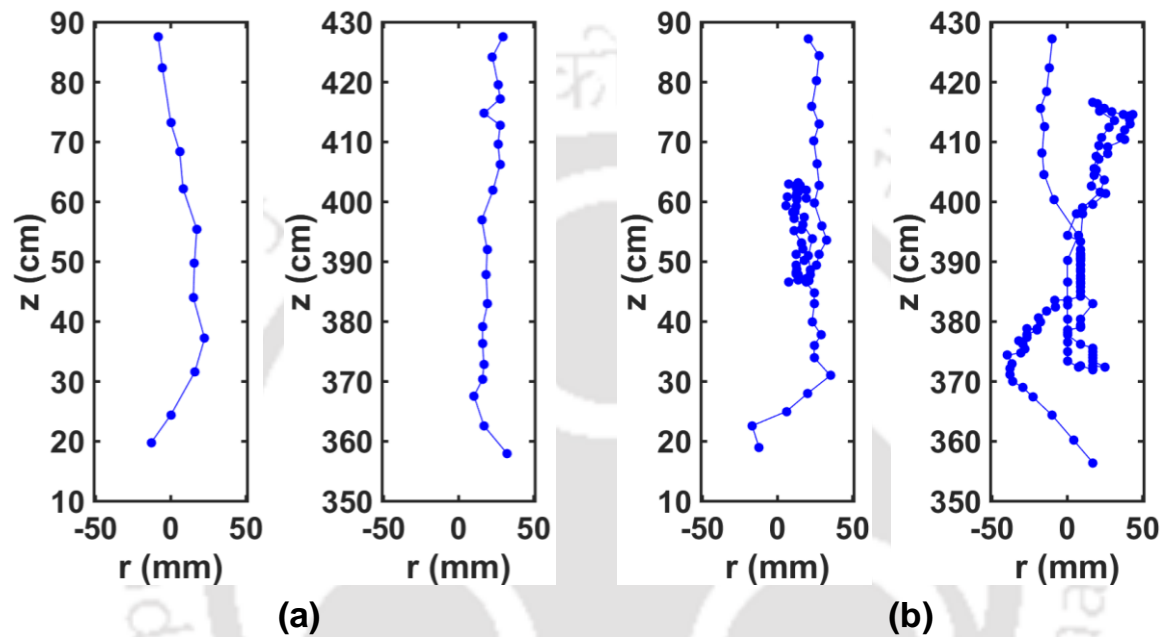


Figure 4.9: Typical tracer particle tracks (a) without back mixing and (b) with back mixing for gas inlet velocity of 7.6 m/s and solid flux of 150 kg/m²s

Figures 4.10—4.12 shows the movement of a group of particles at the bottom section of the riser with time. In each case, 30 tracks are selected randomly, which can be considered as a group of particles moving together. The particle start positions are selected when it enters the scan zone at the center of the riser, near the wall of the riser from the solid inlet side and the opposite of the solid inlet wall. It can be observed from Figure 4.11 that even though the tracer entered the scan zone from the center or near the wall zone, the particle initially stayed in the same zone. It is visible that after 50 milliseconds of entry into the scan zone, the particle starts to spread, and after 100 milliseconds the particle is all over the radial positions. It indicates all particles that do not follow a straight path, and irrespective

of their entry region, they can travel to any radial position after a certain period of time, though initially, they remain in the zone. It demonstrates that not every particle moves the same distance over time. Despite the fact that all particles travel on tortuous paths, not all particles do so to the same degree. Due to intricate particle-particle and particle-wall collisions, some follow a more tortuous path while others follow a relatively less tortuous path. The particle which travels relatively straight covers a greater distance than the one which follows a relatively more tortuous path. As the flow is developing at the bottom section, it can be observed from Figures 4.10, 4.11 and 4.12 that particle movements are nearly similar in the first 50 milliseconds after entering the riser, irrespective of operating conditions. However, the difference in height that the particles attained under various operating conditions are noticeable in the next 50 milliseconds (after 100 milliseconds). In comparison to 8.2 m/s and 7.6 m/s, particles travel a greater distance when the inlet gas velocity is 9.2 m/s. However, with varying solid flux, there is no noticeable difference in particle height.

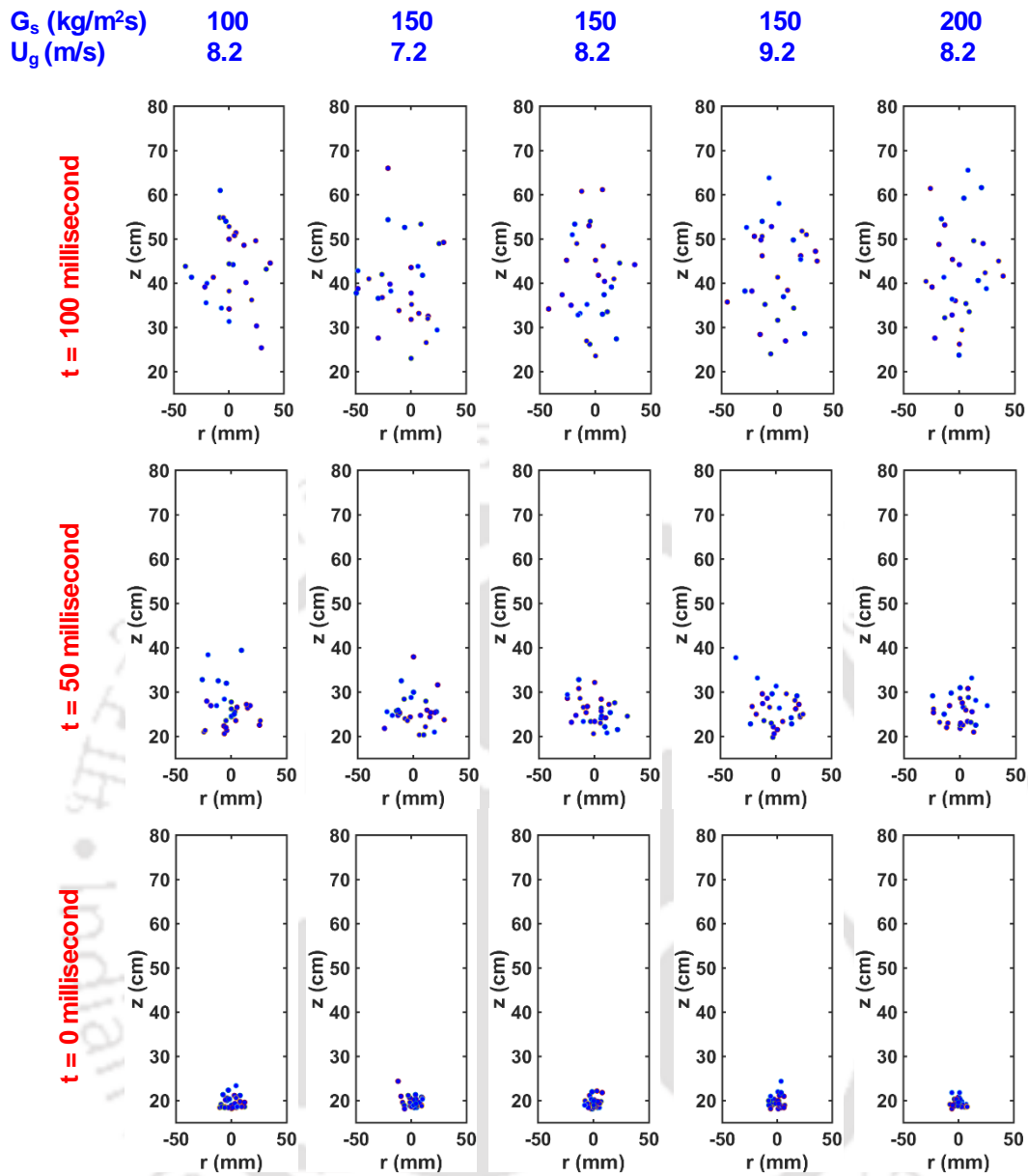


Figure 4.10: Particle position after 50 and 100 milliseconds when the tracer enters the scan zone from the center

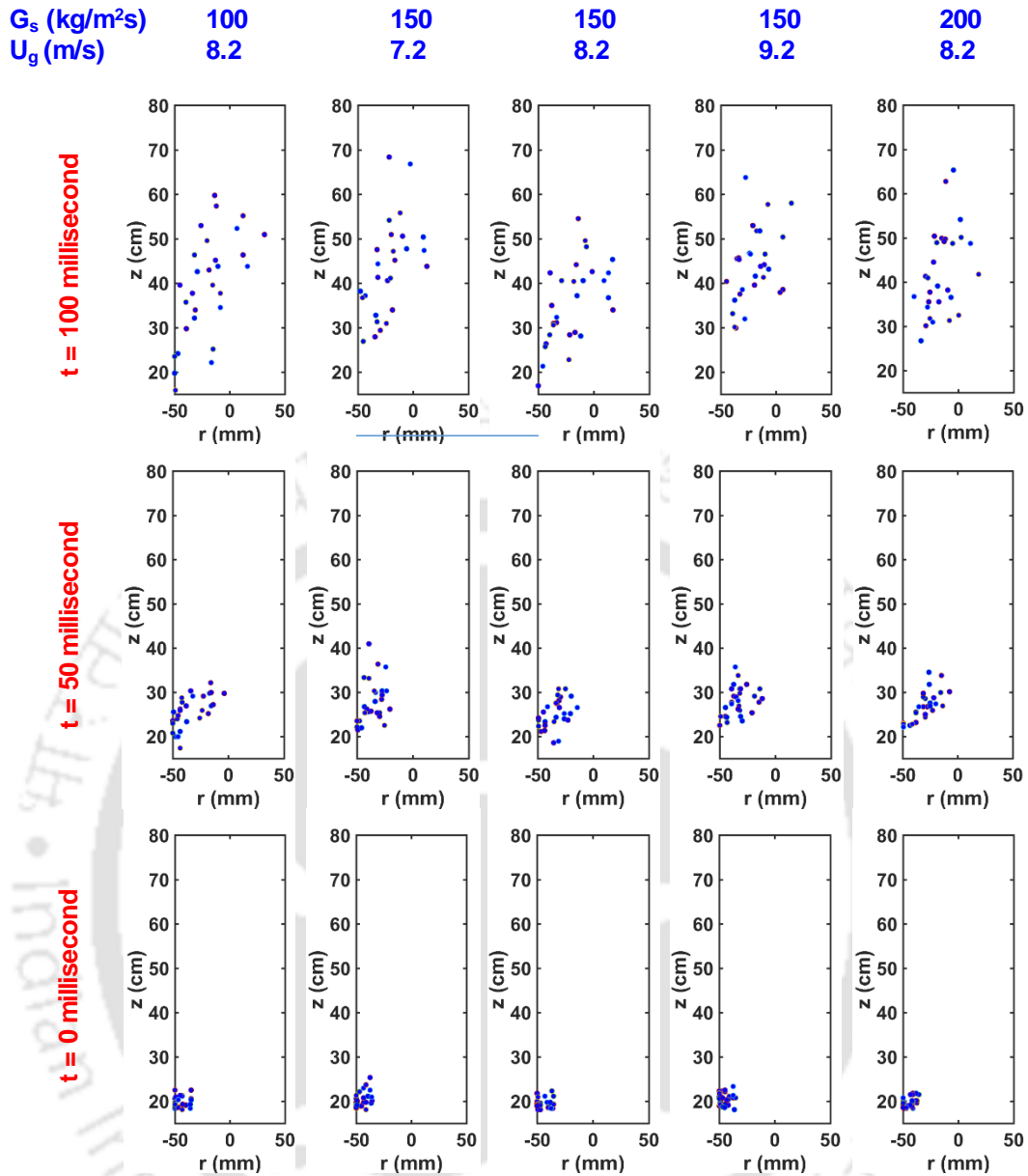


Figure 4.11: Particle position after 50 and 100 milliseconds when the tracer enters the scan zone from the wall region (solid inlet side)

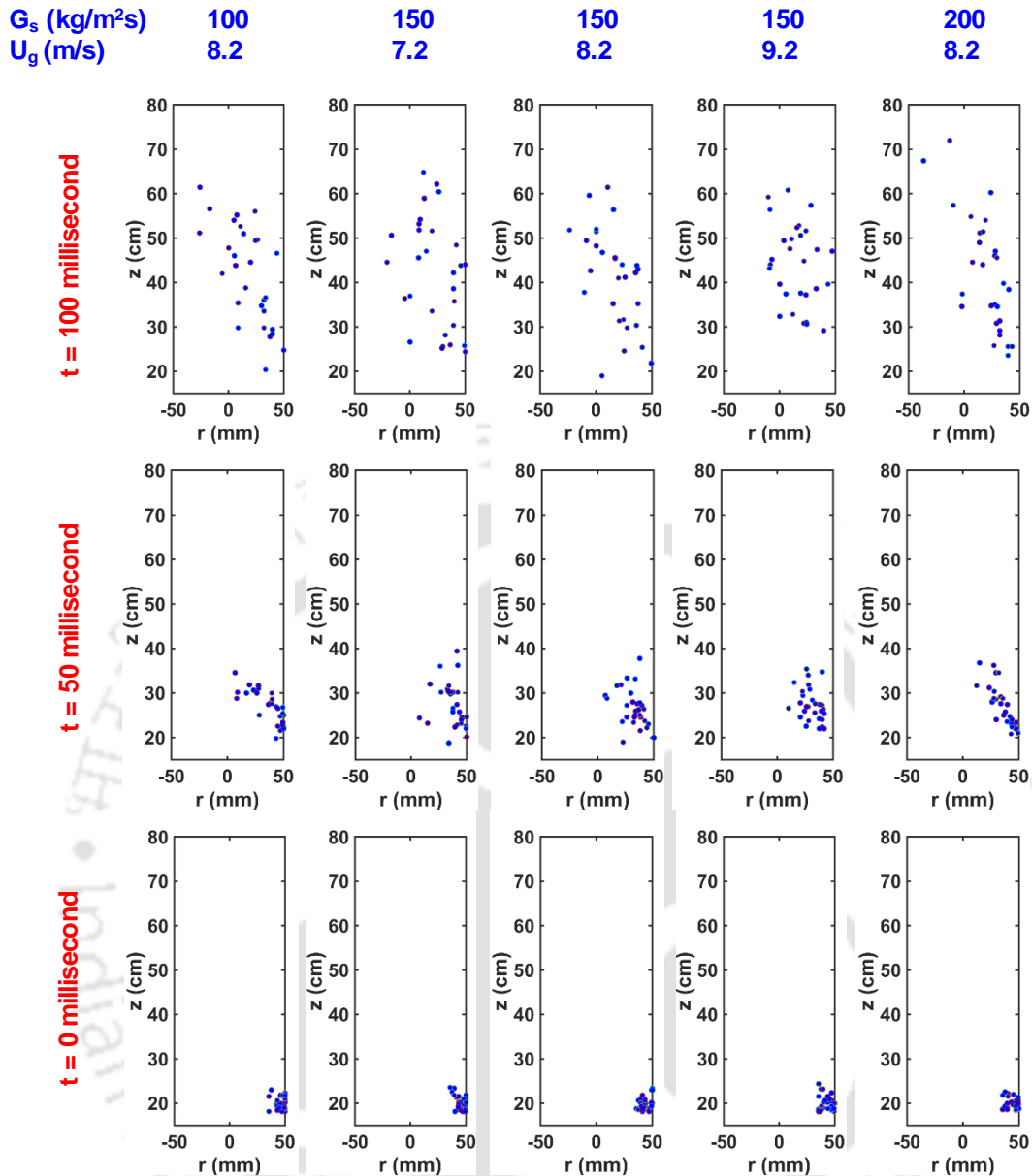


Figure 4.12: Particle position after 50 and 100 milliseconds when the tracer enters the scan zone from the wall region (opposite of solid inlet side)

Figure 4.13 shows the cross-sectionally normalized number of occurrence contour (NOC) map of the tracer at different heights for the bottom section. The number of occurrence contour plot, which displays the distribution of particle detections at various points in the flow, is a two-dimensional map. The number of occurrences of contour plots can provide insight into the fluid flow, such as the location of particle concentrations and the paths taken by particles. However, it is not possible to directly convert the NOC contour map to the concentration plot. Apart from concentration, local velocity also influences the occurrence.

When the tracer passes through a low-velocity zone, it travels slowly, and occurrence detections increase. It is difficult to decouple the concentration and velocity effects on occurrence. It can be observed that, irrespective of height and operating condition, NOC is low at the center and higher near the wall. It is a good indicator of a higher solid concentration near the wall. In Figure 4.14, a normalized NOC map for the middle section of the riser is presented. At higher gas velocity (9 m/s), the distribution of NOC appears relatively uniform, implying a uniform distribution of solids. In contrast, at lower gas velocity (7.6 m/s), a noticeable change in NOC near the wall can be observed, indicating a higher solid holdup near the wall region.



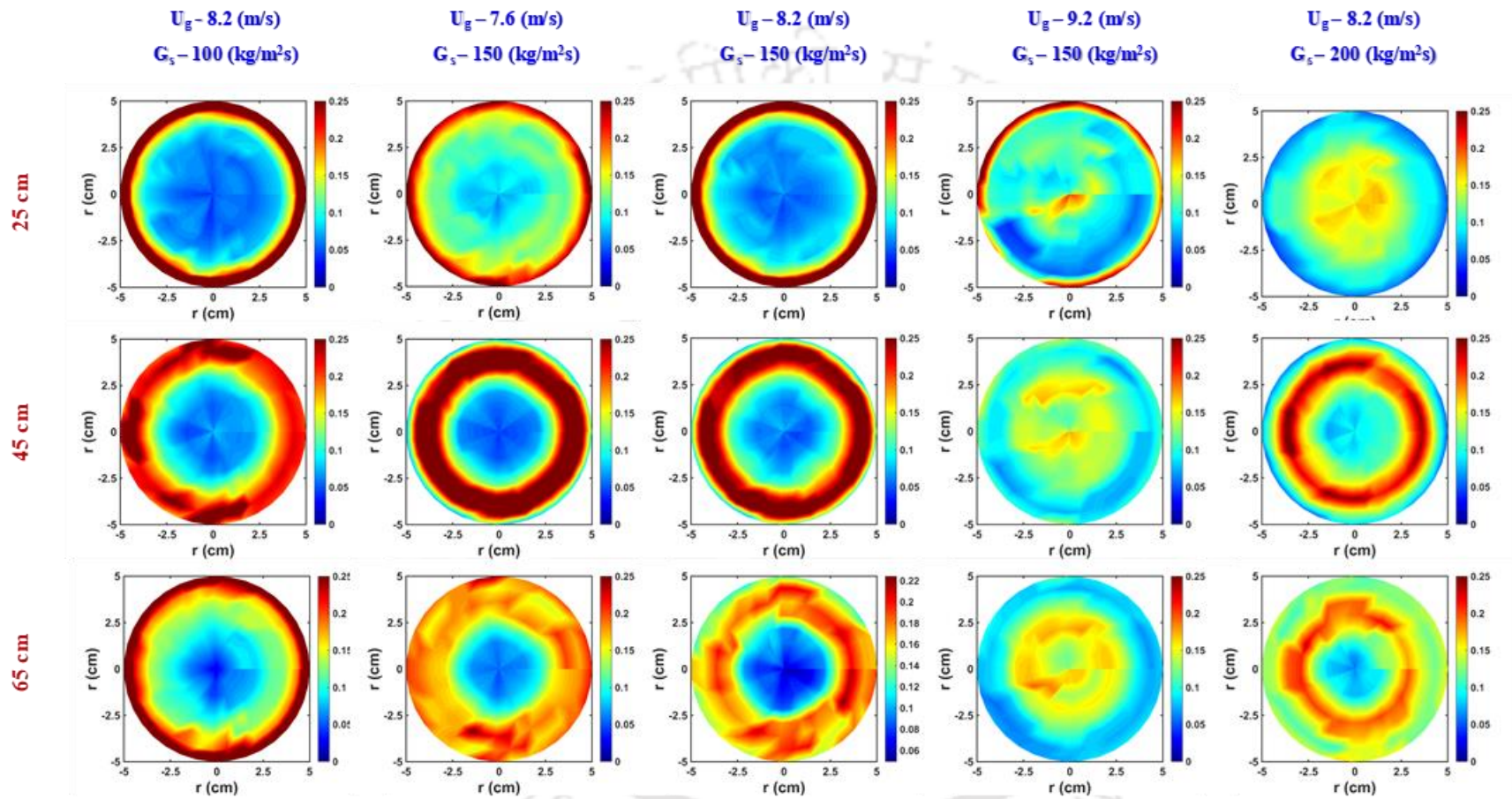


Figure 4.13: Normalized number of occurrence contour plots at different heights and operating conditions at the bottom section

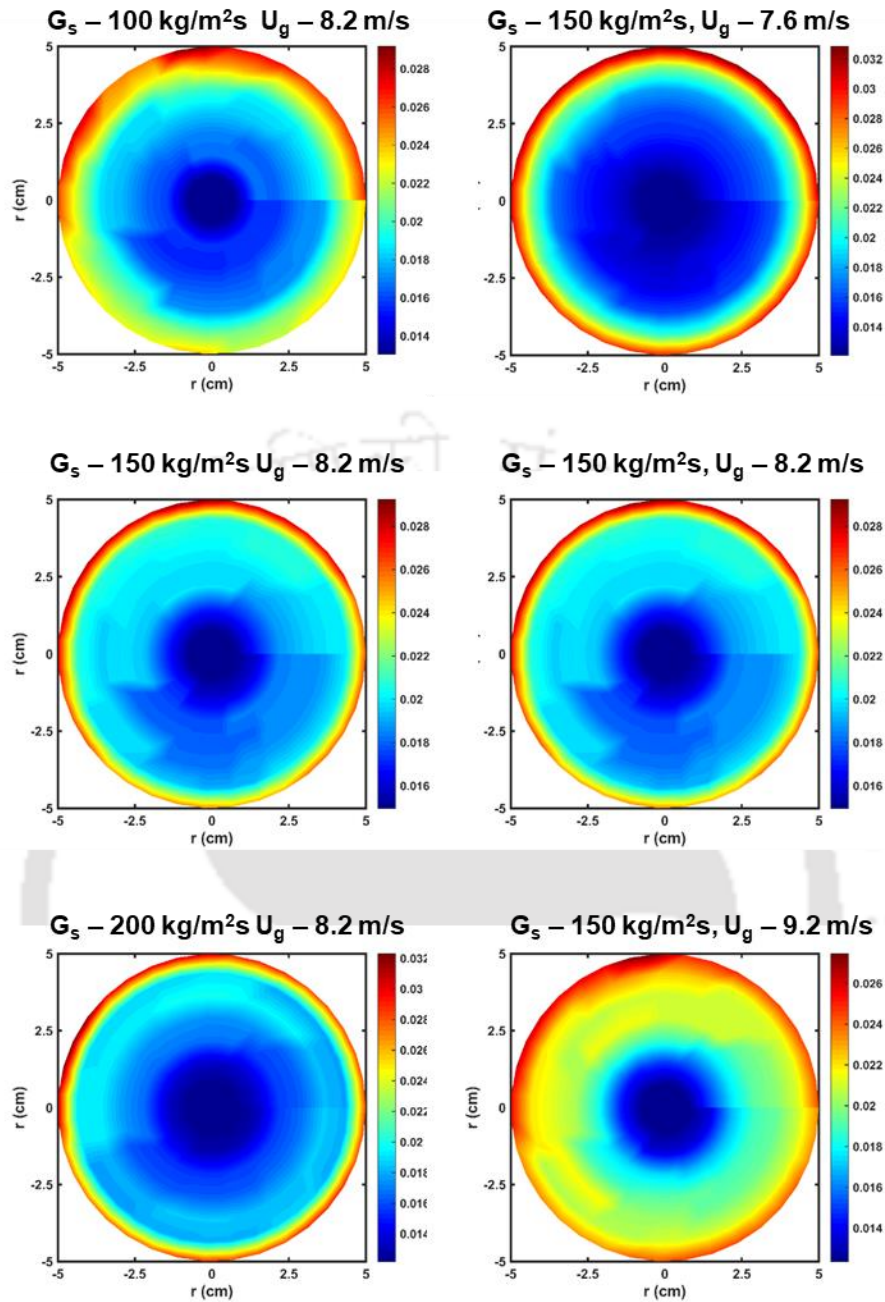


Figure 4.14: Normalized number of occurrence contour plots for (a) different solid flux at a gas velocity of 8.2 m/s and (b) different gas velocities at a solid flux of 150 kg/m²s at the middle section of riser

4.5.2 PDF of Instantaneous Velocity

In Figures 4.15, 4.16, and 4.17, the probability distribution function (PDF) of instantaneous axial velocity is depicted for three different operating conditions at the solid inlet wall, center of the riser, and opposite to the solid inlet wall at 25, 45 and 65 cm height

respectively. In all cases, unimodal velocity distribution can be observed. For all the cases positive instantaneous velocity is observed at the center of the riser. However, near the wall (both solid inlet and opposite to solid inlet) instances of negative instantaneous velocities are observed. This shows that near the wall solid occasionally move downward, but on average, they move upward. Bhusarapu et al. (2006) and Fiedler et al. (1997) presented solid phase instantaneous velocity distribution of gas-solid riser. At the height of 25 cm, some instances of downward motion of the solids are visible even at the center of the riser. As the solids move up in the riser (at the height of 45 and 65 cm) the negative instances of the instantaneous axial velocity disappear at the center of the column. However, for all the conditions, the negative instantaneous velocity is observed near the wall (both at solid inlet and opposite to solid inlet walls) for all heights. This is mainly because of the low gas velocity (due to the no-slip condition) and enhanced particle-particle and particle-wall collision near the wall

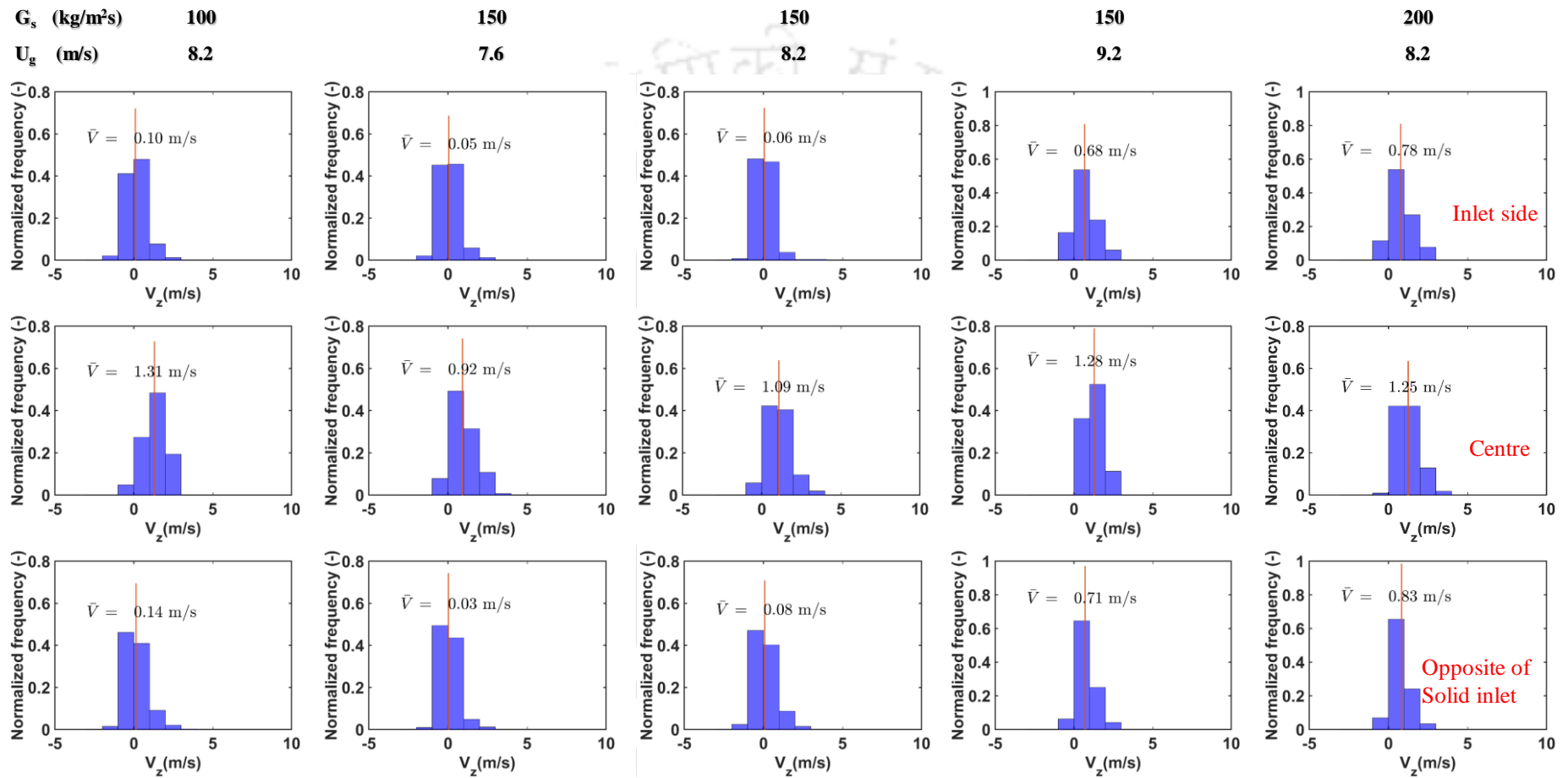


Figure 4.15: Normalized histogram diagram of instantaneous velocity near the wall (solid inlet side) at the center and near the wall (opposite side of the solid inlet) at the height of 25 cm from the primary air inlet

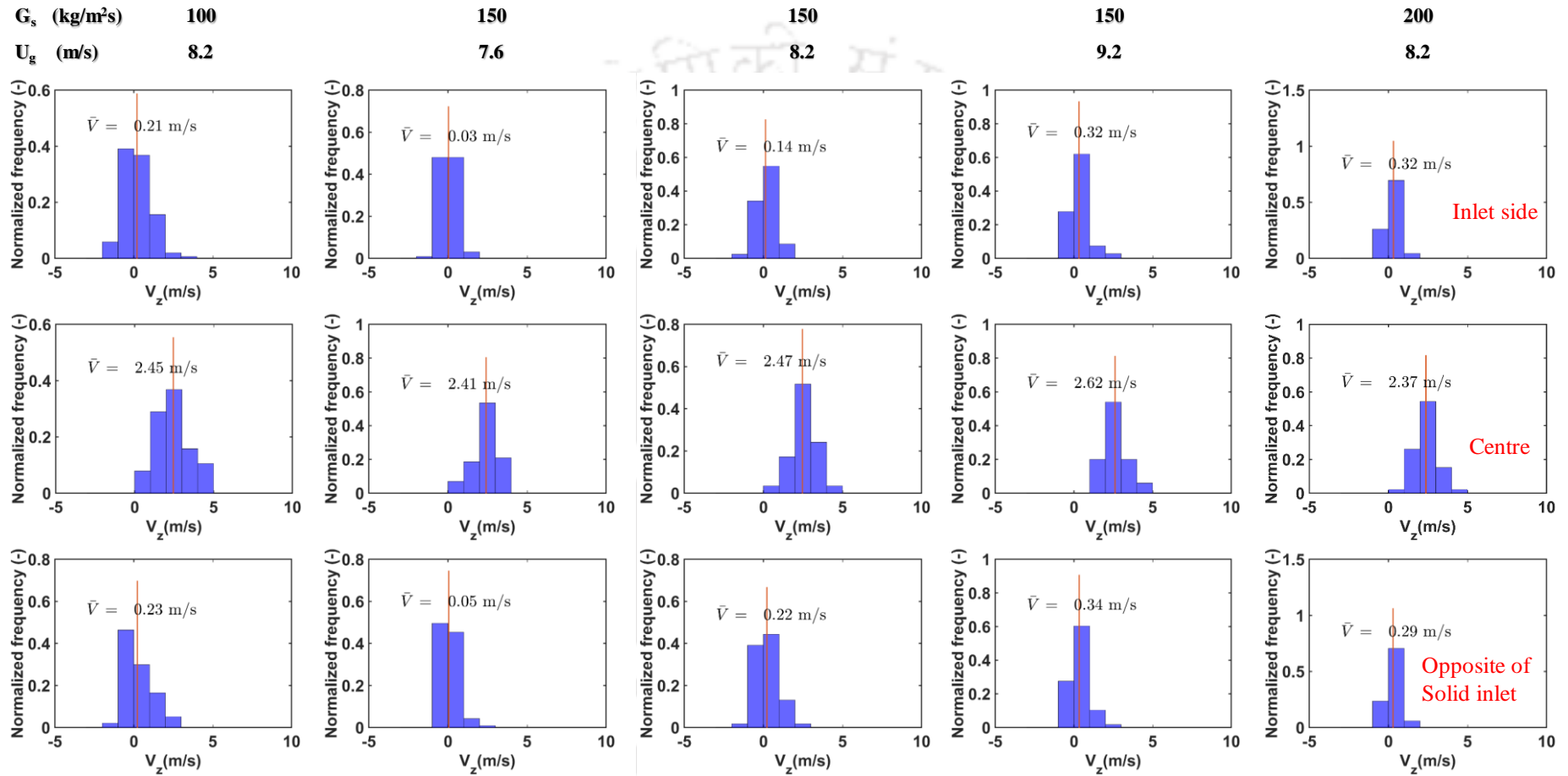


Figure 4.16: Normalized histogram diagram of instantaneous velocity near the wall (solid inlet side) at the center and near the wall (opposite side of the solid inlet) at the height of 45 cm from the primary air inlet

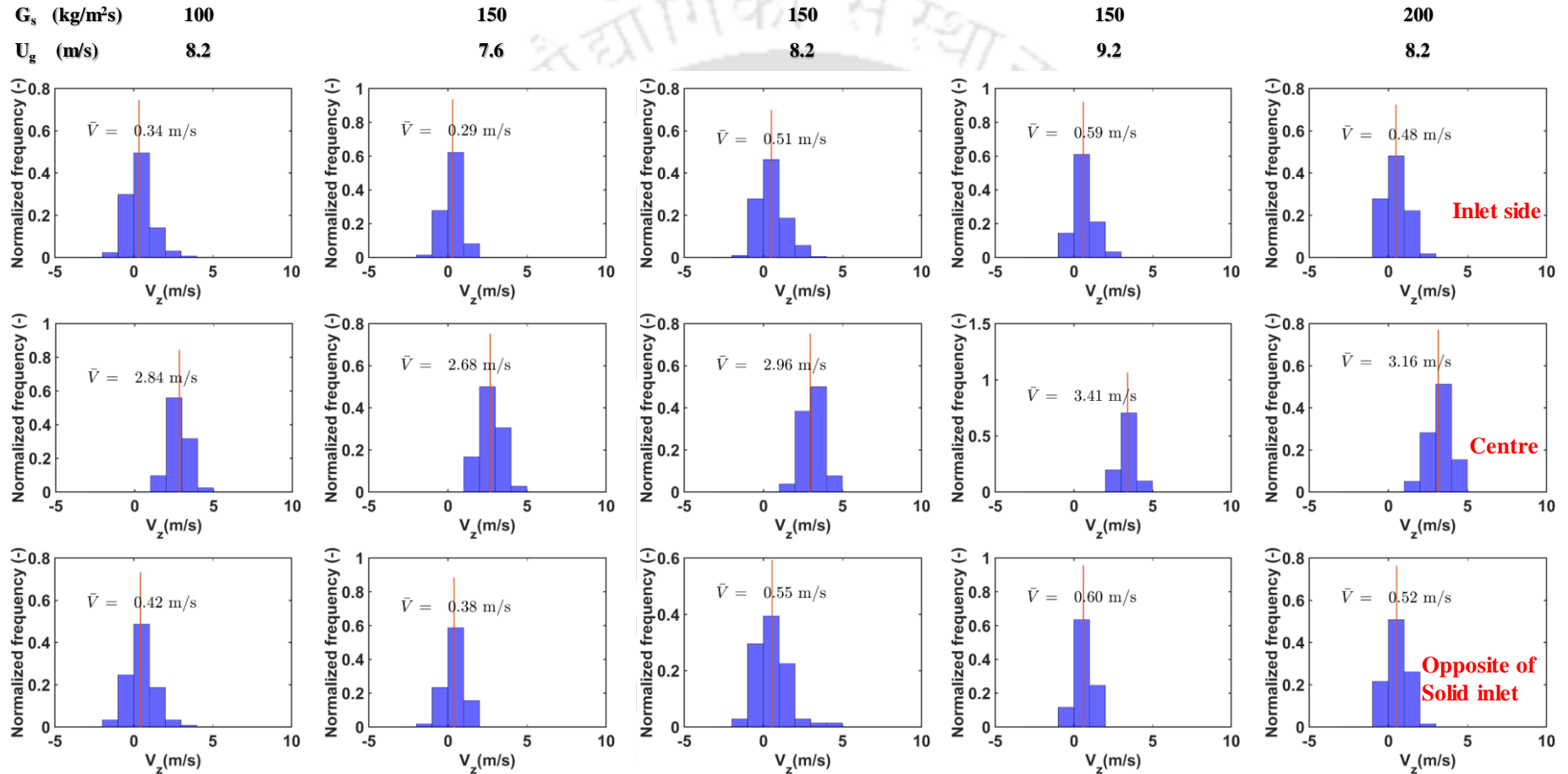


Figure 4.17: Normalized histogram diagram of instantaneous velocity near the wall (solid inlet side) at the center and near the wall (opposite side of the solid inlet) at the height of 65 cm from the primary air inlet

Figure 4.18. shows the probability distribution function (PDF) of instantaneous axial velocity at three radial locations: column center ($r/R=0$), annular zone ($r/R=0.5$) and adjacent to the wall ($r/R=0.96$) for different operating conditions. The results show that at the central zone no negative instantaneous velocity is observed except for the solids flux of $150 \text{ kg/m}^2\text{s}$ and inlet gas velocity of 7.6 m/s . However, even at this condition, the occurrences and magnitude of negative velocity are very low. Therefore, it can be said that the solids are mainly moving upward at the center. At the annular zone and near the wall for all the operating conditions, considerable negative instantaneous velocity occurrences are also observed except for the inlet gas velocity of 9.2 m/s . Though, velocity distribution can be observed in the case of inlet gas velocity of 9.2 m/s , no negative instantaneous particle velocity is observed. This may be due to the high gas velocity which prevents the particles from falling down. Further, it is observed that occurrences of negative velocity are high near the wall as compared to the annular region. This may be due to the no-slip condition at the wall for gases and/or due to the high solids fraction near the wall. Though for most of the operating conditions, negative instantaneous velocity is observed at core annular and wall regions, mean velocity (shown by the red line) is always positive at all the regions irrespective of solids flux and gas velocity values. Hence, though solids are moving downward at some instances, the mean solids movement is upward. This indicates that the negative motion may be correlated with some mesoscale meta-stable structures that form for a certain time and lead to the negative velocity of solids. It may also be due to the particle-particle interaction forces, which may result in similar structures. The results indicate that the frequency of such structure formation is higher for low gas velocity systems than the high gas velocity systems. Bhusarapu et al. (2006) reported bimodal peaks from PDF instantaneous axial velocity at the core and annular region. No such bimodal

velocity distribution is observed at the bottom or middle sections of riser under current operating conditions.

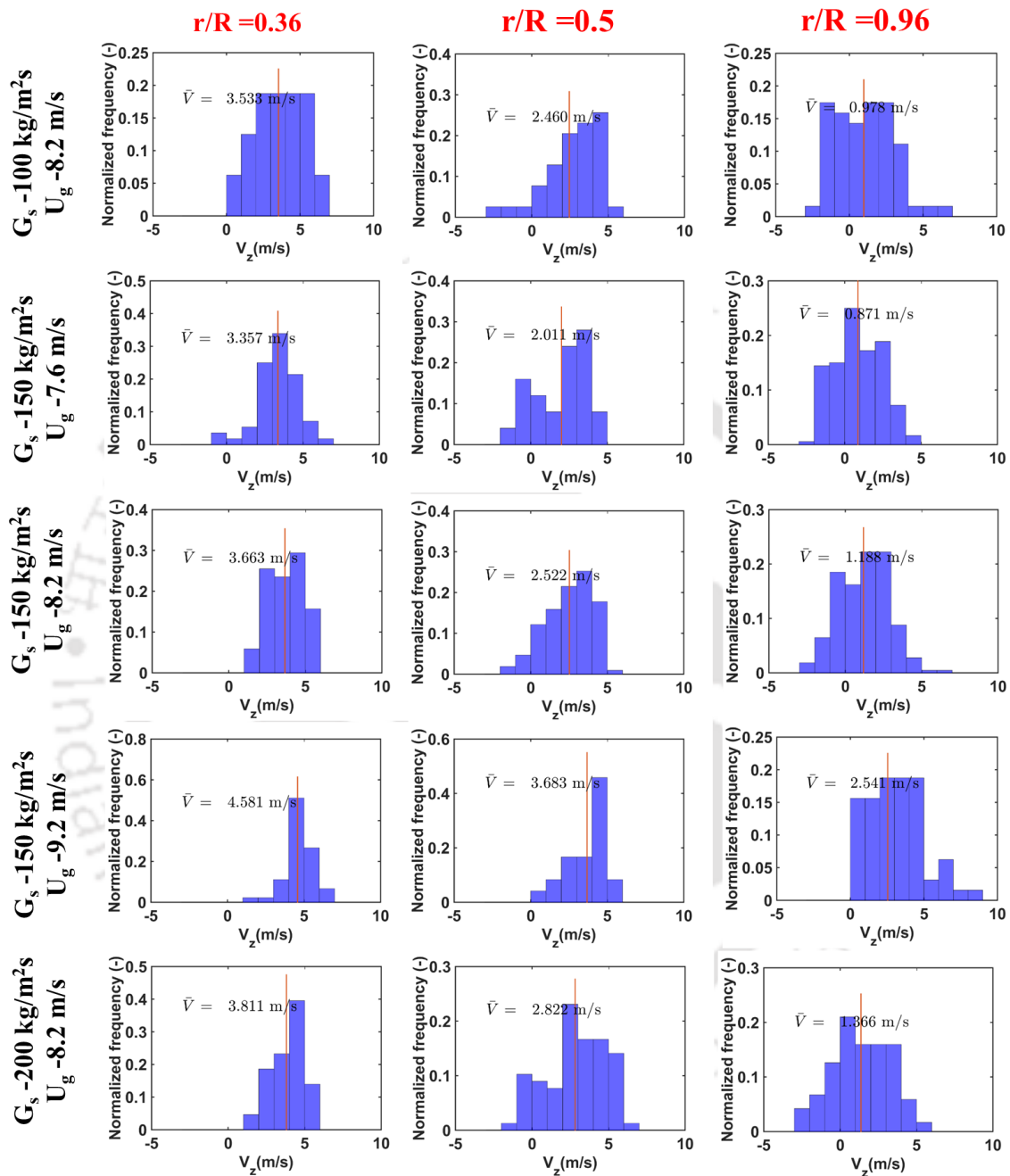


Figure 4.18: Normalized histogram diagram of instantaneous velocity at three radial locations (column center, core-annular zone, and adjacent to the wall) for middle section of the riser

4.5.3 Velocity Vector Plots

The velocity vector is displayed in Figures 4.19 and 4.20, showcasing the lower and middle sections of the riser, respectively. These visuals provide essential information regarding how the flow patterns are exhibited in the riser. In the lower section, a noticeable trend is observed: there is an increase in the average velocity with elevation. Despite the relatively low velocity at the solid inlet, a consistent downward motion is not observed, regardless of the conditions. Both the lower and middle sections depict the velocity within a 0-180 degree range. Although solids enter from one side, their velocity maintains a mostly symmetrical disposition. When examining the instantaneous velocity PDF diagram and the instantaneous position trace, instances of the tracer moving in a circular pattern are evident. Nevertheless, upon assessing the overall velocity vector, internal circulation is generally absent. The mean velocity predominantly points upward.

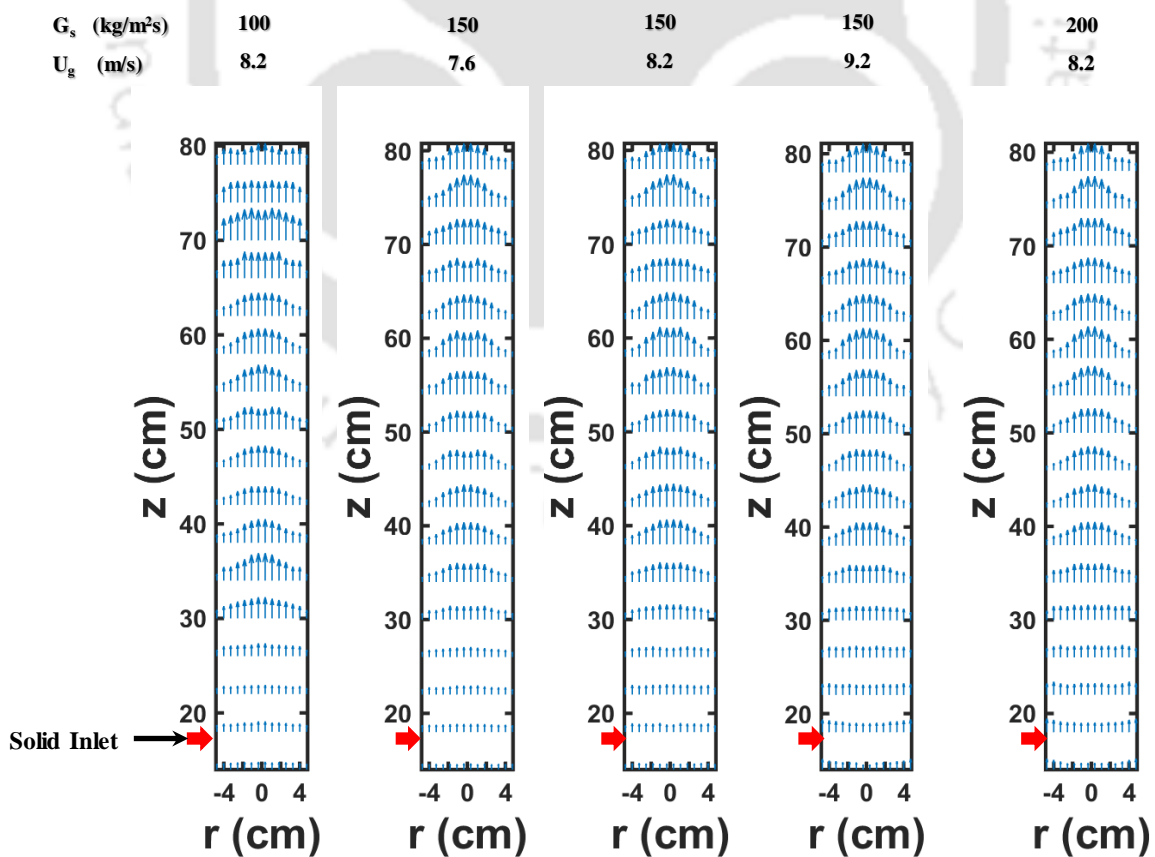


Figure 4.19: Velocity vector plot for the bottom section for different operating condition

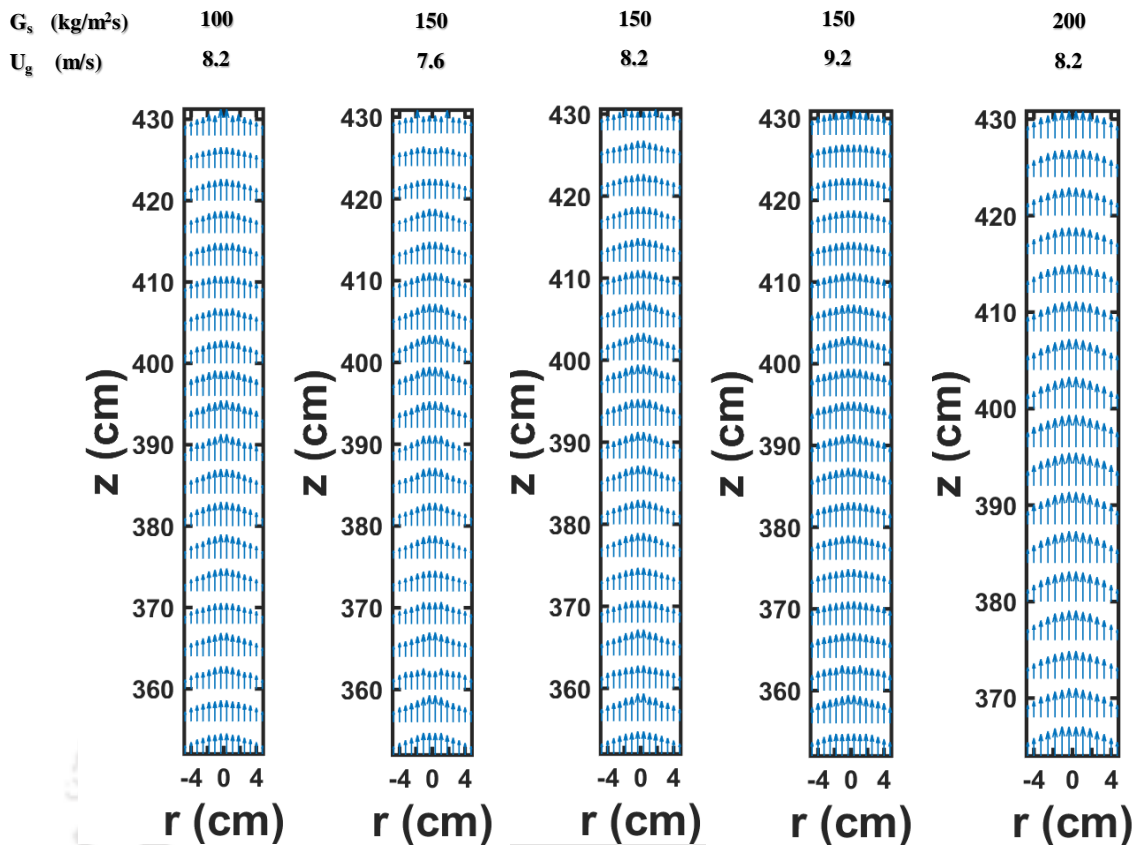


Figure 4.20: Velocity vector plot for the middle section for different operating conditions

4.5.4 Ensemble Averaged Velocity

It is visible from Figure 4.21 that the mean axial velocities are increasing with height. However, this increment is more rapid at the central zone of the riser than at the wall or annular region. The results show that within 65 cm from the inlet, the solid mean velocity at the core reaches almost 80% of its velocity from the middle section, where near the wall region, the velocity develops slowly. At the bottom section, the solid fraction remains high, that causes hindrance to solid motion. Hence, the mean solid velocities remain low at the bottom section. As the solids moves up, the flow starts developing and solid mean velocities increases.

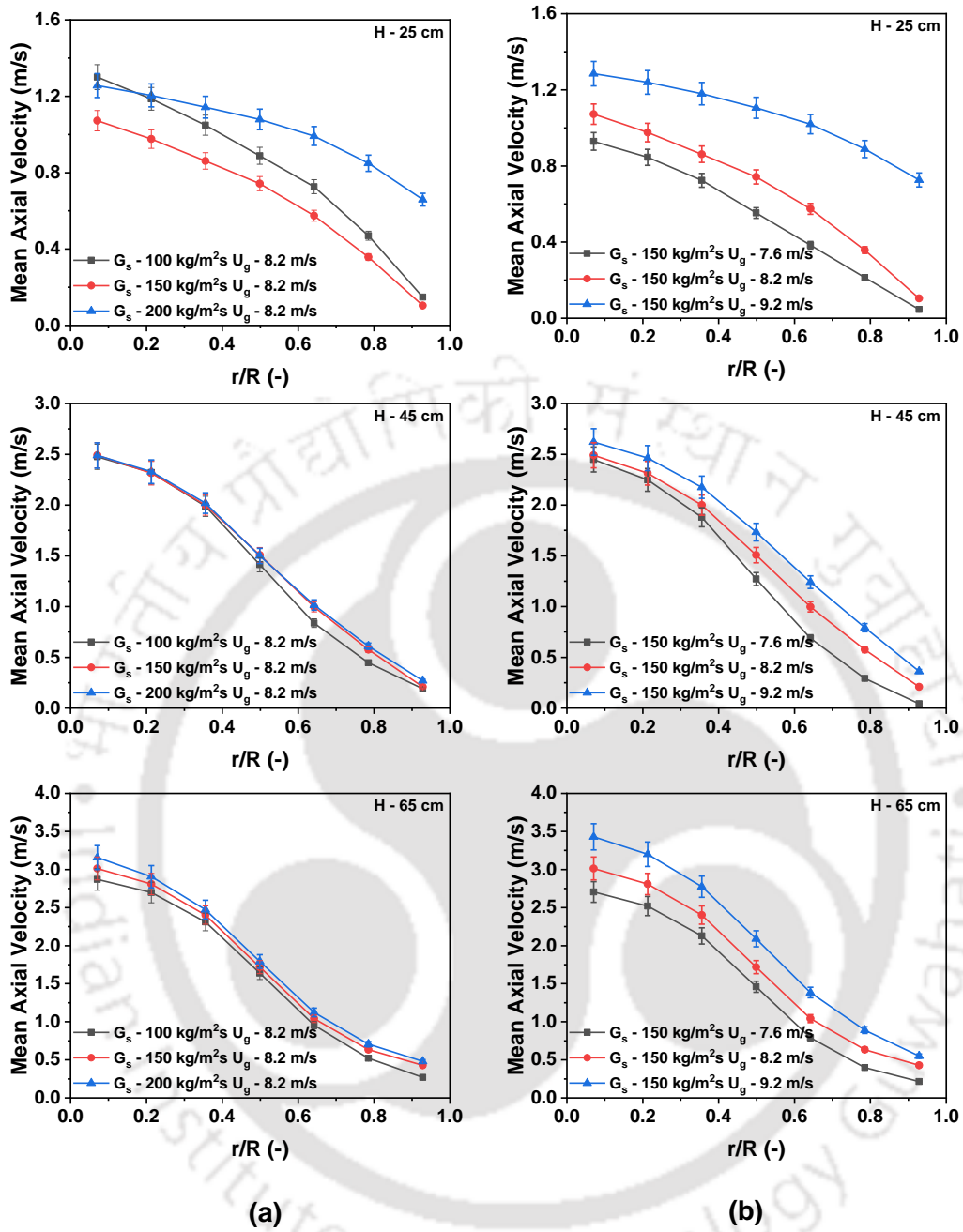


Figure 4.21: Radial variation of azimuthally averaged mean axial velocity with height at the bottom section for (a) different solid flux at a gas velocity of 8.2 m/s and (b) different gas velocities at a solid flux of 150 kg/m²s

Figure 4.21a shows the results at gas inlet velocity of 8.2 m/s for different solid fluxes. The results show that the mean velocity of the solid increases with increasing solid flux. However, the increase in velocity is relatively low at the heights of 45 and 65 cm. At the height of 25 cm, it is observed that the mean solid velocity first decreases with increase in

solid flux (from 100 to 150 kg/m²s) and then increases when solid flux is changed from 150 to 200 kg/m²s. It is because solid holdup is relatively low at lower solid flux, and solids can move relatively freely without any hindrance. With the increase in solid flux, the solid holdup increases and that reduces the mean solid velocity. However, after a critical solid flux (200 kg/m²s in the current case) solid is uniformly distributed across the whole cross-section. This leads to almost a flat solid mean velocity profiles and an increased slip velocity which pushes the solid upward. However, this phenomenon disappeared very fast (within a height range of 45 cm in the current case). Pantzali et al. (2015) and Van engelandt et al. (2007) reported that jet-like dense structure formation at the solid inlet section, which disappears within a few centimeters of the solid inlet. Figure 4.21b shows the mean solid velocity at different gas inlet velocities for 150 kg/m²s solid flux. The results show that solid velocity increases with an increase in gas inlet velocity. The results show that gas inlet velocity has a more significant effect on the solid mean velocity profile compared to the solid flux. Hence, it can be stated that for solid mean velocity, gas-solid interaction is critical and plays a vital role.

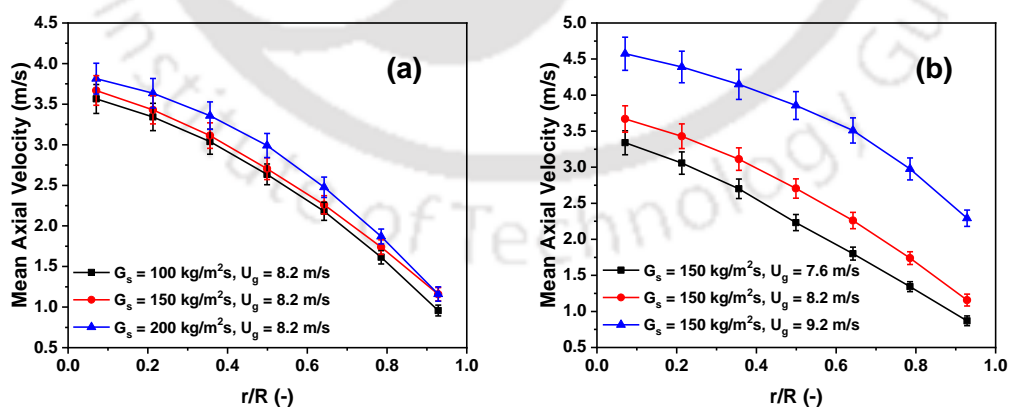


Figure 4.22: Radial variation of azimuthally averaged mean axial velocities at the middle section for (a) different solid flux at a gas velocity of 8.2 m/s and (b) different gas velocities at a solid flux of 150 kg/m²s

Figure 4.22a and 4.22b show the effects of solids flux and gas inlet velocity on the radial variation of azimuthally averaged mean axial solids velocity, respectively. For all the conditions solids velocity is found to be high at the center and low near the wall. This is because of no-slip boundary condition for the gas phase at the wall and higher particle-particle and wall-particle interaction. A similar profile is observed for Geldart Group A particles (Pärssinen and Zhu, 2001) and small size Group B particles (Bhusarapu et al., 2005). However, in those cases (Bhusarapu, 2005; Pärssinen and Zhu, 2001; Wang et al., 2014), the solids velocities were higher at the center than the gas inlet velocity. Tartan and Gidaspow (2004) reported similar kind of profile with Geldart Group B particles of similar size (530 μm) as the size of the particle used in the current work. They reported mean and fluctuating velocity components as well as granular temperature and stress profile at the fully developed section of riser. In the current work, for all the operating conditions, maximum axial velocity of solids is less than half of the inlet gas velocity. Further, the mean solids velocity near the wall and at the annulus are positive for all the conditions. Hence, in an average sense solid is moving upward, even though the particle size is much bigger. Similar phenomenon is reported by Anantharaman et al., (2017) for bigger size group B particles. They have observed upflow annulus for bigger particles in a pilot scale riser while many other researchers have reported downward motion of solid near the wall for Geldart Group A and smaller size Geldart Group B particles (Anantharaman et al., 2017; Bhusarapu et al., 2007; Breault et al., 2008; Huilin and Gidaspow, 2003; Pita and Sundaresan, 1993).

Figure 4.22b shows that for the same solids flux mean axial velocity increases with increase in inlet gas velocity. It may be due to the higher energy input into the system which is exchanged from gas to solid through gas-solid contacting. This shows that the probability of mesoscale meta-stable structure formation increases towards the wall (Chew et al.,

2012). It can be observed that the mean velocity profile in the case of gas inlet velocity 9.2 m/s is flatter as compared to the gas inlet velocity of 7.6 or 8.2 m/s. This shows that the bed becomes dilute at high velocity which reduces the probability of formation of the mesoscale metastable structure. An increase of solids flux at the same gas inlet velocity increases the mean axial solids velocity. However, the increment in mean axial solids velocity is insignificant as compared to the increment caused due to the increase in gas inlet velocity. It indicates that the gas-solid contacting plays a dominant role in deciding the mean solid velocity inside the riser. Increase in solid flux increases over all solid holdup when gas velocity remains unchanged. However, the change in voidage caused by the increased solids flux is not significant to affect the local gas velocity. Hence, the drag force acting on the solids remains almost same which leads to a small change in mean solid velocity. These results are in good agreement with the “similar profiles of mass flux” concept of Rhodes et al. (1992).

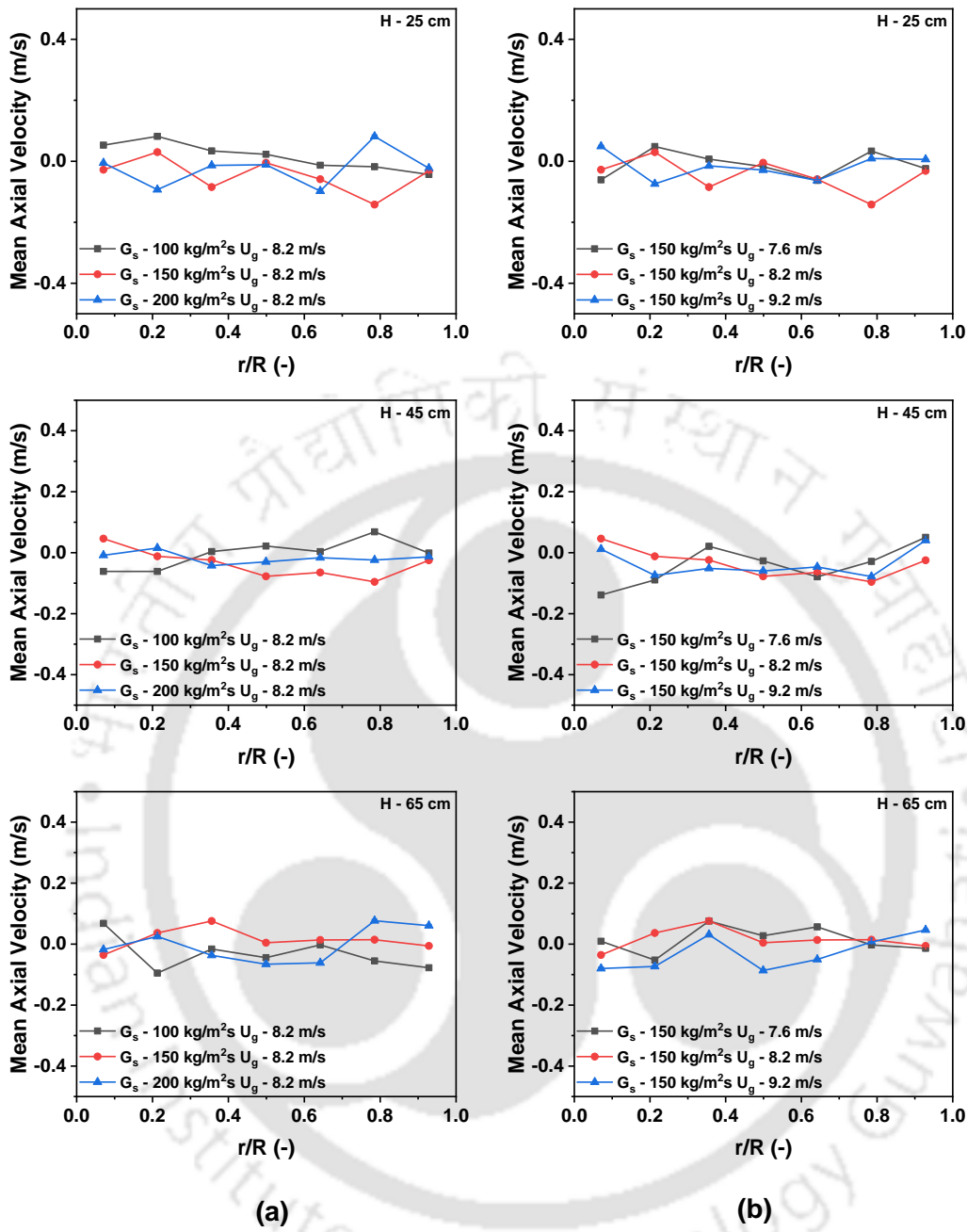


Figure 4.23: Radial variation of azimuthally averaged mean radial velocity with height at the bottom section for (a) different solid flux at a gas velocity of 8.2 m/s and (b) different gas velocities at a solid flux of 150 kg/m²s

Figures 4.23 and 4.24 show the mean radial velocity at the bottom and middle sections, respectively. Regardless of the setup or riser height, the average radial velocity consistently stays between -0.1 and 0.1. Negative radial velocity means particles move toward the wall, while positive axial velocity indicates motion toward the riser center. In the current

experiment, all average radial velocity values are under 0.1, showing minimal radial motion. It's important to highlight that obtaining a precise velocity of zero is indeed a challenging task due to the inherent limitations of any measurement technique. That is why RPT recorded a small value of radial mean velocity.

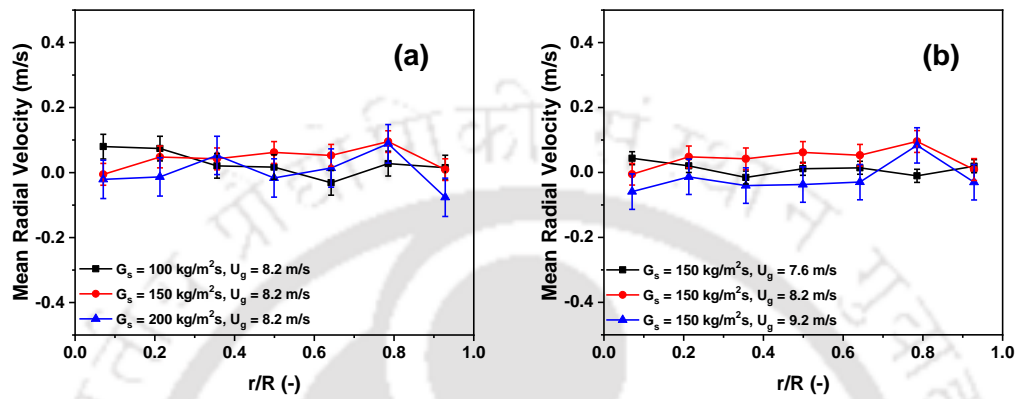


Figure 4.24: Radial variation of azimuthally averaged mean radial velocities at the middle section for (a) different solid flux at a gas velocity of 8.2 m/s and (b) different gas velocities at a solid flux of 150 kg/m²s

4.5.5 Solid Velocity Fluctuations

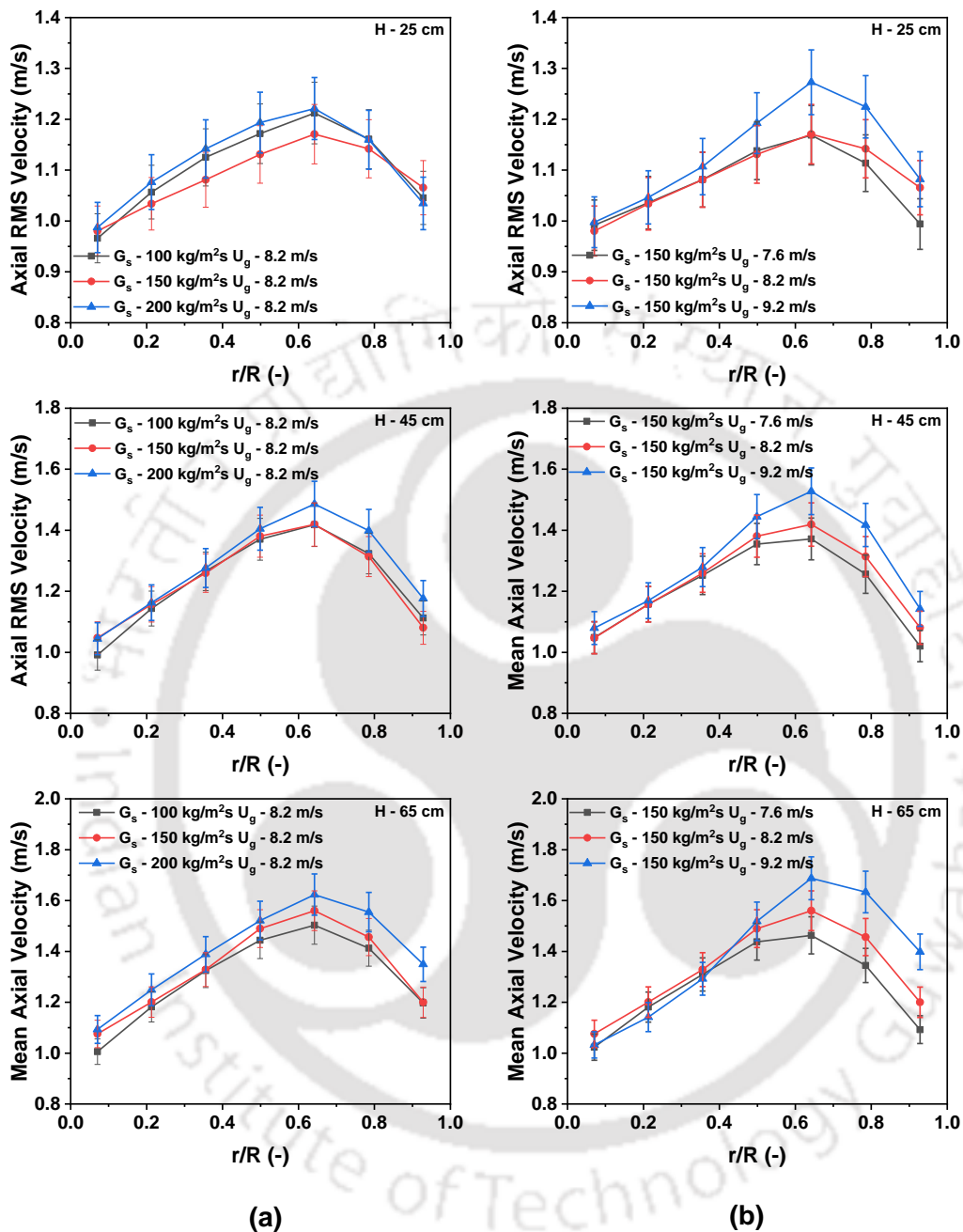


Figure 4.25: Radial variation of azimuthally averaged axial RMS velocity with height at the bottom section for (a) different solid flux at a gas velocity of 8.2 m/s and (b) different gas velocities at a solid flux of 150 kg/m²s

Particle velocity fluctuations is a crucial characteristic in light of the mixing of gases and solids (Van engelandt et al., 2007). Figures 4.25a and 4.25b show the radial variation of

azimuthally averaged axial root-mean-square (RMS) velocity profiles at different gas inlet velocities and solid flux respectively. Regardless of operating condition and height, axial RMS velocity is lower at the center and increases in the radial direction and again decreases near the wall. A similar phenomenon is observed in the middle section also. In the riser, the solid fraction is higher at the annular and near the wall region. However, due to lower axial solid velocities at the wall region, the axial solid RMS velocity remains low. It can be seen from Figure 4.25 that the axial RMS velocity increases with height at the bottom section of the riser regardless of the operating conditions. However, the solid axial RMS velocity at the bottom section is lower than that at the middle section, where the mean axial velocity is high. Pantzali et al. (2013) have discussed two competing mechanisms which influence the velocity fluctuation: collision frequency (particle–particle and particle–wall) and the mean free path between collisions. At higher solid holdup, the collision frequency is expected to be higher, thus increasing the velocity fluctuations. However, at the same time, higher solid holdup causes a lower mean free path between parts, which is responsible for lower velocity fluctuation.

The radial variation of azimuthally averaged root mean square of fluctuating component of solids axial velocity (axial RMS velocity) at different solid fluxes and inlet gas velocities is presented in Figure 4.26b. For all the operating conditions, axial RMS velocity is found to be low at the center, increases towards the core annular region and further decreases near the wall. The probability of mesoscale metastable structure formation increases towards the wall in the case of large Geldart Group B particles (Chew et al., 2012). This leads to an increase in particle-particle interaction and results in high axial solids RMS velocities at the core annular region even though the mean axial velocity of the solid is low. Further, adjacent to the wall solids axial RMS velocity decreases due to low mean solids velocity. However, the axial solids RMS velocity at the wall remains high compared to the column

center. As explained earlier, there are two competing mechanisms that influence the solids velocity fluctuations. At low gas inlet velocity (Figure 4.26b), the axial RMS velocity is higher at the center than high gas inlet velocity, while at the wall region, the trend is the opposite. Local solids concentration is less at the center, and particle-particle interaction is also low. With the increase of gas velocity, keeping the solids flux the same decreases the solids holdup, resulting in less particle-particle coalition. Hence lower gas velocity has a higher RMS axial velocity at the center. However, local solids holdup increases toward the wall as solids are largely pushed toward the wall. As a result, particle-particle collision is expected to be higher toward the wall compared to the central region. The mean free path at higher gas velocity further increases the velocity fluctuation. Hence higher gas velocity shows higher axial RMS velocity at the annular region and adjacent to the wall. These results indicate that solids are largely pushed towards the wall at high gas inlet velocity and the central region remains diluted. Therefore, the particle-particle interaction increases towards the wall where solid concentration is high and leads to higher value of axial RMS velocity. Pantzali et al. (2013) reported similar phenomena for Geldart Group A particle. Figure 4.26a shows the effect of solids flux at same gas inlet velocity. With increase of solids flux the riser becomes more densely packed which enhances the particle-particle interactions. Therefore, axial RMS velocity increases with an increase in solids flux. Bhusarapu et al. (2006) reported the same trend for smaller size Geldart Group B particles. An increase in the value of solids flux increases the solid holdup inside the riser. Therefore, these results also conclude that particle-particle interaction is mainly responsible for the solids velocity fluctuations and particle-particle interaction can be influenced by the gas-particle interaction.

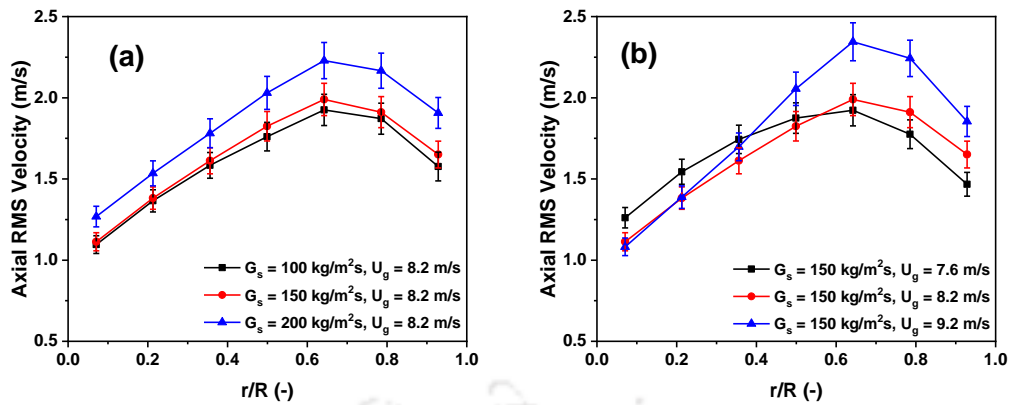


Figure 4.26: Radial variation of azimuthally averaged axial RMS velocities at the middle section for (a) different solid flux at a gas velocity of 8.2 m/s and (b) different gas velocities at a solid flux of 150 kg/m²s

Figures 27a and 27b show the radial variation of the solid radial RMS velocity for different solid fluxes at a gas velocity of 8.2 m/s and different gas velocities at a solid flux of 150 kg/m²s at different heights for the bottom section of the riser. Even though the mean radial velocity is negligible, the radial RMS velocity is significantly higher. Further, results indicate that the solid radial RMS velocity decreases with height for all the conditions, unlike the solid axial RMS velocity. At the bottom section of the column, the solid holdup is high. Hence, the instantaneous radial velocity is higher due to enhanced particle–particle interaction and radial mixing. Similar findings regarding height at the low-density riser bottom with Geldart Group A particles were reported by Pantzali et al. (2015). It is interesting to note that the solid radial RMS velocity at the bottom section is higher than the middle section unlike the axial RMS velocity. This indicates that at the riser bottom, the radial mixing of solids is higher, and with the height radial mixing decreases.

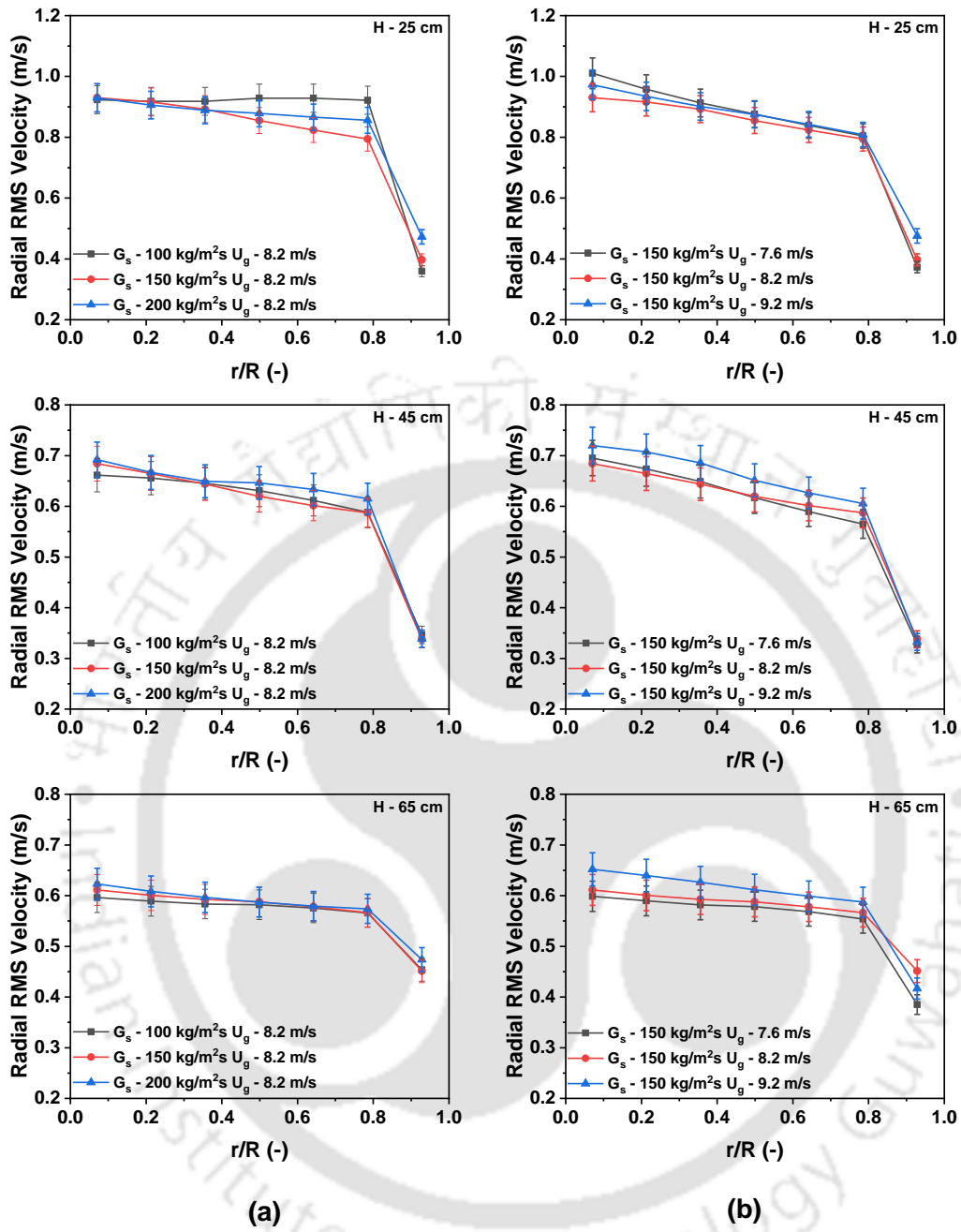


Figure 4.27: Radial variation of azimuthally averaged radial RMS velocity with height at the bottom section for (a) different solid flux at a gas velocity of 8.2 m/s and (b) different gas velocities at a solid flux of 150 kg/m²s

The radial RMS velocity profiles at the middle section of riser for different solid fluxes at a gas velocity of 8.2 m/s and for different gas velocities at a solid flux of 150 kg/m²s are shown in Figures 4.28a and 4.28b, respectively. Although the mean radial solid velocity is very low, significant radial RMS velocity is observed for all the conditions. However, the

magnitude of radial RMS velocity is 2–4 times lower than the axial RMS velocity. The magnitudes of radial RMS velocities are between 0.3–0.7 m/s, where the axial RMS velocity values fall between 1 and 2.5 m/s. This shows that the solid motion is primarily in the axial direction only. The trend of radial RMS velocity is same as that of the axial RMS velocity. This shows that the same mechanism of interaction also governs the radial RMS velocity. At the center, the solid fraction is low; hence, the radial RMS velocity is also low. Toward the wall, the probability of formation of the mesoscale metastable structure increases that enhances the particle–particle interaction. Therefore, the radial RMS velocity is high toward the wall. However, near the wall, the particle radial motion is restricted; hence, a dip can be observed in the radial RMS velocity. Figure 4.28b shows that the radial RMS velocity increases with an increase in the gas inlet velocity. This is mainly due to the enhancement of solid momentum at high gas velocity. Furthermore, with the increase in solid flux, the radial RMS velocity marginally increases (Figure 4.28a) due to an increase in solid holdup.

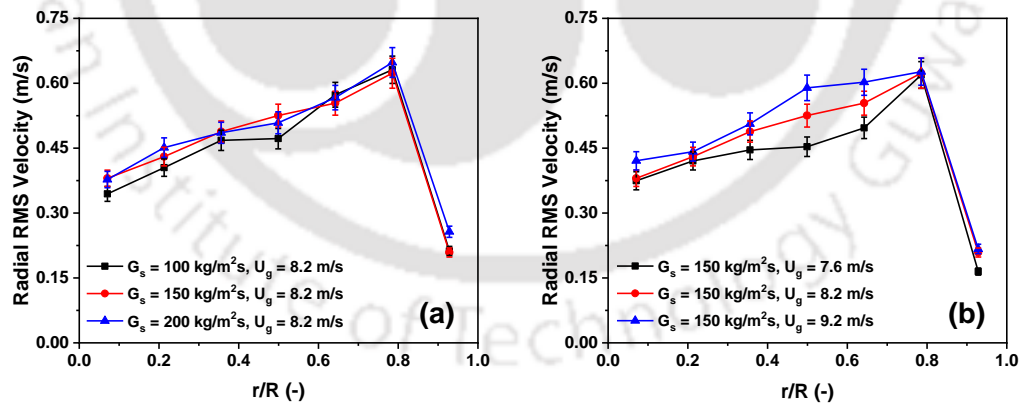


Figure 4.28: Radial variation of azimuthally averaged axial RMS velocities at the middle section for (a) different solid flux at a gas velocity of 8.2 m/s and (b) different gas velocities at a solid flux of 150 kg/m²s

4.5.6 Granular Temperature

The radial profile of the azimuthally averaged particle granular temperature is shown in Figure 4.29 for different solid fluxes at a gas velocity of 8.2 m/s and for different gas velocities at a solid flux of 150 kg/m²s for the bottom section. The average of the variances of the instantaneous velocities component is used to measure the granular temperature. In the present work, a similar approach (Gidaspow et al., 2004) is used to calculate the solid granular temperature from axial and radial velocity fluctuations. Given that the motion is primarily in the axial direction and the axial velocity fluctuation is significantly higher than other components of velocity fluctuations, it can be seen in the current work that the granular temperature exhibits a similar trend as that of the axial RMS velocity. Granular temperature is low at the center and increases in the radial direction and again reduces near the wall. Due to the no-slip gas velocity condition, the magnitude of the overall solid velocity is lower at the wall; hence, the granular temperature is low. The granular temperature of the solid increases with increase in solid flux (Figure 4.29a) as particle–particle collision increases due to enhanced solid holdup. Further, with increase in gas inlet velocity also granular temperature increases (Figure 4.29b). However, the granular temperature at the bottom section is lower than the granular temperature at the middle section of the riser as the axial velocity at the middle section is significantly higher than that at the bottom section.

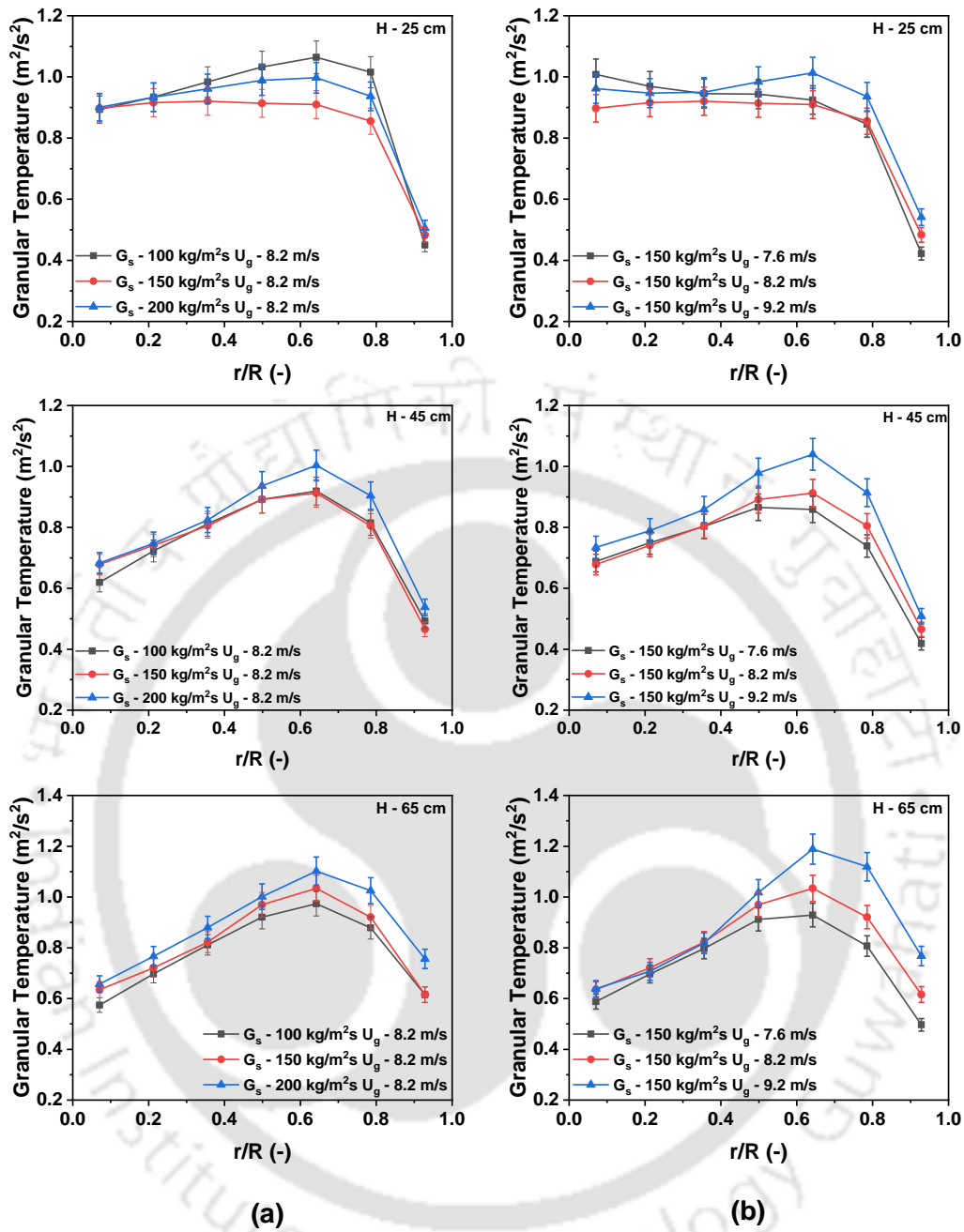


Figure 4.29: Radial variation of azimuthally averaged granular temperature with height at the bottom section for (a) different solid flux at a gas velocity of 8.2 m/s and (b) different gas velocities at a solid flux of 150 kg/m²s

Figure 4.31 shows the radial variation of azimuthally average granular temperature at middle section of the riser which gives the idea of energy available for dissipation. In the current work, it is observed that the granular temperature shows a similar trend as of axial

RMS velocity, much higher than other components of velocity fluctuations as the motion is primarily in the axial direction. The granular temperature is low at the center, increases while moving toward the wall, and decreases further close to the wall for all the conditions. The lower value of granular temperature at the center signifies low turbulent fluctuations. This is mainly due to the low solids present at the center, and gas–solid interaction is dominant there. The probability of structure formation is high at the annular region where the solid holdup is high. Hence, the value of granular temperature increases toward the annular region. Due to the no-slip condition, the gas velocity is relatively low adjacent to the wall, which reduces the magnitude of overall solid velocity fluctuations, although the particle–particle collision frequency remains high there. This results in lower granular temperature adjacent to the wall. These results further signify that both gas–particle and particle–particle interactions are crucial for determining the turbulence in gas–solid risers. Similar to the axial RMS velocity, with an increase in inlet gas velocity and solid flux, the granular temperature also increases due to an increase in turbulent fluctuations.

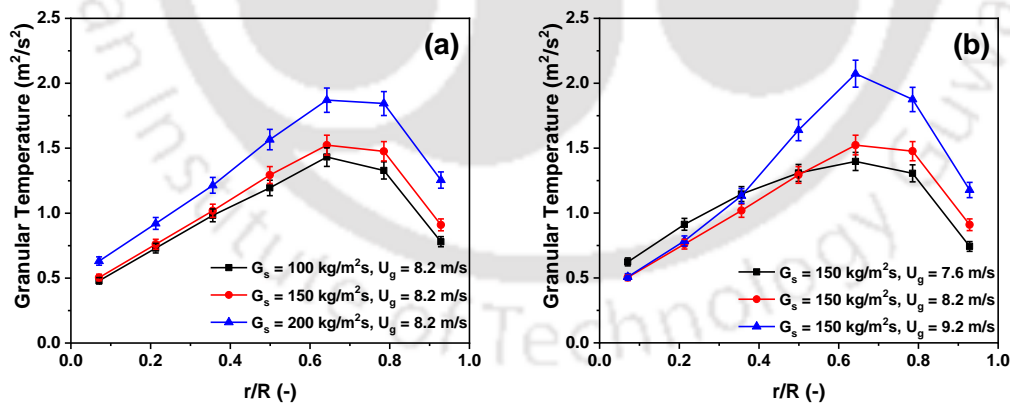


Figure 4.30: Radial variation of azimuthally averaged granular temperature at the middle section for (a) different solid flux at a gas velocity of 8.2 m/s and (b) different gas velocities at a solid flux of $150 \text{ kg/m}^2\text{s}$

4.5.7 Solid Stress

Figures 4.31 and 4.32 show the azimuthally averaged axial normal stress and shear stress with height for different solid flux and gas velocities, respectively, for the bottom section of the riser. Figures 4.33 and 4.34 show the azimuthally averaged axial normal stress and shear stress for the middle section of the riser. Variances of fluctuating velocity in the axial and radial velocities are calculated from instantaneous velocity measurements. This fluctuating or RMS velocity, is used to calculate normal and shear stress. Tartan and Gidaspow (2004) measured shear and normal stress from fluctuating velocity. A similar approach is used by Pantzali et al. (2015, 2013) and Bhusarapu et al. (2006) to calculate normal and shear stress. It can be observed from Figures 4.31 and 4.32 that the axial normal stress is 2 to 3 times higher than the shear stress for all the cases. Similar observations may also be obtained in the middle region, as seen in Figures 4.33 and 4.34. Both normal stress in the axial direction and shear stress are lower at the core region. This shows that both axial and radial components of the fluctuations are lower at the core region. Both normal and shear stress increase in the radial direction; however, it again decreases near the wall. This is mainly due to the increase in fluctuation velocities (as shown in Figures 4.25 and 4.26) and solid concentration (as shown in Figures 4.13 and 4.14) in the core annular region. Near the wall the solid fluctuation reduces due to the hindrance created because of the wall and low gas velocity due to the no-slip condition. The value reported by Pantzali et al. (2015, 2013) and Tartan and Gidaspow (2004) is much lower compared to the value observed for the current set of the experiments. Bhusarapu et al. (2005,2006) reported a much higher value in magnitude for both normal and shear stress as in all the above cases solid flux was very low and hence the fluctuation was higher.

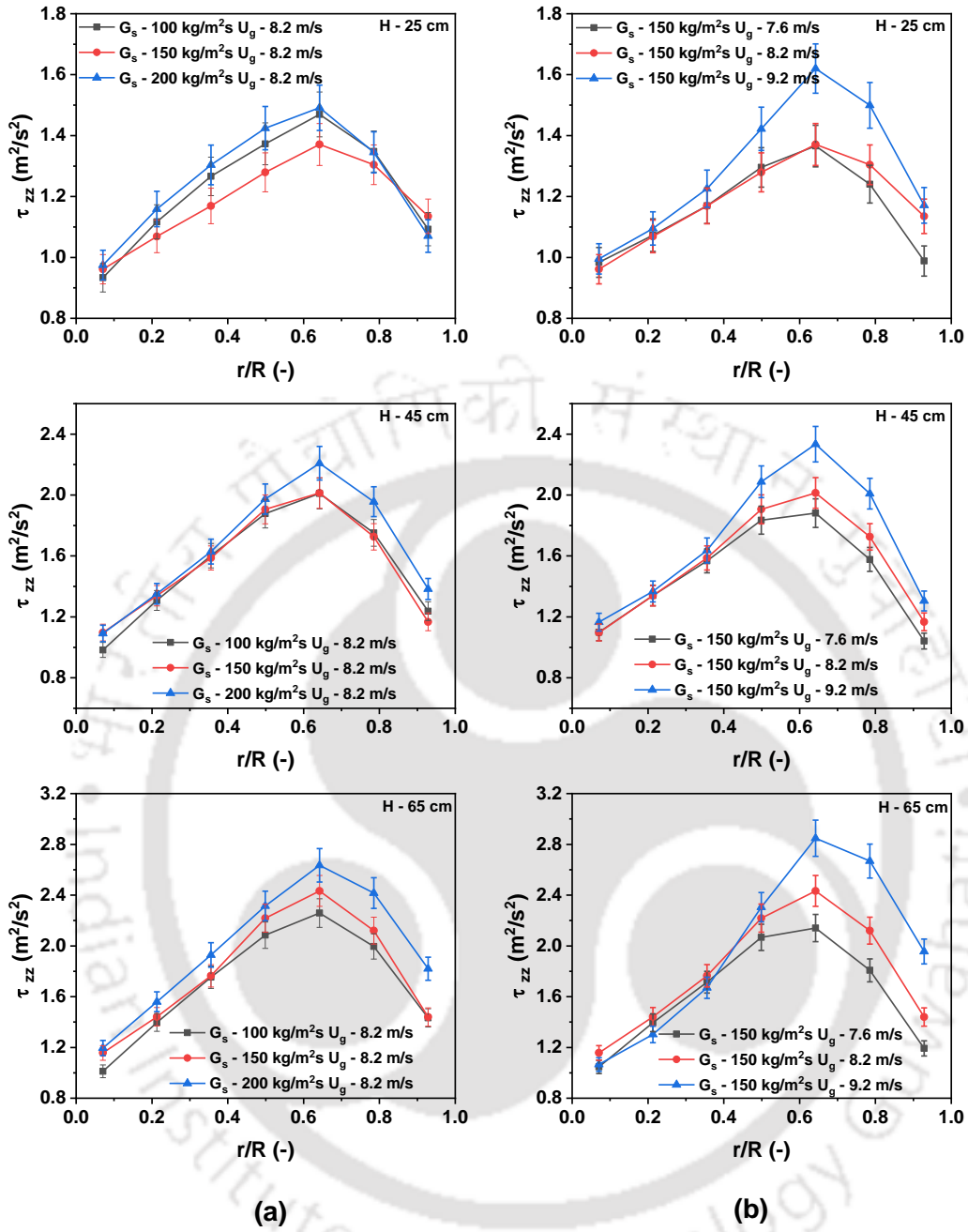


Figure 4.31: Radial variation of azimuthally averaged normal stress with height at the bottom section for (a) different solid flux at a gas velocity of 8.2 m/s and (b) different gas velocities at a solid flux of 150 $\text{kg/m}^2\text{s}$

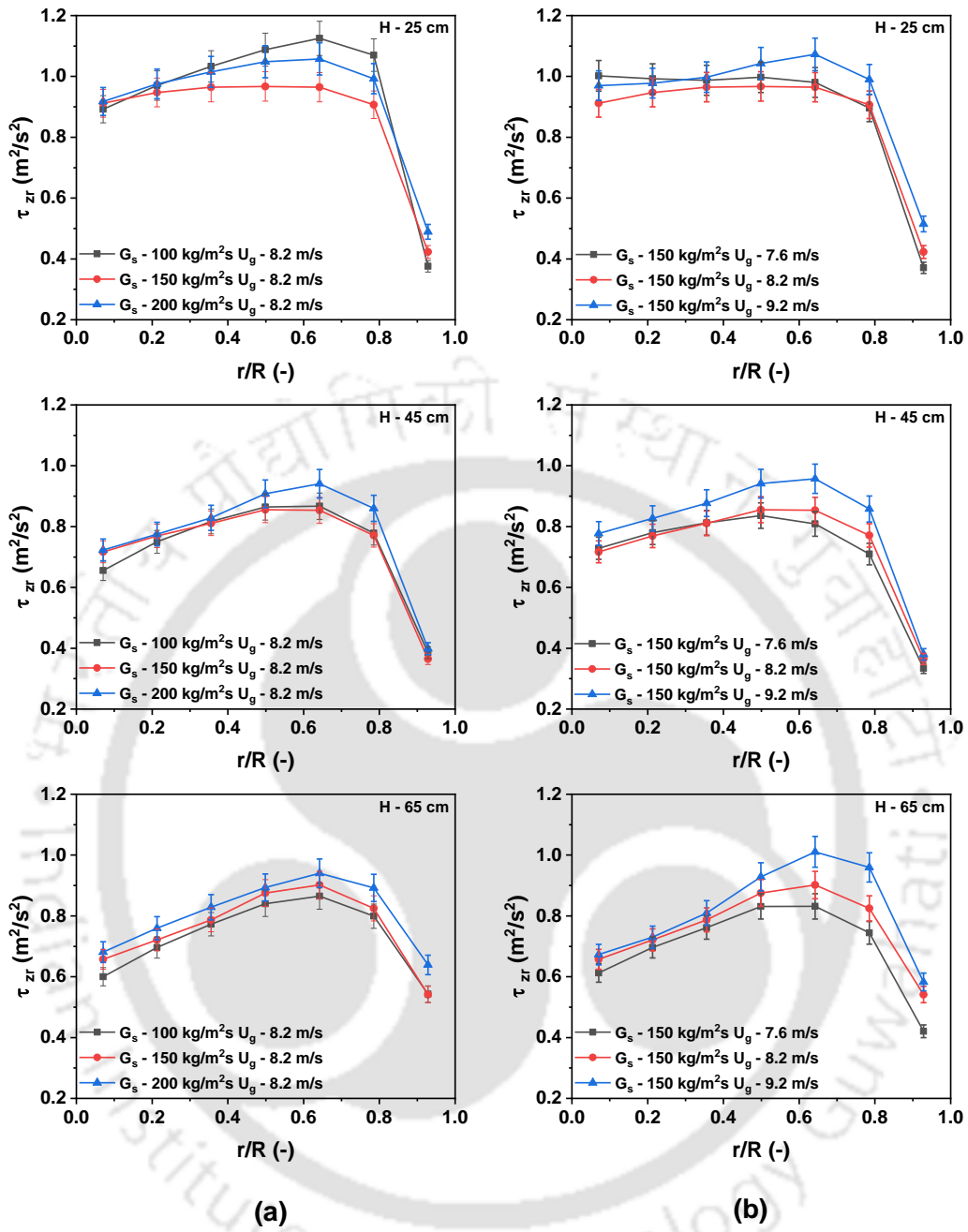


Figure 4.32: Radial variation of azimuthally averaged shear stress with height at the bottom section for (a) different solid flux at a gas velocity of 8.2 m/s and (b) different gas velocities at a solid flux of 150 kg/m²s

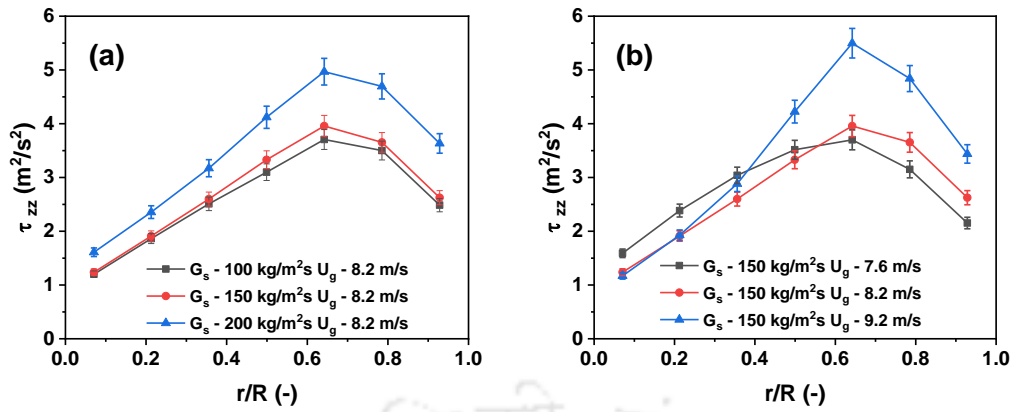


Figure 4.33: Radial variation of azimuthally averaged normal stress at the middle section for (a) different solid flux at a gas velocity of 8.2 m/s and (b) different gas velocities at a solid flux of 150 $\text{kg}/\text{m}^2\text{s}$

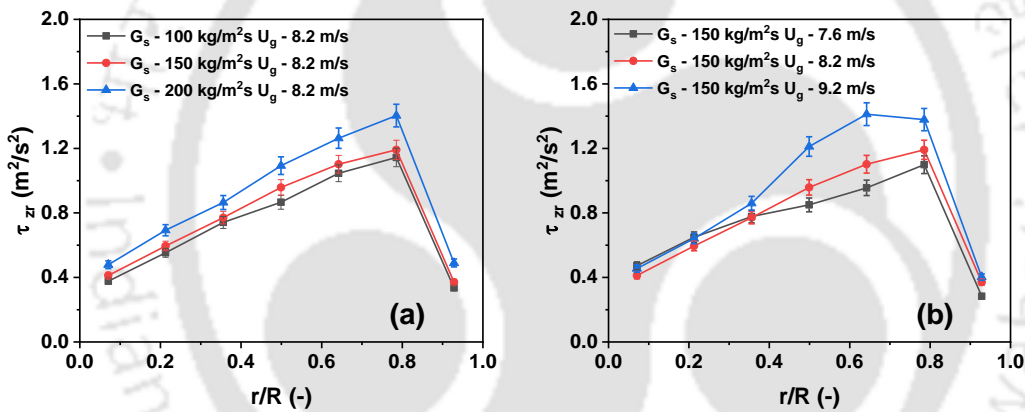


Figure 4.34: Radial variation of azimuthally averaged shear stress at the middle section for (a) different solid flux at a gas velocity of 8.2 m/s and (b) different gas velocities at a solid flux of 150 $\text{kg}/\text{m}^2\text{s}$

4.5.8 Turbulence Intensity

Evaluating turbulence in the system is complex. Relying solely on RMS velocities or granular temperature is not sufficient. This complexity arises because higher gas velocities not only increase mean velocities but also lead to more fluctuations. In the above discussion about axial and radial RMS velocities and granular temperature, it's evident that velocity flocculation heavily depends on gas velocity. As gas velocity rises, both fluctuations and

the mean velocity increase. This demonstrates the necessity of a parameter that normalizes the effect of gas velocity and mean solid velocity magnitude on turbulence.

Therefore, turbulence intensity is used as a measure for the turbulent fluctuation. Turbulence intensity in a fluidized bed refers to the degree of turbulence or chaotic motion present within the bed of solid particles and fluid. Turbulence intensity I is defined as the ratio of root mean square of turbulent velocity fluctuations ($\sqrt{\Sigma v_{rms}^2/3}$) which is basically granular temperature, to mean velocity.

$$TI = \sqrt{\theta}/\bar{v} \quad (4.6)$$

Figure 3.35 shows the turbulence intensity at the bottom section at different heights. It is clearly visible that turbulence intensity decreases with height. At a solid inlet section, the mean solid velocity is lower, and with increasing height, the mean solid velocity increases, resulting in a decline in turbulence intensity. At the middle section of the riser, turbulence intensity further declined. Pantazali et al. (2013, 2015) reported similar observations of decline in turbulence intensity with increasing height.

Irrespective of operating conditions, turbulence intensity is lower at the center of the column and increases toward the wall. It is due to higher particle-particle interaction near the wall region, which causes a higher degree of turbulence near the wall. It is interesting to note that in the RMS velocity profile as well as the granular temperature profile, a dip can be observed adjacent to the wall due to gas phase no-slip velocity and flow restriction near the wall. Although the magnitude of velocity fluctuation is lower adjacent to the region compared to the core-annular region, the degree of turbulence is always higher adjacent to the wall. While fluctuating velocities decrease near the wall region, mean velocities decrease even more. Consequently, turbulence intensity increases near the wall.

With an increase in solid flux, turbulence intensity increases both at the bottom (Figure 4.35a) and the middle sections (Figure 4.36a). Only at the bottom section close to the solid

inlet (0.25m), it can be observed that with increasing solid flux, turbulence intensity increases up to a solid flux of 150 kg/m²s. Again, it reduces at a solid flux of 200 kg/m²s.

The mean velocity profile exhibits similar anomaly as well.

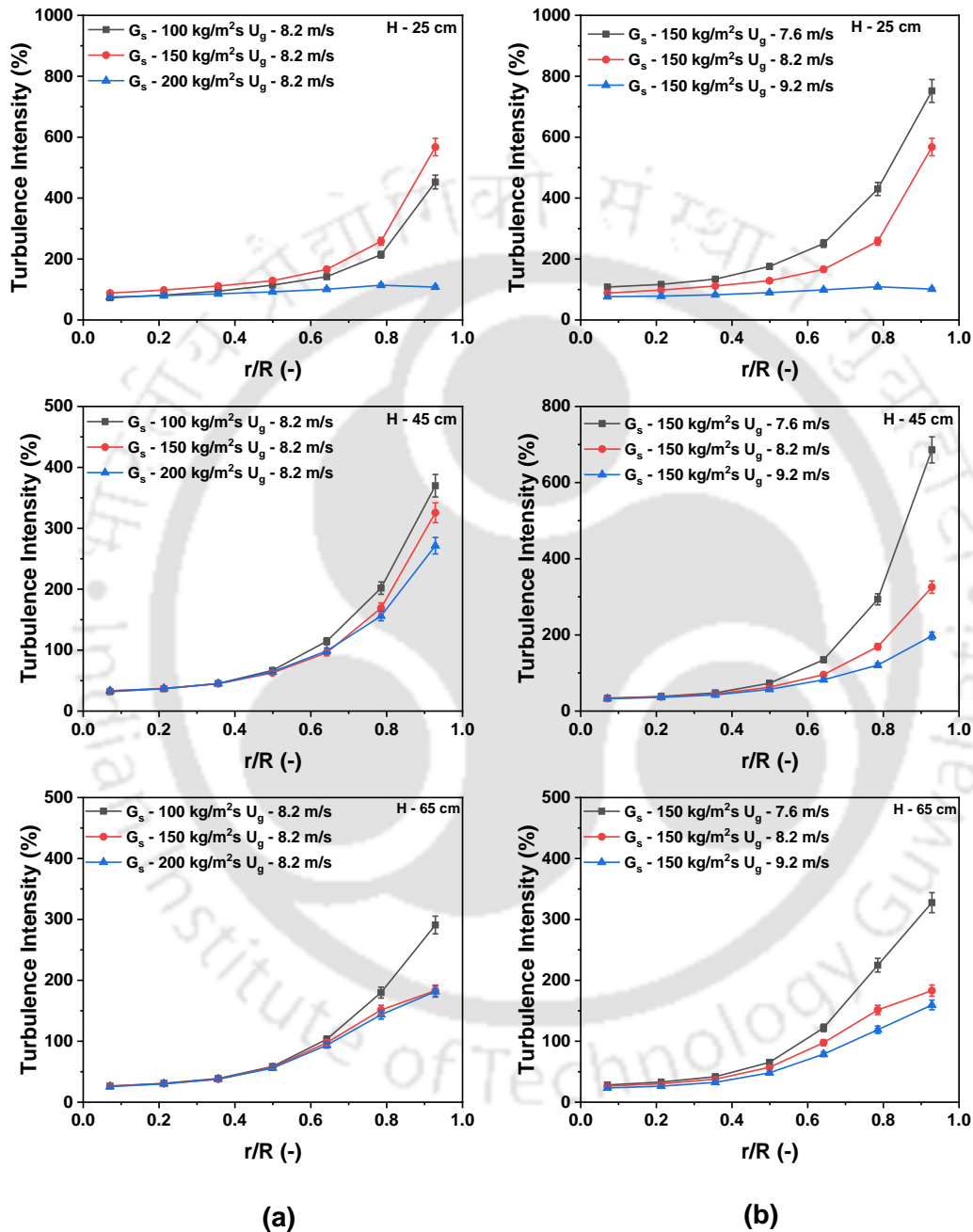


Figure 4.35: Radial variation of azimuthally averaged turbulence intensity with height at the bottom section for (a) different solid flux at a gas velocity of 8.2 m/s and (b) different gas velocities at a solid flux of 150 kg/m²s

Figures 4.35b and 4.36b show the effect of inlet gas velocity on turbulence intensity while solid flux is maintained constant. While granular temperature increases with increasing gas velocity, turbulence intensity exhibits exactly the opposite trend. As the gas velocity increases, solid velocity fluctuation and granular temperature also increase. However, the rise in solid mean velocity is comparatively higher with an increase in gas velocity. That is why turbulence intensity decreases with an increase in inlet gas velocity. It signifies that at lower inlet gas velocities, the degree of turbulence is higher than at higher gas velocities.

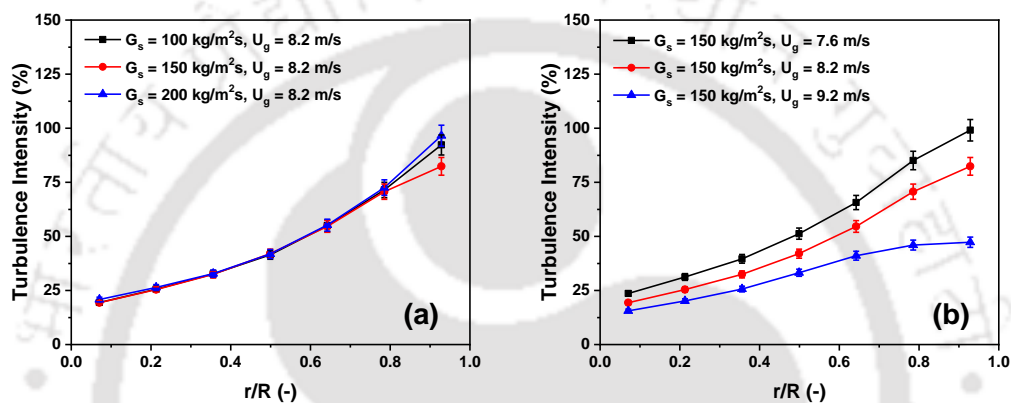


Figure 4.36: Radial variation of azimuthally averaged turbulence intensity at the middle section for (a) different solid flux at a gas velocity of 8.2 m/s and (b) different gas velocities at a solid flux of 150 kg/m²s

4.6 Solids Mixing in Laboratory Scale Setup

Five detectors (D1–D5) are utilized for the RTD study, as depicted in Figure 4.37. The first detector (D1) is precisely placed at the solid inlet plane. As the tracer particle passes through the detector plane, it exhibits a sharp peak at the detector. The peak at detector D1 indicates the entry of the tracer particle in the riser section. The detectors are carefully arranged to measure the RTD with an increasing riser height. D1–D2 are used for bottom section RTD measurement. Similarly, D1–D3 and D1–D4 are used for RTD measurement from the inlet to the start and end of the middle section respectively. D1–D5 are used to measure the overall RTD of the CFB riser. As only a single tracer particle is used in the

current experiment, the count peak (intensity of radiation emitted by the tracer particle) recorded by the detector is unique and represents the presence of the tracer particle at the detector plane. For example, a peak detected at D1 denotes the entry of the tracer particle in the riser, and a peak detected at the top detector (D5) denotes the exit of the tracer particle from the riser. The time interval between these two peaks is the time of flight of a single pass of tracer through the riser. Similarly, the time of flight between D1–D2, D1–D3, D1–D4, and D1–D5 are calculated from each pass of the tracer through the detector plane. The experiment continues until enough time-of-flight statistics are recorded, converting it into a histogram diagram. The RTD curve is defined for a mass tracer and plotted against concentration data. Mass conservation is crucial for obtaining a RTD curve, and the E curve (exit age distribution) is obtained by dividing concentration data with the tracer's mass. However, in single tracer time of flight experiments, mass conservation is not possible, making the histogram of time of flight ineffective. Multiple tracer passes are recorded, representing particle detection. The normalized frequency curve is fitted using the axial dispersion model (ADM), and the Peclet number and dispersion coefficient are calculated using the dispersion number. Detailed RTD measurement technique is presented in Chapter 3.

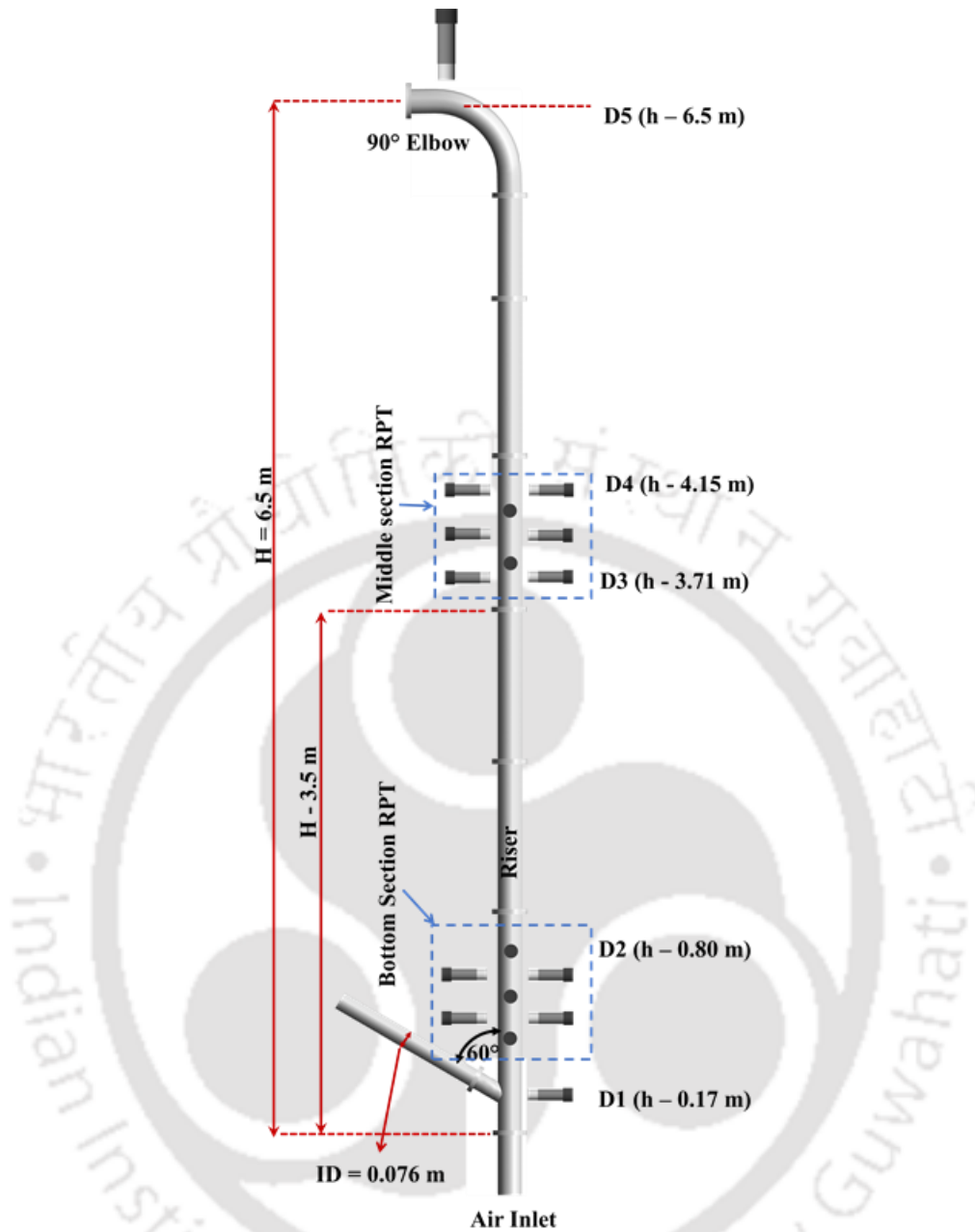


Figure 4.37: Detector arrangement for RTD experiment for pilot scale riser

4.6.1 Residence Time Distribution

Figure 4.38 shows the probability distribution function of the residence time of the tracer particle inside the riser at different sections for a solid flux of $150 \text{ kg/m}^2\text{s}$ and an inlet gas velocity of 9.2 and 7.6 m/s (maximum and minimum gas velocities). Figure 4.38a,b shows that D1–D2, which represents the bottom section, has longer tail than the other sections (D1–D3 and D1–D4) for both the velocities. This shows high back mixing/ recirculation

at the bottom section. At the bottom section, the solids enter in the riser section. The solid inlet velocity is much lower than the gas inlet velocity and the solid fraction is close to the solid fraction under minimum fluidization condition. Due to the high solid fraction, the bottom section behaves like a bubbling bed and therefore, the back mixing is severe. The solid accelerates as it moves up in the riser. Hence, the velocity at the bottom section is lower compared to the middle section that leads to the wider distribution in the residence time at the bottom section. Figure 4.38c–f shows the RTD curve for bottom to start and end of middle section, respectively, for both the gas velocities. Results indicate that the RTD curve for these two sections is dominated by the bottom section. The mean residence time of solid is higher in case of 7.6 m/s gas inlet velocity compared to the 9.2 m/s for all the sections. It should be noted that for all the sections longer tail is observed for 7.6 m/s gas inlet velocity as compared to 9.2 m/s. This shows higher degree of back mixing at lower velocity compared to higher gas inlet velocity for the same solid flux. This may be due to the meso-scale meta-stable structure formation at lower velocity. Figure 4.38g,h shows an overall RTD curve for 9.2 and 7.6 m/s gas inlet velocities, respectively. A longer tail is observed for 7.6 m/s as compared to 9.2 m/s gas inlet velocity. The mean residence time and standard deviation are higher for lower gas inlet velocity. These results confirm the higher degree of back mixing in lower velocity CFB. However, for all the operating conditions, only single peak is observed in the RTD curve. This shows that there is no dominant internal recirculation in CFB for all the conditions used in the current work.

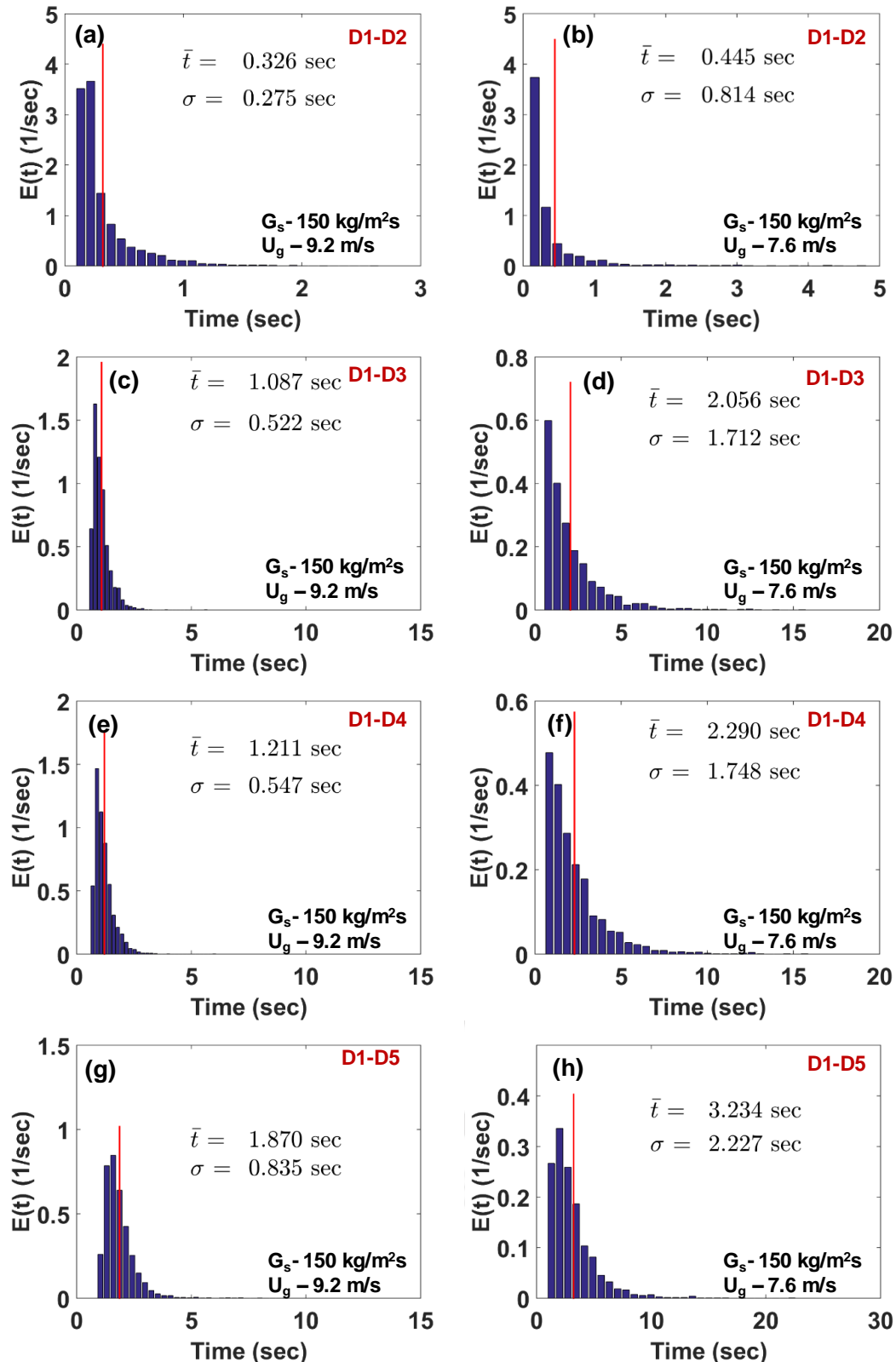


Figure 4.38: RTD for (a,b) inlet section, (c,d) inlet to start of the middle section, (e,f) inlet to end of the middle section and (g,h) overall riser at inlet gas velocities $U_g = 9.2$ m/s and $U_g = 7.6$ m/s

RTD data for all the operating conditions are summarized in Table 4.2. With the increase in gas velocity, the mean residence time decreases as expected. The Peclet number for all the operating conditions is calculated to find the mixing behavior. For an ideal mixed flow system, the Peclet number tends to zero, whereas for an ideal plug flow system, the Peclet number tends to infinity. Results show that for all the conditions, the Peclet number is lower for the bottom section and increases with the height. This shows that irrespective of the operating condition, the degree of back mixing is always higher in the bottom section. However, the values are significantly higher than zero; hence, even though back mixing is observed at the bottom section, it does not behave like a mixed flow reactor. With the increasing height, the Peclet number increases; hence, its flow patterns deviate towards that of a plug flow reactor. However, solid flow in the riser is considered near plug flow (Wei and Zhu, 1996) when the Peclet number is higher than 100, which is much higher than what is observed under current operating conditions. For a fixed solid flux of $150 \text{ kg/m}^2\text{s}$, with the increase in gas inlet velocity, the Peclet number increases significantly for all the sections. This shows that with the increase in gas velocity, the degree of back mixing reduces and CFB works more like a plug flow reactor. The effect of solid flux on the mixing pattern is less significant compared to the effect of gas velocity. However, it is observed that with the increase in solid flux at the same gas inlet velocity, Peclet number decreases marginally. This is mainly due to the enhanced particle–particle collision generated at higher solid flux. Therefore, from RTD studies, it can be concluded that with the increase in gas inlet velocity, CFB works more like a plug flow, and with the increase in solid flux, solid mixing increases.

Table 4.2: Residence time distribution and Peclet number

U_g m/s	G_s kg/m ² s		D1-D2	D1-D3	D1-D4	D1-D5
8.2	100	\bar{t} (Sec)	0.403	2.129	2.286	3.234
		σ^2/\bar{t}^2	2.160	0.424	0.372	0.283
		Pe	2.442	7.306	8.053	9.919
7.6	150	\bar{t} (Sec)	0.445	2.056	2.290	3.327
		σ^2/\bar{t}^2	3.343	0.693	0.582	0.448
		Pe	1.875	5.135	5.802	7.011
8.2	150	\bar{t} (Sec)	0.372	1.979	2.175	2.921
		σ^2/\bar{t}^2	2.126	0.560	0.480	0.346
		Pe	2.466	5.968	6.664	8.500
9.2	150	\bar{t} (Sec)	0.326	1.087	1.211	1.870
		σ^2/\bar{t}^2	0.713	0.231	0.204	0.288
		Pe	5.034	11.634	12.873	13.090
8.2	200	\bar{t} (Sec)	0.368	1.749	1.893	2.862
		σ^2/\bar{t}^2	2.332	0.792	0.505	0.382
		Pe	2.330	4.684	6.426	7.892

4.6.2 Trajectory Length Distribution (TLD)

RPT experiments are also performed for all the conditions at the bottom and middle sections as described in the previous section. Figure 4.9 shows a typical Lagrangian track of the tracer particle passing through the bottom section which is obtained through RPT experiments at a gas inlet velocity of 8.2 m/s and a solid flux of 150 kg/m²s. A huge set of trajectories are obtained for the bottom and middle sections where RPT experiments are

performed. For each trajectory, the particles exact path (length it traversed before exiting the zone of interest) can be obtained through the RPT experiments. This can be plotted as a histogram as each trajectory is independent and can be used to find the macromixing index to quantify the degree of back mixing. Villermaux, (1996) defined the macromixing index M (shown in equation 4.7) as the ratio of average path length travelled by the tracer particle to the actual distance between the inlet and outlet.

$$M = \langle l \rangle / L \quad (4.7)$$

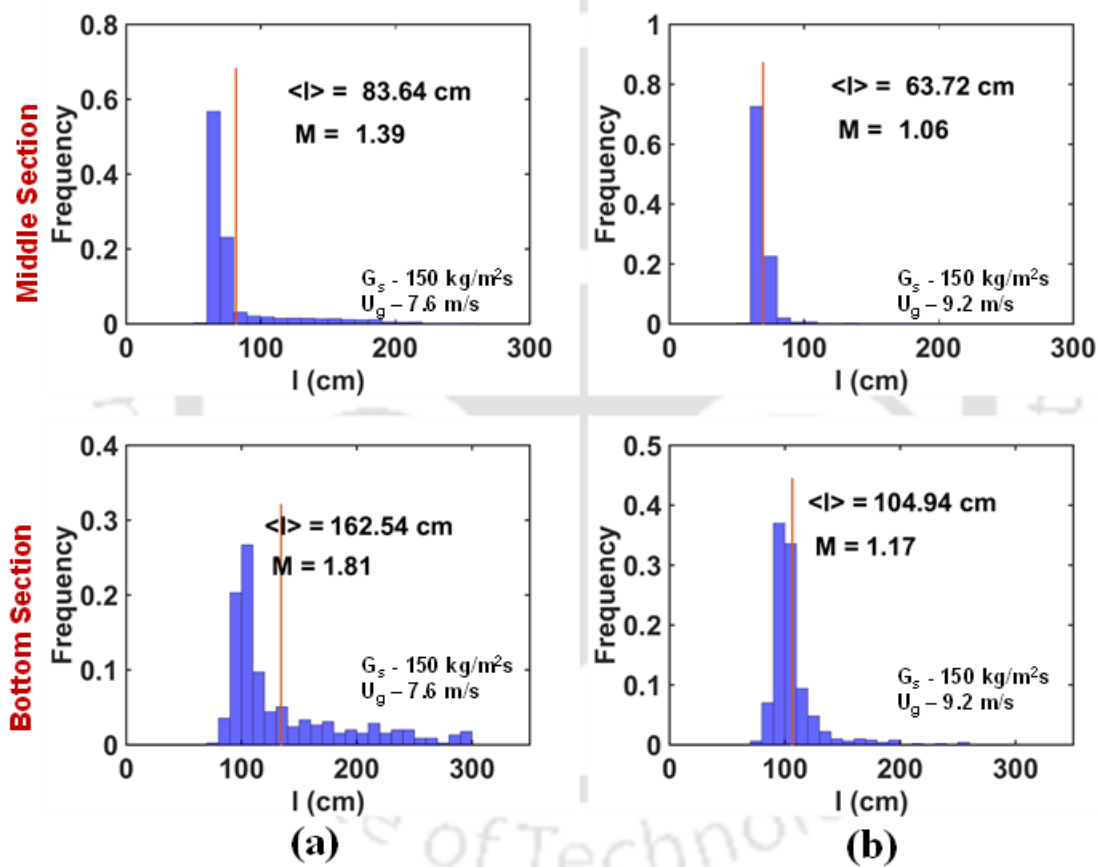


Figure 4.39: Trajectory length distribution for solid flux of 150 kg/m²s and different gas inlet velocities of (a) 7.6 m/s and (b) 9.2 m/s

Here, L is the distance between the starting and endpoint of the zone of interest and l denotes the actual path traveled by the tracer particle in a particular scan zone. A high value of M indicates that macromixing is particularly effective as that particle elements travel a

considerable distance before leaving the zone of interest. For an ideal plug flow system, the value of M is unity, and for an ideal mixed flow system, M tends to infinity. In a way, the trajectory length distribution (TLD) curve is similar to the RTD curve as both of them can be processed to get information about the macromixing behavior of the reactor. Figure 4.39 a,b shows the histogram of TLD for the middle and bottom sections for the solid flux of $150 \text{ kg/m}^2\text{s}$ at gas inlet velocities of 7.6 and 9.2 m/s, respectively. Similar to the RTD curve, a longer tail is observed for 7.6 m/s gas inlet velocity in both the bottom and middle sections. This shows a higher degree of back mixing in the case of lower gas velocity CFB. The value of M is higher for the bottom section as compared to the middle section for both the gas inlet velocity. This confirms a higher degree of back mixing in the bottom section. Furthermore, for both the velocities with move up in the column, M values reduce. This shows that the upper section of CFB behaves more toward the plug flow. It is observed that for 9.2 m/s gas inlet velocity and solid flux of $150 \text{ kg/m}^2\text{s}$, the M value is very close to 1 that indicates plug flow behavior. Similar results were also obtained by processing the RTD data. The mean trajectory length, the standard deviation of trajectory length, and the macromixing index are given in Table 4.3 for all the operating conditions for both the bottom and middle sections of the riser. It can be observed from Table 4.3 that the mean trajectory length is higher at higher solid flux and lower gas velocity. Furthermore, for all the conditions, the mean trajectory length is higher for the bottom section as compared to the middle section. This shows that the particle follows more “zig-zag” path in the bottom section and travels relatively straight in the middle section. This can also be observed from the values of the macromixing index (M) which is lower in the middle section and higher at the bottom section. Moreover, it is observed that with the increase in gas inlet velocity at a fixed solid flux, M value reduces for both sections. The macromixing index for the fully developed middle section with a gas velocity of 9.2 m/s is near to unity (1.06),

indicating that at higher velocities, radial and downwind motion of solids are essentially negligible and the riser almost behaves as plug flow. Furthermore, results indicate that with the increase in solid flux at a fixed gas inlet velocity, the M value increases. This further confirms increase in random motion with the increase in solid flux due to enhanced particle–particle collision. For all the cases, the value of M is higher at the bottom section. However, the values at the bottom section are not far away from the middle section. This further confirms that though some back mixing is observed at the bottom section of the riser, it is not behaving as a mixed flow reactor. Similar observations are recorded from RTD data. This indicates that the data obtained from RPT and RTD are highly correlated and any of these can be used with the same accuracy to quantify the macromixing behavior of any process vessel/reactor.

Table 4.3: Trajectory length distribution of the bottom and middle section of the riser

U_g (m/s)	G_s kg/m ² s	Bottom Section		Middle Section	
		$\langle l \rangle$ cm	M (-)	$\langle l \rangle$ cm	M (-)
8.2	100	107.10	1.19	68.82	1.15
7.6	150	162.54	1.81	83.64	1.39
8.2	150	120.51	1.34	72.6	1.21
9.2	150	104.94	1.17	63.72	1.06
8.2	200	132.57	1.47	79.62	1.33

4.7 Scale Up

CFB riser reactors have garnered significant attention due to their practical applications and inherent academic intrigue. However, the current stage of model development presents

a challenge in translating theoretical frameworks into the design, scalability, and operation of CFB reactors. The intricate hydrodynamics of co-current upward gas-solid flow within CFB risers adds complexity to this task. Different researchers (Glicksman, 1984; Glicksman et al., 1993; Kislev, 2022; Qi et al., 2008) proposed different methodologies and many sets of dimensionless scaling parameters to ensure hydrodynamic similarity at different scales. Qi et al. (2008) summarized typical sets of dimensionless scaling parameters presented by different researchers. Riser geometry, particle properties (e.g., sphericity and size distribution), as well as operational parameters (e.g., superficial gas velocity and solid circulation rate) play a big role in how the complicated hydrodynamics of gas-solid flow in CFB risers work. Other crucial determinants involve the sauter mean particle diameter, particle density, riser hydraulic diameter, gas density, gas viscosity and gravity (Van Der Meer et al., 1999). These elements collectively contribute to the comprehensive control of flow dynamics. It is important to note that for the purpose of analysis, certain aspects such as particle restitution, inter-particle friction, interaction with column walls, electrostatic forces, and cohesive effects can be feasibly overlooked (Glicksman et al., 1993). During the operation of CFB riser reactors, variations in superficial gas velocities and solid circulation rates are inevitable due to changing operating conditions. But for these reactors to work steadily, it is very important to keep the hydrodynamics of the flow of gas and solids the same under different operating conditions. Therefore, it is necessary to investigate the hydrodynamic similarity in a CFB riser reactor under various operating conditions.

For designers, a quick approximation of the mean velocity would be of immense help. However, it is evident that obtaining such information on the mean solid velocity is quite challenging due to the complex interactions involved. There have been earlier attempts (Patience et al., 1992) made in the literature to forecast volume fraction and velocity.

Patience et al. (1992) presented correlation in terms of slip factor and Froude number as given in equation 4.9. Slip factor is the ratio of actual gas velocity to the solid velocity.

$$\emptyset = 1 + \frac{5.6}{Fr} + 0.47 * Fr^{0.41} = \frac{U_g}{\varepsilon V_p} \quad (4.8)$$

Although solid holdup and solid velocities are unknown, the pressure drop is related to volume fraction and can match the scales. As a result, one is able to calculate the mean velocity. The correlation that Patience et al. (1992) found is often utilized as the initial estimate because of its simplicity and its ability to be applied. On the other hand, the correlation provided by Patience et al. (1992) over-predicts the slip factor (Qi et al., 2008)). Additionally, it is impossible to forecast the velocity of the flow for the initial design since there is no information available on pressure drop. In situations like these, predicting the velocity based on the operating parameters and the geometry would be of considerable assistance. The goal of this work was to develop a correlation for estimating mean solid velocity from operating conditions.

Table 4.4 Experimental and solid particles used for empirical correlation

	H (m)	D (mm)	d _p (μm)	Solid Material	ρ _p (kg/m ³)	U _g (m/s)	G _s (kg/m ² s)
Godfroy et al. (1999)	7	82	150	Sand	2500	4	23-75
Bhusarapu et al. (2005)	7.93- 5.77	152, 140	150	Glass	2500	3.2-4.5; 5.4-7.71	26.6-36; 102-109
This Work (Lab Scale)	3	50	500	Glass	2500	6-9	40-180
This Work (Pilot Scale)	6.5	100	500	Glass	2500	7.6-9.2	100-200

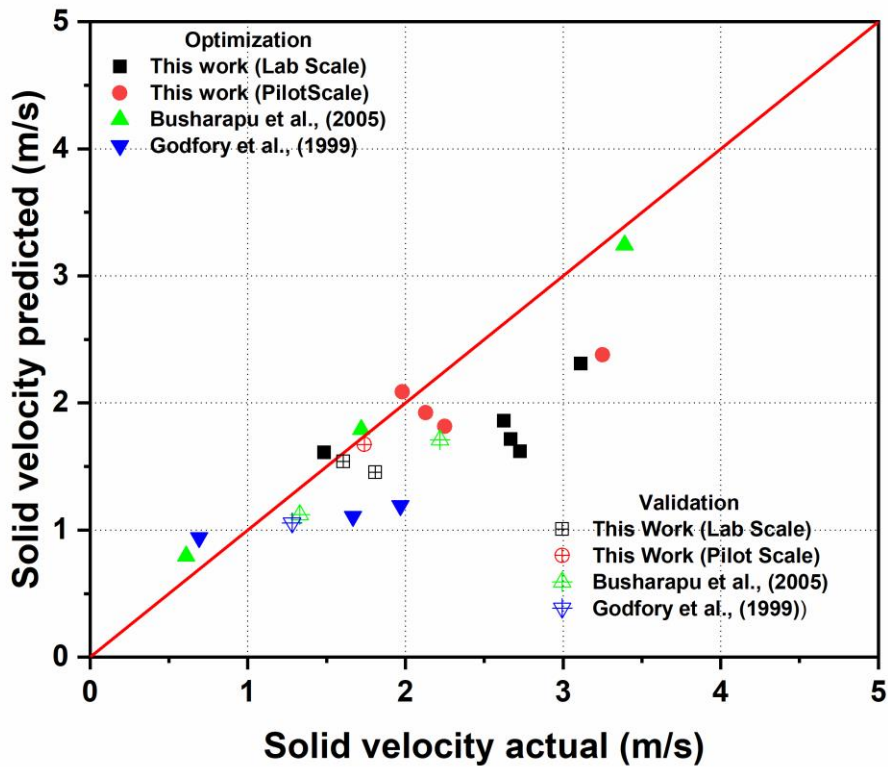


Figure 4.40: Comparison of the mean velocity predicted from the empirical correlation and the actual mean velocity

The correlation that was generated in the current work may be found in equation 4.9. GRG non-linear solver is used in the current scale-up relation to find the optimal value of constants using excel. However, some velocity data points are initially not taken into account in the GRG non-linear solver. Later, those unused data points are used for validation as shown in Figure 4.40. The data used for developments and validation the correlation from this work and literature are presented in Table 4.4. Only data Geldart Group B particles is used to correlation development and validation work. The average solid velocity is contingent upon factors such as solid concentration, gas velocity, diameter, metastable structures, wall friction, wall surface and solid properties. Defining all of these parameters explicitly in relation to operating conditions, established solid properties, and geometric factors presents a challenge at this point. Dimensionless numbers

$(G_s/\rho_g U_g, U_g/gD)$ are used to develop a correlation similar to the dimensionless number used by Qi et al., (2008).

$$\phi = \frac{U_g}{V_p} = 0.32 \left(\frac{m_p}{m_g} \right)^{-0.2} \left(\frac{U_g}{U_t} \right)^{0.84} (Fr)^{-0.2} \quad (4.9)$$

The comparison between the mean velocity that was predicted by the equation 4.9 and the actual mean velocity is shown in Figure 4.40. The majority of inaccuracies in predictions are less than 30%. It has also been noticed that the margin for error is rather large in situations in which the mass loading is greater than 8 and the ratio of U_g/U_t is lower than 1.8. Consequently, the following limitations may be placed on a forecast of the mean velocity with this correlation.

4.8 Summary

The results of this chapter are summarized based on the consideration effect on gas velocity and solid flux on pilot scale solid flow field and solid mixing and scale studies.

Solid flow field:

The solid flow field is investigated using a single radioactive tracer particle mimicking the solid phase's motion.

- The observed velocity vector plots show that there is axisymmetric flow, and it can also be seen that there is no negative motion in the time-averaged case.
- Axial motion is predominantly in the axial direction irrespective of operating conditions and riser height .
- Axil velocity is highest at the center and lowest near the wall due to the no-slip boundary condition of the gas phase.
- The probability distribution function of instantaneous velocity shows negative instantaneous velocity near the wall. However, the mean axial velocity is always

positive. No negative axial instantaneous velocity can be observed at the center of the middle section. In the bottom section, some noticeable instants of negative velocity can be observed in the center region.

- Although the mean radial motion is negligible, the radial RMS velocity is noticeable. However, the axial RMS velocity is always higher than the radial RMS velocity.
- The number of occurrences contour plot indicates that the solid distribution is higher near the wall region.
- The mean solid velocity profile is flat in the middle section compared to the bottom section. In the middle section (RPT zone), flow is developed, and the change in velocity parameter is negligible. The mean velocity profile is flat at higher gas velocity condition (e.g. 9.2 m/s) compared to lower velocity conditions.

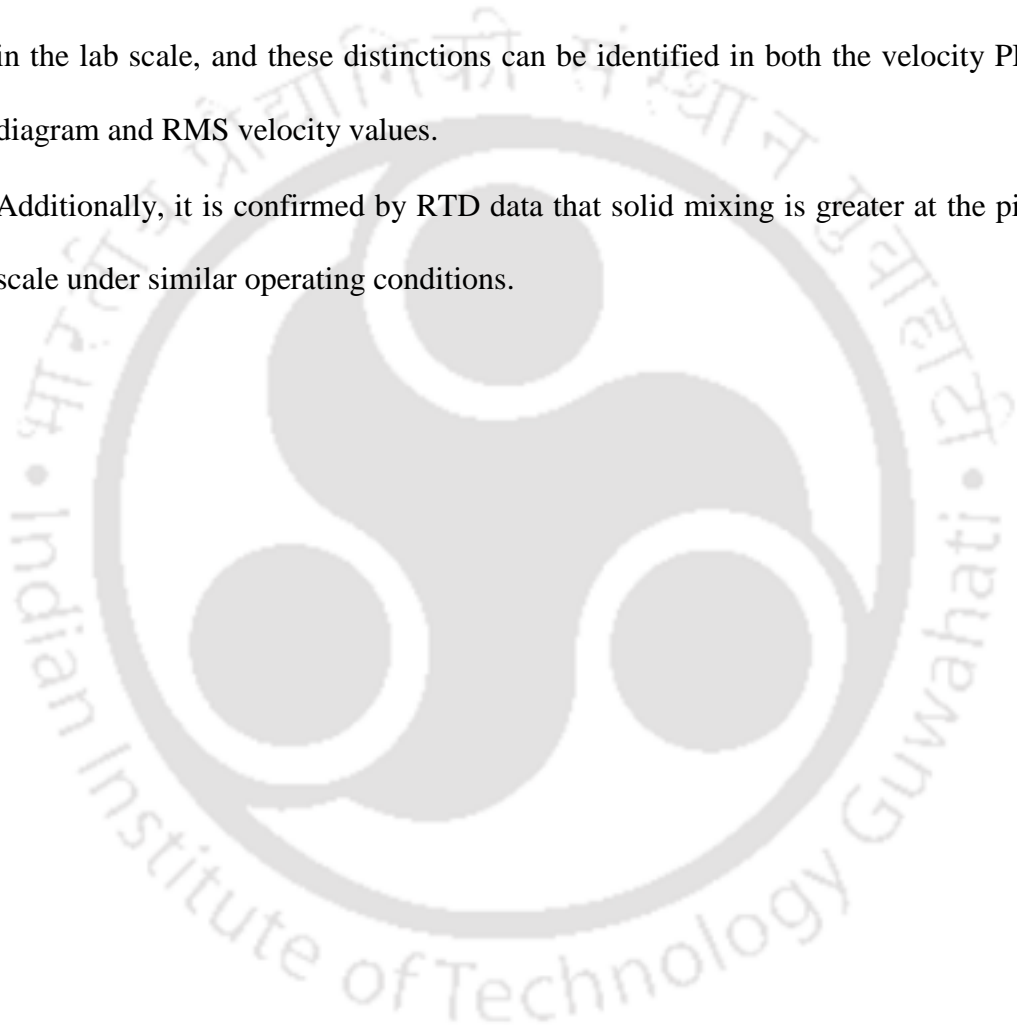
Solid Mixing:

- Residence time distribution studies in various sections reveal that solid mixing at the bottom section dominates overall solid mixing in the riser. With increasing height, the Péclet number also increases, which implies that solid mixing reduces with height.
- Moreover, it is found that the degree of back mixing decreases with an increase in gas inlet velocity. However, it marginally increases with an increase in solid flux mainly due to enhanced particle-particle interactions.
- From TLD data it can be observed that for all the conditions, more solid back mixing is observed in the bottom section, however the degree of back mixing at the bottom section is not very high does not deviate much from the middle
- Results confirm that RPT and RTD data are highly correlated, and either can be used with the same accuracy to quantify macromixing behavior in any process

vessel or reactor. It's noteworthy that RTD obtained from a single particle time of flight experiment can offer similar insights into mixing behavior as the RPT experiment, all without the need for tedious calibration or data processing.

Scale Up:

- The lab-scale velocity profile is found to be flatter when compared to the pilot plant.
- The velocity fluctuation is observed to be significantly higher in the pilot scale than in the lab scale, and these distinctions can be identified in both the velocity PDF diagram and RMS velocity values.
- Additionally, it is confirmed by RTD data that solid mixing is greater at the pilot scale under similar operating conditions.



Notations

A	Column cross section area,	$[m^2]$
G_s	Solid flux	$[kg/m^2s]$
V_{CA}	Transition velocity between fast fluidization and core-annular dilute phase flow	$[m/s]$
V_{CC}	Classical choking velocity	$[m/s]$
V_{mp}	Transition velocity to homogeneous dilute flow	$[m/s]$
d_p	Particle diameter	$[m]$
v_s	Solid velocity	$[m/s]$
ε_s	Solid fraction	$[-]$
ρ_G	Gas density	$[kg/m^3]$
ρ_p	Particle density	$[kg/m^3]$
Ar	Archimedes number	$[-]$
L	Distance between the starting and endpoint of tracer track	$[m]$
M	Macromixing index	$[-]$
l	Actual path traveled by the tracer particle	$[m]$
TI	Turbulence intensity	$[-]$
θ	Granular Temperature	m^2/s^2

References

- Anantharaman, A., Issangya, A., Karri, S.B.R., Findlay, J., Hrenya, C.M., Cocco, R.A., Chew, J.W., 2017. Annulus flow behavior of Geldart Group B particles in a pilot-scale CFB riser. *Powder Technol.* 305, 816–828.
- Beam, G.B., Wielopolski, L., Gardner, R.P., Verghese, K., 1978. Monte Carlo calculation of efficiencies of right-circular cylindrical NaI detectors for arbitrarily located point sources. *Nucl. Instruments Methods* 154, 501–508.
- Berruti, F., Chaouki, J., Godfroy, L., Pugsley, T.S., Patience, G.S., 1995. Hydrodynamics of Circulating Fluidized Bed Risers : A Review. *Can. J. Chem. Eng.* 73, 579–602.
- Bhusarapu, S., Al-Dahhan, M.H., Duduković, M.P., 2006. Solids flow mapping in a gas-solid riser: Mean holdup and velocity fields. *Powder Technol.* 163, 98–123.
- Bhusarapu, S., Al-Dahhan, M.H., Duduković, M.P., Trujillo, S., O'Hern, T.J., 2005. Experimental study of the solids velocity field in gas-solid risers. *Ind. Eng. Chem. Res.* 44, 9739–9749.
- Bhusarapu, S., Cassanello, M., Al-Dahhan, M.H., Dudukovic, M.P., Trujillo, S., O'Hern, T.J., 2007. Dynamical features of the solid motion in gas-solid risers. *Int. J. Multiph. Flow* 33, 164–181.
- Bhusarapu, S., Fongarland, P., Al-Dahhan, M.H., Duduković, M.P., 2004. Measurement of overall solids mass flux in a gas-solid Circulating Fluidized Bed. *Powder Technol.* 148, 158–171.
- Bhusarapu, S.B., 2005. Solids Flow Mapping In Gas-Solid Risers. D.Sc Thesis, Washington University, Saint Louis, Missouri, USA.
- Bi, H.T., Grace, J.R., 1995. Flow regime diagrams for gas-solid fluidization and upward transport. *Int. J. Multiph. Flow* 21, 1229–1236.
- Biswal, J., Joseph, A., Shah, J.G., Pant, H.J., Dash, A., 2016. Preparation of 46Sc glass

- microspheres by combined melt-quenching and microwave methods for applications in radioactive particle tracking experiments. *J. Radioanal. Nucl. Chem.* 308, 335–340.
- Breault, R.W., Guenther, C.P., Shadle, L.J., 2008. Velocity fluctuation interpretation in the near wall region of a dense riser. *Powder Technol.* 182, 137–145.
- Burkell, J.J., Grace, J.R., Zhao, J., Lim, C.J., 1988. Measurement of Solids Circulation Rates in Circulating Fluidized Beds, in: *Circulating Fluidized Bed Technology II*. Pergamon Press plc, pp. 501–509.
- Chang, J., Zhang, K., Zhu, W., Yang, Y., 2016. Gas–solid flow in a high-density circulating fluidized bed riser with Geldart group B particles. *Particuology* 29, 103–109.
- Chew, J.W., Hays, R., Findlay, J.G., Knowlton, T.M., Reddy Karri, S.B., Cocco, R.A., Hrenya, C.M., 2012. Cluster characteristics of Geldart Group B particles in a pilot-scale CFB riser. I. Monodisperse systems. *Chem. Eng. Sci.* 68, 72–81.
- Dubé, O., Dubé, D., Chaouki, J., Bertrand, F., 2014. Optimization of detector positioning in the radioactive particle tracking technique. *Appl. Radiat. Isot.* 89, 109–124.
- Fiedler, O., Werther, J., Labahn, N., Kumpart, J., Christofori, K., 1997. Measurement of local particle velocities and velocity distributions in gas-solid flows by means of the spatial filter method. *Powder Technol.* 94, 51–57.
- Gidaspow, D., Jung, J., Singh, R.K., Tartan, M., 2004. Two kinds of turbulence in fluidization. *AIChE Annu. Meet. Conf. Proc.* 2877–2883.
- Glicksman, L.R., 1984. Scaling relationships for fluidized beds. *Chem. Eng. Sci.* 39, 1373–1379.
- Glicksman, L.R., Hyre, M., Woloshun, K., 1993. Simplified scaling relationships for fluidized beds. *Powder Technol.* 77, 177–199.
- Horio, M., 1997. Hydrodynamics, in: *Circulating Fluidized Beds*. (Eds Grace. J. R., Avidan, A. A., Knowlton, T. M.), Chapman & Hall, London, 2., pp. 21–85.

- Huilin, L., Gidaspow, D., 2003. Hydrodynamics of binary fluidization in a riser: CFD simulation using two granular temperatures. *Chem. Eng. Sci.* 58, 3777–3792.
- Kamalanathan, P., Kalo, L., Pant, H.J., Upadhyay, R.K., 2017. Effect of dynamic bias on accuracy of radioactive particle tracking (RPT) technique at different data acquisition frequencies. *Appl. Radiat. Isot.* 128, 13–21.
- Khane, V., Al-Dahhan, M.H., 2017. Hybrid dynamic radioactive particle tracking (RPT) calibration technique for multiphase flow systems. *Meas. Sci. Technol.* 28.
- Kislev, E., 2022. Relationships 5.0. *Relationships* 5.0 43, 95–112.
- Larachi, F., Chaouki, J., Kennedy, G., 1995. 3-D mapping of solids flow fields in multiphase reactors with RPT. *AIChE J.* 41, 439–443.
- Larachi, F., Kennedy, G., Chaouki, J., 1994. A γ -ray detection system for 3-D particle tracking in multiphase reactors. *Nucl. Inst. Methods Phys. Res. A* 338, 568–576.
- Ludlow, J.C., Monazam, E.R., Shadle, L.J., 2008. Improvement of continuous solid circulation rate measurement in a cold flow circulating fluidized bed. *Powder Technol.* 182, 379–387.
- Matsen, J.M., 1997. Design and scale-up of CFB catalytic reactors., in: *Circulating Fluidized Beds.* (Eds Grace. J. R., Avidan, A. A., Knowlton, T. M.), Chapman & Hall, London, 14,. pp. 489–503.
- Pantzali, M.N., De Ceuster, B., Marin, G.B., Heynderickx, G.J., 2015. Three-component particle velocity measurements in the bottom section of a riser. *Int. J. Multiph. Flow* 72, 145–154.
- Pantzali, M.N., Lozano Bayón, N., Heynderickx, G.J., Marin, G.B., 2013. Three-component solids velocity measurements in the middle section of a riser. *Chem. Eng. Sci.* 101, 412–423.
- Pärssinen, J.H., Zhu, J.X., 2001. Particle velocity and flow development in a long and high-

- flux circulating fluidized bed riser. *Chem. Eng. Sci.* 56, 5295–5303.
- Pateence, G.S., Chaouki, J., Grandjean, B.P.A., 1990. Solids flow metering from pressure drop measurement in circulating fluidized beds. *Powder Technol.* 61, 95–99.
- Patience, G.S., Chaouki, J., Berruti, F., Wong, R., 1992. Scaling considerations for circulating fluidized bed risers. *Powder Technol.* 72, 31–37.
- Pita, J.A., Sundaresan, S., 1993. Developing flow of a gas-particle mixture in a vertical riser. *AIChE J.* 39, 541–552.
- Qi, X., Zhu, J., Huang, W., 2008. Hydrodynamic similarity in circulating fluidized bed risers. *Chem. Eng. Sci.* 63, 5613–5625.
- Rhodes, M.J., Wang, X.S., Cheng, H., Hiramata, T., Gibbs, B.M., 1992. Similar profiles of solid flux in circulating fluidized-bed risers. *Chem. Eng. Sci.* 47, 1635–1643.
- Roy, S., Kemoun, A., Al-Dahhan, M., Dudukovic, M.P., 2001. A method for estimating the solids circulation rate in a closed-loop circulating fluidized bed. *Powder Technol.* 121, 213–222.
- Roy, S., Larachi, F., Al-Dahhan, M.H., Duduković, M.P., 2002. Optimal design of radioactive particle tracking experiments for flow mapping in opaque multiphase reactors. *Appl. Radiat. Isot.* 56, 485–503.
- Tartan, M., Gidaspo, D., 2004. Measurement of granular temperature and stresses in risers. *AIChE J.* 50, 1760–1775.
- Upadhyay, R.K., Kaim, J., Roy, S., 2009. Investigation of downflow bubble columns: Experiments and modeling. *J. Chem. Eng. Japan* 42, 156–161.
- Upadhyay, R.K., Roy, S., 2010. Investigation of hydrodynamics of binary fluidized beds via radioactive particle tracking and dual-source densitometry. *Can. J. Chem. Eng.* 88, 601–610.
- Van Der Meer, E.H., Thorpe, R.B., Davidson, J.F., 1999. Dimensionless groups for

- practicable similarity of circulating fluidised beds. *Chem. Eng. Sci.* 54, 5369–5376.
- Van engelandt, G., De Wilde, J., Heynderickx, G.J., Marin, G.B., 2007. Experimental study of inlet phenomena of 35 ° inclined non-aerated and aerated Y-inlets in a dilute cold-flow riser. *Chem. Eng. Sci.* 62, 339–355.
- Villermaux, J., 1996. Trajectory length distribution (TLD), a novel concept to characterize mixing in flow systems. *Chem. Eng. Sci.* 51, 1939–1946.
- Wang, C., Zhu, J., Li, C., Barghi, S., 2014. Detailed measurements of particle velocity and solids flux in a high density circulating fluidized bed riser. *Chem. Eng. Sci.* 114, 9–20.
- Wei, F., Zhu, J.X., 1996. Effect of flow direction on axial solid dispersion in gas-solids cocurrent upflow and downflow systems. *Chem. Eng. J. Biochem. Eng. J.* 64, 345–352.
- Wu, W., Gerhart, A.L., Chen, Z., Dellenback, P.A., Agarwal, P.K., 2001. A device for measuring solids flowrate in a circulating fluidized bed. *Powder Technol.* 120, 151–158.
- Zhu, J., Bi, H.T., 1995. Distinctions Between Low Density and High Density CFB. *Can. J. Chem. Eng.* 73, 644–649.

CHAPTER 5

Conclusions and Recommendations

At the end of each of the previous chapters, a summary is presented based on the research findings of the subject of the respective chapter. This chapter presents a broader finding of this thesis, and a recommendation for potential future work is given.

5.1 Conclusions

The current thesis aims to quantify the solid phase flow behavior of gas-solid circulating fluidized beds at the bottom and fully developed middle sections with Geldart Group B particles and develop a simplified scale-up relation for solid phase velocity prediction. There are three different aspects of the current work. One is to implement RPT simultaneously at two different sections of the gas-solid riser at two different scales for similar operating conditions. Although there is limited literature (Bhusarapu, 2005; Godfroy et al., 1999; Kamalanathan, 2016) available in which RPT is implemented to map solid flow fields in CFB risers, no one has implemented it for two sections simultaneously for any reactor. In addition to the current work, only Kamalanathan (2016) implemented RPT at the high-velocity riser. Nevertheless, that was concentrated on the middle section of the riser only. Improvement in data acquisition, post-processing strategies and data representation strategies was done to implement RPT in two sections. The second aspect is an analysis of solid phase velocity flow field data for the middle and bottom sections of the riser and the effect of gas velocity and solid flux on it. The third and final aspect of the work is to develop a generalized and simplified scale-up relation for solids' mean velocity based on operating conditions. A brief summary of the particular conclusion presented is given at the end of each chapter. The purpose of this chapter is to provide an overview of

the overall key findings and the broader conclusions drawn from the present thesis, as follows:

- In current work, PRT measurement is simultaneously performed at the bottom section and the fully developed section of the riser and velocity flow field data is presented for both sections with varying heights.
- The mean solid velocity profile is always higher at the center of the column and lower near the wall, irrespective of height, operating condition and scale. Solid motion is predominantly in the axial direction and mean radial velocity is negligible.
- Mean velocity increases with an increase in inlet gas velocity and solid flux. However, the effect of inlet gas velocity on mean solid velocity is much higher than solid flux. Axial RMS velocity increases with an increase in inlet gas velocity as the magnitude of fluctuation is higher for higher gas velocity. With an increase in solid flux, axial RMS velocity also increases due to an increase in the particle-particle collision.
- Solid flow behavior is mainly influenced by inlet gas velocity, as drag is the main force responsible for solid motion. So, at the same inlet gas velocity, increasing solid flux caused an increase in particle-particle interaction.
- Since mean velocity magnitude has an impact on velocity fluctuation (i.e., RMS velocity component and granular temperature), it is impossible to quantify the level of turbulence in a system on its own. It can be observed that with increasing gas velocity, though RMS velocity or granular temperature increases, turbulence intensity decreases as the increase in mean velocity is relatively higher than the increment in velocity fluctuation. So, with an increase in inlet gas velocity, though velocity fluctuation and granular temperature increase, the turbulence intensity decreases.
- RTD experiments are conducted at varying heights. Back mixing is consistently more significant in the lower section. As the height increases, back mixing decreases. Inlet

gas velocity plays a significant role in back mixing, reducing solid back mixing with higher inlet gas velocities. The same thing was observed with the instantaneous position track and PDF diagram of instantaneous velocity. Also, solid back mixing increases very slightly when the solid flux increases.

- In contrast to the steeper mean velocity profile of the pilot scale riser, the profile at the laboratory scale riser is relatively flat. The smaller laboratory-scale riser experiences lower velocity fluctuations than its pilot-scale counterpart. As the riser diameter increases, solids have more room to move radially, resulting in increased particle-particle collisions compared to when solids only move axially.
- The findings from RTD experiments reveal that the pilot-scale riser exhibits greater back mixing compared to the laboratory-scale riser. Both RPT and RTD data confirm that a larger riser diameter leads to increased velocity fluctuations and back mixing in contrast to a smaller one.

This thesis aims to address the lack of detailed velocity flow field data for Geldart Group B particles at higher solid flux, which has been partially addressed. Gas-solid interaction plays a significant role in mean velocity, and similar interactions between solids and walls and solid-solid interactions influence velocity fluctuations. The bottom section primarily dominates solid mixing.

The data generated from the current work may be used to identify the optimal operating conditions (e.g., gas velocity and solid flux) for a CFB system with Geldart group B particles for a particular application. The data generated in this study has the potential to predict the slip velocity of the solid phase. Mean and fluctuating velocities offer valuable insights for identifying regimes and understanding local solid mixing characteristics. For example, observing the negative velocity in the local velocity probability density function (PDF) provides a clear indication of solid backmixing near the wall. These data can be used

to validate CFD model. RTD data helps in understanding the distribution of residence times of particles within the system and provides insights into the mixing efficiency of the fluidized bed system. When scaling up a CFB system from laboratory to industrial scale, RTD data helps to predict how the residence time distribution evolves. It also helps to determine the efficiency of the fluidized bed by assessing how effectively reactants are utilized. RTD data is a crucial tool for design engineers in the chemical and process industries.

5.2 Recommendations and Future Directions

Future recommendations are deemed vital in the field of research endeavors. As research progresses, it is often observed that more unknowns than knowns come to our attention. Here, well-thought-out suggestions are put forward as mentioned below:

- The precise determination of the tracer's exact position during position reconstruction poses challenges. Consequently, there may be instances of error in determining the instantaneous position, impacting the accuracy of velocity measurements. Further efforts are needed to improve the hardware of data acquisition system (MIDAS) to achieve higher data acquisition frequencies and refine algorithms. Kamalanathan et al. (2017) conducted a study on the accuracy of axial velocity, but additional work is essential to establish a comprehensive accuracy map for RPT.
- Achieving higher solid flux with Geldart Group B particles is always a challenging task. With the current single solid inlet setup, solid flux of up to $200 \text{ kg/m}^2\text{s}$ can be achieved. At higher solid fluxes, multiple solid inlets are necessitated for Geldart Group B particles. A scarcity of high-flux velocity flow field data for Geldart Group B particles is noted, and an effort is made in this study to address this issue. To operate a high-density CFB riser with Geldart Group B particles, greater attention should be

given to the overall design, starting from solid feed to riser to solid separation (Zhu and Bi, 1995). CFB should be operated at a solid flux ($> 400 \text{ kg/m}^2\text{s}$), and velocity data should be compared with a low flux CFB riser. In high-density operation, there is a possibility of cluster formation. The solid flux variation is found to fall under the "similar profile" regime in the current work because all operating conditions (variation of solid flux) have a limited impact on overall solid motion (Rhodes et al., 1992). It will be interesting to investigate the velocity flow field and solid mixing when particle-particle interaction dominates over gas-particle interaction. In the current work, velocity data for both the bottom and middle sections has been sought to be presented. It is thought to be truly intriguing to measure the velocity field precisely at the transition region between the bottom section and the fully developed middle section.

- It is observed that velocity fluctuations are higher in the pilot-scale setup, and the mean velocity profile is also more parabolic in nature in the case of the pilot-scale setup. Though a mean downward motion is observed even when adjusted to the wall section in current work with the pilot-scale setup. According to Anantharaman et al., (2017) solids with a larger diameter are less likely to move downward near the wall region. It will be interesting to investigate whether there is a mean downward motion of particles near the wall in cases with a higher riser diameter (20 cm or above).
- In the current work, scale-up relation is developed for mean axial velocity only. It is important to develop scale-up relation that take into account the root mean square (RMS) velocities to predict outcomes more accurately, especially when dealing with meso-scale structures in the system. These relations play a pivotal role in enhancing our ability to make more precise predictions and informed decisions, contributing significantly to various fields of study and applications.

References

- Anantharaman, A., Issangya, A., Karri, S.B.R., Findlay, J., Hrenya, C.M., Cocco, R.A., Chew, J.W., 2017. Annulus flow behavior of Geldart Group B particles in a pilot-scale CFB riser. *Powder Technol.* 305, 816–828.
- Bhusarapu, S.B., 2005. Solids Flow Mapping In Gas-Solid Risers. D.Sc Thesis, Washington University, Saint Louis, Missouri, USA.
- Godfroy, L., Patience, G.S., Chaouki, J., 1999. Radial Hydrodynamics in Risers. *Ind. Eng. Chem. Res.* 38, 81–89.
- Kamalanathan, P., 2016. Investigation of Gas – Solid Circulating Fluidized Bed at Two Scales Using Experimental and Numerical Techniques. PhD Thesis, Indian Institute Of Technology Guwahati, India.
- Kamalanathan, P., Kalo, L., Pant, H.J., Upadhyay, R.K., 2017. Effect of dynamic bias on accuracy of radioactive particle tracking (RPT) technique at different data acquisition frequencies. *Appl. Radiat. Isot.* 128, 13–21.
- Rhodes, M.J., Wang, X.S., Cheng, H., HIRAMA, T., Gibbs, B.M., 1992. Similar profiles of solid flux in circulating fluidized-bed risers. *Chem. Eng. Sci.* 47, 1635–1643.
- Zhu, J., Bi, H.T., 1995. Distinctions Between Low Density and High Density CFB. *Can. J. Chem. Eng.* 73, 644–649.

Appendix A: Axial Dispersion Model

The solids dispersion in the risers is grossly characterized by a one-dimensional axial dispersion model (ADM). The solids axial Peclet number and the axial dispersion coefficient found by fitting the ADM in the time domain to the E-curve are indicated in the plots.

$$\frac{\partial C}{\partial t} = D \frac{\partial^2 C}{\partial x^2} - u \frac{\partial C}{\partial x} \quad \text{A.1}$$

t = time of tracer in the reactor.

C = concentration at time t .

Z = distance of the detector from the inlet, In this case, height from the inlet.

u = Velocity of fluid.

D = Axial dispersion coefficient.

In dimensionless form where $z = \frac{(ut+x)}{L}$ and $\theta = \frac{t}{\bar{t}} = \frac{tu}{L}$, the basic differential equation representing this dispersion model becomes

$$\frac{\partial C}{\partial \theta} = \left(\frac{D}{uL} \right) \frac{\partial^2 C}{\partial z^2} - \frac{\partial C}{\partial z} \quad \text{A.2}$$

It is evident that in the context of ADM, a concentration versus time plot is essential. However, with the single tracer particle RTD technique, generating a concentration versus time plot not feasible. Instead, the scenario of multiple passes through the riser is considered. As the tracer particle traverses the entry detector, it registers a peak on detector 1 count. Similarly, peaks are observed on detectors D2, D3, D4, and D5 upon passage. Similarly, multiple passes of the tracer and time of flight are recorded. This multiple pass is considered the group of tracer

particles and pulse injection from the inlet. The time of flight between detectors is derived from data collected through multiple passes, leading to the generation of a histogram diagram based on this time of flight data. However, to convert this data into an E curve, the histogram plot undergoes normalization as described in the equation below.

$$E(t) = \frac{f(t)}{\sum f(t) * \Delta t} \quad \text{A.3}$$

$E(t)$ = Normalized histogram points, equivalent to the RTD E curve.

$f(t)$ = frequency for histogram,

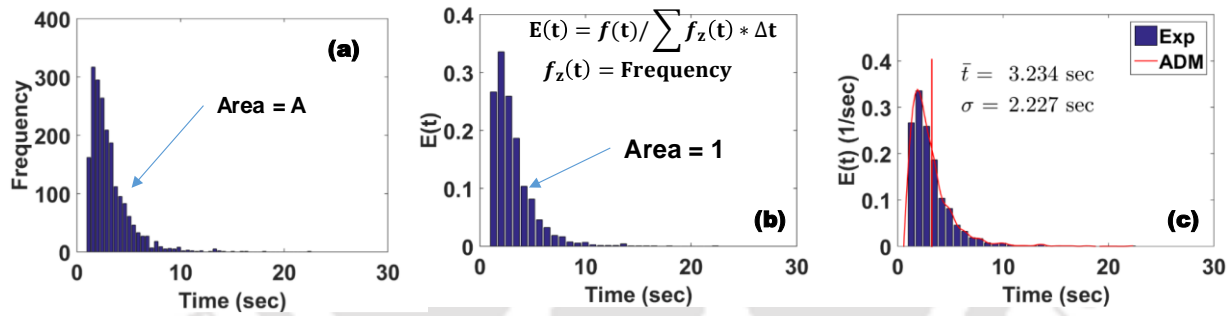


Figure A1: Evolution of histogram of time of flight to E curve.

Meantime \bar{t} and standard deviation σ , are then calculated from E plot.

Based on the particle flow across the boundary there could be two kinds of boundary condition

Closed-Closed boundary condition:

In a closed system, where no particles flow across boundaries, the solute concentration remains constant over time. Recent observations indicate that particles occasionally fall and cross the

detector multiple times, particularly in conditions of lower gas velocity. Consequently, the closed-closed boundary condition proves unsuitable. The equation for the closed-closed boundary condition is provided below.

$$\sigma_{\theta}^2 = \frac{\sigma_t^2}{\bar{t}^2} = 2 \left(\frac{D}{uL} \right) + 2 \left(\frac{D}{uL} \right)^2 [1 - e^{-uL/D}] \quad \text{A4}$$

Open-Open boundary condition:

In contrast, an open boundary condition allows the particles to flow into or out of the system. In many practical applications, such as chemical reactors open boundary conditions are more realistic. In current work, the time of flight is calculated when the tracer crosses the detector last time (if it crosses any detector multiple times during a single pass). So, open-open boundary condition is applicable in the current situation. The equation for open-open boundary condition is given below.

$$\sigma_{\theta,oo}^2 = \frac{\sigma_{t,oo}^2}{\bar{t}^2} = 2 \left(\frac{D}{uL} \right) + 2 \left(\frac{D}{uL} \right)^2 \quad \text{A4}$$

Dispersion number $\frac{D}{uL}$ is calculated from this equation. In the current dissertation, the Peclet number $\left(\frac{uL}{D}\right)$ is given and explained, which is just an inverse of vessel dispersion number.

It is important to note that unlike liquid tracers, solid single radioactive tracers don't have a long trailing effect. After a certain time, the frequency drops to zero, so there's no need to cut off any tails.

Appendix B: Reproducibility and stationarity

To validate the reproducibility and stationarity, the mean axial velocity and RMS velocity with 12, 24, 48 hours data are plotted in Figure B1 for the middle section of the laboratory scale riser, and 24, 48, and 96 hour data are plotted in Figure B2 for the middle section of the pilot scale riser.

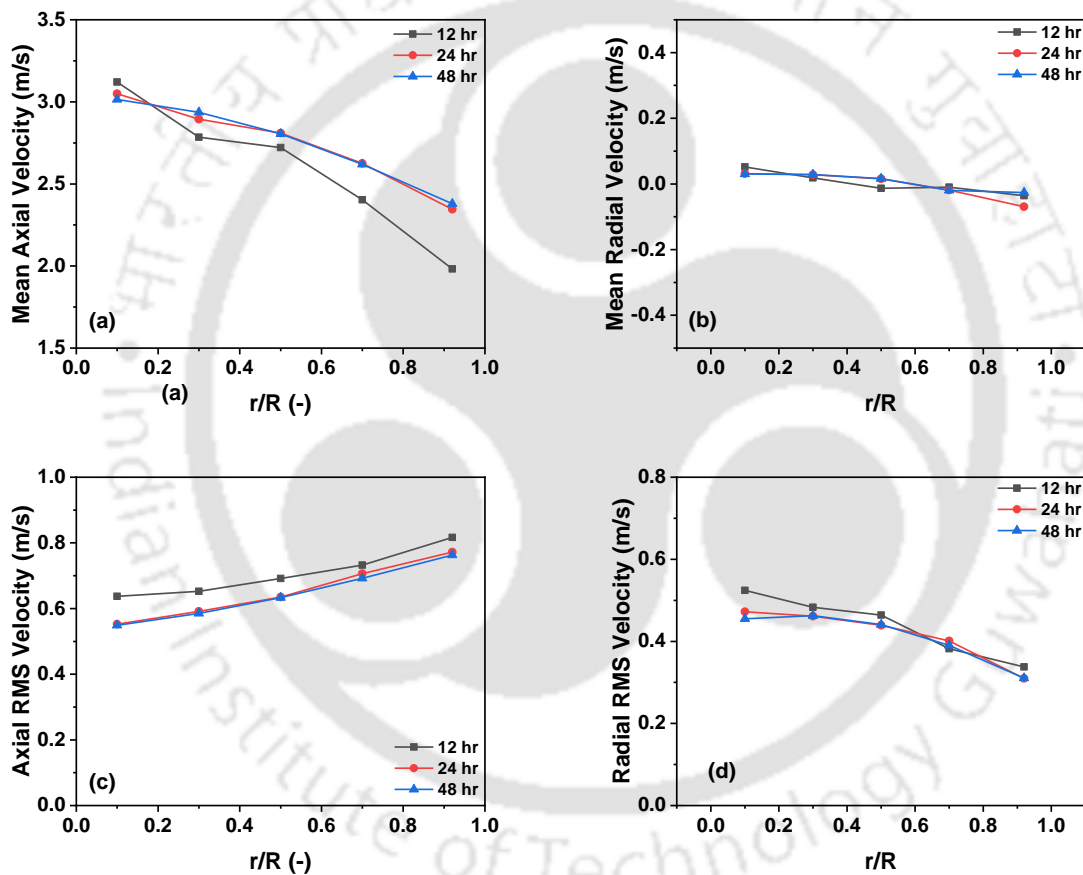


Figure B1: Validation of stationarity (a) mean axial velocity, (b) mean radial velocity, (c) axial RMS velocity and (d) radial RMS velocity for middle section of pilot scale riser at $G_s = 100$ $\text{kg/m}^2\text{s}$, $U_g = 8$ m/s .

Figures B1 and B2 show validation of stationarity for mean axial, mean radial, axial RMS and radial RMS velocity in the middle section. For the laboratory scale riser, there was no remarkable change obtained in the plot after 24 hours of data collection, even though the number of occurrences increased with an increase in the number of data points. For the pilot scale riser, there was no remarkable change obtained in the plot after 48 hours of data collection. This confirmed the reproducibility and stationarity of the RPT experiments. In order to confirm this, stationarity for all operating conditions was verified.

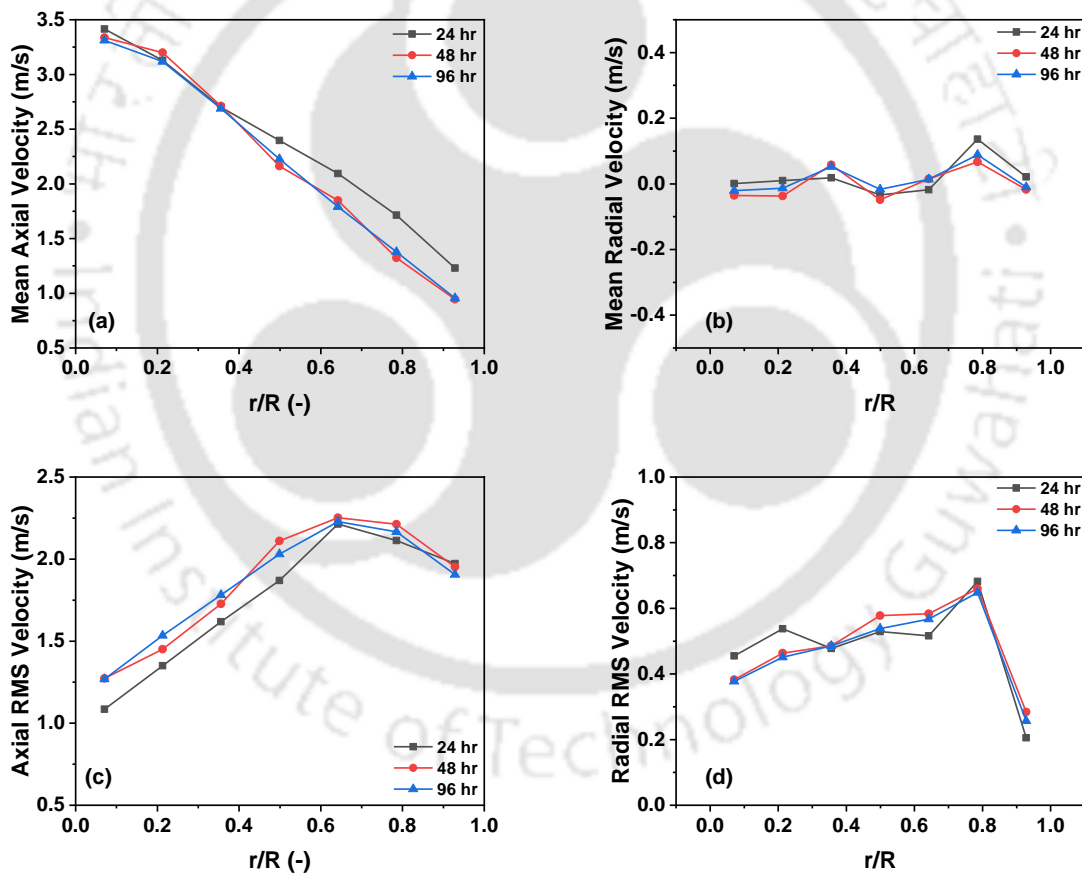


Figure B2: Validation of stationarity (a) mean axial velocity, (b) mean radial velocity, (c) axial RMS velocity and (d) radial RMS velocity for middle section of pilot scale riser at $G_s = 150 \text{ kg/m}^2\text{s}$, $U_g = 7.6 \text{ m/s}$.



BIO-DATA

Trilokpati Tribedi

Date of Birth : 20th July 1993

Place of Birth : Uttar Dinajpur, India

Degrees : B.E. Chemical Engineering, June 2014

Jadavpur University, Kolkata, India

M.Tech. Chemical Engineering (Petroleum Science and Technology), July 2016

Indian Institute of Technology Guwahati, Guwahati, India

Ph.D., Chemical Engineering, April 2024

Indian Institute of Technology Guwahati, Guwahati, India

Publications:

National Conferences:

Tribedi, T., Kamalanathan, P., Baro, R.K., Upadhyay, R. K. Simulation of Gas-Solid CFB Riser Using EMMS Drag Model. CHEMCON 2015, IIT Guwahati, India, 27th - 30th, December, 2015.

Kamalanathan, P., Tribedi, T., Pant. H. J, and Upadhyay, R.K. Dense Discrete Phase Model(DDPM) Simulation of Circulating Fluidised Bed(CFB) Riser, CHEMCON 2015, IIT Guwahati, India, 27th - 30th December, 2015.

International Conferences:

Kamalanathan, P., Tribedi, T., Pant. H.J, and Upadhyay, R.K. Experimental Study of Circulating Fluidized Bed Using Radioactive Particle Tracking Technique. GLS 12, New York, USA, 28th June to 1st July 2015.

Kamalanathan, P., Tribedi, T., Pant, H.J., and Upadhyay, R.K. Investigation of circulating fluidized bed using radioactive particle tracking and Euler-Euler simulation. 3rd Indo-German Workshop 2016, IIT Guwahati, India, 23rd - 26th February, 2016.

Tribedi, T., Kamalanathan, P., Upadhyay, R. K. Investigation of gas-solid flow behavior of circulating fluidized bed riser using pressure probe data and gamma-ray densitometry. CAMURE 10, Qingdao, China, 7th - 10th July 2017.

Tribedi, T., Kamalanathan, P., Baro, R.K., Upadhyay, R. K. Upadhyay Nonlinear Modeling of Chaotic Dynamics in a Circulating Fluidized Bed, NICSTAR 2018 NAARRI, Mumbai, India 2018 NICSTAR-2018.

Tribedi, T., Pant, H. J., Tiwari, P., Upadhyay, R.K., Details Analysis of Solid-Phase velocity of Pilot-Scale Circulating Fluidized Bed Riser Using Radioactive Particle Tracking. ISCRE 26 & APCRE 9, IIT Delhi India, 5th - 8th December, 2021.

Tribedi, T., Parveen, R., Tiwari, P., Upadhyay, R. K. Solids residence time distribution studies through single particle tracer in circulating fluidized bed riser. ISCRE 26 & APCRE 9, IIT Delhi India, 5th - 8th December, 2021.

Journals:

Tribedi, T., Pillajetti, P., Kumari, R., Pant, H.J., Tiwari, P., Upadhyay, R.K., 2022. Measurements of Solid Velocity in a Pilot-Scale Geldart's Group B Circulating Fluidized Bed Using a Radioactive Particle Tracking Technique. Ind. Eng. Chem. Res. 61, 9110–9121.

Tribedi, T., Tiwari, P., Pant, H.J., Upadhyay, R.K., 2023. Solid Phase Macromixing Study in a Pilot-Scale Geldart Group B Circulating Fluidized Bed Riser Using Single Particle RTD and RPT Measurements. ACS Eng. Au 3, 165–172.

Tribedi, T., Tiwari, P., Pant, H.J., Upadhyay, R.K., 2023. Solid Flow Mapping at the Bottom Section of a Pilot-Plant Scale Riser with the Help of a Radioactive Particle Tracking Technique. *Ind. Eng. Chem. Res.* 62, 19133–19144.

